Solving low-Mach two-phase flows in closed domains : from pressure centering to a novel artificial compressibility method

Cong-Huan Phan

N°d'ordre NNT : **2021LYSEC33**

THESE de DOCTORAT DE L'UNIVERSITE DE LYON
opérée au sein de l'Ecole centrale de Lyon

Ecole Doctorale N° 162
ED MEGA

Spécialité de doctorat : Mécanique, Energétique, Génie Civil et Acoustique
Discipline : Mécanique des fluides

Soutenue publiquement le 09/09/2021 par :
Cong-Huan PHAN

Solving low-Mach two-phase flows in closed domains: from pressure centering to artificial compressibility

---

Devant le jury composé de :

VINCENT Stéphane	Professeur	Université Gustave Eiffel	Rapporteur
HOARAU Yannick	Professeur	Université de Strasbourg	Rapporteur
ABGRALL Rémi	Professeur	Universität Zürich	Président
PELANTI Marica	Maître de conférences	ENSTA Paris	Examinatrice
CORRE Christophe	Professeur	Ecole Centrale de Lyon	Directeur de thèse
BECCANTINI Alberto	Chercheur	CEA Saclay	Co-directeur de thèse

Acknowledgments

Every story has an end and so does my Ph.D thesis at the CEA. At least, it was a joyful ending where I was still able to make a presentation in front of many members of the laboratory DYN and some members of the Ph.D committee, since the pandemic situation in France allows us to have more freedom in daily life. However, I understand that the end of a Ph.D thesis is just the new beginning for ones who continue the research career.

On this occasion, I would like to send my acknowledgment to many people that helped me a lot during my Ph.D thesis. First of all, I would like to thank my advisors: Professor Christophe Corre and Doctor Alberto Beccantini who taught and mentored me many things and helped me grow up in research. Christophe, you are such a dedicated professor that always had time for the project whenever needed even in the weekends, though I know that you are always very busy. I think you should take more time taking care of yourself so that you are able to mentor more Ph.D students. Alberto, you helped me a lot, not only on the technical aspect but also on my personal life. I remembered the time that you were on your motorcycle buying drugs for me and my wife or milk for my daughter when we were both sick because of Covid. There were so many things to remember. It was my honor to work with you both for many years and I hope that we can still collaborate on different projects in the near future.

Finally, I would like to thank my family: my parents in Vietnam, my little daughter Charlotte Minh Uyen and especially my wife Minh Tuyen. I know that you have suffered a lot since the presence of our little daughter. Our life in France was not easy and the pandemic situation pushed us to a lot of difficulties and stress. It was thanks to your continuous encouragement, your patience and your time taking care of our daughter that my burden and my worry decreased. Charlotte, I do not know if you are the motivation or the main complexity and worry of my life. I was sometimes very happy and motivated when seeing your smile and I was sometimes very angry when you cried all the day or when you were sick and my head was unable to concentrate anymore on my work. However, at any situations, it always ends by my love for you. When you grow up, see and understand my words, you should be very proud of your parents since we did not give up and you should take this as example when facing difficulties in your future. I just want to say that I love you both and I hope that many years later, when having a brighter future and looking back at these difficult times, we feel appreciative for what we have been through.

Contents

AC	*Artificial compressibility*
ALE	*Arbitrary Lagrangian-Eulerian Method*
CFL	*Courant-Friedrichs-Lewy number*
DEM	*Discrete equation method*
DEM-LM	*Discrete equation method in the low-Mach number regime*
EOS	*Equation of state*
HCDA	*Hypothetical core disruptive accident*
IC	*Initial condition*
RP	*Riemann problem*
SG-EOS	*Stiffened gas equation of state*
UDCS	*Upwind Downwind Controlled Splitting*
WPIC	*Well-prepared initial condition*

Nomenclature

$(\cdot)_k$	Corresponding variable of phase k
$(\hat{\cdot})$	Dimensionless variable
α	Volume fraction
$\mathcal{U}$	Vector of conservative variables
$\mathcal{W}$	Vector of primitive variables
ρ	Density
$\mathbf{F}$	Vector of numerical flux estimating the physical one $\mathbf{f}$
$\mathbf{U}$	Vector of averaged conservative variables
$\mathbf{Y}$	Vector of mass fractions
$\mathbf{v}_m$	Vector of mesh velocity
c	Physical sound speed
C_s	Shock speed
c_{AC}	Artificial sound speed
e	Internal energy per unit mass
e^t	Total energy per unit mass
eff	Efficiency factor
k	Phase indicator
$L(t)$	Effective length of the 1D planar piston
L_0	Maximum length of the 1D planar piston
M	Mach number
P	Thermodynamic pressure

p	Total pressure
p'	Dynamic pressure
R_0	Initial radius of the cylindrical piston
R_{ext}	Maximum radius of the cylindrical cylinder
t_f	Final time of the simulation
t_m	Mounting time of the piston velocity
u	Flow velocity in 1D
u_m	Mesh velocity in 1D
V_p	Piston velocity
X_k	Characteristic function
$\mathbf{v}$	Vector of flow velocity

List of Figures

List of Tables

Introduction

Industrial context: nuclear safety

High pressure bubble expansion in liquid is involved in several safety problems studied in the Nuclear Industry, such as BORAX-type [1] accidents in pool-type experimental reactors or Hypothetical Core Disruptive Accident (HCDA) in a liquid-sodium fast breeder reactor. A BORAX-type accident involves a high-pressure bubble created by the interaction of melted metal materials with water. A typical accident of this type has occurred (USA, 1961) for the SL-1 reactor (Stationary Low Power Reactor Number One) (see Figure 1).

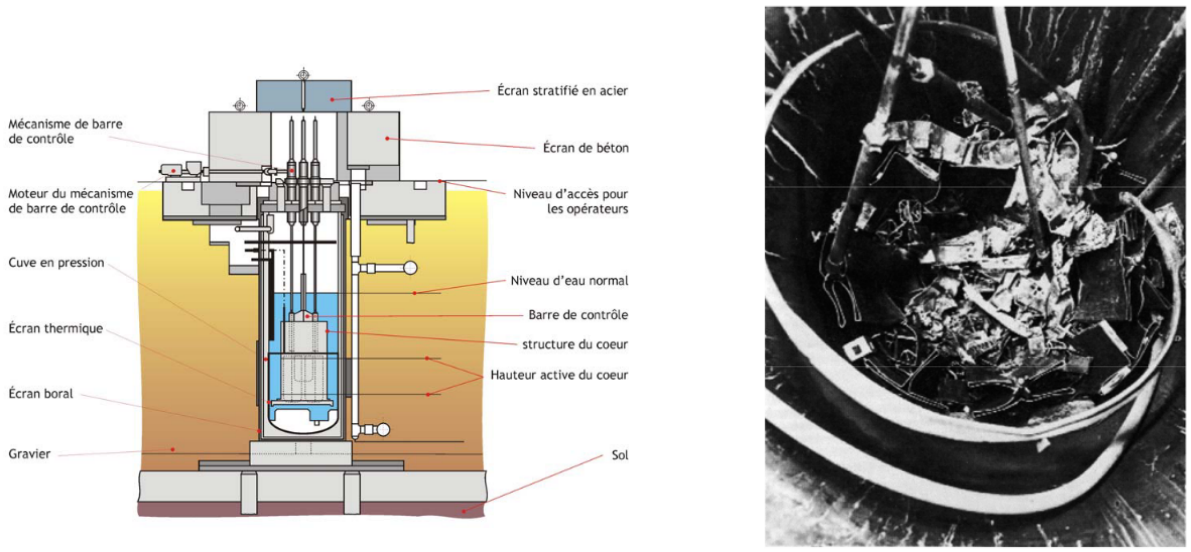

Figure 1: Schematic view of reactor SL-1 (left); three mechanism of control rods ("mécanisme de barre de contrôle" on the left figure) were damaged (right) after the BORAX-type accident in 1961 [Couturier, 2011].

For a liquid-sodium fast breeder reactor, the scenario of an HCDA supposes the reactor core has partially melted and the molten fuel chemically interacts with the liquid sodium to produce a large quantity of gaseous components. The explosive expansion of the high-pressure gas bubble thus formed yields significant loads on the reactor vessel. A series of experiments corresponding to the HCDA configuration has been performed at the CEA on the test-rig MARA2 . This test-rig, displayed in Figure 2, is of a reduced scale 1/30 with respect to a full scale containment. In the MARA2 experiment, a solid explosive material is ignited in water instead of sodium. Sensors are positioned at various locations in the containment in order to measure the time evolution of flow fields such as pressure, density, velocity and displacement of the structure. These measurements provide the validation basis for nuclear safety computational codes. Before reviewing some of the numerical difficulties raised by the simulation of such a bubble expansion problem, let us briefly describe some of the key physical features of this flow configuration.

[1] BORAX stands for BOiling water ReActor eXperiment [Couturier, 2011].

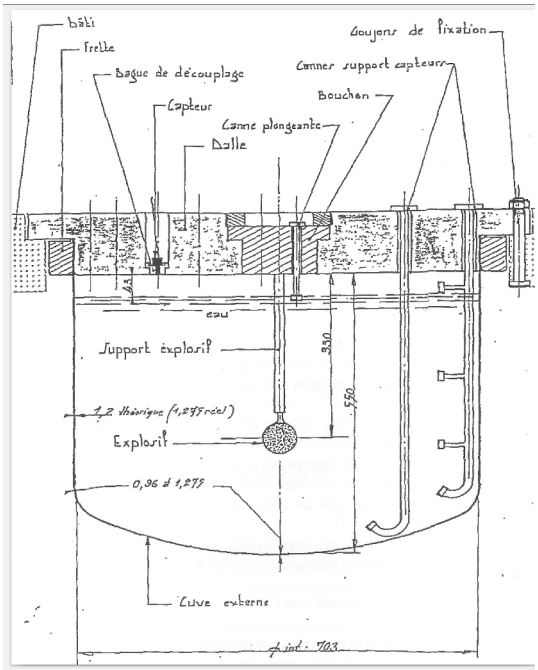

Figure 2: MARA experiment to study the HCDA at 1/30 of the full scale [Galon, 2002]. Note the sphere containing the explosive material at the center of the liquid (water) volume in the vessel.

Bubble expansion: physical description

The primary physical phenomena are graphically illustrated in Figure 3. In a first stage, after the combustible-liquid contact, a first pulse of pressure or a shock wave is dispatched radially outward and imparts a large momentum to the liquid (Figure 3, left). The intensity of the shock wave falls off rapidly as a consequence of the multidimensional expansion. In a second stage, due to this large momentum, a vapor sphere or vapor bubble begins to expand in the confined medium of liquid initially at rest (Figure 3, right). Such motion creates the second pulse of pressure which is much less intense than the first one but still higher than the hydrostatic pressure. It also contributes to the motion of the surrounding medium.

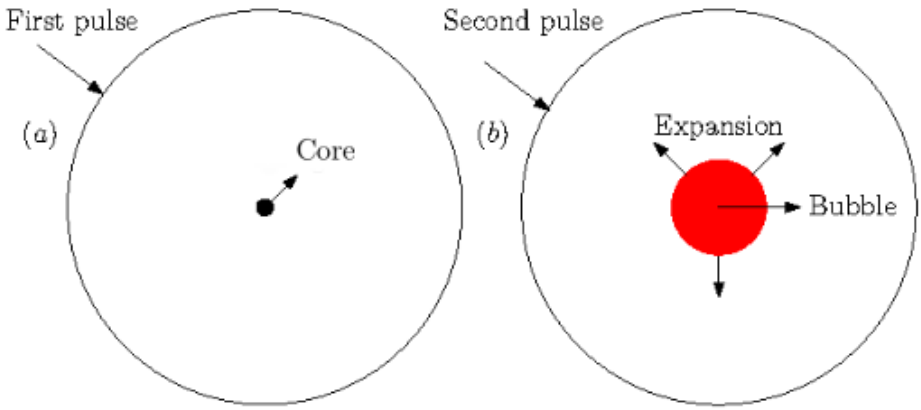

Figure 3: Primary physical phenomena for HCDA: (a): First pulse, (b): Second pulse and bubble expansion.

It is clear that for a *short time* after the initial explosion, the flow is not in the low-Mach number regime and the pressure waves are responsible for possible damage of a structure. Such regime does not last long

however and one quickly deals with a flow is in the low-Mach regime since the pressure waves are physically dissipated and moreover because their intensity, as already mentioned, rapidly decreases in time due to multidimensional effects. In *long time*, it is the kinetic energy of the liquid rather than the pressure waves that is responsible for the deformation or even the rupture of the containment structure. In this work, we mainly focus on the low-Mach stage of the problem where we have a (slow) expansion of the bubble accompanied by the propagation of acoustic waves of small amplitude. .

Numerical solution of a HCDA-type problem

As briefly discussed in the previous paragraph, the HCDA problem involves two distinct scales: the fast-propagating scale of pressure waves and the (slow) fluid scale of bubble and liquid. An incompressible model is therefore not suited to the HCDA simulation as it will not account for the compressible flow features. Consequently, when computing the HCDA problem or similar nuclear safety problems, compressible solvers are retained, generally based on a finite volume method of Godunov type. Approximate Riemann solvers are well suited for compressible flow calculation and can be extended to deal with two-phase (liquid-gas) flows governed by hyperbolic conservation law systems. However, they display some issues when applied to flow computations with a wide range of Mach number [Rieper and Bader, 2009]: an efficiency or stiffness issue and an accuracy issue.

The efficiency problem comes from the fact there is a large disparity between the speed of the acoustic waves c and the fluid velocity $\mathbf{v}$ in the low-Mach case: $c >> |\mathbf{v}|$. For compressible solvers, the CFL number is determined by the speed of the fastest wave, *i.e.* that of the acoustic waves instead of the speed of the fluid despite the fact that the acoustic waves do not actually play a dominant role in the low-Mach analysis:

$$\Delta t = CFL \times min\left(\frac{\Delta x}{|\mathbf{v}|}, \frac{\Delta x}{|\mathbf{v}| + c}\right) = CFL \times \frac{\Delta x}{|\mathbf{v}| + c} \approx CFL \times \frac{\Delta x}{c}$$

The CFL stability condition yields therefore a very small time step leading to a lack of efficiency of compressible solvers.

The accuracy problem was initially pointed out by [Volpe, 1993] and can be illustrated using an example taken from [Dellacherie, 2010]. The simple configuration under study is the inviscid flow through a 2D channel with an upper straight wall and a lower wall displaying a bump (see Figure 4). The flow is entering the channel with a velocity such that the inlet Mach number (based on the inlet velocity and the inlet speed of sound computed from the inlet temperature) is small, equal to $M_{in} = 10^{-2}$. The discrete steady solution obtained on a rather coarse mesh using the standard Roe solver is reported in Figure 4. It is found that this standard Roe scheme is actually unable to converge to the expected quasi-incompressible steady-state and provides a totally spurious numerical solution. The lack of accuracy of standard compressible solvers when computing low-Mach flows has been explained in [Guillard and Viozat, 1999] for the Roe scheme or in [Guillard and Murrone, 2004] for the Godunov scheme, by performing a rigorous asymptotic analysis at the discrete level. It turns out that the incompressible pressure perturbation of order $\mathcal{O}(M^2)$ is falsely computed, at the discrete level, as a term of order $\mathcal{O}(M)$, leading to the previously illustrated spurious numerical results.

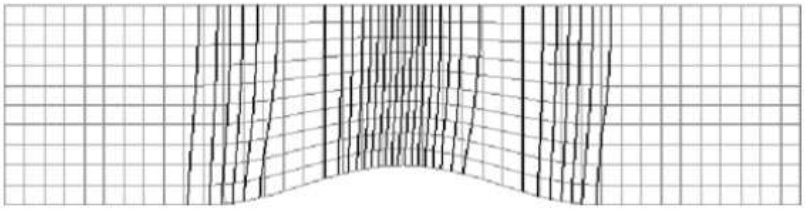

Figure 4: Pressure contours at $M = 10^{-2}$. Standard Roe scheme [Dellacherie, 2010].

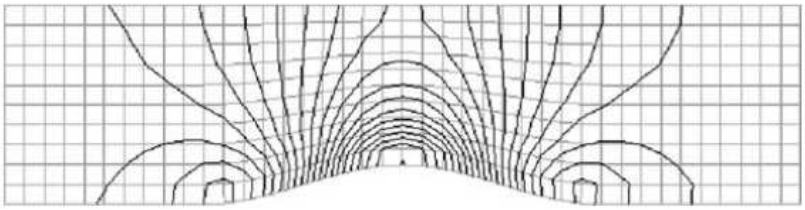

Figure 5: Pressure contours at $M = 10^{-2}$. Low-Mach Roe scheme [Dellacherie, 2010].

Various methods have been developed in order to circumvent the stiffness and lack-of-accuracy issues displayed by conventional approximate Riemann solvers:

- The preconditioning method of Turkel [Turkel, 1987] originally solves the stiffness problem. The time-derivative of the vector of conservative variables is premultiplied by a suitable preconditioning matrix with the purpose of scaling the eigenvalues of the system to similar orders of magnitude. As a result, the disparity in wave-speeds is removed and the convergence towards a steady-state solution is accelerated. As a side effect, it is also successful in rescaling the wrongly computed pressure perturbation at $\mathcal{O}(M)$ to the correct order of magnitude [Miczek, 2012, Miczek et al., 2015]. The Roe-Turkel flux preconditioning technique for steady state flows can also be adapted for time-dependent flow [Guillard and Viozat, 1999]. This is achieved by applying the preconditioning matrix only on the upwind dissipation term. The Roe-Turkel method has been recently extended to the two-phase gas-liquid case in [Pelanti, 2017]. However, the approach filters acoustic waves as shown in [Bruel et al., 2019] for instance and is also proved to be expensive as one must decrease significantly the time step ($\Delta t \approx O(M^2)$) to guarantee the numerical stability.

- The method of [Dellacherie, 2010, Dellacherie et al., 2016] relies on the centering of the pressure term in the numerical flux. The implementation of this method is quite simple and it was shown to be able to fix the accuracy issue for physical problems free of acoustic waves (see the low-Mach channel flow in Figure 5). For problems where acoustic waves are present, it will be shown later in this work that the method is unstable due to a lack of numerical viscosity. Moreover, the fix has been limited up to now to single-phase flow problems (perfect gas flows) and the efficiency problem still remains.

- [Rieper, 2008, Rieper and Bader, 2009] have proved the accuracy issue of low-Mach computations using approximate Riemann solvers can be actually fixed by using triangular meshes (in 2D and grids with tetrahedra in 3D). The approach is interesting since it does not modify the underlying numerical schemes. However, using purely triangular or tetrahedral grids is not always desirable, for high-Reynolds number flows for instance, and the efficiency problem remains open.

It is also possible to turn to alternative solution strategies:

- The asymptotic approach introduced by [Paolucci, 1982] and further discussed in [Beccantini et al., 2008], [Roller et al., 2005], [Rieper, 2008] expands flow variables in power of the Mach number and

injects them into the compressible equations yielding a so-called asymptotic system, free of acoustic waves. This method seems to be a good candidate for approximating loads applied on a structure. However, the main remaining issue is how to efficiently solve the asymptotic system. Moreover, the method is still limited to single-phase flow problems.

- When focusing on the calculation of a quasi-incompressible flow with a solution strategy taking advantage of an existing framework targeted on hyperbolic systems of conservation laws, the artificial compressibility method originally developed by Chorin [Chorin, 1967] appears as an option. Note that it was also extended in [Nourgaliev et al., 2004] to deal with unsteady multifluid flows, using a level set approach to describe the fluid-fluid interface. However, in the present work, as will be described in chapter 4, the Discrete Equation Method (DEM), already implemented in the Europlexus code to tackle multiphase flows, is the approach of choice which should be extended to deal with low-Mach configurations.

It can be stated there is currently no off-the-shelf numerical method or strategy that would readily provide an efficient and accurate numerical solution for low-Mach two-phase flow problems. This observation motivates the present PhD thesis, the objective of which is to develop the expected numerical strategy building on available tools implemented in the Europlexus code, namely approximate Riemann solvers, DEM for multiphase flows and Arbitrary Lagrangian Eulerian method to deal with fluid-structure interaction. The final application targeted in this work is an HCDA-type problem, that is a bubble expansion in a closed vessel with the interaction between the flow and the containment walls taken into account.

Thesis contribution

To investigate the numerical low-Mach problems encountered when computing two-phase flows, we first proceed by analyzing the accuracy issue for single-phase flows of liquid with the purpose of understanding the numerical behavior of 1-D and multi-D problems including open and closed computational domains. Some available numerical fixes are thus adapted to the liquid governed by the Stiffened Gas Equation of State (SG-EOS) and are applied to compute a series of numerical test problems. It will be shown that such fixes are indeed curing the accuracy issue, while leaving the efficiency issue an open problem.
Motivated by the development of a novel numerical strategy that can not only solve the accuracy problem for low-Mach two-phase flow problems but also reduce the computational cost, we propose next the so-called Discrete Equation Method - Low Mach (DEM-LM) numerical strategy. The method extends to the low-Mach number regime the existing DEM method [Abgrall and Saurel, 2003] by borrowing ideas from the Artificial Compressibility (AC) approach. It can be combined with the anti diffusive UDCS approach [Tang, 2012] capable of sharply capturing fluid/fluid interface. Moving boundaries can also be taken into account by employing the ALE approach.

Outline

The thesis is divided in two parts, as summarized in Tables 1-2.
In the first part of the thesis, the low-Mach accuracy problem is discussed for liquid flows, with a focus on a pressure centering strategy proposed in the literature:

- In Chapter 1, we review the reasons for the lack of accuracy of standard compressible solvers when computing low-Mach flows. Some available numerical fixes, in particular the pressure centerin strategy proposed by Dellacherie [Dellacherie, 2010,Dellacherie et al., 2016] is adapted to the computation of low-Mach liquid flows governed by the stiffened gas equation of state.

- In Chapter 2, we perform a series of test cases to assess the advantages and drawbacks of the standard compressible schemes with and without low-Mach correction.

In the second part of the thesis, we present the development of a novel numerical method able to efficiently compute accurate solutions of two-phase flows in the low-Mach number regime. The strategy builds upon existing methods available in the Europlexus code used throughout the thesis (DEM method for two-phase flows, ALE method for fluid-structure interaction) and introduces an original Artificial Compressibility approach. The development is described from single-phase low-Mach computations to the application to the MARA problem (HCDA experiments):

- In Chapter 3, the new Artificial Compressibility (AC) method is first developed for single-phase flows and analyzed on a series of piston test problems.
- In Chapter 4, we briefly recall the Discrete Equation Method (DEM) approach used for computing two-phase flow problems.
- In Chapter 5, the new method presented in Chapter 3 is combined with the DEM method to tackle low-Mach two-phase flows. The new method is denoted as DEM-LM where LM stands for Low Mach.
- In Chapter 6, the original DEM and novel DEM-LM methods are applied to the computation of the MARA problem (HCDA-type problem involving the expansion of a bubble in a closed domain filled with liquid), with and without fluid-structure interaction.

Conclusions on the achievements of the thesis and detailed perspectives of future developments to address the missing steps not yet covered are finally provided.

	Objectives
Chapter 1	• Analyze the low-Mach accuracy problem through the asymptotic behavior of standard compressible solvers applied to the computation of low-Mach single-phase flows governed by the stiffened gas equation of state. • Propose and assess low-Mach correction methods to fix the accuracy problem.
Chapter 2	• Evaluate the accuracy of numerical solutions given by standard and low-Mach correction methods described in Chapter 1. Test problems: • 2D cylindrical axisymmetric piston: assess the accuracy of standard schemes with the presence of acoustic waves. • 2D Gresho vortex: assess the accuracy of standard schemes with and without low-Mach correction when computing the slow fluid scale. • Gresho vortex acoustic: assess the accuracy of standard schemes with low-Mach correction when computing fast acoustic and slow fluid scales. • 1D low-Mach shock tube: assess the accuracy of standard schemes with low-Mach correction when computing wave propagation problems.

Table 1: Organization of the thesis: Part I: Pressure centering as a fix for low-Mach liquid flows.

	Objectives
Chapter 3	• Review existing methods based on the artificial compressibility approach for computing low-Mach single-phase flow problems. • Propose a novel numerical strategy to fix the drawbacks observed in classical approaches. Test problems: • 1D planar piston problem with acoustic waves: demonstrate the advantages and drawbacks of the classical methods and evaluate the accuracy as well as the efficiency of the new strategy. • 1D and 2D cylindrical piston problems with well-prepared initial condition: evaluate the accuracy and the efficiency of the new method in computing closed domain problems without presence of acoustic waves.
Chapter 4	• Overview of the Discrete Equation Method (DEM) used for solving two-phase flow problems and analysis of its numerical solutions in the low-Mach number regime. Test problem: • 1D bubble expansion problem: compare the solutions given by the asymptotic (analytical) model and the DEM method in the low-Mach number regime.
Chapter 5	• Extend the DEM method to the low-Mach number regime. The new method is named DEM-LM and is based on the numerical strategy introduced in Chapter 3 for single-phase flows. Test problem: • 1D low-Mach bubble expansion problem: compare the solutions given by the asymptotic model, the DEM and DEM-LM methods and evaluate the accuracy as well as the efficiency of the DEM-LM strategy.
Chapter 6	• Application to the industrial two-phase multidimensional test problem (MARA) with fluid structure interaction. Test problems: • 2D MARA problem: validate the DEM method in computing a fluid-structure problem. • 2D low-Mach MARA problem: evaluate the performance of the DEM-LM method by comparing its solutions with those given by DEM.

Table 2: Organization of the thesis: Part II: Development of a novel artificial compressibility method for low-Mach two-phase flows.

Part I

Pressure centering as a fix for low-Mach liquid flows

1

Analysis of exact and approximate Riemann solvers for low-Mach flows

Contents

Introduction

The purpose of this chapter is to review the reasons why exact or approximate Riemann solvers successfully used for compressible flow applications fail to provide accurate solutions of low-Mach single-phase flows. The diagnosis relies first on an asymptotic analysis in section 1.2 for the Euler equations briefly introduced in section 1.1. The same procedure is next applied at the discrete level in section 1.4 for some standard

numerical schemes briefly described in section 1.3.
The asymptotic analysis is in fact used by many researchers to analyze the low-Mach behavior of a finite volume scheme but has been usually applied to the case of flows in open domains [Guillard and Viozat, 1999, Guillard and Murrone, 2004]. We will extend the analysis in section 1.4 to the case of a closed domain, for one dimensional and multidimensional problems, as this is the case of interest in our work (with low-Mach flow in a containment as a final target).
Once understood the reasons for the lack of accuracy of low-Mach computations using conventional exact or approximate Riemann solvers, we adapt in section 1.5 corrections which have been proposed in the literature to compute accurately low-Mach flows. These corections, usually proposed for low-Mach flows of perfect gases, are adapted for liquid flows governed by the stiffened gas equation of state.

1.1 Euler equations

1.1.1 Conservative formulation

In a non-reacting (absence of chemical reaction) single-phase flow where the body forces (gravity, magnetic or electrical fields, etc), and the dissipation effects (related to the viscosity or thermal conductivity of fluid) are assumed to be negligible, the conservation equations describing the flow evolution form the compressible Euler system of equations. In its conservative form, the system can be written as:

$$\begin{aligned} \frac{\partial \rho}{\partial t} + \nabla \cdot (\rho \mathbf{v}) &= 0 \\ \frac{\partial (\rho \mathbf{v})}{\partial t} + \nabla \cdot (\rho \mathbf{v} \otimes \mathbf{v} + p\mathcal{I}) &= 0 \\ \frac{\partial \rho e^t}{\partial t} + \nabla \cdot ((\rho e^t + p)\mathbf{v}) &= 0 \end{aligned} \tag{1.1}$$

where the total energy per unit mass e^t is the sum of the internal energy per unit mass e and the kinetic energy per unit mass $\frac{1}{2}\mathbf{v} \cdot \mathbf{v}$. The velocity field is a three-component vector, for example in the Cartesian coordinate system $\mathbf{v} = (u, v, w)$ and $\mathcal{I}$ is the identity tensor. The pressure field is coupled with other fields and the above system is closed by an equation of state (EOS) which links pressure, density and specific internal energy:

$$p = p(\rho, e) \tag{1.2}$$

System (1.1) can be rewritten in compact form as:

$$\frac{\partial \mathcal{U}}{\partial t} + \nabla \cdot \mathbf{f} = 0 \tag{1.3}$$

with $\mathcal{U}$ the vector of conservative variables and $\mathbf{f}$ the physical flux:

$$\mathcal{U} = \begin{pmatrix} \rho \\ \rho \mathbf{v} \\ \rho e^t \end{pmatrix}, \quad \mathbf{f} = \begin{pmatrix} \rho \mathbf{v} \\ \rho \mathbf{v} \otimes \mathbf{v} + p\mathcal{I} \\ (\rho e^t + p)\mathbf{v} \end{pmatrix}$$

This conservative formulation is frequently used as it allows the calculation of discontinuities in flow (shocks, contact surfaces) since jump relationships at discontinuities are implicitly contained in the flux vector $\mathbf{f}$.
It can be useful to study the Euler system in the case of a simple one-dimensional situation, where the conservative vector and the flux vector of the general system (1.3) become:

$$\mathcal{U} = \begin{pmatrix} \rho \\ \rho u \\ \rho e^t \end{pmatrix}, \quad \mathbf{f} = \begin{pmatrix} f_1 \\ f_2 \\ f_3 \end{pmatrix} = \begin{pmatrix} \rho u \\ \rho u^2 + p \\ (\rho e^t + p)u \end{pmatrix}$$

The one-dimensional Euler system may also be written in quasi-linear form:

$$\frac{\partial \mathcal{U}}{\partial t} + A(\mathcal{U})\frac{\partial \mathcal{U}}{\partial x} = 0 \tag{1.4}$$

with:

$$\mathcal{U} = \begin{pmatrix} u_1 \\ u_2 \\ u_3 \end{pmatrix} = \begin{pmatrix} \rho \\ \rho u \\ \rho e^t \end{pmatrix}, \; A(\mathcal{U}) = \frac{\partial \mathbf{f}}{\partial \mathcal{U}} = \begin{pmatrix} \frac{\partial f_1}{\partial u_1} & \frac{\partial f_1}{\partial u_2} & \frac{\partial f_1}{\partial u_3} \\ \frac{\partial f_2}{\partial u_1} & \frac{\partial f_2}{\partial u_2} & \frac{\partial f_2}{\partial u_3} \\ \frac{\partial f_3}{\partial u_1} & \frac{\partial f_3}{\partial u_2} & \frac{\partial f_3}{\partial u_3} \end{pmatrix}$$

1.1.2 Primitive formulation

Another useful formulation for the Euler equations, though not suitable for calculations involving shocks or strong discontinuities, is the primitive formulation which writes:

$$\begin{aligned} \frac{\partial \rho}{\partial t} + \mathbf{v}\cdot\nabla\rho + \rho\nabla\cdot\mathbf{v} &= 0 \\ \frac{\partial \mathbf{v}}{\partial t} + \mathbf{v}\cdot\nabla\mathbf{v} + \frac{1}{\rho}\nabla p &= 0 \\ \frac{\partial p}{\partial t} + \mathbf{v}\cdot\nabla p + \rho c^2\nabla\cdot\mathbf{v} &= 0 \end{aligned} \tag{1.5}$$

and describes the evolution of the so-called primitive variables, namely density, velocity and pressure. This formulation is fully relevant in the low-Mach number regime, devoid of discontinuities. The compact form of the primitive formulation in the 1D case can be written as:

$$\frac{\partial \mathcal{W}}{\partial t} + A(\mathcal{W})\frac{\partial \mathcal{W}}{\partial x} = 0$$

with:

$$\mathcal{W} = \begin{pmatrix} \rho \\ u \\ p \end{pmatrix}, \; A(\mathcal{W}) = \begin{pmatrix} u & \rho & 0 \\ 0 & u & 1/\rho \\ 0 & \rho c^2 & u \end{pmatrix}$$

The above primitive system is closed by defining the sound speed c:

$$c^2 = \frac{\partial p}{\partial \rho}\Big)_s = \frac{\left[\frac{p}{\rho^2} - \frac{\partial e}{\partial \rho}\Big)_p\right]}{\frac{\partial e}{\partial p}\Big)_\rho} \tag{1.6}$$

The eigenvalues of the matrix $A(\mathcal{W})$ correspond to the propagation velocities of the density, velocity and pressure waves:

$$\lambda_1 = u - c, \; \lambda_2 = u, \; \lambda_3 = u + c$$

Since these eigenvalues are real and distinct values, the 1D Euler system is said to be strictly hyperbolic [Toro, 2009].

1.1.3 Equation of state

The equation of state (EOS) closing the governing equations will be the stiffened gas EOS (SG-EOS) [Ivings et al., 1998] well suited to describe liquid flows:

$$p(\rho, e) = (\gamma - 1)\rho e - \gamma P_\infty \tag{1.7}$$

In (1.7), the first term represents the thermal agitation and the second term γP_∞ corresponds to the attractive effects of molecules leading to matter cohesion in liquid and solid states [Le Métayer and Saurel, 2016]. The correction of pressure P_∞ can be considered as the resistance of a medium to the compression (or the stiffness of a medium) while γ is an empirical constant characterizing its compressibility. For liquid water, these constants take the typical values $\gamma = 4.4$ and $P_\infty = 6.0 \times 10^8$.
Concerning a perfect gas such as air, the attractive effect disappears since the molecules are far from each other and can be supposed to evolve freely without interaction between them. Consequently, the constant P_∞ is equal to 0 and the SG-EOS (1.7) becomes:

$$p(\rho, e) = (\gamma - 1)\rho e$$

For a perfect gas, $\gamma = c_p/c_v$ and takes a value in the range $1 < \gamma < 2$ (for air $\gamma = 1.4$) with c_p and c_v the heat capacities respectively at constant pressure and constant volume.
It can be demonstrated by substituting (1.7) into (1.6) that the sound speed in a medium governed by the SG-EOS is given by:

$$c^2 = \frac{\gamma(p + P_\infty)}{\rho} > 0 \tag{1.8}$$

1.2 Dimensionless system and asymptotic analysis

1.2.1 Dimensionless system

In the particular case of the Euler system, the dimensionless form is beneficial when investigating the behavior of the system in the low-Mach number regime as will be discussed in section 1.2.2.
The primitive Euler equations in the multidimensional case are made non-dimensional by setting:

$$\hat{\rho} = \frac{\rho}{\rho_{ref}},\ \hat{\mathbf{v}} = \frac{\mathbf{v}}{v_{ref}},\ \hat{p} = \frac{p}{\rho_{ref} c_{ref}^2},\ \hat{c} = \frac{c}{c_{ref}},\ \hat{t} = \frac{t}{l_{ref}/v_{ref}},\ \hat{\mathbf{x}} = \frac{\mathbf{x}}{l_{ref}}$$

where the hat variables are dimensionless and normalized by reference (ref) states. The dimensionless Euler equations for the primitive formulation can be written as:

$$\begin{aligned}
\frac{\partial \hat{\rho}}{\partial \hat{t}} + \mathbf{v}\cdot\nabla\rho + \hat{\rho}\nabla\cdot\hat{\mathbf{v}} &= 0 \\
\frac{\partial \hat{\mathbf{v}}}{\partial \hat{t}} + \hat{\mathbf{v}}\cdot\nabla\hat{\mathbf{v}} + \frac{1}{M^2}\frac{1}{\hat{\rho}}\nabla\hat{p} &= 0 \\
\frac{\partial \hat{p}}{\partial \hat{t}} + \hat{\mathbf{v}}\cdot\nabla\hat{p} + \hat{\rho}\hat{c}^2\nabla\cdot\hat{\mathbf{v}} &= 0
\end{aligned} \tag{1.9}$$

The dimensionless system (1.9) introduces the Mach number (M) defined as the ratio between the fluid reference velocity and the reference sound speed:

$$M = \frac{v_{ref}}{c_{ref}} \tag{1.10}$$

System (1.9) is closed by defining the dimensionless sound speed $\hat{c}$:

$$\hat{c}^2 = \frac{\gamma(\hat{p} + \hat{P_\infty})}{\hat{\rho}} \tag{1.11}$$

We notice that the choice of the reference time t_{ref} in the above dimensionless system is based on the velocity of the (slow) fluid scale. This means that acoustic waves of small amplitude are neglected in the system. The choice of a reference time t_{ref} based on the acoustic speed c_{ref} yields another system with a focus on the acoustic scale (see [Rieper, 2008], section 2.3.2).

1.2.2 Asymptotic analysis in the low-Mach number regime

Many authors have used asymptotic analysis to study the behavior of the Euler equations as the Mach number tends to zero. For the primitive Euler equations, the primitive/physical variables can be developed in the power of the Mach number as:

$$\begin{aligned}
\hat{p}(\hat{\mathbf{x}},\hat{t},M) &= \hat{p}^{(0)}(\hat{\mathbf{x}},\hat{t}) + M\hat{p}^{(1)}(\hat{\mathbf{x}},\hat{t}) + M^2\hat{p}^{(2)}(\hat{\mathbf{x}},\hat{t}) + o(M^2)\\
\hat{\mathbf{v}}(\hat{\mathbf{x}},\hat{t},M) &= \hat{\mathbf{v}}^{(0)}(\hat{\mathbf{x}},\hat{t}) + M\hat{\mathbf{v}}^{(1)}(\hat{\mathbf{x}},\hat{t}) + M^2\hat{\mathbf{v}}^{(2)}(\hat{\mathbf{x}},\hat{t}) + o(M^2)\\
\hat{\rho}(\hat{\mathbf{x}},\hat{t},M) &= \hat{\rho}^{(0)}(\hat{\mathbf{x}},\hat{t}) + M\hat{\rho}^{(1)}(\hat{\mathbf{x}},\hat{t}) + M^2\hat{\rho}^{(2)}(\hat{\mathbf{x}},\hat{t}) + o(M^2)\\
\hat{c}(\hat{\mathbf{x}},\hat{t},M) &= \hat{c}^{(0)}(\hat{\mathbf{x}},\hat{t}) + M\hat{c}^{(1)}(\hat{\mathbf{x}},\hat{t}) + M^2\hat{c}^{(2)}(\hat{\mathbf{x}},\hat{t}) + o(M^2)
\end{aligned} \tag{1.12}$$

The leading order of the sound speed can be demonstrated to be linked to the leading order pressure and density terms. Indeed, by injecting (1.12) into (1.11) and neglecting $\mathcal{O}(M^2)$ terms, we obtain:

$$\begin{aligned}
\hat{c}^2 &= \frac{\gamma[\hat{p}^{(0)} + M\hat{p}^{(1)} + P_\infty]}{\hat{\rho}^{(0)} + M\hat{\rho}^{(1)}} = \frac{\gamma[\hat{p}^{(0)} + M\hat{p}^{(1)} + P_\infty]}{\hat{\rho}^{(0)}} \cdot \frac{1}{1 + M\dfrac{\hat{\rho}^{(1)}}{\hat{\rho}^{(0)}}}\\
&= \frac{\gamma[\hat{p}^{(0)} + M\hat{p}^{(1)} + P_\infty]}{\hat{\rho}^{(0)}} \left[1 - M\frac{\hat{\rho}^{(1)}}{\hat{\rho}^{(0)}}\right]
\end{aligned}$$

At the leading order $\mathcal{O}(M^0)$, the above relation yields:

$$[\hat{c}^{(0)}]^2 = \frac{\gamma(\hat{p}^{(0)} + P_\infty)}{\hat{\rho}^{(0)}} \tag{1.13}$$

In order to understand the asymptotic behavior of the continuous solutions, we suppose that the system (1.9) admits solutions of the form (1.12). By substituting (1.12) into the dimensionless system (1.9), we obtain (see for instance [Beccantini et al., 2008], [Roller et al., 2005], [Rieper, 2008] for fully detailed calculations):

$$\begin{aligned}
&(1.9)_2, \mathcal{O}(M^{-2}): && \nabla\hat{p}^{(0)} &&= 0\\
&(1.9)_2, \mathcal{O}(M^{-1}): && \nabla\hat{p}^{(1)} &&= 0\\
&(1.9)_2, \mathcal{O}(M^0): && \frac{\partial\hat{\mathbf{v}}^{(0)}}{\partial\hat{t}} + \hat{\mathbf{v}}^{(0)}\cdot\nabla\hat{\mathbf{v}}^{(0)} + \frac{1}{\hat{\rho}^{(0)}}\nabla\hat{p}^{(2)} &&= 0\\
&(1.9)_3, \mathcal{O}(M^0): && \frac{\partial\hat{p}^{(0)}}{\partial\hat{t}} + \hat{\mathbf{v}}^{(0)}\cdot\nabla\hat{p}^{(0)} + \hat{\rho}^{(0)}[\hat{c}^{(0)}]^2\nabla\cdot\hat{\mathbf{v}}^{(0)} &&= 0
\end{aligned} \tag{1.14}$$

where $(1.9)_2$ denotes the velocity evolution equation in system (1.9) while $(1.9)_3$ denotes the pressure evolution equation in the same system. The first and second equations of (1.14) are derived from the expansion of the momentum equation $(1.9)_2$ at the order $\mathcal{O}(M^{-2})$ and $\mathcal{O}(M^{-1})$. From these equations, we can state that the leading and the first order pressure terms are independent of space:

$$\begin{aligned}
\hat{p}^{(0)} &= \hat{p}^{(0)}(\hat{t})\\
\hat{p}^{(1)} &= \hat{p}^{(1)}(\hat{t})
\end{aligned}$$

From $(1.14)_3$, we can state that it is the second order pressure term that ensures the balance of forces in low-Mach flows. The respective roles of each pressure term have been discussed in [Klein, 1995, Roller et al., 2005]:

- The leading order term $\hat{p}^{(0)}$ is called the thermodynamic or background pressure.
- The first order term $\hat{p}^{(1)}$ plays the role of the acoustic pressure and satisfies the linear acoustic equations in the (fast) acoustic scale but is spatially constant in the (slow) fluid scale. In fact, due to the choice of t_{ref} which assumes that the low-Mach flow is free of acoustic waves, this term becomes a function of time. A choice of t_{ref} based on the acoustic speed c_{ref} yields the linear acoustic equations (see for instance [Rieper, 2008], section 2.3.2).
- The second order term $\hat{p}^{(2)}$ act as the balance-of-forces agent and can be regarded as the incompressible pressure or dynamic pressure.

As the leading order term for pressure is dependent on time only, $\hat{p}^{(0)} = \hat{p}^{(0)}(\hat{t})$, the equation $(1.14)_4$ becomes:

$$\nabla \cdot \hat{\mathbf{v}}^{(0)} = -\frac{1}{\hat{\rho}^{(0)}[\hat{c}^{(0)}]^2}\frac{d\hat{p}^{(0)}}{d\hat{t}} = f(\hat{t}) \tag{1.15}$$

The relation (1.15) is also called the compatibility condition. We emphasize that the divergence of the leading order velocity is a function of time only since $\hat{\rho}^{(0)}[\hat{c}^{(0)}]^2 = \gamma[\hat{p}^{(0)}(\hat{t}) + P_\infty]$. However, the leading order terms $\hat{\rho}^{(0)}$ and $\hat{c}^{(0)}$ are still functions of time and space as defined in (1.12). Despite this fact, we recognize that the density changes very little in the low-Mach number regime and therefore we can assume that it is constant up to the first order: $\hat{\rho}^{(0)} = \text{const}$. It follows that the leading order sound speed is only time-dependent: $\hat{c}^{(0)} = \hat{c}^{(0)}(\hat{t})$. The asymptotic expansion (1.12) reduces to:

$$\begin{aligned}
\hat{p}(\hat{\mathbf{x}},\hat{t},M) &= \hat{P}(\hat{t}) + M^2\hat{p}^{(2)}(\hat{\mathbf{x}},\hat{t}) + o(M^2)\\
\hat{\mathbf{v}}(\hat{\mathbf{x}},\hat{t},M) &= \hat{\mathbf{v}}^{(0)}(\hat{\mathbf{x}},\hat{t}) + M\hat{\mathbf{v}}^{(1)}(\hat{\mathbf{x}},\hat{t}) + M^2\hat{\mathbf{v}}^{(2)}(\hat{\mathbf{x}},\hat{t}) + o(M^2)\\
\hat{\rho}(\hat{\mathbf{x}},\hat{t},M) &= \hat{\rho}^{(0)} + M\hat{\rho}^{(1)}(\hat{\mathbf{x}},\hat{t}) + M^2\hat{\rho}^{(2)}(\hat{\mathbf{x}},\hat{t}) + o(M^2)\\
\hat{c}(\hat{\mathbf{x}},\hat{t},M) &= \hat{c}^{(0)}(\hat{t}) + M\hat{c}^{(1)}(\hat{\mathbf{x}},\hat{t}) + M^2\hat{c}^{(2)}(\hat{\mathbf{x}},\hat{t}) + o(M^2)
\end{aligned} \tag{1.16}$$

with:

$$\hat{P}(\hat{t}) = \hat{p}^{(0)}(\hat{t}) + M\hat{p}^{(1)}(\hat{t}) \tag{1.17}$$

From (1.16), we also conclude that the pressure fluctuation scales like the square of the Mach number. The pressure field in the original system (1.5) can be decomposed into the so-called homogeneous thermodynamic pressure $P(t)$ and the dynamic fluctuation $p'(\mathbf{x},t)$:

$$p(\mathbf{x},t) = P(t) + \underbrace{p'(\mathbf{x},t)}_{\mathcal{O}(M^2)}, \qquad p'(\mathbf{x},t) << P(t) \tag{1.18}$$

In the following, we define the so-called asymptotic system, derived by substituting the pressure decomposition (1.18) into the primitive Euler equations (1.5). For a multidimensional case, this asymptotic system writes:

$$\begin{aligned}
\frac{\partial\rho}{\partial t} &+ \mathbf{v}\cdot\nabla\rho &+ \rho\nabla\cdot\mathbf{v} &= 0\\
\frac{\partial\mathbf{v}}{\partial t} &+ \mathbf{v}\cdot\nabla\mathbf{v} &+ \frac{1}{\rho}\nabla p' &= 0\\
\frac{dP}{dt} &+ \rho c^2\nabla\cdot\mathbf{v} & &= 0, \quad P = P(t)
\end{aligned} \tag{1.19}$$

Note the contribution of the dynamic fluctuation $p'(x,t)$ can be neglected in the pressure evolution equation while it must be retained in the velocity equation evolution where it acts as the balance-of-forces agent. The divergence of velocity, is time-dependent only as $\rho c^2 = \gamma[P(t) + P_\infty]$.

Further simplifications:

By integrating the compatibility condition (1.15) over a volume $\mathcal{V}$ with boundaries $\mathcal{S}$ and using the divergence theorem, we obtain the identity:

$$\frac{1}{\hat{\rho}^{(0)}[\hat{c}^{(0)}]^2}\frac{d\hat{p}^{(0)}}{d\hat{t}} = -\frac{1}{\mathcal{V}}\int_{\mathcal{S}} \hat{\mathbf{v}}^{(0)} \cdot \mathbf{n} d\mathcal{S} \tag{1.20}$$

Depending on the physical problem under study, the relationship (1.20) can be further simplified.

- For a physical problem in an **open domain**, the volume $\mathcal{V}$ of the (potentially unbounded) domain can be made arbitrarily large so that the right-hand-side of (1.20) vanishes. The leading pressure becomes a constant, resulting in the divergence free constraint for incompressible flow. It also explains why $\hat{p}^{(0)}$ is also called the background pressure.

$$\frac{d\hat{p}^{(0)}}{d\hat{t}} = 0 \Rightarrow \nabla \cdot \hat{\mathbf{v}}^{(0)} = 0$$

- For a physical problem in a **closed domain** (with no-slip/periodic boundary conditions), (1.20) states that it is the boundary $\mathcal{S}$ of the domain which drives the leading order pressure term $\hat{p}^{(0)}$.

1.3 Standard exact and approximate Riemann solvers

In this section, we are interested in solving the Euler equations using the finite volume method. Let us therefore consider the integral form of the Euler system obtained by integrating system (1.3) over a finite control volume with fixed boundaries $C_i = [x_{i-1/2}, x_{i+1/2}]$ and over time $[t^n, t^{n+1}]$:

$$\int_{t^n}^{t^{n+1}}\int_{x_{i-1/2}}^{x_{i+1/2}} \frac{\partial \mathcal{U}}{\partial t} dt dx + \int_{t^n}^{t^{n+1}}\int_{x_{i-1/2}}^{x_{i+1/2}} \frac{\partial \mathbf{f}}{\partial x} dt dx = 0$$

which can be turned into:

$$\mathbf{U}_i^{n+1} = \mathbf{U}_i^n - \frac{\Delta t}{\Delta x}(\tilde{\mathbf{f}}_{i+1/2} - \tilde{\mathbf{f}}_{i-1/2}) \tag{1.21}$$

where:

- $\mathbf{U}_i^n$ is the average of the vector of conservative variables $\mathcal{U}$ at time t^n over cell C_i of length $\Delta x = x_{i+1/2} - x_{i-1/2}$.

$$\mathbf{U}_i^n = \frac{1}{\Delta x}\int_{x_{i-1/2}}^{x_{i+1/2}} \mathcal{U}(x, t^n) dx$$

- $\tilde{f}_{i\pm1/2}$ is the average of the flux vector during time $\Delta t = t^{n+1} - t^n$ at the intercells.

$$\tilde{\mathbf{f}}_{i\pm1/2} = \frac{1}{\Delta t}\int_{t^n}^{t^{n+1}} \mathbf{f}_{i\pm1/2} dt = \frac{1}{\Delta t}\int_{t^n}^{t^{n+1}} \mathbf{f}(\mathcal{U}(x_{i\pm1/2}, t)) dt$$

So far, no numerical scheme has been introduced yet and the formulation (1.21) is nothing else but a reformulation of the integral form of the conservation laws. Formulation (1.21) will be used as starting point to construct a numerical method.
It is obvious that $\mathbf{U}_i^{n+1}$ can be computed if we are able to compute the fluxes $\tilde{f}_{i\pm1/2}$ which requires knowing the conservative variables $\mathcal{U}(x_{i\pm1/2}, t)$ at the intercells. This task is not trivial since we do not know the exact solutions at the intercells. The known quantities in the finite volume framework are the cell-averaged values $\mathbf{U}$.

Consequently, it is necessary to derive so-called numerical fluxes $F_{i\pm1/2}$ which approximate the average physical ones $\tilde{f}_{i\pm1/2}$ and are functions of the cell-averaged values:

$$\mathbf{F}_{i-1/2} = \mathbf{F}_{i-1/2}(\mathbf{U}_i^n, \mathbf{U}_{i-1}^n) \approx \tilde{\mathbf{f}}_{i-1/2}$$

The formulation (1.21) now becomes a numerical scheme:

$$\mathbf{U}_i^{n+1} = \mathbf{U}_i^n - \frac{\Delta t}{\Delta x}(\mathbf{F}_{i+1/2} - \mathbf{F}_{i-1/2}) \tag{1.22}$$

The computation of $\mathbf{U}_i^{n+1}$ requires knowing the numerical fluxes $\mathbf{F}_{i\pm1/2}$. Well known expressions for the numerical fluxes will be now discussed in sections 1.3.1, 1.3.2.

1.3.1 Godunov scheme

The Godunov scheme [Godunov, 1959] applied to the Euler equations is made of three steps:

- The solution $\mathbf{U}_i^n$ defined at the cell center is supposed to be piecewise constant with value $\mathbf{U}_i^n$ within each cell. This piecewise constant data leads to discontinuities at the cell interfaces $x_{i\pm1/2}$. This is often called as the reconstruction step.

$$\mathbf{U}_{i-1/2}^- = \mathbf{U}_{i-1}^n \quad \text{and} \quad \mathbf{U}_{i-1/2}^+ = \mathbf{U}_i^n$$

- Since there are two distinct states at the intercells, the solution at the intercells is obtained by solving (analytically) the Riemann problem (RP) with $\mathbf{U}_{i-1}^n$, $\mathbf{U}_i^n$ as the left and right states respectively. The analytical solution for the RP can be found for instance in [Toro, 2009].

- Having computed the solution $\mathcal{U}_{i\pm1/2}$ at the intercells, the numerical fluxes can be computed as: $\mathbf{F}_{i\pm1/2} = \mathbf{F}_{i\pm1/2}(\mathcal{U}_{i\pm1/2})$ and the solution at time t^{n+1} can be updated using (1.22).

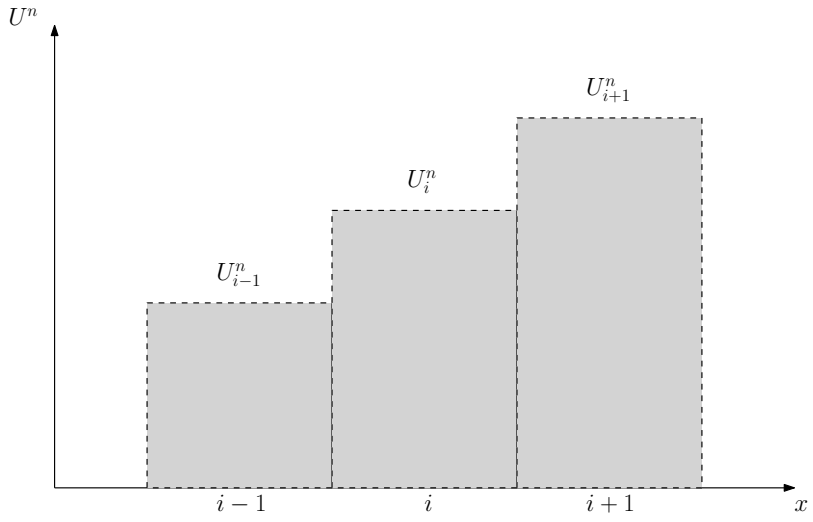

Figure 1.1: Piecewise constant data at time $t = t^n$

1.3.2 HLLC scheme

The HLLC method belongs to the family of approximate Riemann solvers, thus defined because they replace the exact solution of the Riemann problem at the intercell performed in the Godunov scheme by a much cheaper approximate solution of the intercell Riemann problem. The HLLC method [Toro

et al., 1994], which is based on the HLL method of Harten-Lax-Leer [Harten et al., 1983], proposes an approximate Riemann solver assuming a wave structure that includes the fastest waves and the contact wave (wave that is missed in the HLL scheme). The wave structure is plotted in Figure 1.2. In the HLLC approach, the solution consists of four regions R_0, R_1, R_2 and R_3 with piecewise constant states. In R_0 we have the initial state (in the sense, state at the known time level n) on the left $\mathbf{U}_L$ and in R_3 we have the initial right state $\mathbf{U}_R$. In the regions R_1, R_2 between the fastest waves, the intermediate states $\mathbf{U}_L^*, \mathbf{U}_R^*$ need to be determined. Note that in the HLL method, the regions R_1, R_2 are unified with a unique piecewise constant state denoted as $\mathbf{U}_{HLL}$.

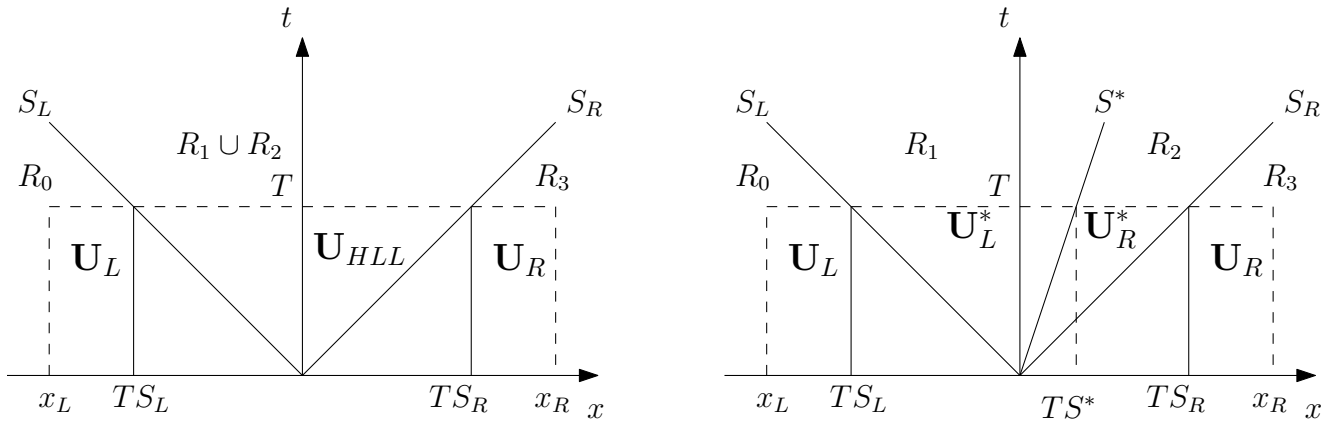

Figure 1.2: HLL wave structure (left) and HLLC wave structure (right) Piece-wise constant data $\mathbf{U}_L, \mathbf{U}_R$ at $t = t^n$. Piece-wise constant solutions $\mathbf{U}_L, \mathbf{U}_R, \mathbf{U}_L^*, \mathbf{U}_R^*, \mathbf{U}_{HLL}$, at $t = T$.

In order to compute these intermediate states, we start from the conservation laws:

$$\frac{\partial \mathcal{U}}{\partial t} + \frac{\partial \mathbf{f}}{\partial x} = 0$$

and we integrate over the space-time control volume $[x_L; x_R] \times [0; T]$, sketched in dashed line in Figure 1.2.

$$\int_{x_L}^{x_R} (\mathcal{U}(x,T) - \mathcal{U}(x,0))dx + \int_0^T (\mathbf{f}(\mathcal{U}(x_R,t)) - \mathbf{f}(\mathcal{U}(x_L,t)))dt = 0 \tag{1.23}$$

In the HLL case, (1.23) results in (see for example [Toro, 2009] for more details):

$$\mathbf{U}_{HLL}(S_R - S_L) + \mathbf{U}_L S_L - \mathbf{U}_R S_R + f_R - f_L = 0$$

where:

$$\mathbf{U}_{HLL} = \frac{1}{T(S_R - S_L)} \int_{TS_L}^{TS_R} \mathbf{U}(x,T)dx$$

$$f_L = f(\mathbf{U}_L) \text{ and } f_R = f(\mathbf{U}_R)$$

The approximate state $\mathbf{U}_{HLL}$ is thus given by:

$$\mathbf{U}_{HLL} = \frac{S_R \mathbf{U}_R - S_R \mathbf{U}_R + f_L - f_R}{S_R - S_L} \tag{1.24}$$

In the HLLC case, the HLL approximate state can be decomposed into two parts to take into account the missing contact wave:

$$\mathbf{U}_{HLL} = \frac{1}{T(S_R - S_L)} \int_{TS_L}^{TS^*} \mathbf{U}(x,T)dx + \frac{1}{T(S_R - S_L)} \int_{TS^*}^{TS_R} \mathbf{U}(x,T)dx$$

or:

$$\mathbf{U}_{HLL} = \frac{S^* - S_L}{S_R - S_L}\mathbf{U}_L^* + + \frac{S_R - S^*}{S_R - S_L}\mathbf{U}_R^* = \beta_1 \mathbf{U}_L^* + \beta_2 \mathbf{U}_R^* \tag{1.25}$$

where:

$$\mathbf{U}_L^* = \frac{1}{T(S^* - S_L)} \int_{TS_L}^{TS^*} \mathbf{U}(x,T)dx,\ \mathbf{U}_R^* = \frac{1}{T(S_R - S^*)} \int_{TS^*}^{TS_R} \mathbf{U}(x,T)dx$$

In the above relations, S_R, S_L, S^* are respectively the estimates for the velocities of the fastest waves propagating to the left and to the right and of the contact wave . The determination of these quantities will be addressed later in this section. Note the HLL state is known since it depends only on the left and right states (see (1.24)). The variables $\mathbf{U}_L^*, \mathbf{U}_R^*$ can be computed from (1.25). Explicitly, (1.25) can be written in 1D as:

$$\beta_1 \begin{pmatrix} \rho_L^* \\ \rho_L^* u_L^* \\ \frac{p_L^* + \gamma P_\infty}{\gamma - 1} + \frac{1}{2}\rho_L^* u_L^{*,2} \end{pmatrix} + \beta_2 \begin{pmatrix} \rho_R^* \\ \rho_R^* u_R^* \\ \frac{p_R^* + \gamma P_\infty}{\gamma - 1} + \frac{1}{2}\rho_R^* u_R^{*,2} \end{pmatrix} = \mathbf{U}_{HLL} \tag{1.26}$$

The system (1.26) has three equations but six unknowns $(\rho_L^*, \rho_R^*, u_L^*, u_R^*, p_L^*, p_R^*)$. Consequently, we need to impose extra relations so that the system is solvable. Following [Toro, 2009], we impose:

$$u_L^* = u_R^* = u^* = S^*$$

$$p_L^* = p_R^* = p^*$$

which are the conditions that satisfy the exact solution for the pressure and the velocity in the intermediate state. The system (1.26) is now solvable for the three unknowns $(\rho_L^*, \rho_R^*, p^*)$.
The HLLC approximate Riemann solver is defined as follows:

$$\tilde{\mathbf{U}}(x,t) = \begin{cases} \mathbf{U}_L, \text{ if } x/t \leq S_L \\ \mathbf{U}_L^*, \text{ if } S_L \leq x/t \leq S^* \\ \mathbf{U}_R^*, \text{ if } S^* \leq x/t \leq S_R \\ \mathbf{U}_R, \text{ if } x/t \geq S_R \end{cases}$$

with x/t the velocity of the intercell ($x/t = 0$ in the Eulerian case and $x/t \neq 0$ in the ALE case, described in the next section).
The corresponding HLLC numerical flux is expressed as follows:

$$\mathbf{F}_{i-1/2}^{HLLC} = \begin{cases} \mathbf{F}_L, \text{ if } x/t \leq S_L \\ \mathbf{F}_L^*, \text{ if } S_L \leq x/t \leq S^* \\ \mathbf{F}_R^*, \text{ if } S^* \leq x/t \leq S_R \\ \mathbf{F}_R, \text{ if } x/t \geq S_R \end{cases}$$

The intermediate fluxes can be determined by integrating over an appropriate control volume containing the waves S_L, S_R, which yields:

$$\begin{aligned} \mathbf{F}_L^* &= \mathbf{F}_L + S_L(\mathbf{U}_L^* - \mathbf{U}_L) \\ \mathbf{F}_R^* &= \mathbf{F}_R + S_R(\mathbf{U}_R^* - \mathbf{U}_R) \end{aligned} \tag{1.27}$$

Knowing the numerical fluxes, one can now update the variables using (1.22).
To compute the wave speeds, the estimates of [Batten et al., 1997] for the fastest waves are used, such as implemented in EUROPLEXUS :

$$S_L = min(u_L - c_L; \tilde{u} - \tilde{c}),\ S_R = min(u_R + c_R; \tilde{u} + \tilde{c})$$

where $\tilde{u}$, $\tilde{c}$ are the Roe average states for the velocity and sound speed (formulae not detailed here but Roe average is basically a weighted average at the intercell with weights being the squareroot of the left and right states). Concerning the estimate for the speed of the contact wave S^*, it can be directly deduced from (1.27) via the intermediate pressure relations:

$$p^* = p_L^* = p_R^* = p_L + \rho_L(S_L - u_L)(S^* - u_L) = p_R + \rho_R(S_R - u_R)(S^* - u_R) \tag{1.28}$$

which results in:

$$S^* = \frac{p_R - p_L + \rho_L u_L(S_L - u_L) - \rho_R u_R(S_R - u_R)}{\rho_L(S_L - u_L) - \rho_R(S_R - u_R)}$$

1.3.3 ALE formulation

The scheme (1.22) is a general formulation derived for a fixed mesh. In this work, meshes with moving boundaries will be also considered since the nuclear safety applications we are interested involve the deformation of the containment structure enclosing the liquid and the gas bubble expanding within this liquid (see chapter 6). This is also why the model problems used next to assess numerical schemes will involve a piston problem in section 2.1 in which the computational domain varies in time. The strategy applied to deal with moving meshes is the so-called Arbitrary Lagrangian Eulerian (ALE), available in the Europlexus code. Since the developments performed in this work have been systematically extended to account for moving meshes, we will briefly describe in this section the key design principles of the ALE formulation. In the 1D case, by integrating (1.3) over a cell $C_i = [x_{i-1/2}(t), x_{i+1/2}(t)]$ using the Reynolds transport theorem, we obtain:

$$\frac{d}{dt}\int_{x_{i-1/2}(t)}^{x_{i+1/2}(t)} \mathcal{U}dx + \int_{x_{i-1/2}(t)}^{x_{i+1/2}(t)} \frac{\partial \mathbf{f}^{ALE}}{\partial x}dx = 0 \tag{1.29}$$

where $\mathbf{f}^{ALE} = \mathbf{f} - u_m\mathcal{U}$ is called the ALE flux and u_m is the velocity of the intercells.

$$\mathbf{f}^{ALE} = \begin{pmatrix} \rho(u - u_m) \\ \rho u(u - u_m) + p \\ \rho e^t(u - u_m) + pu \end{pmatrix}$$

The conservative flux is computed using the classical finite volume technique:

$$\int_{x_{i-1/2}(t)}^{x_{i+1/2}(t)} \frac{\partial \mathbf{f}^{ALE}}{\partial x}dx = \mathbf{f}_{i+1/2}^{ALE} - \mathbf{f}_{i-1/2}^{ALE} \tag{1.30}$$

The integration of (1.30) over time $[t^n, t^{n+1}]$ gives:

$$\int_{t^n}^{t^{n+1}} \int_{x_{i-1/2}(t)}^{x_{i+1/2}(t)} \frac{\partial \mathbf{f}^{ALE}}{\partial x}dxdt = \Delta t(\tilde{\mathbf{f}}_{i+1/2}^{ALE} - \tilde{\mathbf{f}}_{i-1/2}^{ALE})$$

where $\tilde{f}_{i\pm1/2}^{ALE}$ is the average of the ALE flux vector at the intercells during time $\Delta t = t^{n+1} - t^n$.

$$\tilde{\mathbf{f}}_{i\pm1/2}^{ALE} = \frac{1}{\Delta t}\int_{t^n}^{t^{n+1}} \mathbf{f}_{i\pm1/2}^{ALE}dt = \frac{1}{\Delta t}\int_{t^n}^{t^{n+1}} \mathbf{f}^{ALE}(\mathcal{U}(x_{i\pm1/2}(t), t))dt$$

Concerning the time-derivative term in (1.29), its integration over time $[t^n, t^{n+1}]$ yields:

$$\begin{aligned} \int_{t^n}^{t^{n+1}} \left(\frac{d}{dt}\int_{x_{i-1/2}(t)}^{x_{i+1/2}(t)} \mathcal{U}dx\right) dt &= \int_{x_{i-1/2}(t^{n+1})}^{x_{i+1/2}(t^{n+1})} \mathcal{U}dx - \int_{x_{i-1/2}(t^n)}^{x_{i+1/2}(t^n)} \mathcal{U}dx \\ &= \Delta x_i^{n+1}\mathbf{U}_i^{n+1} - \Delta x_i^n \mathbf{U}_i^n \end{aligned}$$

The equation (1.29) then becomes:

$$\mathbf{U}_i^{n+1} = \frac{\Delta x_i^n}{\Delta x_i^{n+1}} \mathbf{U}_i^{n+1} - \frac{\Delta t}{\Delta x_i^{n+1}} (\tilde{f}_{i+1/2}^{ALE} - \tilde{f}_{i-1/2}^{ALE}) \tag{1.31}$$

Similarly to the Eulerian case, (1.31) is not yet a scheme but merely a reformulation of (1.29) and it remains to specify how the physical flux is approximated. Let $\mathbf{F}_{i\pm1/2}^{ALE}$ be the numerical ALE fluxes approximating the corresponding physical ones $\mathbf{f}_{i\pm1/2}^{ALE}$; the first order scheme in the ALE case reads:

$$\mathbf{U}_i^{n+1} = \frac{\Delta x_i^n}{\Delta x_i^{n+1}} \mathbf{U}_i^{n} - \frac{\Delta t}{\Delta x_i^{n+1}} (F_{i+1/2}^{ALE} - F_{i-1/2}^{ALE}) \tag{1.32}$$

In general, the computation of $\mathbf{U}_i^{n+1}$ requires:

- $\mathbf{F}_{i\pm1/2}^{ALE}$, the numerical conservative ALE fluxes which can be computed using the exact or the approximate Riemann solvers as described in the Eulerian case. These fluxes in the ALE case are evaluated at the moving intercells.
- the new volumes of the cells involved in the cell-averaged procedure of $\mathcal{U}_i^{n+1}$.

In order to obtain the volume of a cell at time t^{n+1}, ones need the so-called geometric conservation law (GCL) [Ma et al., 2015]:

$$\frac{d}{dt} \int_{\mathcal{V}_i} d\mathcal{V}_i = \int_{\varphi_i} \mathbf{v}_m \cdot \mathbf{n} d\varphi_i \tag{1.33}$$

Equation (1.33) states that the variation in the volume of each cell $\mathcal{V}_i$ must be equal to the volume swept by the cell boundaries of that cell φ_i during the time interval in consideration. By integrating equation (1.33) over time interval $[t_n; t_{n+1}]$, we obtain the so-called discrete geometric conservation law (DGCL):

$$\mathcal{V}_i^{n+1} - \mathcal{V}_i^n = \int_{t^n}^{t^{n+1}} \int_{\varphi_i} \mathbf{v}_m \cdot \mathbf{n} d\varphi_i dt = \Delta t \sum_{j=1}^{Nface} \mathbf{v}_m \cdot \mathbf{n}_j^l \varphi_j^l \tag{1.34}$$

The discussion concerning the choice of of t^l (time at which we compute $\mathbf{n}_j^l$ and φ_j^l) is out of the scope of this work. We refer for instance to [Daude et al., 2014] for the detailed determination of these quantities.

1.4 Standard schemes behavior in the low-Mach number regime

In section 1.2.2, we have investigated the behavior of the (continuous) Euler system using the asymptotic analysis. In the present section, we investigate the low-Mach behavior of the standard schemes reviewed in section 1.3 when applied to the discrete solution of the Euler equations. The analysis at the discrete level is performed in a way similar to that followed in the continuous case: the numerical solution of the (discrete or discretized) Euler system is expanded using the asymptotic expansion. The asymptotic analysis is presented in section 1.4.2 for the Godunov scheme following the rigorous analysis performed by [Guillard and Murrone, 2004] and in section 1.4.3 for the HLLC scheme. The analysis is performed using the concept of well-prepared initial condition introduced in section 1.4.1.

1.4.1 Well-prepared initial condition

The concept of well-prepared initial condition (WPIC) has been discussed in a number of references in the literature devoted to the numerical analysis of schemes in the low-Mach number regime [Schochet, 1994, Guillard and Murrone, 2004, Dellacherie, 2010]. This special class of initial condition is inherited from the asymptotic analysis in section 1.2.2 in which the pressure fluctuation (if it exists) is initially

correctly scaled at the square of the Mach number (cf. $(1.16)_1$, (1.17)) and the velocity at the leading order satisfies the so-called compability condition (cf. (1.15)).
The WPIC is usually expressed for the case of a closed domain with slip or periodic boundary condition where one satisfies the divergence free constraint for the velocity (see for instance [Dellacherie, 2010]). The same constraint holds in case of an **open domain** as discussed in section 1.2.2. In this work, the WPIC is extended so as to be valid for the case of a **closed domain** (with non-slip/periodic boundary condition) where the divergence of the velocity is a function of time (cf. (1.15)). The dimensionless form of the WPIC is given by:

$$\begin{cases} \hat{p}(\hat{\mathbf{x}}, \hat{t}=0) = \hat{P}(\hat{t}=0) + M^2 \hat{p}^{(2)}(\mathbf{x}, \hat{t}=0) + o(M^2) \\ \hat{\mathbf{v}}(\hat{\mathbf{x}}, \hat{t}=0) = \hat{\mathbf{v}}^{(0)}(\hat{\mathbf{x}}, \hat{t}=0) + M\hat{\mathbf{v}}^{(1)}(\hat{\mathbf{x}}, \hat{t}=0) + M^2 \hat{\mathbf{v}}^{(2)}(\hat{\mathbf{x}}, \hat{t}=0) + o(M^2) \end{cases} \tag{1.35}$$

where

$$\begin{cases} \hat{P}(\hat{t}=0) = \hat{p}^{(0)}(\hat{t}=0) + M\hat{p}^{(1)}(\hat{t}=0) = \text{const of order } \mathcal{O}(M^0) \\ \nabla \cdot \hat{\mathbf{v}}^{(0)} = f(\hat{t}) \end{cases} \tag{1.36}$$

The equivalent dimensional form is expressed as:

$$\begin{cases} p(\mathbf{x}, t=0) = P_0(t=0) + \underbrace{p'(\mathbf{x}, t=0)}_{\mathcal{O}(M^2)} \\ \mathbf{v}(\mathbf{x}, t=0) = \mathbf{v}_0(\mathbf{x}, t=0) + \underbrace{\mathbf{v}'(\mathbf{x}, t=0)}_{\mathcal{O}(M)} \end{cases} \quad \text{with} \quad \begin{cases} P_0 = \text{const of order } \mathcal{O}(M^0) \\ \nabla \cdot \mathbf{v}_0 = f(t) \end{cases} \tag{1.37}$$

In the above expressions, no special initial conditions are specified for the density field. In fact, as in the asymptotic analysis at the continuous level, we assume that the density is constant at the leading order.

1.4.2 Godunov scheme low-Mach behavior

We consider two adjacent cells and denote respectively L, R the left and right cells. In the finite volume method, all the initial fields are projected on the computational mesh by taking the spatial average to obtain the piece-wise constant data (for the first order method). As a result, any function that is constant or time-dependent only is not affected by the cell-averaged procedure. This is the case for the leading and first-order terms of the pressure field and the leading-order term of the density field for WPIC. Concerning the leading-order term of the velocity field, since it depends on the physical problem, we keep at this stage the most general form as possible and make further simplifications later in this section. The WPIC, at the discrete level, takes the following form:

$$\begin{aligned} p_{L,R} &= \rho_{ref} c_{ref}^2 \left[\hat{p}_{L,R}^{(0)}(\hat{t}=0) + M\hat{p}_{L,R}^{(1)}(\hat{t}=0) + M^2 \hat{p}_{L,R}^{(2)}(\hat{x}, \hat{t}=0) + o(M^2) \right] \\ \rho_{L,R} &= \rho_{ref} \left[\hat{\rho}^{(0)} + M\hat{\rho}_{L,R}^{(1)}(\hat{x}, \hat{t}=0) + M^2 \hat{\rho}_{L,R}^{(2)}(\hat{x}, \hat{t}=0) + o(M^2) \right] \\ u_{L,R} &= M c_{ref} \left[\hat{u}_{L,R}^{(0)}(\hat{x}, \hat{t}=0) + M\hat{u}_{L,R}^{(1)}(\hat{x}, \hat{t}=0) + M^2 \hat{u}_{L,R}^{(2)}(\hat{x}, \hat{t}=0) + o(M^2) \right] \end{aligned} \tag{1.38}$$

The sound speed, as in the continuous level, is constant in space up to first-order:

$$c_{L,R} = c_{ref} \left[\hat{c}^{(0)}(\hat{t}=0) + M\hat{c}_{L,R}^{(1)}(\hat{x}, \hat{t}=0) + M^2 \hat{c}_{L,R}^{(2)}(\hat{x}, \hat{t}=0) + o(M^2) \right] \tag{1.39}$$

We also assume that the solutions of the intermediate state can be expanded in power of the Mach number as:

$$\begin{aligned} p^* &= \rho_{ref} c_{ref}^2 \left[\hat{p}^{(0)}(\hat{x}, \hat{t}) + M\hat{p}^{(1)}(\hat{x}, \hat{t}) + M^2 \hat{p}^{(2)}(\hat{x}, \hat{t}) + o(M^2) \right] \\ \rho^* &= \rho_{ref} \left[\hat{\rho}^{(0)}(\hat{x}, \hat{t}) + M\hat{\rho}^{(1)}(\hat{x}, \hat{t}) + M^2 \hat{\rho}^{(2)}(\hat{x}, \hat{t}) + o(M^2) \right] \\ u^* &= M c_{ref} \left[\hat{u}^{(0)}(\hat{x}, \hat{t}) + M\hat{u}^{(1)}(\hat{x}, \hat{t}) + M^2 \hat{u}^{(2)}(\hat{x}, \hat{t}) + o(M^2) \right] \end{aligned} \tag{1.40}$$

By applying the same procedure described in [Guillard and Murrone, 2004], we substitute (1.38) (1.40) into the exact solution of the RP and neglect the $o(M^2)$ terms. The intermediate pressure solution writes:

Right-running shock (compression) wave:

$$\begin{aligned} &\mathcal{O}(M^0): \quad \hat{p}^{(0)}(\hat{x},\hat{t}) = \hat{p}_R^{(0)} \\ &\mathcal{O}(M): \quad \hat{p}^{(1)}(\hat{x},\hat{t}) = \hat{p}_R^{(1)} + \hat{\rho}^{(0)}\hat{c}^{(0)}(\hat{u}^{(0)} - \hat{u}_R^{(0)}), \quad \hat{p}^{(1)} > \hat{p}_R^{(1)} \end{aligned} \tag{1.41}$$

Right-running rarefaction wave:

$$\begin{aligned} &\mathcal{O}(M^0): \quad \hat{p}^{(0)}(\hat{x},\hat{t}) = \hat{p}_R^{(0)} \\ &\mathcal{O}(M): \quad \hat{p}^{(1)}(\hat{x},\hat{t}) = \hat{p}_R^{(1)} + \hat{\rho}^{(0)}\hat{c}^{(0)}(\hat{u}^{(0)} - \hat{u}_R^{(0)}), \quad \hat{p}^{(1)} < \hat{p}_R^{(1)} \end{aligned} \tag{1.42}$$

Left-running shock (compression) wave:

$$\begin{aligned} &\mathcal{O}(M^0): \quad \hat{p}^{(0)}(\hat{x},\hat{t}) = \hat{p}_L^{(0)} \\ &\mathcal{O}(M): \quad \hat{p}^{(1)}(\hat{x},\hat{t}) = \hat{p}_L^{(1)} - \hat{\rho}^{(0)}\hat{c}^{(0)}(\hat{u}^{(0)} - \hat{u}_L^{(0)}), \quad \hat{p}^{(1)} > \hat{p}_L^{(1)} \end{aligned} \tag{1.43}$$

Left-running rarefaction wave:

$$\begin{aligned} &\mathcal{O}(M^0): \quad \hat{p}^{(0)}(\hat{x},\hat{t}) = \hat{p}_L^{(0)} \\ &\mathcal{O}(M): \quad \hat{p}^{(1)}(\hat{x},\hat{t}) = \hat{p}_L^{(1)} - \hat{\rho}^{(0)}\hat{c}^{(0)}(\hat{u}^{(0)} - \hat{u}_L^{(0)}), \quad \hat{p}^{(1)} < \hat{p}_L^{(1)} \end{aligned} \tag{1.44}$$

From (1.41)-(1.44), we notice that the solutions across the right-running and the left-running waves are given by similar formulas. This is due to the fact that the shock (compression) and rarefaction waves become similar acoustic waves in the low-Mach limit. Moreover, the formulas used to determine the first order pressure term are similar to Joukowski acoustic formula meaning that this term plays the role of the acoustic wave. The pressure and velocity are linearly connected by curves of constant slope $\hat{\rho}^{(0)}\hat{c}^{(0)}$. The intersection of these curves gives the solution of the acoustic couple $(\hat{p}^{(1)}, \hat{u}^{(0)})$ and is graphically illustrated in Figure 1.3 via four different situations. In fact, the acoustic waves scaled at $\mathcal{O}(M)$ should not arise in the numerical solution to remain consistent with the asymptotic analysis performed at the continuous level in section 1.2.2. Consequently, these acoustic waves must be regarded as parasite waves.

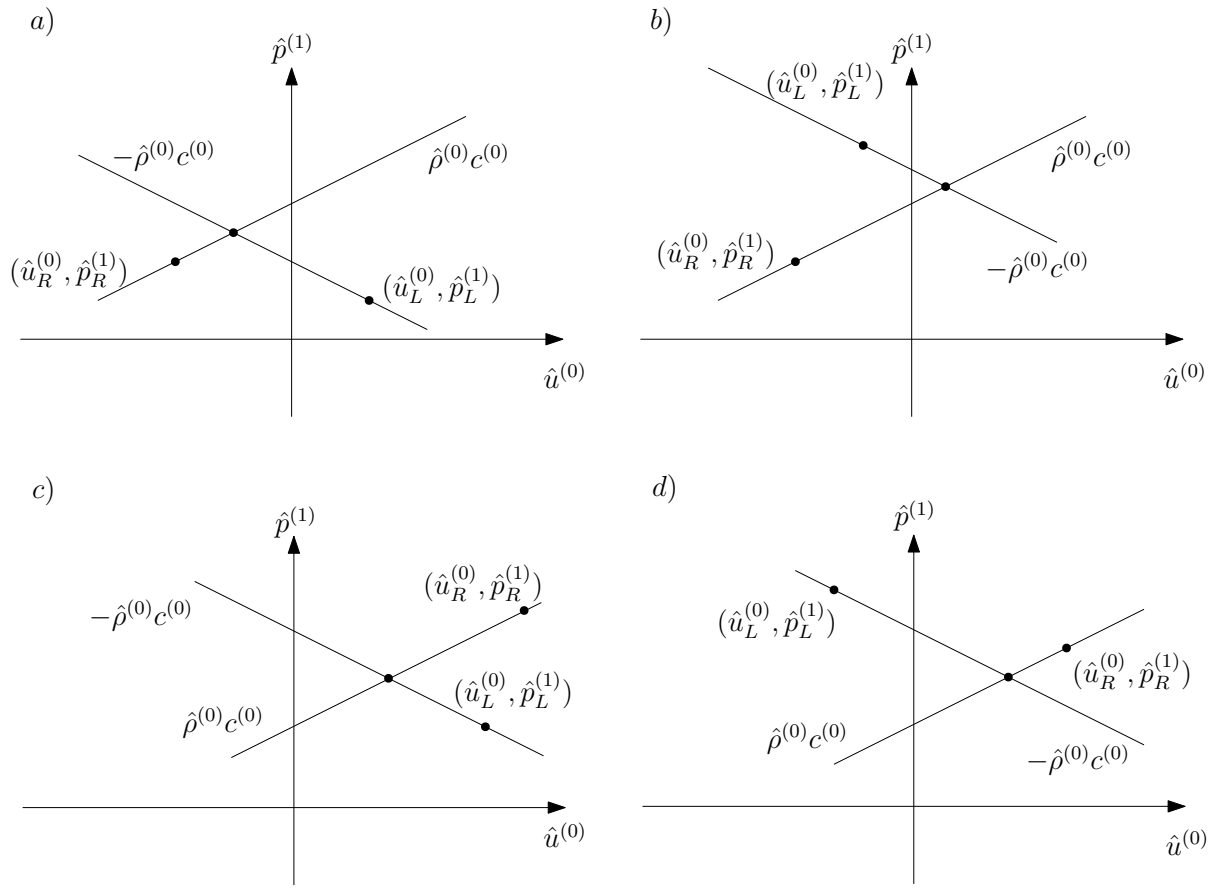

Figure 1.3: Qualitative parasite acoustic couple solution: *a*) Right shock-Left shock, *b*) Right shock-Left rarefaction, *c*) Right rarefaction-Left shock, *d*) Right rarefaction-Left rarefaction

From $(1.41)_1 - (1.44)_1$ we can also observe that:

$$\hat{p}^{(0)} = \hat{p}_R^{(0)} = \hat{p}_L^{(0)} = \frac{\hat{p}_L^{(0)} + \hat{p}_R^{(0)}}{2} \tag{1.45}$$

which means the leading-order pressure solution is a time-dependent function only. Concerning the first-order pressure solution, by combining $(1.41)_2 - (1.44)_2$, it can be expressed as:

$$\hat{p}^{(1)} = \frac{\hat{p}_R^{(1)} + \hat{p}_L^{(1)}}{2} - \frac{1}{2}\hat{\rho}^{(0)}\hat{c}^{(0)}(\hat{u}_R^{(0)} - \hat{u}_L^{(0)}) \tag{1.46}$$

Substituting (1.45), (1.46) into (1.40), we obtain:

$$\begin{aligned} p^* &= \rho_{ref}c_{ref}^2\left[\frac{\hat{p}_L^{(0)} + \hat{p}_R^{(0)}}{2} + M\left(\frac{\hat{p}_R^{(1)} + \hat{p}_L^{(1)}}{2} - \frac{1}{2}\hat{\rho}^{(0)}\hat{c}^{(0)}(\hat{u}_R^{(0)} - \hat{u}_L^{(0)})\right) + \mathcal{O}(M^2)\right] \\ &= \rho_{ref}c_{ref}^2\left[\frac{\hat{P}_L + \hat{P}_R}{2} - \frac{M}{2}\hat{\rho}^{(0)}\hat{c}^{(0)}(\hat{u}_R^{(0)} - \hat{u}_L^{(0)}) + \mathcal{O}(M^2)\right] \end{aligned} \tag{1.47}$$

where the first order pressures $\hat{p}_{L,R}^{(1)}$ are combined with the leading order pressures $\hat{p}_{L,R}^{(0)}$ to define:

$$\hat{P}_{L,R} = \hat{p}_{L,R}^{(0)} + M\hat{p}_{L,R}^{(1)}$$

Formula (1.47) is now analyzed in the 1D or multiD case and for an open or a closed domain.
For a **one-dimensional open domain**, the divergence free constraint $\nabla \cdot \hat{u}^{(0)}_{R,L} = 0$ yields a constant leading velocity $\hat{u}^{(0)}_L = \hat{u}^{(0)}_R = \text{const}$ at the discrete level. Formula (1.47) becomes then:

$$p^* = \rho_{ref} c^2_{ref} \left[\frac{\hat{P}_L + \hat{P}_R}{2} + \mathcal{O}(M^2) \right]$$

which indicates that we do not suffer from the low-Mach accuracy problem since the pressure fluctuation given by the Godunov solver correctly scales as the square of the Mach number, similarly to the analysis at the continuous level in section 1.2.2. The pressure solution can therefore be decomposed as:

$$p(\mathbf{x}, t) = P(t) + \underbrace{p'(\mathbf{x}, t)}_{\mathcal{O}(M^2)} \tag{1.48}$$

For a **multidimensional open domain**, the divergence free constraint $\nabla \cdot \hat{\mathbf{v}}^{(0)}_{R,L} = 0$ does not allow to draw further conclusions as in the 1D case. As a result, the fluctuation of acoustic nature scales as the Mach number and we suffer from a low-Mach accuracy problem at the discrete level. The pressure solution in this case can be indeed decomposed as:

$$p(\mathbf{x}, t) = P(t) + \underbrace{p'(\mathbf{x}, t)}_{\mathcal{O}(M)} \tag{1.49}$$

For a **one-dimensional closed domain**, the divergence of velocity is a function of time $\nabla \cdot \hat{u}^{(0)}_{R,L} = f(\hat{t} = 0)$. The integration of this relation (in Cartesian coordinates for the sake of simplicty) and the projection on the centers of two adjacent cells of coordinates x_L, x_R with $\Delta x = x_R - x_L$ yields the initial piecewise constant data:

$$\hat{u}^{(0)}_L = f(\hat{t} = 0) x_L + C, \;\; \hat{u}^{(0)}_R = f(\hat{t} = 0) x_R + C$$

It follows that:

$$\hat{u}^{(0)}_R - \hat{u}^{(0)}_L = f(\hat{t} = 0) \Delta x$$

and the formula (1.47) becomes:

$$p^* = \rho_{ref} c^2_{ref} \left[\frac{\hat{P}_L + \hat{P}_R}{2} - \frac{M}{2} \hat{\rho}^{(0)} \hat{c}^{(0)} f(\hat{t} = 0) \Delta x + \mathcal{O}(M^2) \right]$$

If the mesh under consideration is regular, the space step Δx is constant for all cells in the Eulerian case and is a function of time in the ALE case and the above relation states in all cases that the pressure solution is constant in space up to the second order of the Mach number. Consequently, we do not suffer from the accuracy problem since the pressure fluctuation is correctly scaled and the pressure solution can be correctly decomposed as in (1.48).

For a **multidimensional closed domain**, the divergence of velocity is a function of time $\nabla \cdot \hat{\mathbf{v}}^{(0)}_{R,L} = f(\hat{t} = 0)$ and this relationship does not yield further simplification. The pressure fluctuation therefore remains scaled as the Mach number and we therefore suffer from the low-Mach accuracy problem with the pressure solution in this case decomposed as in (1.49).

1.4.3 HLLC scheme low-Mach behavior

Without loss of generality, we assume the following estimates for fastest wave speeds:

$$S_L = min(u_L - c_L, \tilde{u} - \tilde{c}) = u_L - c_L, \;\; S_R = max(u_R + c_R, \tilde{u} + \tilde{c}) = u_R + c_R \tag{1.50}$$

Similarly to the analysis presented for the Godunov scheme, we adopt the form of the WPIC and the numerical solutions defined in (1.38) (1.40). The remaining variable in the HLLC scheme which needs to be defined is the estimate for the speed of the contact wave S^*, which takes the following form:

$$S^* = Mc_{ref}\left[\hat{S}^{*,(0)}(\hat{x},\hat{t}) + M\hat{S}^{*,(1)}(\hat{x},\hat{t}) + M^2\hat{S}^{*,(2)}(\hat{x},\hat{t}) + o(M^2)\right] \tag{1.51}$$

In the HLLC scheme, the pressure solution in the intermediate state can be deduced from (1.28) and regarded as the arithmetic average of p_L^* and p_R^*:

$$p^* = \frac{1}{2}\left[p_L + p_R + \rho_L(S_L - u_L)(S^* - u_L) + p_R + \rho_R(S_R - u_R)(S^* - u_R)\right] \tag{1.52}$$

Using (1.50), the expression (1.52) for p^* becomes:

$$p^* = \frac{p_L + p_R}{2} + \frac{\rho_R c_R(S^* - u_R) - \rho_L c_L(S^* - u_L)}{2} \tag{1.53}$$

By substituting (1.38) (1.40) (1.39) and (1.51) into (1.53), we obtain:

$$\begin{aligned} \mathcal{O}(1): &\quad \hat{p}^{(0)}(\hat{x},\hat{t}) = \frac{\hat{p}_L^{(0)} + \hat{p}_R^{(0)}}{2} \\ \mathcal{O}(M): &\quad \hat{p}^{(1)}(\hat{x},\hat{t}) = \frac{\hat{p}_L^{(1)} + \hat{p}_R^{(1)}}{2} - \frac{\hat{\rho}^{(0)}\hat{c}^{(0)}(\hat{u}_R^{(0)} - \hat{u}_L^{(0)})}{2} \end{aligned} \tag{1.54}$$

which results in a pressure solution having the same form as the pressure solution (1.47) for the Godunov scheme. Consequently, we can state that the HLLC approximate Riemann solver behaves similarly as the Godunov exact Riemann solver in the low-Mach number limit. As explicited in section 1.4.2, we can therefore also distinguish four cases: the 1D/multidimensional case of an open or a closed domain. Similar conclusions can be drawn: in the low-Mach limit, the HLLC scheme will display an accuracy problem (with a wrongly scaled pressure fluctuation) for multidimensional closed or open domains.

1.5 Low-Mach correction

In this section, we investigate some low-Mach treatments which can be used to fix the accuracy problem identified in the previous section. The purpose is clear: the wrongly computed pressure fluctuation of order $\mathcal{O}(M)$ should be rescaled to order $\mathcal{O}(M^2)$, as in the continuous level (see (1.47), (1.49), (1.16), (1.18)). In section 1.5.1, we present a correction applied to the numercial flux which has been proposed by [Dellacherie et al., 2016] for low-Mach perfect gas computation and which will be extended in this work to low-Mach liquid flows governed by the SG-EOS. For the sake of completeness, another type of correction introduced in [Rieper, 2008, Rieper and Bader, 2009] will be also briefly presented in section 1.5.2: this so-called "topology-based" correction relies on a specific grid topology to cure the low-Mach accuracy problem.

1.5.1 Scheme-based correction

Over the past 30 years, many efforts have been devoted to devise ways to rescale the parasite acoustic waves at the discrete level to the correct order $\mathcal{O}(M^2)$. In [Guillard and Viozat, 1999], the proposed Roe-Turkel method alters only the dissipative terms of the standard Roe scheme using the preconditioning matrix proposed in [Turkel, 1987]. The method has shown its capacity in fixing the accuracy problem. Nevertheless, it filters the (physical) acoustic wave at the very beginning for a physical problem where the (slow) fluid and (fast) acoustic scales of the same order of magnitude coexist [Bruel et al., 2019]. Moreover, this method requires a very restrictive CFL condition ($\Delta t = \mathcal{O}(M^2)$) which significantly decreases the

computational efficiency. In this work, we rather consider the method proposed by [Dellacherie et al., 2016] (which is adapted to deal with liquid flow governed by SG-EOS).
Let $(\cdot)^*$ indicate the solution of the (exact or approximate) Riemann problem at the intercell. The numerical flux of a X scheme (X=Godunov or HLLC in our study) can be expressed as:

$$\mathbf{F}^X_{i-1/2} = \begin{pmatrix} \rho^*(\mathbf{v}^* \cdot \mathbf{n}) \\ \rho^*(\mathbf{v}^* \cdot \mathbf{n})\mathbf{v}^* + p^*\mathbf{n} \\ (\rho^* e^{*t} + p^*)(\mathbf{v}^* \cdot \mathbf{n}) \end{pmatrix}_{i-1/2} \tag{1.55}$$

As discussed in sections 1.4.2 and 1.4.3, the pressure solution in the low-Mach limit can be expressed as the combination of a centered term scaling as $\mathcal{O}(M^0)$ and a term of acoustic nature scaling as $\mathcal{O}(M)$:

$$p^*_{i-1/2} = \underbrace{\frac{p_{i-1} + p_i}{2}}_{\mathcal{O}(M^0)} - \underbrace{\frac{1}{2}\rho c(u_i - u_{i-1})}_{\mathcal{O}(M)}$$

where ρ and c can be determined by the states of cell $i-1$ or cell i in the low-Mach number regime.
The undesirable term containing the acoustic waves in the low-Mach number regime should be corrected. The method of [Dellacherie et al., 2016] proposes to rescale this term to the correct square of the Mach number. The corrected numerical flux at the intercell between cells i and $i-1$ can be written as:

$$\mathbf{F}^{corrected,X}_{i-1/2} = \begin{pmatrix} \rho^*(\mathbf{v} \cdot \mathbf{n})^* \\ \rho^*(\mathbf{v} \cdot \mathbf{n})^*\mathbf{v}^* + p^{**}\mathbf{n} \\ (\rho^* e^{*t} + p^*)(\mathbf{v} \cdot \mathbf{n})^* \end{pmatrix}_{i-1/2} \tag{1.56}$$

with:

$$p^{**}_{i-1/2} = \theta_{i-1/2} p^*_{i-1/2} + (1 - \theta_{i-1/2})\frac{p_{i-1} + p_i}{2}$$

$$\theta_{i-1/2} = min\left(M_{i-1/2}, 1\right) = min\left(\frac{|\mathbf{v}_{i-1/2}|}{c_{i-1/2}}, 1\right)$$

X : Godunov or Godunov-like schemes (HLLC, Roe, etc)

The corrected scheme (1.56) replaces in the momentum equation the pressure solution $p^*_{i-1/2}$ given by the standard schemes with a corrected pressure $p^{**}_{i-1/2}$ defined as a weighted combination between the standard pressure formula and a purely centered approximation. The weight $\theta_{i-1/2}$ of the combination depends on the local Mach number:

$$\begin{aligned} p^{**}_{i-1/2} &= \theta_{i-1/2} p^*_{i-1/2} + (1 - \theta_{i-1/2})\frac{p_{i-1} + p_i}{2} \\ &= \frac{p_{i-1} + p_i}{2} - \frac{\theta_{i-1/2}}{2}\rho c(u_i - u_{i-1}) \end{aligned}$$

For a low-Mach flow (or more generally a subsonic flow), the parameter $\theta_{i-1/2}$ is of the order of the Mach number and consequently the acoustic term is correctly rescaled to the order $\mathcal{O}(M^2)$.
For a supersonic flow, meaning $\theta_{i-1/2} = 1$, the standard schemes remain unmodified:

$$\mathbf{F}^{corrected,X}_{i-1/2} = \mathbf{F}^X_{i-1/2}$$

We can also notice that the acoustic term plays the role of a numerical viscosity: it complements the purely centered flux with a stabilizing numerical viscosity. The rescaling of the acoustic term reduces the numerical viscosity.

1.5.2 Topology-based correction

In [Rieper and Bader, 2009, Rieper, 2008], another fix has been presented by using triangular meshes for low-Mach computations. In contrast with quadrangular meshes, the numerical multiD solutions obtained using regular triangular meshes do not contain any spurious pressure fluctuations scaling as the Mach number. A detailed asymptotic analysis of the Roe scheme for such specific meshes (structured triangular meshes being obtained from regular Cartesian meshes by dividing along a diagonal each quadrangular cell into two triangular cells) allows to explain how the occurence of spurious terms is actually avoided . In [Guillard, 2009], the author provides an extended proof for two dimensional unstructured triangular meshes as well as three dimensional tetrahedral ones.
We do not attempt in this work to reproduce the asymptotic analysis on 2D triangular meshes or 3D tetrahedral meshes; rather, we simply include in the numerical testcases developed to assess the low-Mach behavior of exact or approximate Riemann solvers the use of regular triangular grids in order to confirm these observations and proofs from the literature. We anticipate regular grids cannot be systematically used so that the topology-based correction has only a limited practical interest.

Conclusion

The asymptotic analysis performed for the Godunov scheme and the approximate Riemann solver HLLC scheme in section 1.4 shows that the pressure fluctuation of acoustic nature which is falsely computed at the order $\mathcal{O}(M)$ is responsible for the accuracy problem in the low-Mach regime. Some correction methods have been proposed in section 1.5 to rescale the wrongly computed term to the correct order $\mathcal{O}(M^2)$ as analyzed at the continuous level in section 1.2. The baseline and corrected schemes are applied in chapter 2 to a range of test problems so as to assess the respective performance of the approximate Riemann solvers with and without low-Mach correction for liquid flows.

2

The accuracy test problems

Contents

Introduction

In this chapter, we perform some low-Mach test problems to evaluate the accuracy of the standard compressible solvers with and without low-Mach corrections presented in chapter 1.
In section 2.1, we perform the 2D-axisymmetric piston test problem. The purpose of this test case is to evaluate the accuracy of the standard compressible solvers in capturing (physical) fast acoustic waves in the low-Mach number regime, meaning that the WPIC is not considered.
In section 2.2, we analyze the so-called Gresho vortex problem where only the slow motion of the fluid scale (the vortex) is involved. In this test case, the standard compressible solvers with and without low-Mach correction are evaluated using the WPIC.
Besides the aforementioned scales-separated test problems, we also consider the Gresho vortex acoustic test case in section 2.3 so as to evaluate the accuracy of both the standard and low-Mach correction schemes for a problem where the two scales (fast acoustic scale and slow fluid scale) coexist. An elementary 1D low-Mach shock tube test case is also investigated in section 2.4 to further analyze the performance of the low-Mach correction schemes in solving wave propagation problems.

2.1 2D axisymmetric cylindrical piston problem

We investigate in this section the ability of the standard compressible solvers to compute (physical) acoustic waves. In particular, the 2D axisymmetric single-phase piston problem is considered: it consists of a piston expanding radially in water initially at rest (see Figure 2.1). When expanding at low-Mach number (defined as the ratio between the moving piston velocity and the initial speed of sound in water), the (solid) piston generates an acoustic wave propagating inside the domain. The test problem mimics the expansion of the vapor bubble inside the liquid within a containment, such as taking place in Borax-type or HCDA configurations in the context of nuclear safety analysis. More precisely, the focus with the model piston problem is on reproducing the short-time behavior of these configurations; for longer times, the waves interact back with the bubble region after reflection on the containment walls while for the piston model problem they can only be reflected at the piston-liquid interface.

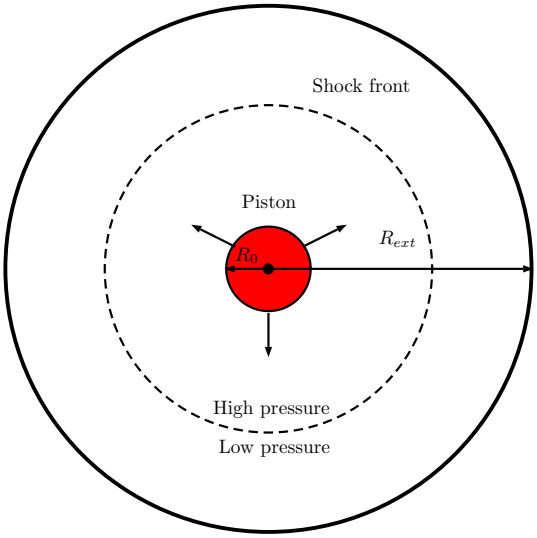

Figure 2.1: Configuration for the 2D-axisymmetric piston problem.

2.1.1 Reference 1D solution

In the following sections, the 2D-axisymmetric piston problem will be numerically solved on 2D meshes. However, it is clear the axisymmetry property of the problem yields an exact solution which depends only on time t and radial position r, being independent from the azimuthal θ coordinate. It is therefore logical to look for an exact solution of the 1D cylindrical piston problem so as to use it as a reference solution to which the 2D discrete solutions will be next compared. In [Taylor, 1946], the solution of the 1D spherical piston problem moving in a calorically perfect gas initially at rest can be found. The governing equations are turned into a system of ODEs which is numerically solved for an initial radial location $R_0 = 0$ of the piston and a constant piston velocity V_p. This so-called 1D reference solution is not stricty exact since obtained using numerical integration of the system of ODEs but the accuracy of this numerical integration can be easily made very high by a proper refinement of the numerical integration step. In [Beccantini, 2017], these same ideas are extended to the case of 1D planar, cylindrical and spherical piston problems, with a piston moving through water initially at rest and governed by the SG-EOS for the liquid. For the simplest 1D planar case, an analytical solution can actually be found by employing the Rankine-Hugoniot conditions. For the 1D cylindrical (and spherical) cases, the resulting ODE is accurately integrated to yield a reference 1D solution.

This 1D reference / quasi-exact solution of the 1D cylindrical piston problem is however limited to the case of an initial zero radial position for the piston. This is clearly a limitation of the reference solution since the future 2D experiments will be performed for an initial non-zero radial extension of the piston

($R_0 > 0$). Therefore, the 1D problem for $R_0 = 0$ is also solved with the exact Riemann solver of second-order accuracy in both time and space. The ALE approach is also considered to take into account the variation of mesh size due to the moving piston. This comparison between the 1D reference solution and the 1D numerical solution obtained using a standard compressible solver should allow on one hand to validate the compressible solver within an ALE framework and with the SG-EOS to close the physical description of the flow and will provide on the other hand a reference 1D discrete solution which will be computable for any value of the initial radial location ($R_0 > 0$ and not only $R_0 = 0$) and will be available for comparison with 2D discrete solutions.
In the tables below, we specify the initial conditions, the dimension, the parameters and the material properties retained for this test case. The left boundary condition corresponds to the moving piston surface while the right boundary condition is a fixed wall.

Initial conditions	
ρ (kg/m^3)	1000.0
P (Pa)	1×10^5
u (m/s)	0.0

Dimension and parameters	
R_{ext} (m)	1.0
R_0 (m)	0.0
V_p (m/s)	10

Material properties	
γ	4.4
P_∞ (Pa)	6.0×10^8

The problem is a low-Mach one since the sound speed c in the water initially at rest can be computed by (1.8) and is found equal to 1625 m/s while the piston is pushed at 10 m/s. The initial characteristic Mach number defined as the ratio between the piston velocity and the water speed of sound is therefore around 6×10^{-3}. We emphasize that the Initial Condition for this problem is not well-prepared (see section 1.4 for a closed 1D domain).

Results

We present in Figure 2.2 the pressure and the velocity distributons at the final time $t_f = 5 \times 10^{-4}$ s, selected so that no reflection of the wave generated by the piston motion has yet taken place at the rigid exterior (right) wall. The red and the black curves represent respectively the quasi-exact solution (obtained from the solution of the ODE describing the flow problem with $R_0 = 0$ and $V_p = const$) and the solution given by the exact Riemann solver.
Looking at the pressure distribution, a (weak) shock wave can be identified at the position $r_s \approx c \cdot t = 0.8125\ m$ followed by an isentropic compression region between $r \in [0, r_s]$. The numerical solution does not superimpose with the reference solution near the piston surface in the 800 cells mesh used for the present discrete computation but the difference goes to zero with a finer mesh. The discrete velocity distribution is in very good agreement with the reference distribution - it can be checked that velocity near the piston level is 10 m/s as expected.

Conclusion

This first comparison validates the accuracy of the standard exact Riemann solver when applied to the 1D cylindrical piston problem. Consequently, in the following 2D numerical experiments performed with a non-zero initial radius for the piston, the 2D discrete solutions will be compared with a reference 1D cylindrical solution obtained by applying the second-order exact Riemann solver with a very fine mesh on the same flow configuration (same domain, same prescribed velocity for the piston and same initial conditions and thermodynamic description based on the SG-EOS).

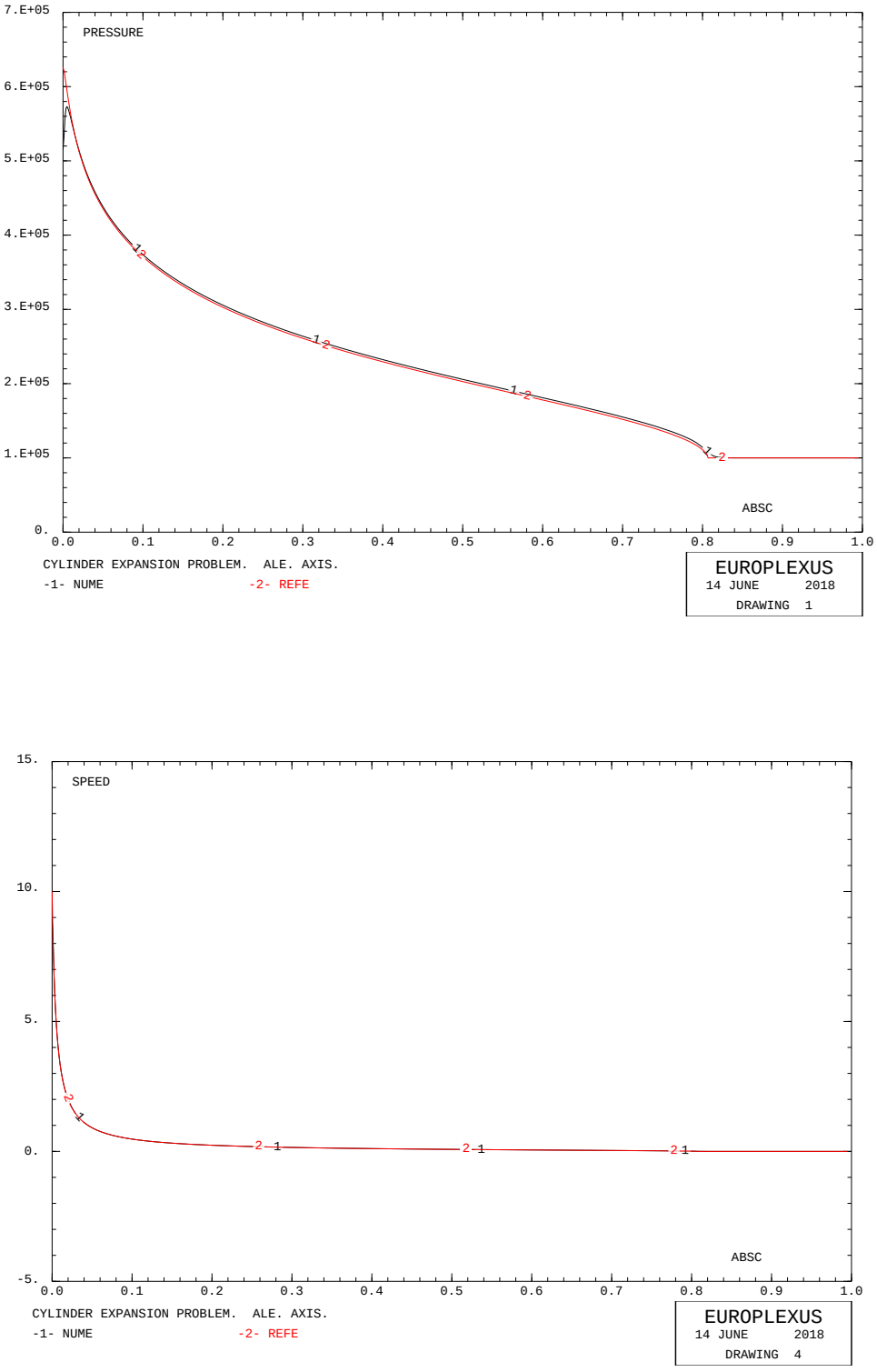

Figure 2.2: Comparison for 1D numerical (black) and reference (red) solutions for pressure (top) and velocity (bottom) at $t_f = 5 \times 10^{-4}$ s given by the exact Riemann solver, limited linear space reconstruction for primitive variables and 2-stage Runge-Kutta time discretization, $CFL = 0.5$, 800 cells.

2.1.2 2D numerical results

In this section, we compute the 2D cylindrical piston problem (with $R_0 > 0$) and compare the numerical solutions with the 1D (cylindrical) reference numerical solution. Before displaying and discussing these 2D/1D comparisons in section 2.1.2.2, we provide some detailed information about the 2D computational mesh and the piston velocity in section 2.1.2.1.

2.1.2.1 Preliminaries

Mesh generation

The 2D flow could be computed on a structured grid such as the one displayed on the right side of Figure 2.3. However such a regular mesh in the azimuthal direction θ is not really representative of the unstructured meshes generated in practice for nuclear safety problems involving the expansion of a gas bubble in a non-spherical containment (see chapter 6). Moreover it tends to favor the r direction with potential numerical error in the azimuthal direction artificially avoided by the uniformity of the grid along that direction. Consequently, we rather choose to use a computational domain corresponding to one-fourth of the real geometry. The unstructured mesh of this domain is generated with an equal spacial step along each boundary of the geometry (see the left side of Figure 2.3) to avoid favoring any direction. Moreover, the non-regular grid topology is representative of that found in the grid used for practical applications. Naturally working with a 90° domain instead of a full domain is also interesting from a computational cost viewpoint.

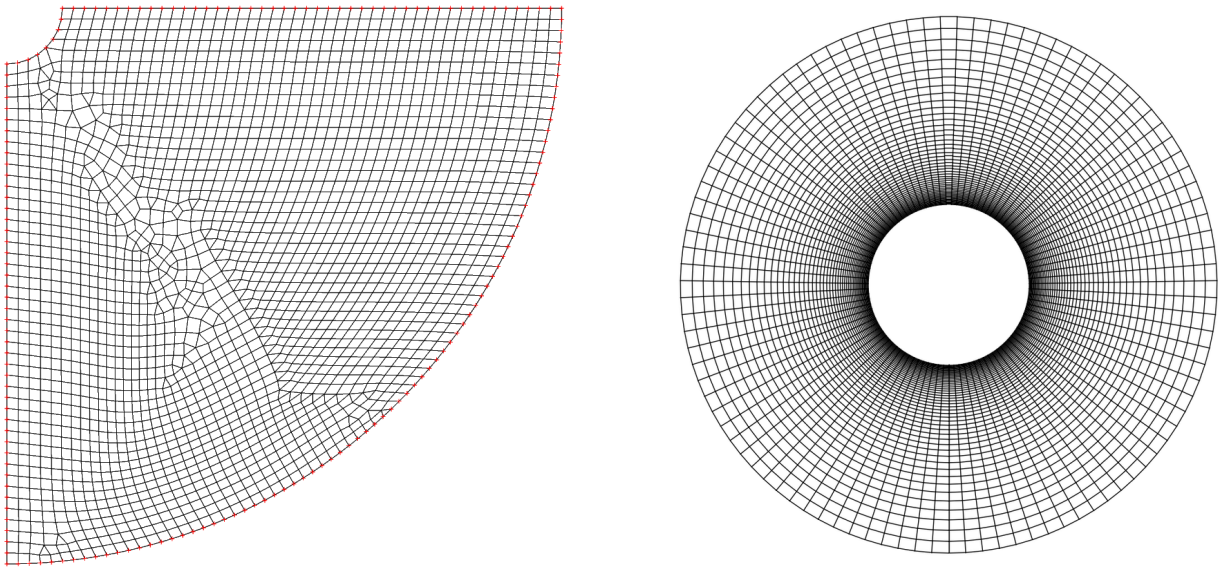

Figure 2.3: Mesh actually used for the 2D computation (left), r-direction favoring mesh not used for 2D computation (right)

Piston velocity profile

A source of potential numerical error in computing the piston problem comes from the overheating issue [Fedkiw et al., 1999]. This type of error is related to the undesirable production of numerical entropy when pushing the piston impulsively at a constant speed. In order to get rid of this type of error (so as to focus on the potential low-Mach error), we decide to increase the piston velocity gradually from $V_p = 0$ to $V_p = V_{p0}$ over a time interval $t \in [0; t_m]$ (where t_m is the climbing time or "temps de montée") and to

keep $V_p = V_{p0} = \text{const}$ at later times and until the prescribed final time is reached:

$$V_p(t) = \begin{cases} \dfrac{V_{p0}}{t_m}, t & 0 \leq t \leq t_m \\ V_{p0}, t & t_m \leq t \leq t_f \end{cases} \tag{2.1}$$

The corresponding distances that the piston and the shock / acoustic wave cover (respectively ΔR_p and ΔR_s) during t $\in [0; t_m]$ are:

$$\Delta R_p = \int_0^{t_m} V_p(t)dt = \frac{1}{2}\, V_{p0} \cdot t_m \tag{2.2}$$

$$\Delta R_s = C_s \cdot t_m \tag{2.3}$$

They are related by the piston Mach number $M_p = V_{p0}/C_s$ as:

$$\Delta R_s \approx \frac{2}{M_p} \Delta R_p$$

Since we are dealing with flow such that $M_p << 1$, we focus on ΔR_s to adjust the climbing time t_m of the piston velocity and the final time t_f.

Choice of t_m and t_f

Depending on the choice of t_m, we will have different cases ranging from fast acceleration of the piston to slow acceleration. The climbing time can be compared with the characteristic time of propagation of the acoustic / shock wave or with the time t_{imp} of impact of the wave on the exterior wall located at $r = R_{ext}$. If we wish to focus on the propagation of the wave through the liquid domain before any interference of the containment wall we will select the final time t_f such that:

$$t_f \leq t_{imp} = (R_{ext} - R_0) \cdot \frac{1}{C_s}$$

Using the exterior radius R_{ext} and the acoustic velocity C_s to make all times non-dimensional:

$$t^* = \frac{tC_s}{R_{ext}}$$

the non-dimensional impact time is given by:

$$t^*_{imp} = 1 - \left(\frac{R_0}{R_{ext}}\right)$$

For the geometry under study, we will retain $R_{ext} = 10 \times R_0$ hence $t^*_{imp} = 0.9$.
The climbing time is computed as a factor η multiplying the characteristic time R_0/C_s, that is $t_m = \eta \times \dfrac{R_0}{C_s}$. The corresponding non-dimensional climbing time is $t^*_m = \eta \times \dfrac{R_0}{R_{ext}}$ or, for the geometry under consideration, $t^*_m = \eta/10$. We will retain as maximum non-dimensional climbing time $t^*_m = 0.8 < t^*_{imp}$ (or $\eta = 8$) and divide this time by a factor 10 to define an intermediate case and another factor 10 to define the minimum non-dimensional climbing time. Consequently, we will consider the 3 following cases, ranging from a fast acceleration of the piston to a slow acceleration:

1. $t_m = 0.08\ R_0/C_s$ (fast acceleration case)
2. $t_m = 0.8 R_0/C_s$ (intermediate case)
3. $t_m = 8\ R_0/C_s$ (slow acceleration case)

Concerning the final time, we will consider t_f such that $t_m < t_f < t_{imp}$ to analyze the short time behavior of the numerical simulation and t_f such that $t_f >> t_{imp}$ to analyze the long time behavior.

2.1.2.2 Numerical results

The initial, boundary conditions and material properties are similar to the 1D problem in section 2.1.1. The initial dimensions of the computational domain and the piston velocity at $t > t_m$ are defined as:

Dimension and parameters	
R_{ext} (m)	1.0
R_0 (m)	0.1
V_{p0} (m/s)	10

The sound speed in water is as in 1D case $c = 1625$ m/s which leads to the maximum piston Mach number $M_{p0} = 6.0 \times 10^{-3}$. The dimensional time of impact is $t_{imp} = 0.554$ ms so that we consider the 2 values of the final time: $t_f = 0.5$ ms and $t_f = 10$ ms to define respectively the short time and long time behavior. The former value is such that no reflection of the propagating wave on the exterior wall occurs during the computation while the latter corresponds to approximately 20 reflections. The short climbing time corresponding to the fast acceleration of the piston (case 1) is $t_m = 4.9 \times 10^{-3}$ ms while the climbing time corresponding to the slow acceleration of the piston (case 3) is $t_m = 0.49$ ms. In all the computations, the ALE approach is employed to take into account the time-dependent computational domain. Increasingly refined meshes are considered, corresponding to a number N_r of elements in the radial direction successively equal to $N_r = 90,\ 180,\ 360,\ 720$. The solutions presented next are those obtained using the second-order exact Riemann solver (Godunov scheme) with a primitive variable reconstruction including a limitation procedure. The time integration is performed using a 2-stage Runge-Kutta method. Calculations have also been performed using approximate Riemann solvers and results similar to those obtained with the Godunov scheme have been obtained.

Case 1 (fast acceleration) short time behavior ($t_f = 0.5$ ms)

In Figure 2.4 we present the 2D pressure solution and Figure 2.5 displays its projection (black curve) on two different lines of -45^o (LIG45) and -88^o (LIG88) with respect to the horizontal line in order to facilitate the comparison with the reference 1D cylindrical solution (red curve). From Figure 2.4, we can state that the pressure solution is independent of the azimuthal direction. A shock wave is identified as expected in case 1 at the position:

$$r_s \approx R_0 + C_s \cdot t_f = 0.1 + 1625 \cdot 5.0 \times 10^{-4} = 0.9125 \text{ m}$$

The intensity of this shock wave decreases rapidly in magnitude when moving towards the exterior wall due to the multi-dimensional propagation effect.
In Figures 2.6, 2.7, we present the results for the velocity field. A jump in velocity at $r_s = 0.9125$ m is also identified and there are also small oscillations near the piston surface, with an overshoot of about 1% for the maximum computed velocity. However, these numerical errors reduce with finer meshes and the solutions are clearly independent of the azimuthal direction. The comparison with the 1D reference solution demonstrates the accuracy of the 2D numerical solution: apart from the expected truncation error which yields a slightly diffused shock wave, there is no evidence of a low-Mach issue with the 2D calculation for this quickly accelerating piston observed in short time.

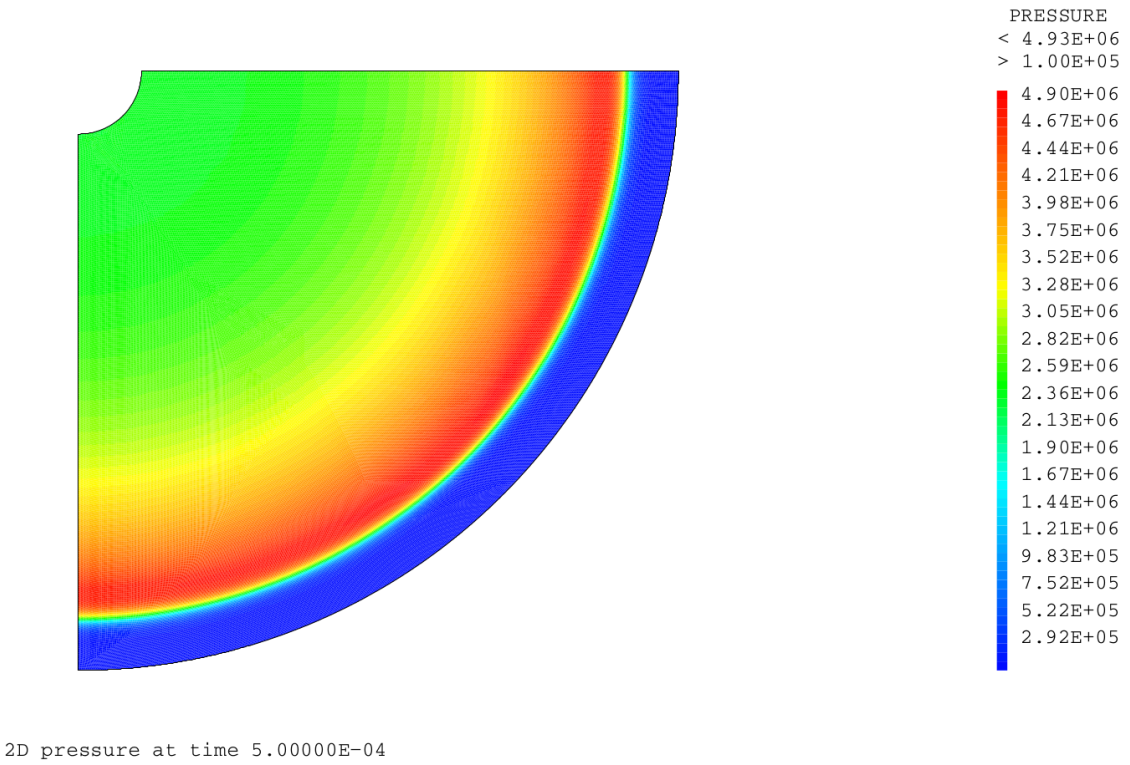

Figure 2.4: 2D-axisymmetric piston problem. Case 1 short time. 2D pressure solution given by the exact Riemann solver, limited linear space reconstruction for primitive variables and 2-stage RK time discretization. $CFL = 0.5$, $N_r = 360$.

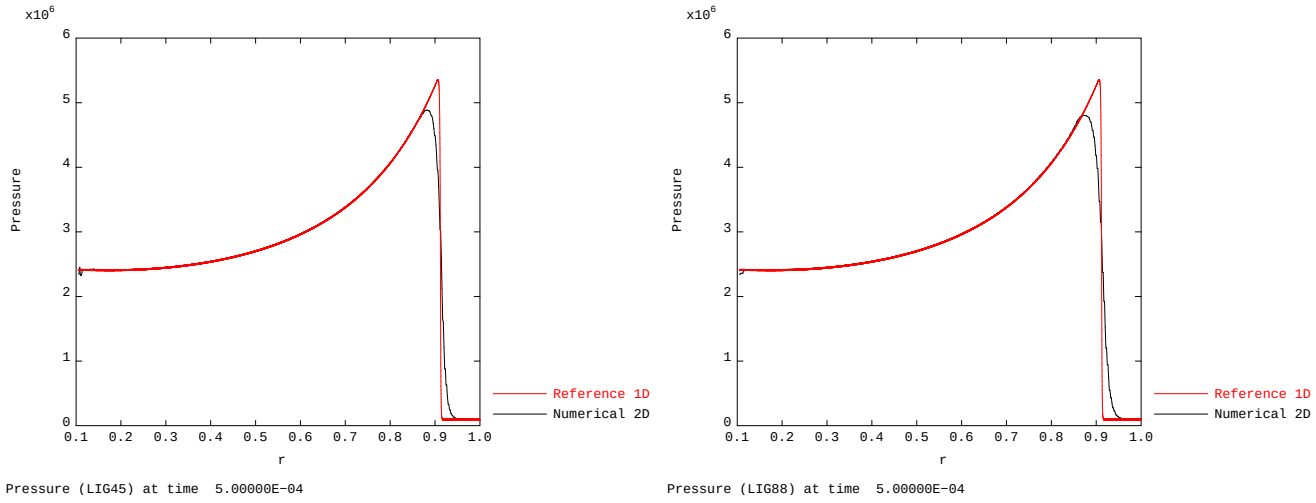

Figure 2.5: 2D-axisymmetric piston problem. Case 1 short time. 2D/1D pressure solutions on LIG45 (Left) and on LIG88 (Right) given by the exact Riemann solver, limited linear space reconstruction for primitive variables and 2-stage RK time discretization. $CFL = 0.5$, $N_r = 360$, $N_{1D,ref} = 10000$.

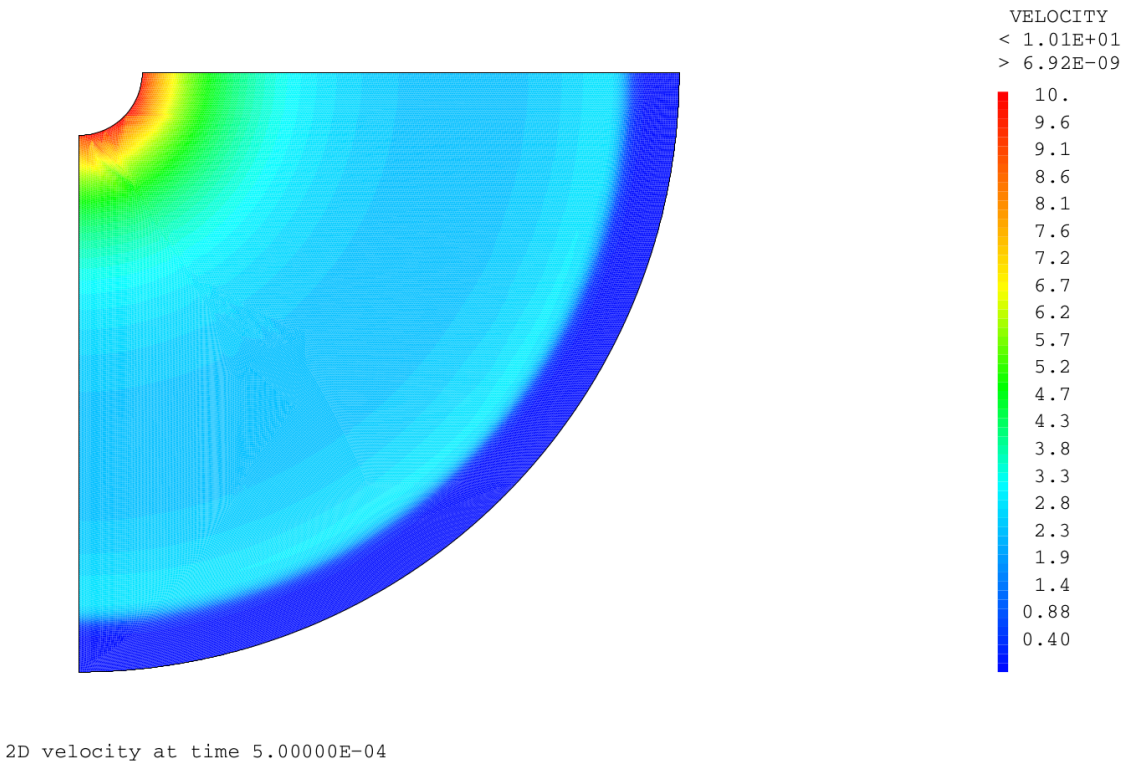

Figure 2.6: 2D-axisymmetric piston problem. Case 1 short time. 2D velocity solution given by the exact Riemann solver, limited linear space reconstruction for primitive variables and 2-stage RK time discretization. $CFL = 0.5$, $N_r = 360$.

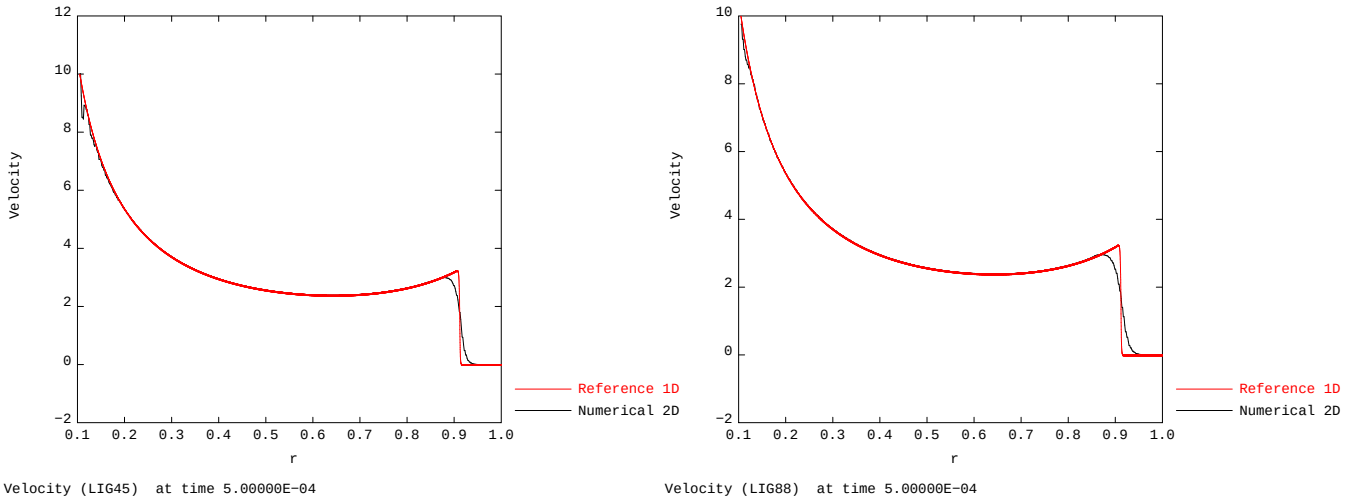

Figure 2.7: 2D-axisymmetric piston problem. Case 1 short time. 2D/1D velocity solutions on LIG45 (Left) and on LIG88 (Right) given by the exact Riemann solver, limited linear space reconstruction for primitive variables and 2-stage RK time discretization. $CFL = 0.5$, $N_r = 360$, $N_{1D,ref} = 10000$.

Case 3 (slow acceleration) short time behavior ($t_f = 0.5$ ms)

In the case of a slowly accelerating piston, no pressure jump is observed in Figures 2.8 and 2.9. Since the period of linear acceleration of the piston ends at $t_m = 0.49$ ms which is close to the final time of our simulation $t_f = 0.5$ ms, the pressure is found to reach its maximum value near the piston surface. The pressure solution is independent of the azimuthal direction as shown in Figure 2.8. The comparisons

between the projected 2D solution along the same radial lines (45 and 88 degrees below the horizontal) and the reference 1D solution confirm the accuracy of the 2D calculation. Figures 2.10 and 2.11 display the solutions for the velocity field. Negligible oscillations can be observed in the 2D solution near the piston surface but those are reduced on finer meshes. Overall, the 2D solution agrees very well with the 1D reference one.

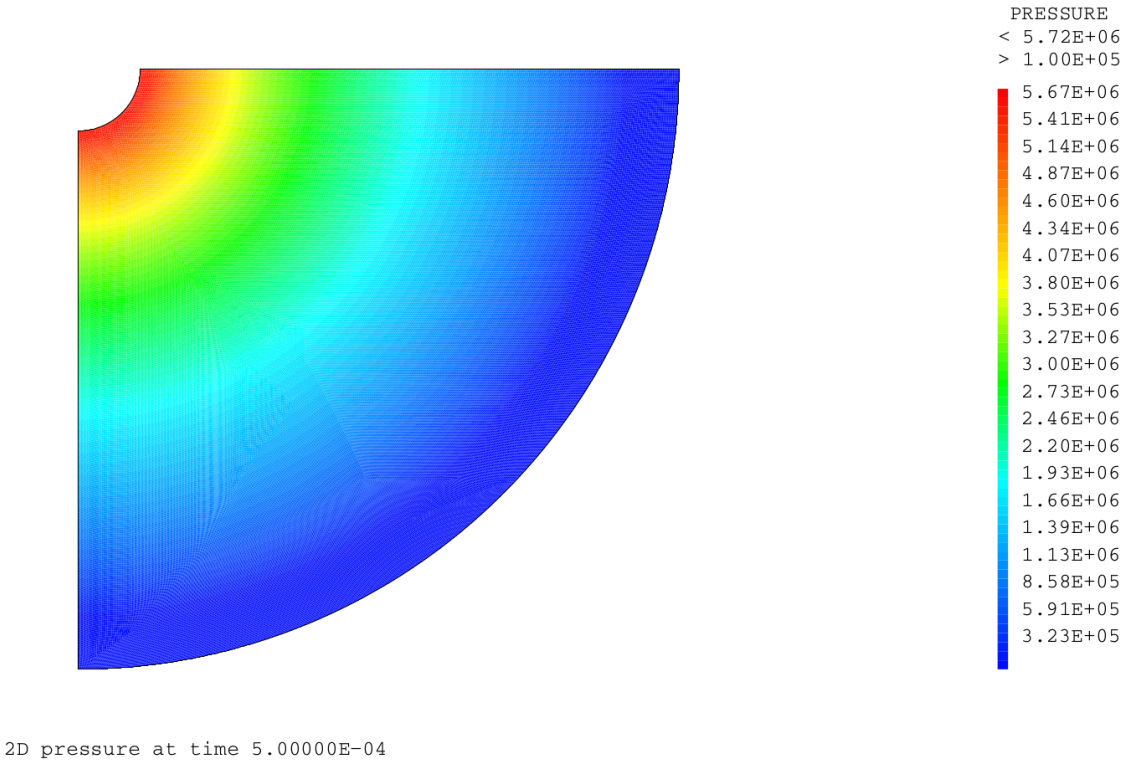

Figure 2.8: 2D-axisymmetric piston problem. Case 3 short time. 2D pressure solution given by the exact Riemann solver, limited linear space reconstruction for primitive variables and 2-stage RK time discretization, $CFL = 0.5$, $N_r = 360$.

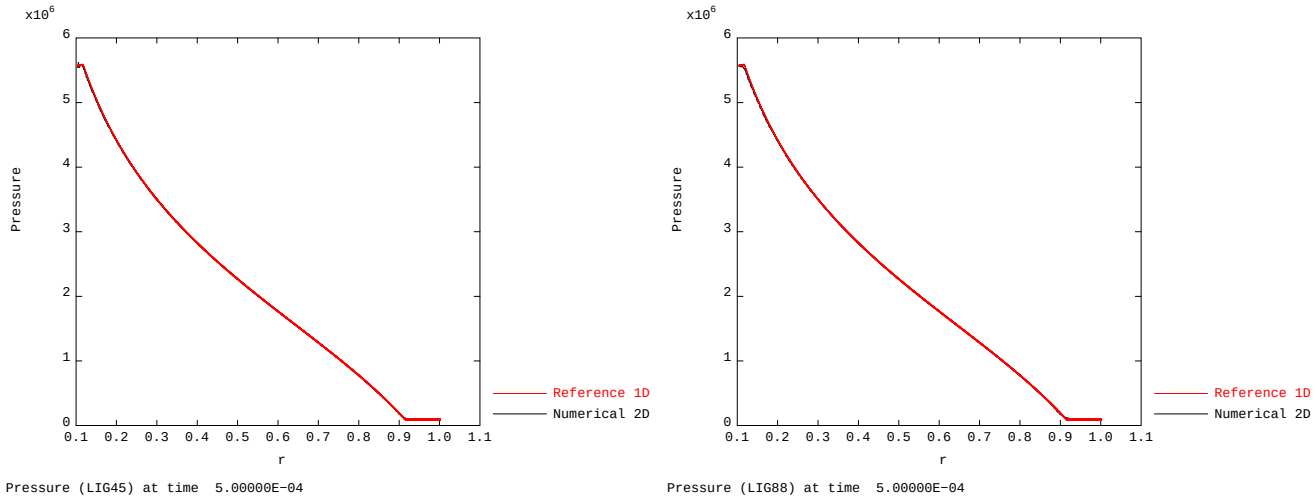

Figure 2.9: 2D-axisymmetric piston problem. Case 3 short time. 2D/1D pressure solutions on LIG45 (Left) and on LIG88 (Right) given by the exact Riemann solver, limited linear space reconstruction for primitive variables and 2-stage RK time discretization. $CFL = 0.5$, $N_r = 360$, $N_{1D,ref} = 10000$.

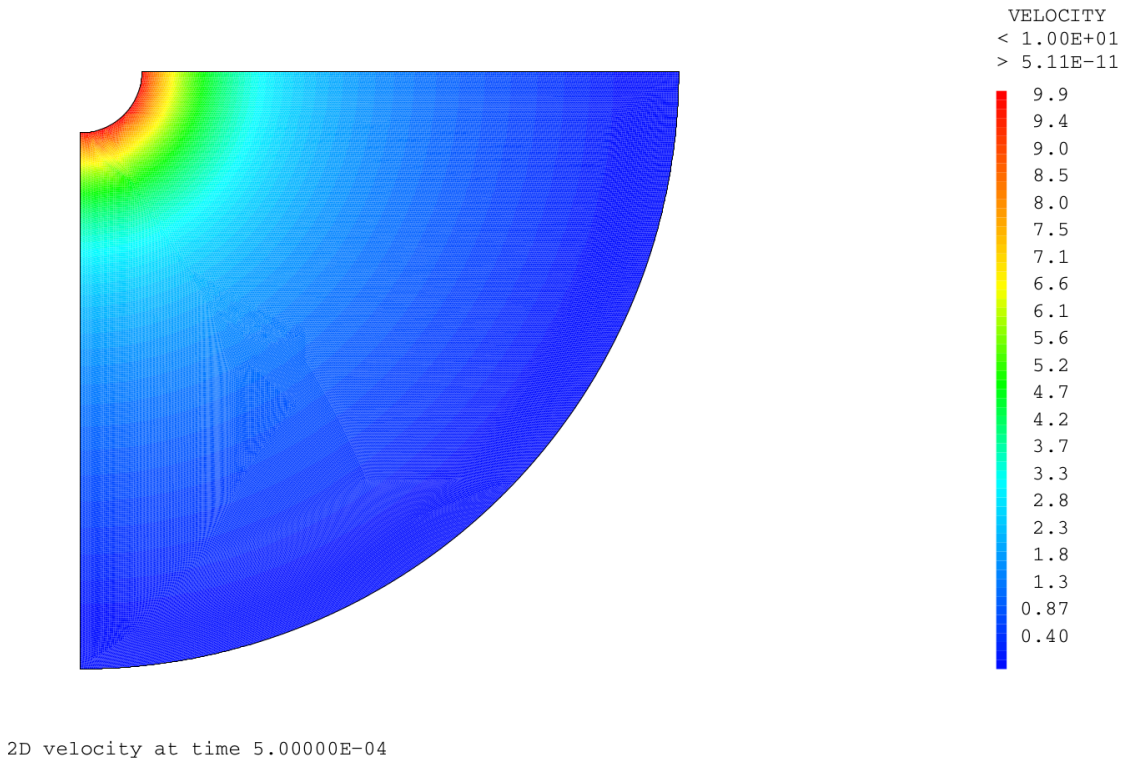

Figure 2.10: 2D-axisymmetric piston problem. Case 3 short time. 2D velocity solutions given by the exact Riemann solver, limited linear space reconstruction for primitive variables and 2-stage RK time discretization. $CFL = 0.5$, $N_r = 320$.

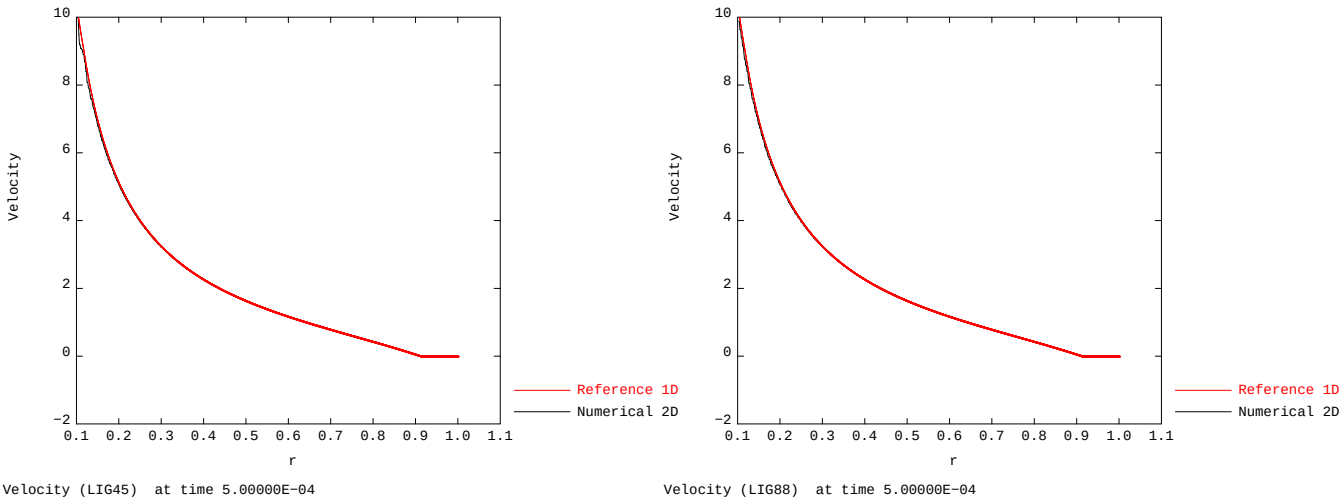

Figure 2.11: 2D-axisymmetric piston problem. Case 3 short time. 2D/1D velocity solutions on LIG45 (Left) and on LIG88 (Right) given by the exact Riemann solver, limited linear space reconstruction for primitive variables and 2-stage RK time discretization. $CFL = 0.5$, $N_r = 360$, $N_{1D,ref} = 10000$.

Conclusion for the short time behavior:

- We can state that there is no sign of a low-Mach accuracy problem when computing acoustic wave in short time using a conventional exact Riemann solver (Godunov scheme).
- Other (approximate) Riemann solvers have also been tested (*e.g.* HLLC, Roe) and the same conclu-

sions could de drawn regarding the lock of low-Mach accuracy issue. Note this does not contradict the theoretical analysis performed in the previous chapter since the testcase does not include well prepared initial conditions (WPIC).

- Note the same configuration has also been computed for air governed by the perfect gas EOS (with relevant changes in the characteristic times to account for the change of acoustic speed). The flow physics was found to remain well predicted by the standard compressible solvers in that case as well.

Case 1 (fast acceleration) long time behavior ($t_f = 10$ ms)

The low-Mach accuracy problem identified in [Guillard and Viozat, 1999, Miczek et al., 2015, Bruel et al., 2019] correspond usually to stationary test cases. Consequently, we decide to analyze the long time solutions of the piston problem computed using standard compressible solvers to check whether the acoustic scale remains correctly computed.
In Figure 2.12, the pressure solutions projected on LIG45 and LIG88 show that they remain independent of the azimuthal direction. In smooth flow regions (where the maximum grid refinement of the 2D calculation is sufficient to capture the flow gradients), the 2D solution and the reference 1D solution are almost superimposed, with however a slight under-estimation of the pressure peak. This error comes from the numerical diffusion inherent to all the numerical solvers applied to the problem and more significant for the multiD computations. It is this same usual numerical diffusion (and not the specific low-Mach accuracy issue) which is also responsible for smoothing the pressure and velocity variations.
Concerning the velocity solution, presented in Figure 2.13, on top of the underestimation of the velocity peak, one can also notice some errors in the smooth flow region with respect to the reference 1D solution, on the piston side of the domain. These errors indicate a loss of azimuthal invariance for the 2D numerical solution which could be a sign of low-Mach accuracy issue in long time but would remain a limited problem with a numerical solution still physically consistent with the reference one after about 20 reflections

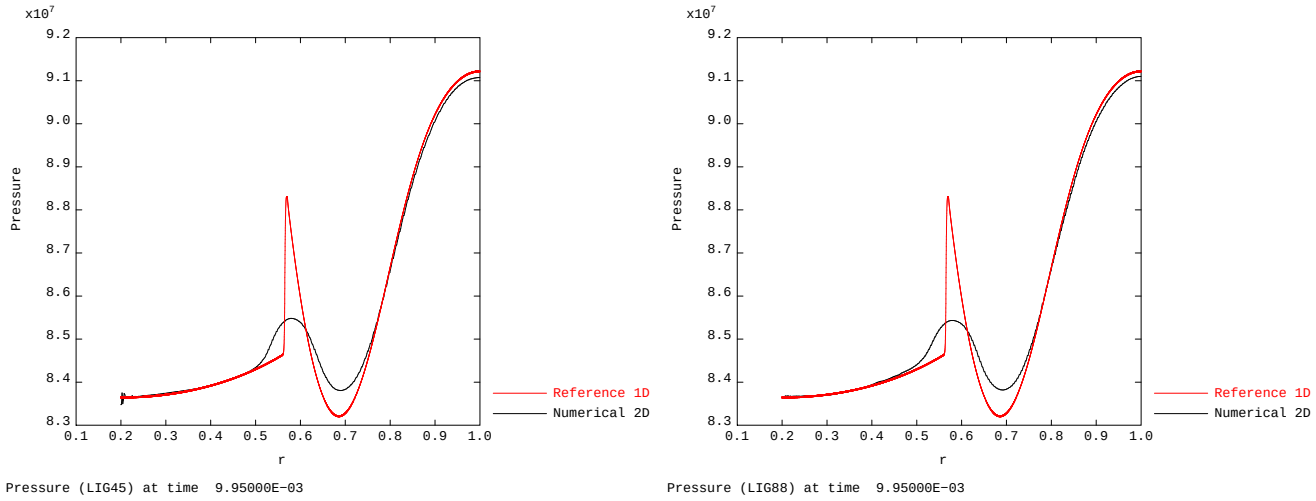

Figure 2.12: 2D-axisymmetric piston problem. Case 1 long time. 2D/1D pressure solutions on LIG45 (Left) and on LIG88 (Right) given by the exact Riemann solver, limited linear space reconstruction for primitive variables and 2-stage RK time discretization, $CFL = 0.5$, $N_r = 360$, $N_{1D,ref} = 10000$.

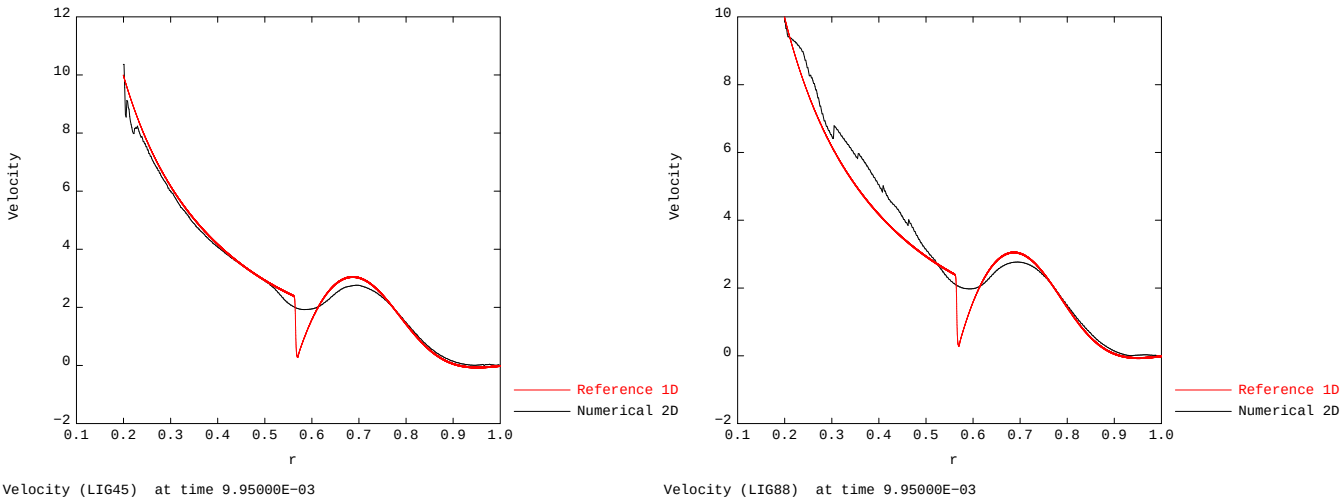

Figure 2.13: 2D-axisymmetric piston problem. Case 1 long time. 2D/1D velocity solutions on LIG45 (Left) and on LIG88 (Right) given by the exact Riemann solver, limited linear space reconstruction for primitive variables and 2-stage RK time discretization. $CFL = 0.5$, $N_r = 360$, $N_{1D,ref} = 10000$.

Case 3 (slow acceleration) long time behavior ($t_f = 10$ ms)

Results for the long time computations for the slowly accelerating piston are presented in Figures 2.14 and 2.15. In general, we observe that the physics remains well predicted for the pressure in the 2D calculations while the velocity tends to display small errors with respect to the reference 1D solution near the piston surface.

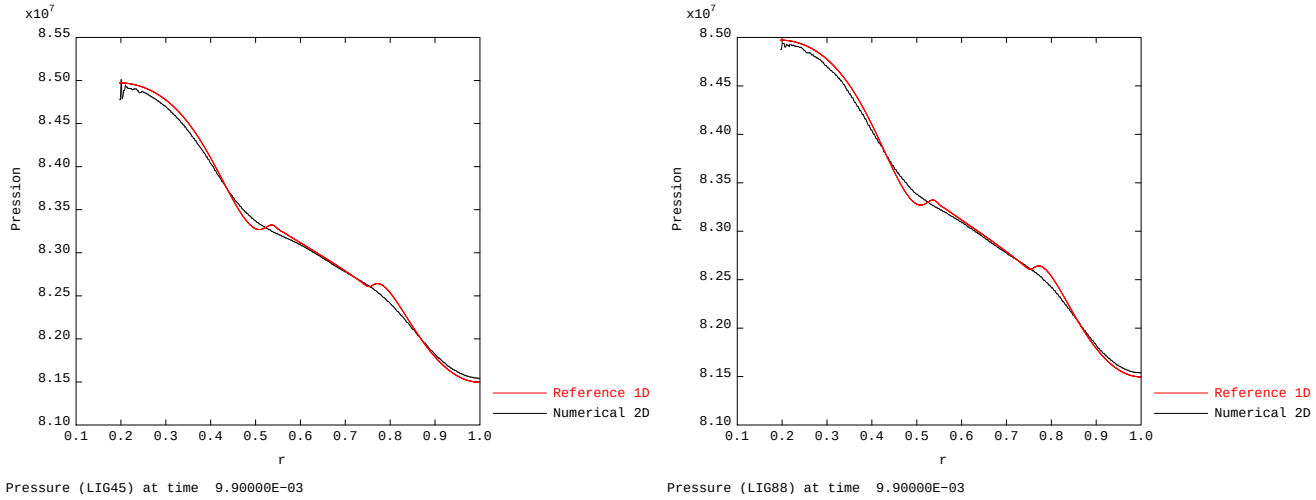

Figure 2.14: 2D-axisymmetric piston problem. Case 3 long time. 2D/1D pressure solutions on LIG45 (Left) and on LIG88 (Right) given by the exact Riemann solver, limited linear space reconstruction for primitive variables and 2-stage RK time discretization. $CFL = 0.5$, $N_r = 360$, $N_{1D,ref} = 10000$.

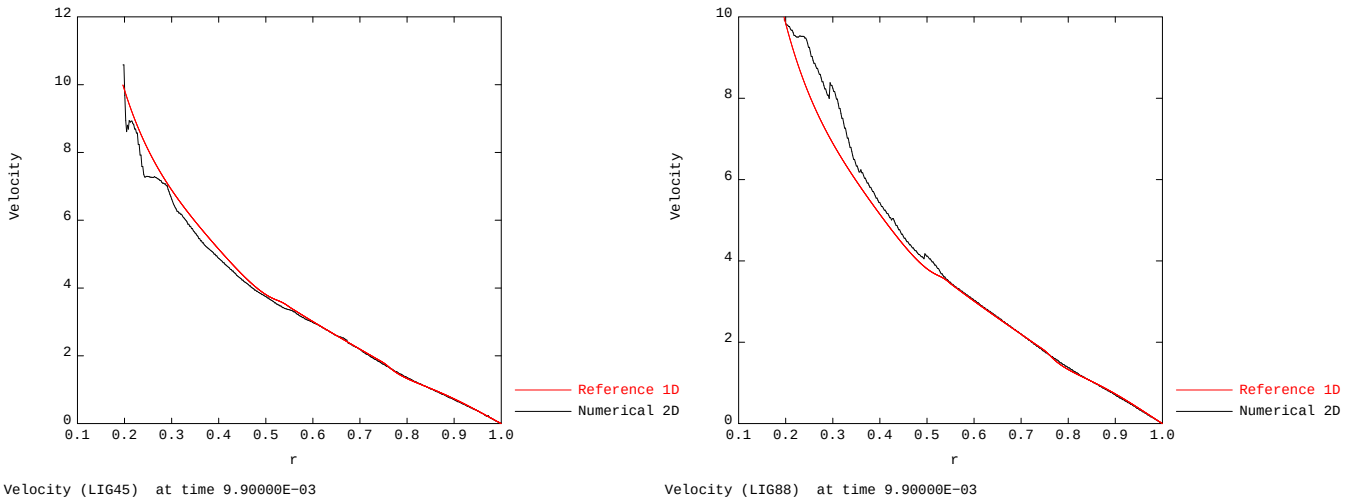

Figure 2.15: 2D-axisymmetric piston problem. Case 3 long time. 2D/1D velocity solutions on LIG45 (Left) and on LIG88 (Right) given by the exact Riemann solver, limited linear space reconstruction for primitive variables and 2-stage RK time discretization. $CFL = 0.5$, $N_r = 360$, $N_{1D,ref} = 10000$.

Conclusion for the long time behavior

- The physical phenomena remain globally well predicted for the 2D case computed using the standard exact Riemann solver, be it for the quickly or slowly accelerating piston. More precisely, in the fast acceleration case, it can be observed the pressure peak created by the piston motion tends to be underestimated but this is mostly due to a "natural" numerical diffusion of the upwind scheme (Godunov exact Riemann solver) used for the simulation and not to a spurious excessive numerical diffusion in the low-Mach limit. The errors appearing on the velocity profile, for short and long time calculations, could be due to parasite acoustic waves but they remain limited with respect to the amplitude of the physical waves.

- The results and comments presented here for the second-order Godunov scheme extend to approximate Riemann solvers (such as HLLC or Roe) which have also been tested using their implementation in Europlexus. Computing the propagation of an acoustic wave in a liquid using these standard approximate Riemann solvers does not introduce a low-Mach accuracy issue (apart maybe from some oscillations on the velocity distribution with a loss of azimuthal invariance, as pointed out for the previous calculations using the exact Riemann solver).

- When considering the piston moving through air governed by the perfect gas EOS, it could also be concluded that the physical phenomena were still well predicted by the standard compressible solver, without the need to introduce low-Mach corrections.

Conclusion for the 2D-axisymmetric piston problem:

The numerical results obtained in this section demonstrate the ability of the standard compressible solvers to properly capture the acoustic scale in the low-Mach number regime for both short and long time calculations of a cylindrical piston moving through a fluid (liquid or gas) initially at rest. Small oscillations on the velocity field, in the region near the piston surface, have been observed, which could be possibly due to parasite acoustic waves but their amplitude remains limited with respect to the physical waves. These findings were confirmed by a systematic grid convergence study (not reported here for the sake of conciseness) where the accuracy order of the 2D standard (without low-Mach correction) numerical schemes was computed for decreasing values of the piston characteristic Mach number M_p and found independent of M_p (which would not have been the case if the low-Mach accuracy issue occur).
The observations made in this section could be seen somehow as in contradiction with the theoretical

analysis performed in the previous chapter regarding the occurence of low-Mach accuracy issue for multiD low-Mach flows in closed domains. However, we emphasize that the initial conditions for the computed piston testcases are not well-prepared. We have indeed made the choice to retain natural initial conditions, representative of those found in practical applications. It is consequently interesting to observe the impact of the choice of initial conditions on the occurrence of the low-Mach accuracy issue.
Note that we provide in Appendix C some results for the same test case but slightly modified to account for WPIC: in that case, the low-Mach accuracy problem is present.
In chapter 3, we will repeat the same problem with WPIC and demonstrate the newly proposed numerical method introduced in the second part of this work to address the efficiency issue will also fix this accuracy issue for the piston problem with WPIC.

2.2 Gresho vortex problem

In this section, we investigate the ability of the standard and corrected compressible solvers to compute the (slow) fluid scale in the low-Mach number regime by solving the Gresho vortex problem. This flow configuration is a stationary vortex rotating around its center with an azimuthal velocity depending only on the radial direction. The numerical treament of the compressible Euler equations governing the flow should be able to preserve the initial vortex over time. As discussed in the previous chapiter, it is expected the propagation of parasite acoustic waves scaling as $\rho c \Delta u$ will pollute the numerical solution when using a standard compressible scheme without low-Mah correction.
The test problem was initially introduced in [Gresho and Chan, 1990], hence its denomination, with some slight modifications introduced in [Miczek et al., 2015], [Bruel et al., 2019] which will be also adopted here. It is usually computed with the fluid assumed to behave as a perfect gas. In the present work we will consider this vortex in water described using the SG-EOS. Since the quantity ρc for water is much larger than for gases, it is expected that the low-Mach accuracy problem for water will be espcially severe.

2.2.1 Problem description

Computational domain and mesh

We perform our computations on a rectangle domain with the following dimensions $[x_1, x_2] \times [y_1, y_2] = [-1\text{m}, 1\text{m}] \times [0\text{m}, 1\text{m}]$. The origin $(0, 0)$ and the vortex center are superimposed and located at the center of the domain. As discussed in section 1.5.2, the topology of the mesh may help fix the low-Mach accuracy problem. We therefore consider meshes with different topologies: quadrangular (QUAD) and triangular (TRI) meshes. The triangular mesh is formed by dividing a quadrangular cell into 4 triangles (see Figure 2.16). In case of the TRI mesh, we further distinguish two configurations (see Figure 2.17) since we will observe the numerical solution can be sensitive to the detail of this initial location of the vortex center:

- TRI-CEN-FAC: the center of the initial vortex is on the face of the cell.
- TRI-CEN-VER: the center of the initial vortex is on a vertex of the cell.

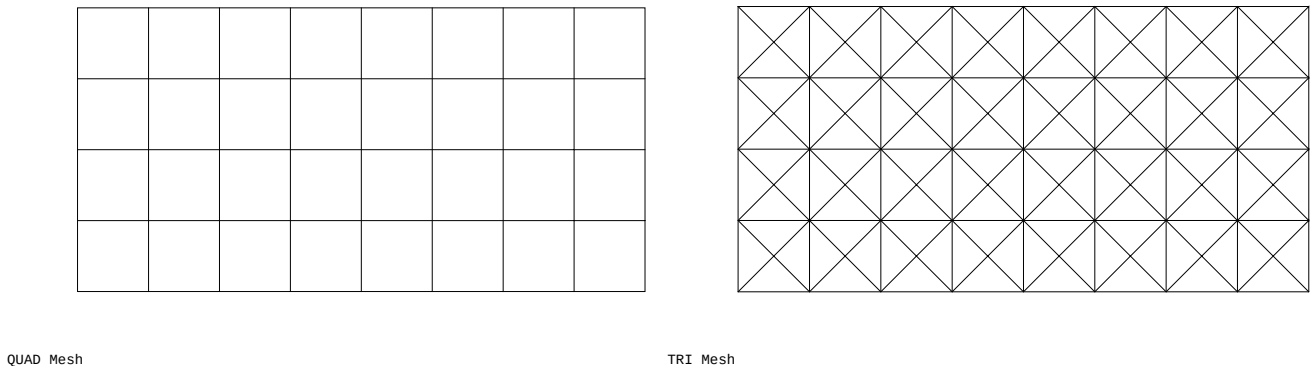

Figure 2.16: Computational mesh: QUAD (left) , TRI (right)

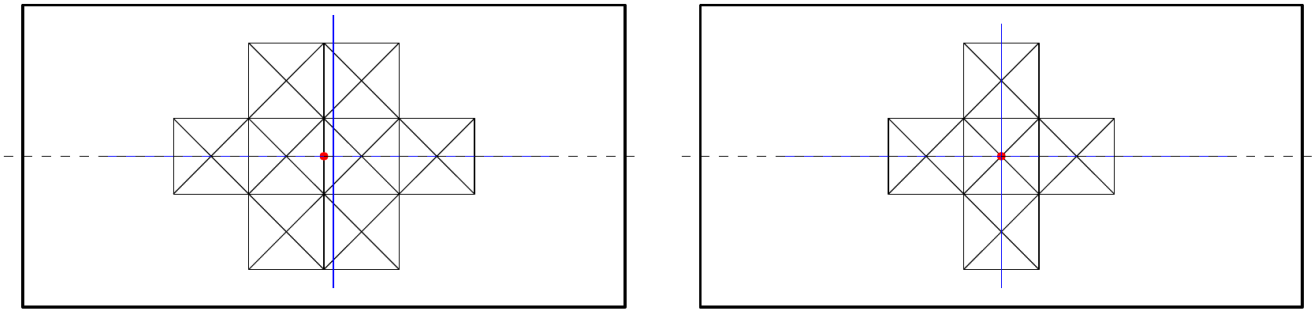

Figure 2.17: TRI meshes: TRI-CEN-FAC (left), TRI-CEN-VER (right). The center of the initial vortex is indicated by the red dot.

Initial and boundary condition

The initial velocity profile for the Gresho vortex problem is specified in (2.4). The maximum velocity is 1 m/s located at radius of $r = 0.2$ m from the vortex center. The fluid is at rest at the vortex center $r = 0$ and outside the vortex region ($r \geq 0.4$) (cf. Figure 2.18).

$$u_{\theta,0}(r) = \begin{cases} 5r, \ 0 \leq r < 0.2 \\ 2 - 5r, \ 0.2 \leq r < 0.4 \\ 0, \ 0.4 \leq r \end{cases} \tag{2.4}$$

In the absence of gravity, viscosity and discontinuity, the flow is governed by the following two-dimensional Euler system in cylindrical coordinates:

$$\begin{aligned} \frac{\partial \rho}{\partial t} + \frac{1}{r}\frac{\partial}{\partial r}(r\rho u_r) + \frac{1}{r}\frac{\partial}{\partial \theta}(\rho u_\theta) &= 0 \\ \rho(\frac{\partial u_r}{\partial t} + u_r\frac{\partial u_r}{\partial r} + \frac{u_\theta}{r}\frac{\partial u_r}{\partial \theta} - \frac{u_\theta^2}{r}) &= -\frac{\partial p}{\partial r} \\ \rho(\frac{\partial u_\theta}{\partial t} + u_r\frac{\partial u_\theta}{\partial r} + \frac{u_\theta}{r}\frac{\partial u_\theta}{\partial \theta} - \frac{u_r u_\theta}{r}) &= -\frac{\partial p}{\partial \theta} \\ \frac{\partial \rho e^t}{\partial t} + \frac{1}{r}\frac{\partial}{\partial r}(r(\rho e^t + p)u_r) + \frac{1}{r}\frac{\partial}{\partial \theta}((\rho e^t + p)u_\theta) &= 0 \end{aligned} \tag{2.5}$$

If the initial velocity distribution is a steady solution for the flow, the solution at all time remains equal to this initial state. Since the initial velocity has only a non-zero azimuthal component depending only

on the radial direction, the momentum equations $(2.5)_2$, $(2.5)_3$ reduce to only one equation describing the balance between the centrifugal force and the pressure gradient:

$$(2.5)_2 \rightarrow \rho \frac{u_\theta^2}{r} = \frac{\partial p}{\partial r} \tag{2.6}$$

By integrating (2.6) supposing that the density field is constant in low-Mach number regime, we obtain the initial pressure profile specified in (2.7). The initial fields are illustrated in Figure 2.18.

$$p_0(r) = p(r) = \begin{cases} p_c + \frac{25}{2}\rho r^2, \ 0 \leq r < 0.2 \\ p_c + \frac{25}{2}\rho r^2 + 4\rho(1 - 5r - ln(0.2) + ln(r)), \ 0.2 \leq r < 0.4 \\ p_c + \rho(4ln(2) - 2), \ 0.4 \leq r \end{cases} \tag{2.7}$$

where p_c is the constant pressure at the center of the vortex ($r = 0$) and is chosen such that $\frac{p - p_c}{p_c} \approx O(M^2)$. We notice that the specified initial conditions (2.4), (2.7) are WPIC since we satisfy the divergence free constraint $\nabla \cdot u_\theta = 0$ and the pressure fluctuation scales like $\mathcal{O}(M^2)$. The Euler system is closed by the SG-EOS (1.7) with $\gamma = 4.4$ and $p_\infty = 6.0 \times 10^8$ for water.
The following table specifies the magnitude of the initial fields:

	Water
ρ (kg/m^3)	1000
$\mathbf{u}_{\theta,0,max}(r)$ (m/s)	1
p_c (Pa)	3.0×10^8
M_{max}	5.0×10^{-4}

We impose periodic boundary conditions at the left and right sides of the computational domain while the upper and lower sides are fixed walls.

Expected solution

Since the problem is stationary, the ideal numerical solution should not vary in time and should remain strictly superimposed with the initial state at any time. However, all numerical methods present a numerical diffusion which will modify the initial state. In low-Mach number regime, the numerical diffusion for standard compressible schemes is likely to become excessive and it is expected the low-Mach correction described in the previous chapter should fix this issue. It will be also interesting to monitor the evolution of the flow energy and its preservation by the numerics, keeping in mind that for future application in the field of nuclear safety the correct estimate of the load applied by the fluid on the containment structure is directly linked with this proper energy preservation.

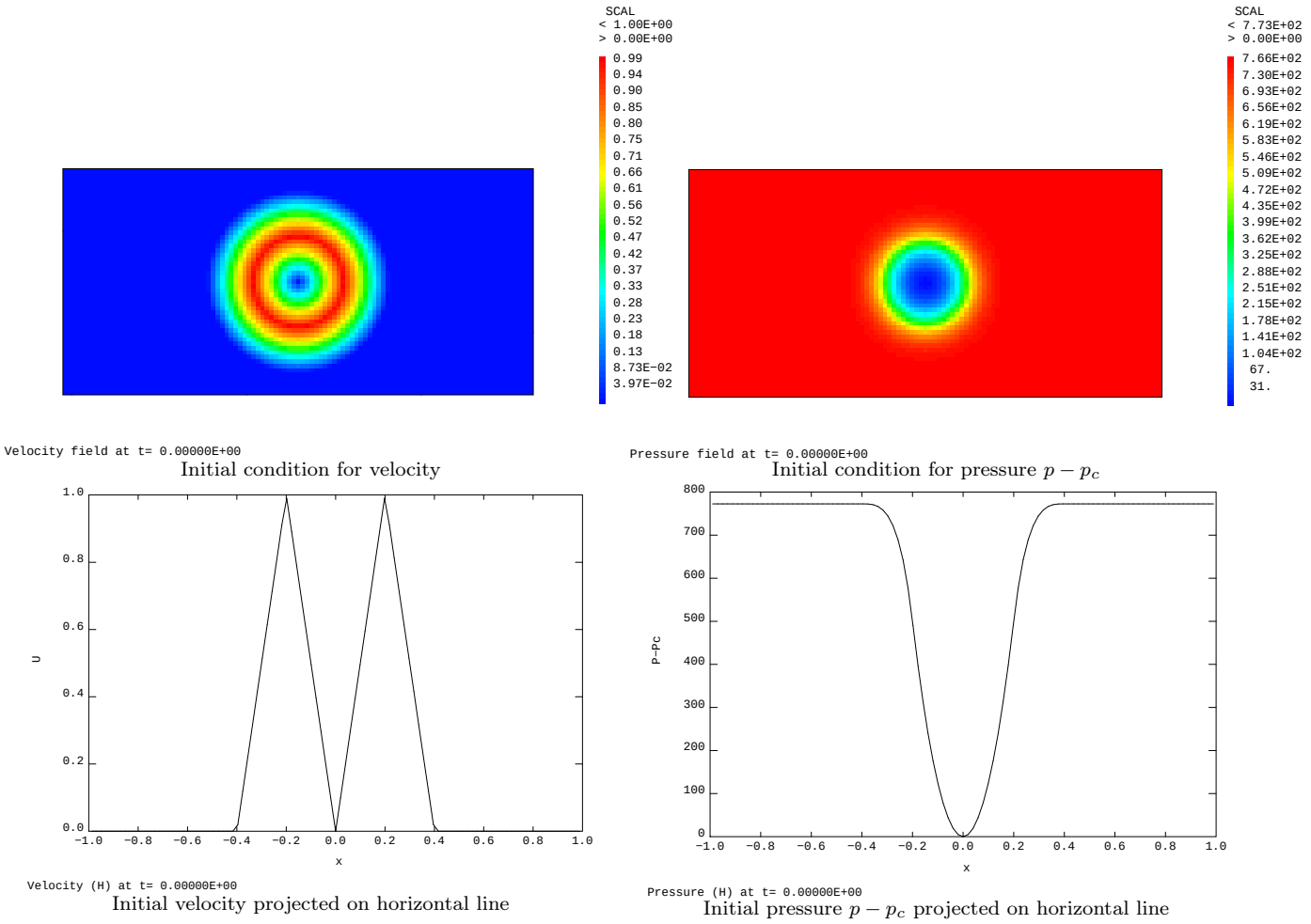

Figure 2.18: Gresho vortex problem. Initial conditions for velocity (top, left) and its projection on the horizontal line crossing the vortex center (bottom, left), for pressure $p - p_c$ (top, right) and its projection on the horizontal line crossing the vortex center (bottom, right)

2.2.2 Numerical results

In this section, we investigate the behavior of the numerical solutions using the standard compressible solvers with and without the low-Mach correction, for a final time of simulation $t_f = 0.125$ s which corresponds to 10% only of a complete revolution of the vortex but is sufficient to achieve relevant observations. The discretization schemes and meshes employed throughout the numerical experiments are clarified in Figure 2.19.
For the test cases 1) $\rightarrow$ 6) in Figure 2.19, the computations are performed using the second order accurate (with limiter) HLLC scheme and its low-Mach correction version denoted as the HLLCDL scheme (where DL refers to the fact the Dellacherie low-Mach correction is applied) considering the following meshes:

- QUAD (101x51) mesh with 101 and 51 quadrangular cells in the horizontal and vertical directions respectively.
- TRI-CEN-FAC(50x25x4) (TRI-CEN-VER(51x25x4)) meshes with 50 (51) and 25 (25) quadrangular cells in the horizontal and vertical directions respectively. Each quadrangle is then divided into 4 triangles.

For the test cases 7) $\rightarrow$ 10) in Figure 2.19, we compute with the first order schemes and TRI meshes.

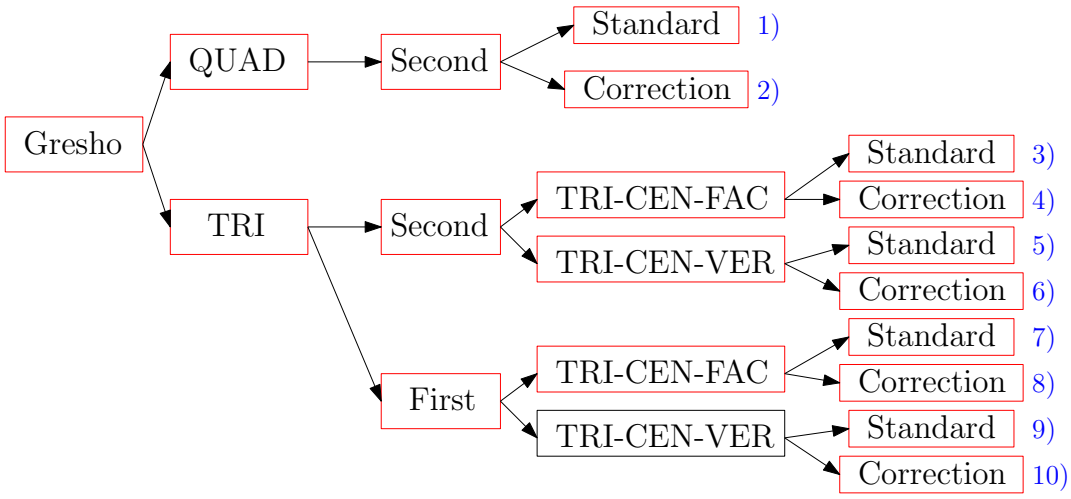

Figure 2.19: Gresho vortex problem: Tree classifications

In Table 2.1, we summarize the results for the test cases 1) → 4). The numerical solutions are presented and compared with the initial state in Figures 2.20, 2.21.

Scheme	Water Gresho vortex test case					
	QUAD			TRI-CEN-FAC		
	Density	Velocity	Pressure	Density	Velocity	Pressure
HLLC	✓	×	×	✓	✓	×
HLLCDL	✓	✓	✓	✓	✓	✓

Table 2.1: Gresho vortex problem: Results for the test cases 1) 2) 3) 4)

×: excessive diffusion solution, ×: oscillation, ✓: satisfactory solution with the numerical scheme in consideration.

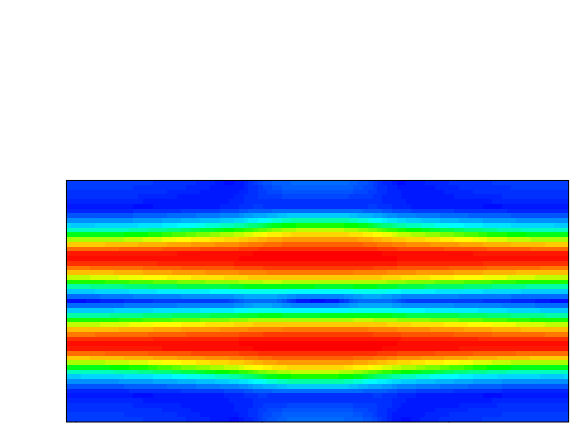

a) QUAD mesh without correction

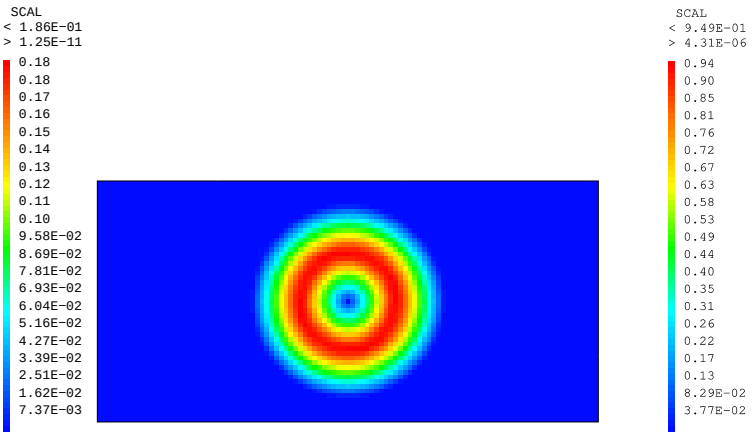

b) QUAD mesh with correction

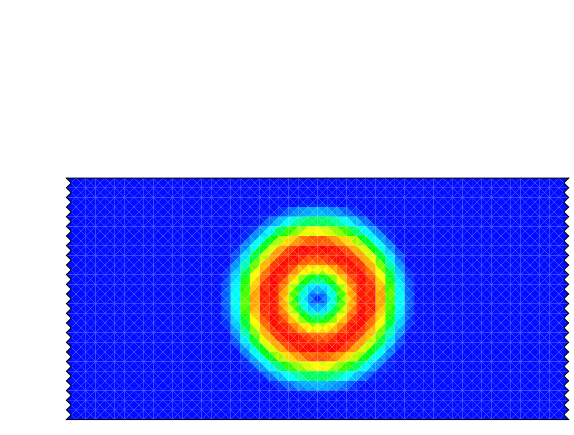

c) TRI-CEN-FAC mesh without correction

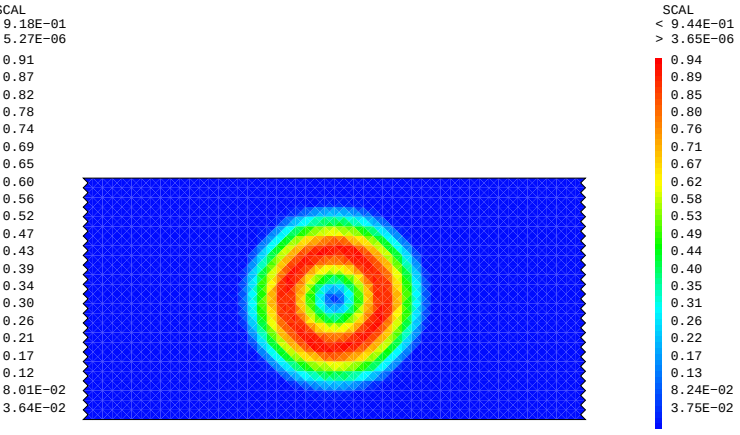

d) TRI-CEN-FAC mesh with correction

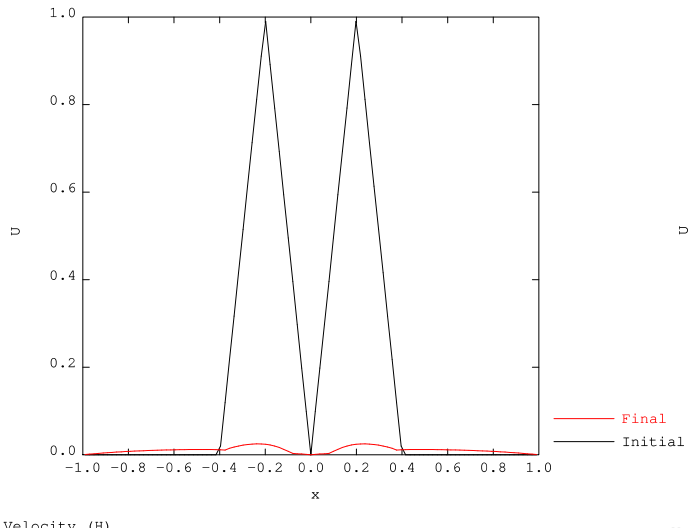

e) Horizontal line: QUAD mesh without correction

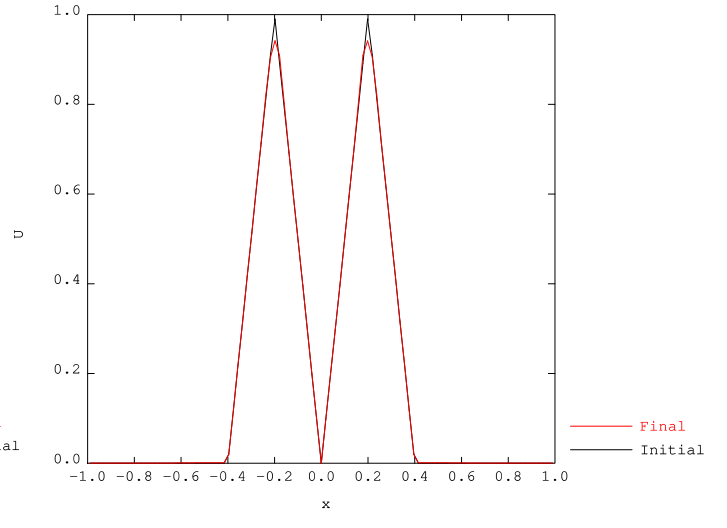

f) Horizontal line: QUAD mesh with correction

Figure 2.20: Gresho vortex problem (water, test cases $1, 2, 3, 4$): Velocity comparison on QUAD and TRI-CEN-FAC meshes, $M_{max} = 5.0 \times 10^{-4}$, $t_f = 0.125$ s (10% of a complete revolution). Second order in space HLLC and HLLCDL schemes (with limiter) and second order in time with 2-stage RK method, $CFL = 0.45$

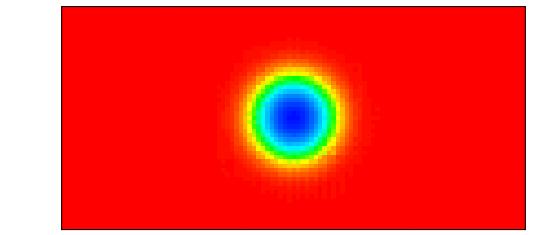

a) QUAD mesh with correction

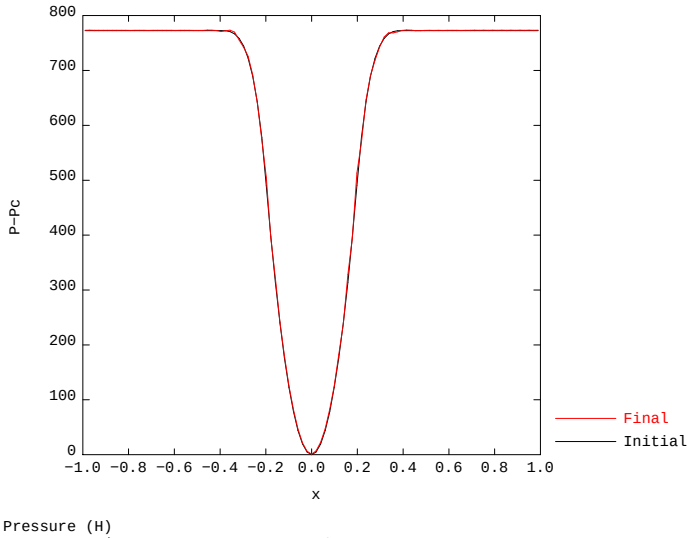

b) Horizontal line: QUAD mesh with correction

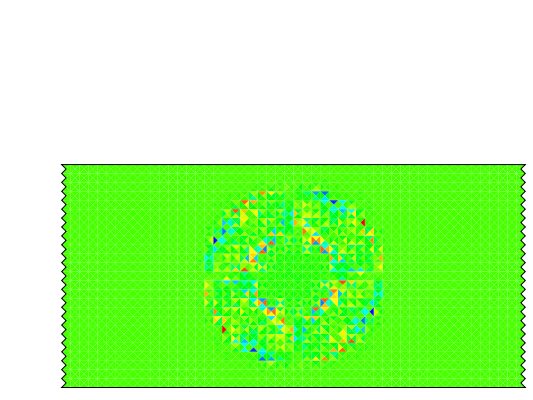

c) TRI-CEN-FAC mesh without correction

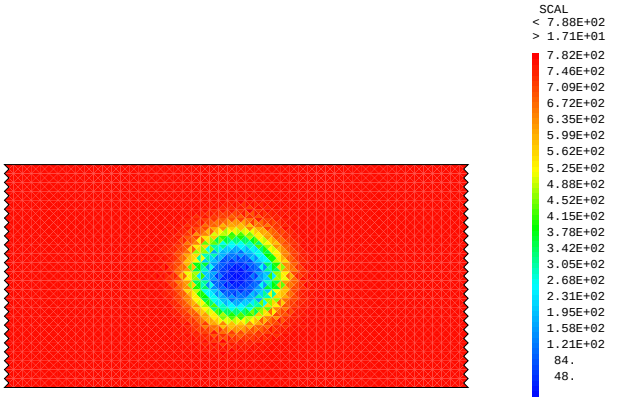

d) TRI-CEN-FAC mesh with correction

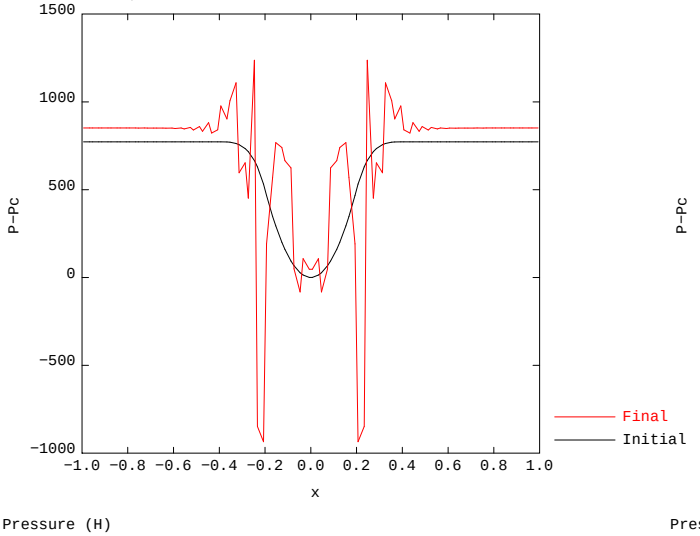

e) Horizontal line: TRI-CEN-FAC mesh without correction

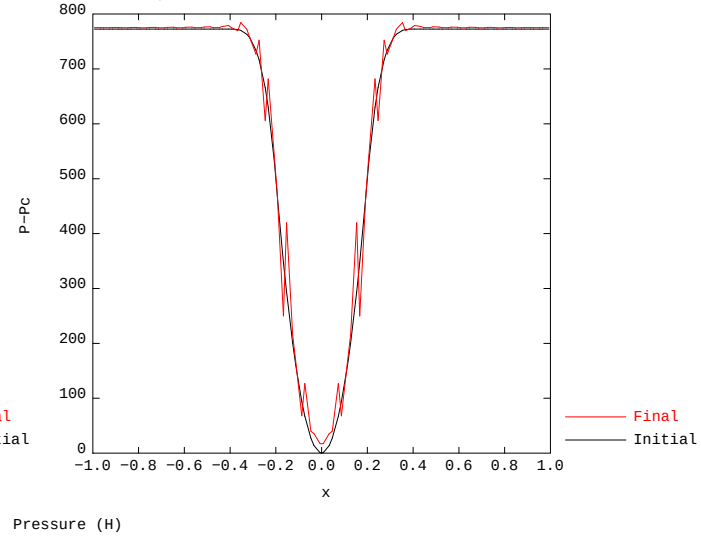

f) Horizontal line: TRI-CEN-FAC mesh with correction

Figure 2.21: Gresho vortex problem (water, test cases $2, 3, 4$): Pressure $p - p_c$ comparison on QUAD and TRI-CEN-FAC meshes, $M_{max} = 5.0 \times 10^{-4}$, $t_f = 0.125$ s (10% of a complete revolution). Second order in space HLLC and HLLCDL schemes (with limiter) and second order in time with 2-stage RK method, $CFL = 0.45$

The results for the test cases 5) 6) are summarized in Table 2.2 and the pressure solution for test case 6) on TRI-CEN-VER mesh with low-Mach correction is shown in Figure 2.2.

Scheme	Water Gresho vortex test case		
	TRI-CEN-VER		
	Density	Velocity	Pressure
HLLC	✓	✓	×
HLLCDL	✓	✓	×

Table 2.2: Gresho vortex problem (water): results for the test cases 5) 6)

×: oscillation, ✓: satisfactory solution with the numerical scheme in consideration.

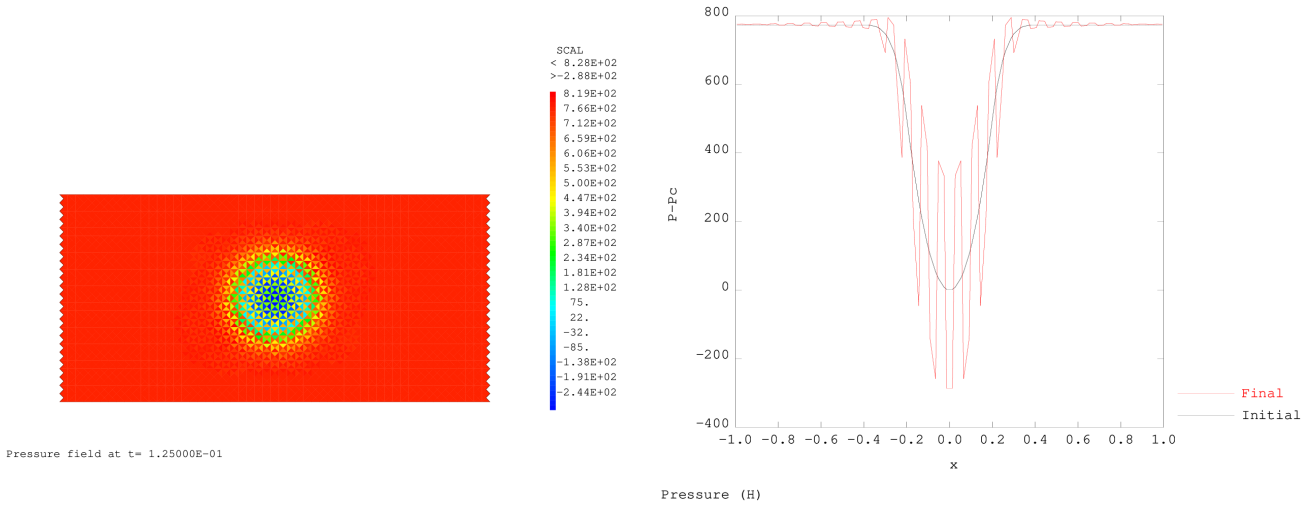

Figure 2.22: Gresho vortex problem (water, test case 6): Pressure $p - p_c$ comparison on TRI-CEN-VER mesh, $M_{max} = 5.0 \times 10^{-4}$, $t_f = 0.125$ s (10% of a complete revolution). Second order in space HLLCDL scheme (with limiter) and second order in time with 2-stage RK method, $CFL = 0.45$

In Figures 2.20, 2.21 we can observe that:

- On QUAD meshes: the velocity field is not correctly computed by the standard HLLC scheme (Figure 2.20a,e). The problem is fixed by using the HLLCDL scheme (Figure 2.20b,f). The pressure solution oscillates strongly when computed with the HLLC scheme; this behavior is significantly improved (though not entirely fixed) thanks to the low-Mach correction HLLCDL scheme (Figures 2.21a,b). The density field presents negligible oscillations in all cases.

- On TRI-CEN-FAC mesh: the velocity field obtained with the HLLC scheme does not present excessive dissipation (Figure 2.20c) as expected from Rieper *et al.* theoretical analysis. However, the pressure field computed by the HLLC scheme presents oscillations (Figures 2.21c,e). The combination between the TRI-CEN-FAC mesh with the HLLCDL scheme gives non-oscillating pressure solution. The density field presents negligible oscillations in all cases.

The oscillating behaviour of the pressure is, to our knowledge, not reported for this test case in the literature: it is systematically through the visualization of the velocity or the Mach number field that the low-Mach accuracy problem is highlighted. Furthermore, the oscillatng behaviour of the pressure field is also sensitive to the detail of the initial solution projection onto a triangular grid. Though the TRI-CEN-FAC mesh when combined with the HLLCDL scheme gives satisfactory solutions, it is not the case for

the TRI-CEN-VER mesh. The observations on the TRI-CEN-VER mesh have been reported in Table 2.2 and can be summarized as follows:

- For the density field: it presents negligible oscillations.
- For the velocity field: the HLLC and HLLCDL schemes on TRI-CEN-VER mesh do not yield excessive numerical diffusion, similarly to the TRI-CEN-FAC case.
- For the pressure field: the HLLC scheme produces oscillating pressure on the TRI-CEN-VER mesh, similarly to the case of TRI-CEN-FAC mesh. However, and this was an unexpected observation, the problem is not fixed when this mesh is combined with the HLLCDL scheme (Figure 2.22).

The oscillating behaviour of the pressure when computing on the TRI-CEN-VER as well as the TRI-CEN-FAC mesh is not yet well-understood. However, tit should also be underlined that he pressure field presented in Figures 2.22, 2.21c,e corresponds to the pressure difference $p - p_c$ (of order 1.0×10^3), which remains negligible when compared to the pressure $p_c = 3.0 \times 10^8$ (the the dominant contribution to the total pressure p). It is concluded that the total pressure p is actually not much affected by these oscillations.
When further analyzing the pressure oscillations on TRI meshes, we also considered first order schemes. The results obtained for these test cases 7) 8) 9) 10) indicate that the first order (both standard and low-Mach correction) schemes give satisfactory results for all fields including the pressure (Figure 2.23). However, such first order schemes display a significant level of numerical diffusion and are therefore not really appropriate from an accuracy viewpoint for the targeted industrial applications.

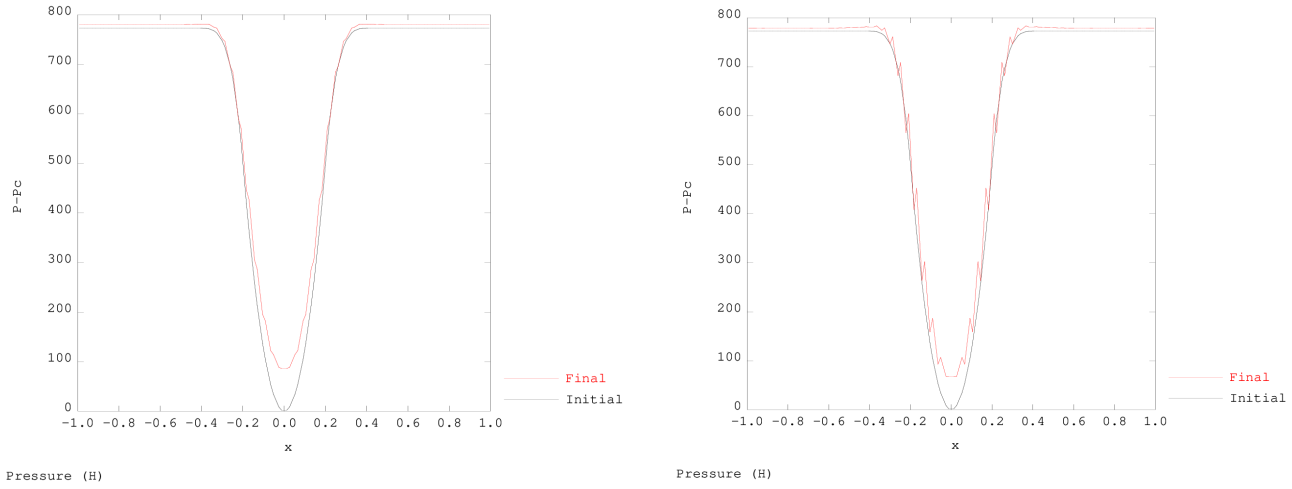

a) TRI-CEN-VER without correction

b) TRI-CEN-VER with correction

Figure 2.23: Gresho vortex problem (water, test cases 9, 10): Pressure $p - p_c$ comparison on TRI-CEN-VER mesh, $M_{max} = 5.0 \times 10^{-4}$, $t_f = 0.125$ s (10% of a complete revolution). First order method for all variables, HLLC scheme (left), HLLCDL scheme (right), $CFL = 0.45$

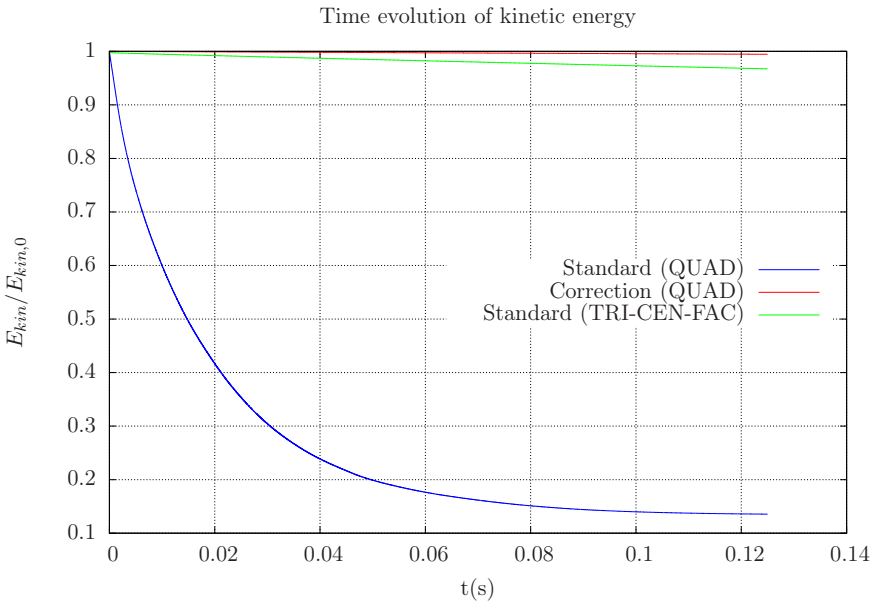

Figure 2.24: Gresho vortex problem (water): Evolution of kinetic energy

As another illustration of the low-Mach accuracy issue,we present in Figure 2.24 the ratio of the computed kinetic energy to the initial kinetic energy in function of time. As we can see, the standard scheme on QUAD mesh cannot preserve the kinetic energy in time while good results are observed using low-Mach correction scheme on QUAD mesh or the standard scheme on TRI-CEN-FAC mesh (or TRI meshes). The preservation of this quantity is particularly important when computing the low-Mach flow in a containment since it represents the loads of the (slow) fluid scale applied on a structure. It is clear that the deformation of a structure could be dramatically underestimated using QUAD meshes without low-Mach corrections (Figure 2.24, blue curve).

2.2.2.1 Computations at $M_{max} = 0.1$

The low-Mach accuracy problem has been mostly reported as an issue of excessive diffusion but the pressure oscillations observed in the previous section have not been connected in the literature with a specific low-Mach issue. With the purpose of assessing whether such oscillating pressure behaviour is related or not to a low-Mach accuracy problem, we perform a numerical experiment for the Gresho vortex problem at a larger reference Mach number, $M_{max} = 0.1$. Since we are no longer in the low-Mach number limit, the numerical error if it exists should not be as significant as in the low-Mach case previously presented. The meshes used for simulation are the same as in the previous section. The initial conditions in this test case are modified but always satisfy the relation (2.6). The magnitude of the initial fields are specified in Table 2.3.

	Water
ρ (kg/m^3)	1000
$\mathbf{u}_{\theta,0,max}(r)$ (m/s)	200
p_c (Pa)	3.0×10^8
M_{max}	0.1

Table 2.3: Gresho vortex problem. Magnitude of the initial fields for computations with $M_{max} = 0.1$

The final time of simulation is $t_f = 6.0 \times 10^{-4}$ s corresponding again to 10% of a complete revolution of the vortex. The numerical results are presented in Figures 2.25, 2.26 and can be summarized as follows:

- For the density field: negligible oscillations are observed.
- For the velocity field: the standard HLLC scheme yields a satisfactory solution for both the QUAD and TRI-CEN-FAC meshes. However, the velocity on a QUAD mesh (Figure 2.25a,c) seems to be a little more diffused than on TRI mesh (Figure 2.25b,d). It means that the QUAD mesh suffers from the accuracy problem but not as severe as in the low-Mach limit case with $M_{max} = 5.0 \times 10^{-4}$.
- For the pressure field: the QUAD and TRI-CEN-FAC meshes give a satisfactory result (Figure 2.26). This means that the wrong pressure field computed at $M_{max} = 5 \times 10^{-4}$ with standard HLLC scheme (c.f. Figures 2.21c,e) is related to the low-Mach accuracy issue.

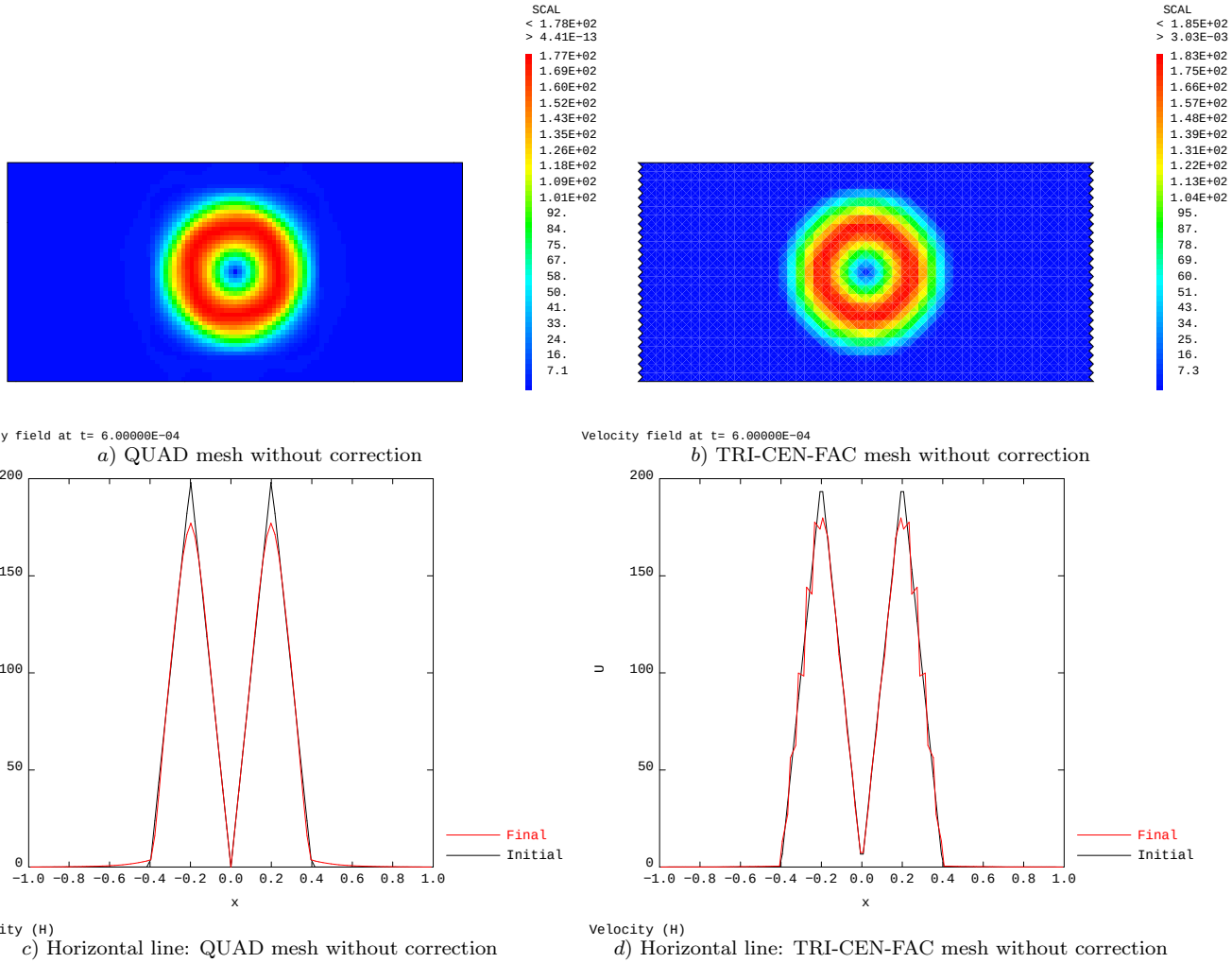

a) QUAD mesh without correction

b) TRI-CEN-FAC mesh without correction

c) Horizontal line: QUAD mesh without correction

d) Horizontal line: TRI-CEN-FAC mesh without correction

Figure 2.25: Gresho vortex problem (water): Velocity comparison on QUAD (a,c) and TRI-CEN-FAC (b,d) meshes, $M_{max} = 0.1$, $t_f = 6.0 \times 10^{-4}$ s (10% of a complete revolution). Second order in space HLLC scheme (with limiter) and second order in time with 2-stage RK method, $CFL = 0.45$

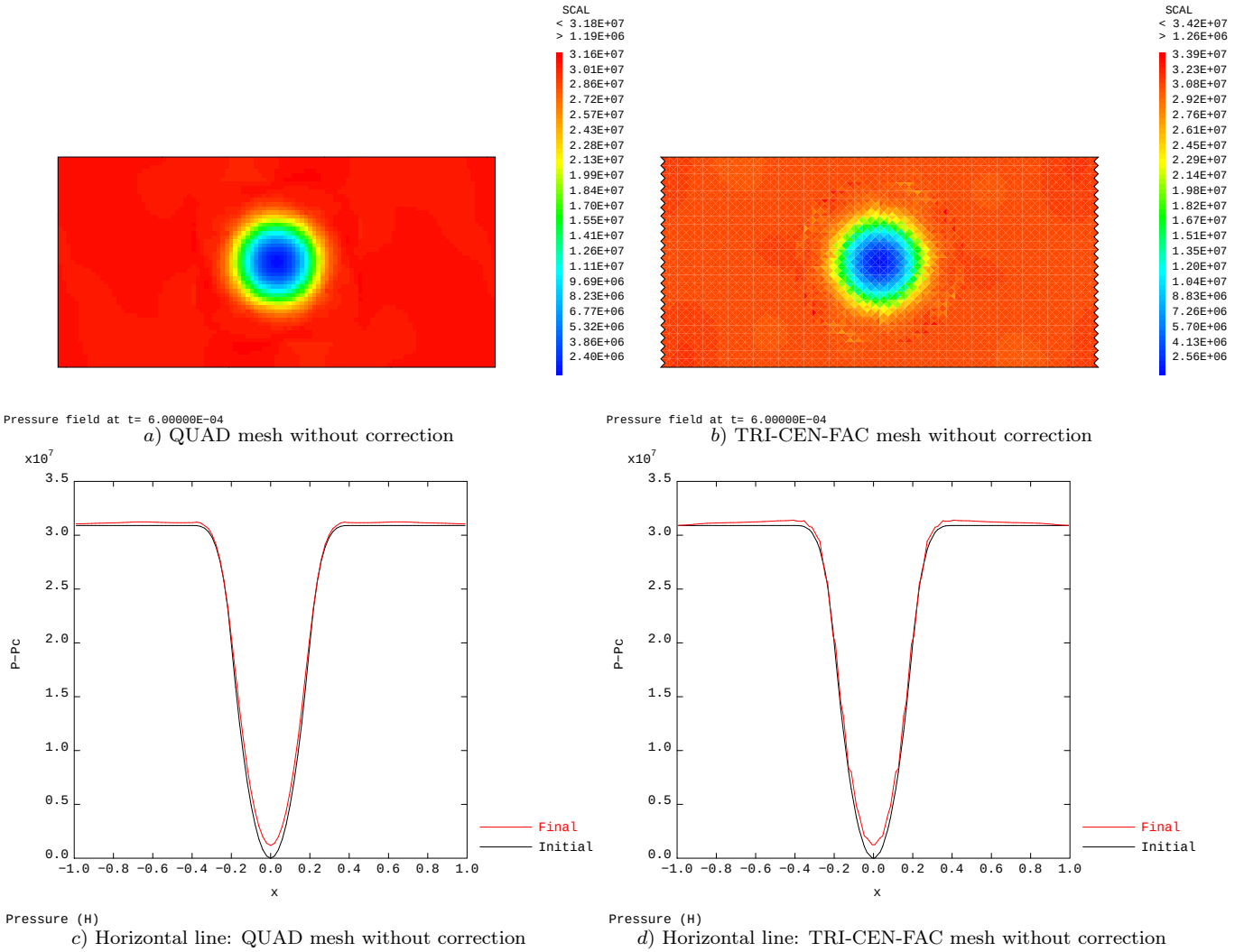

a) QUAD mesh without correction

b) TRI-CEN-FAC mesh without correction

c) Horizontal line: QUAD mesh without correction

d) Horizontal line: TRI-CEN-FAC mesh without correction

Figure 2.26: Gresho vortex problem (water): Pressure $p - p_c$ comparison on QUAD(a,c) and TRI-CEN-FAC(b,d) meshes, $M_{max} = 0.1$, $t_f = 6.0 \times 10^{-4}$ s (10% of a complete revolution). Second order in space HLLC scheme (with limiter) and second order in time with 2-stage RK method, $CFL = 0.45$

Conclusion for the Gresho vortex problem:

The computations of the Gresho vortex problem for water described using SG-EOS and using the second order accurate HLLC approximate Riemann solver show that:

- The low-Mach correction using TRI meshes allows to fix the velocity solution but not the pressure one (cf. Table 2.1).
- The TRI meshes when combined with the low-Mach correction scheme also give a satisfactory solution for the velocity but the pressure solution is very sensitive to the initial location of the vortex center within the meshes (cf. Tables 2.1, 2.2).
- The optimal results are obtained by using the QUAD and TRI-CEN-FAC meshes with HLLCDL scheme (cf. Table 2.1). Note that employing the QUAD mesh with low-Mach correction scheme is however recommended since the solution remains independent of the initial location of the vortex center in the grid.

Table 2.4 summarizes the pressure solution $p - p_c$. We emphasize that though presenting oscillating behavior, the contribution to the total pressure is negligible.

Scheme	Stiffened gas Gresho vortex test case		
	QUAD	TRI-CEN-FAC	TRI-CEN-VER
2^{nd} HLLC	×	×	×
2^{nd} HLLCDL	✓	✓	×
1^{st} HLLC	×	✓	✓
1^{st} HLLCDL	✓	✓	✓

Table 2.4: Gresho vortex problem (water): summary of the pressure solution.

×: oscillation, ✓: satisfactory solution with the numerical scheme in consideration.
We also simulate this problem using a perfect gas and the same numerical schemes with and without low-Mach correction (e.g HLLC, HLLCDL): the solutions are qualitatively similar to what has been observed for the water case with SG-EOS.

2.3 Gresho vortex acoustic problem

In this section, we combine the Gresho vortex defined in section 2.2.1 with an acoustic wave to form a two-scale problem. The accurate capture of both scales and their interaction in the low-Mach regime is subjected to a careful analysis.

2.3.1 Preliminaries

Dimension and mesh

The dimension of the computational domain is increased with respect to the one in the Gresho vortex problem: $[x_1; x_2] \times [y_1; y_2] = [-2\text{m}; 1\text{m}] \times [0\text{m}; 1\text{m}]$. The initial distance between the acoustic wave and the vortex is about 1 m so as to avoid the possible effect of the numerical diffusion of the acoustic wave on the vortex at the beginning of the calculation. As before, we use both QUAD and TRI meshes for our computations.

Initial and boundary conditions

The initial conditions are decomposed into two parts: one part for the vortex and the other for the acoustic wave.

$$\begin{cases} \rho_0(\mathbf{x}) = \rho_0^{GR} + \rho_0^{AC}(\mathbf{x}) \\ \mathbf{v}_0(\mathbf{x}) = \mathbf{v}_0^{GR}(\mathbf{x}) + \mathbf{v}_0^{AC}(\mathbf{x}) \\ p_0(\mathbf{x}) = p_0^{GR}(\mathbf{x}) + p_0^{AC}(\mathbf{x}) \end{cases}$$

The initial conditions for the Gresho vortex (GR) part are the same as in section 2.2. The initial density for the acoustic wave (AC) is specified in (2.8) and is of order of the Mach number.

$$\rho_0^{AC} = \begin{cases} \rho_0^{GR} Mcos[5\pi(x + 0.3)], \quad -1.8 < x < -1.6 \\ 0, \text{ elsewhere} \end{cases} \tag{2.8}$$

The velocity of the acoustic wave specified in (2.9) is derived from the Riemann invariants relation since the physical phenomena can be regarded as isentropic in the low-Mach number regime:

$$\mathbf{v}_0^{AC}(x, y) = \begin{cases} u_0^{AC}(x, y) = \dfrac{2}{\gamma - 1}(c_0(\rho_0^{GR} + \rho_0^{AC}) - c_0(\rho_0^{GR})) \\ v_0^{AC}(x, y) = 0 \end{cases} \tag{2.9}$$

where $c_0(\rho_0^{GR})$ and $c_0(\rho_0^{GR} + \rho_0^{AC})$ are the sound speeds outside and inside the acoustic region respectively. The acoustic wave can also be considered as a small perturbation. The total pressure inside the acoustic

region can be developed as follows:

$$\begin{aligned} p &= p(\rho_0^{GR} + \rho_0^{AC}) \approx p(\rho_0^{GR}) + \left(\frac{\partial p}{\partial \rho}\right)_{\rho_0^{GR}} \rho_0^{AC} \\ &= p_0^{GR} + p_0^{AC} \end{aligned} \tag{2.10}$$

Therefore the acoustic pressure takes the form (2.11):

$$p_0^{AC} = \left(\frac{\partial p}{\partial \rho}\right)_{\rho_0^{GR}} \rho_0^{AC} = c_0^2 \rho_0^{AC} \tag{2.11}$$

where c_0 is the sound speed outside the acoustic region and in case of water it takes the value:

$$c_0 \approx \sqrt{\frac{\gamma_{SG}(p_c + p_\infty)}{\rho_0^{GR}}} \approx 1990 \text{ m/s}$$

Table 2.5 summarizes the magnitude of initial fields. The boundary conditions are periodic for the left and right sides and are fixed walls for the upper and lower sides.

	Stiffened gas
ρ_0^{GR} (kg/m^3)	1000
ρ_{max}^{AC} (kg/m^3)	0.5
$u_{0,max}^{\theta}(r)$ (m/s)	1
$u_{max}^{AC}(x)$ (m/s)	1
p_c (Pa)	3.0×10^8
p_{max}^{AC} (Pa)	1.98×10^6
M_{max}	5.0×10^{-4}

Table 2.5: Magnitude of the IC for Gresho vortex acoustic test case

Expected solution

In the low-Mach number limit, the compressible and the incompressible solutions are decoupled [Miczek et al., 2015], [Dellacherie, 2010]. As a result, we expect the right-propagating acoustic wave to pass through the vortex without having any interaction with it, to leave the domain on the right and reenter on the left through the periodic boundary condition. When the acoustic wave returns to its initial position, the full initial condition is recovered.

2.3.2 Numerical results

We employ both the standard and low-Mach correction schemes. The final time of the simulation is $t_f = 1.5 \times 10^{-3}$ s, corresponding to 0.12% of a complete revolution of the vortex. At this instant, the acoustic wave has passed through the vortex and returned to its initial position.
The computations are performed on:

- QUAD (150x50) mesh with 150 and 50 quadrangular cells in the horizontal and vertical directions respectively.
- TRI(75x25x4) mesh with 75 and 25 quadrangular cells in the horizontal and vertical directions respectively. Each quadrangle is then divided into 4 triangles.

In Figure 2.27*a*, we observe that the magnitude of the acoustic velocity is half of its initial value and the vortex velocity is preserved by about 85.6% of the theoretical value. The acoustic wave is much more

diffused than the vortex as having a much smaller characteristic time. The observed numerical diffusion is not related to the low-Mach problem since the piston problem states that the standard compressible solvers are able to correctly capture acoustic waves.
In Figure 2.27*c*, it is observed that the vortex velocity is preserved by about 98.5% of its initial value thanks to the use of the TRI mesh. The solution for the acoustic wave however remains (almost) unchanged since as stated the numerical error is not related to the low-Mach problem and therefore the TRI mesh has no effect.
In Figures 2.27*b, d*, we present the velocity field on QUAD and TRI meshes using both the standard and low-Mach correction schemes. We observe an oscillating vortex solution on the QUAD mesh while the solution on TRI mesh is however satisfactory.

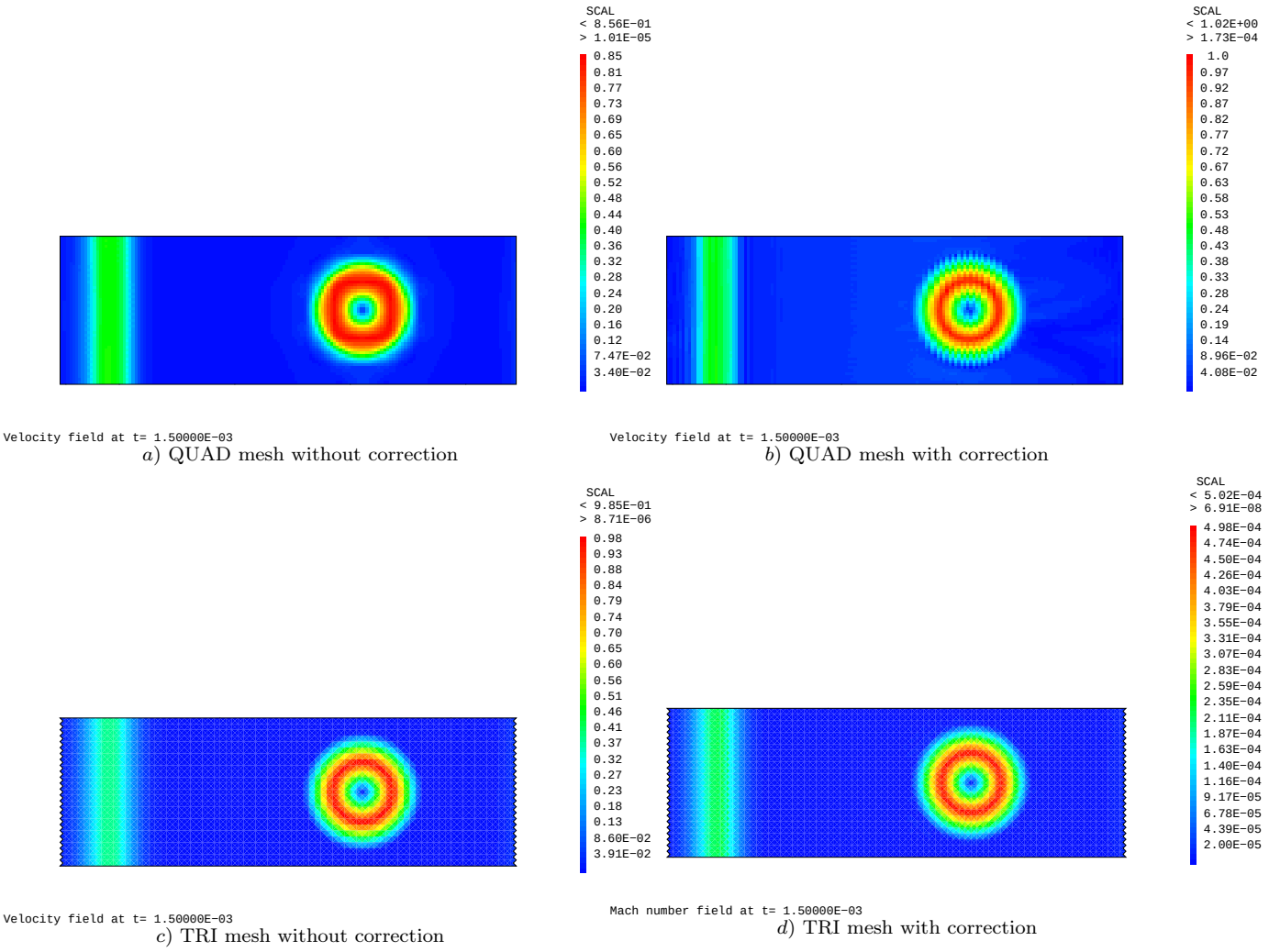

a) QUAD mesh without correction

b) QUAD mesh with correction

c) TRI mesh without correction

d) TRI mesh with correction

Figure 2.27: Gresho vortex acoustic problem (water): Velocity field comparison on QUAD and TRI meshes, $M_{max} = 5.0 \times 10^{-4}$, $t_f = 1.5 \times 10^{-3}$ s (0.12% of a complete revolution). Second order in space HLLC and HLLCDL schemes (with limiter) and second order in time with 2-stage RK method, $CFL = 0.45$

So as to investigate the oscillating behavior of the vortex on the QUAD mesh with low-Mach correction scheme, we stop the computation at $t_f \approx 5.0 \times 10^{-4}$ s. In this way, the acoustic wave propagates and stops in front of the vortex and no interaction between them occurs. It is shown in Figure 2.29 that:

- On QUAD mesh: the HLLCDL gives a non-physical solution behind the acoustic wave (c.f. Figure 2.29 (left)) resulting in interactions between the acoustic wave and the vortex.

- On TRI mesh: the non-physical region (almost) vanishes (cf. Figure 2.29 (right)). Consequently, there is no interaction between the two scales when the acoustic wave crosses the vortex. However, we still recognize small perturbations at the initial position of the acoustic wave.

The observed oscillations can be explained. As noticed in section 1.5.1 the low-Mach correction schemes when rescaling the pressure fluctuation of order $\rho c \Delta u$ tend also to reduce the numerical viscosity of the scheme. The low-Mach correction schemes are therefore less stable in capturing acoustic waves.

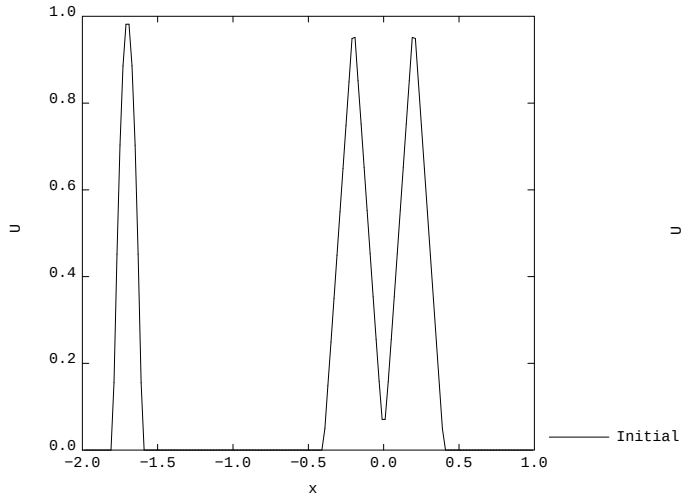

Initial velocity

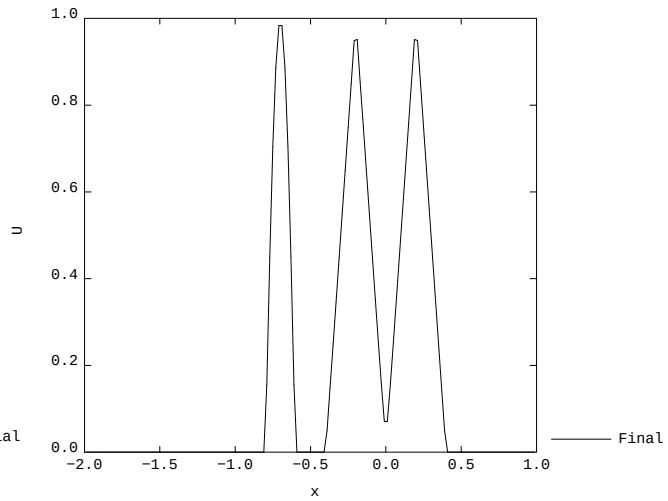

Theoretical solution

Figure 2.28: Gresho vortex acoustic problem (water): Initial (left) and theoretical (right) velocity solutions projected on a horizontal projection line

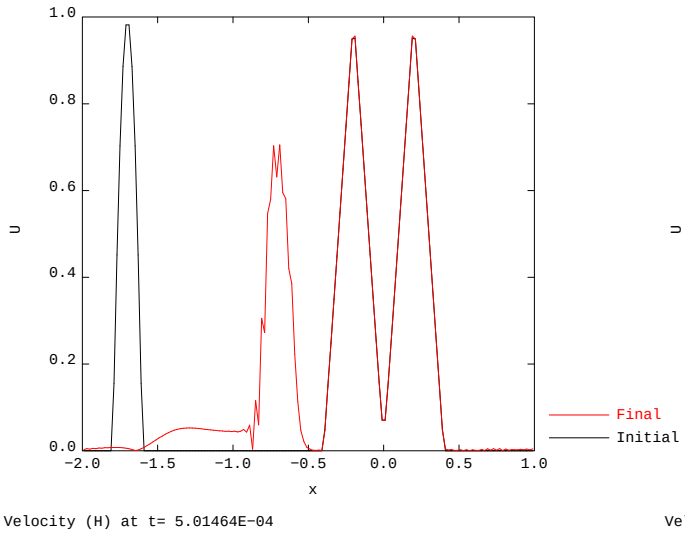

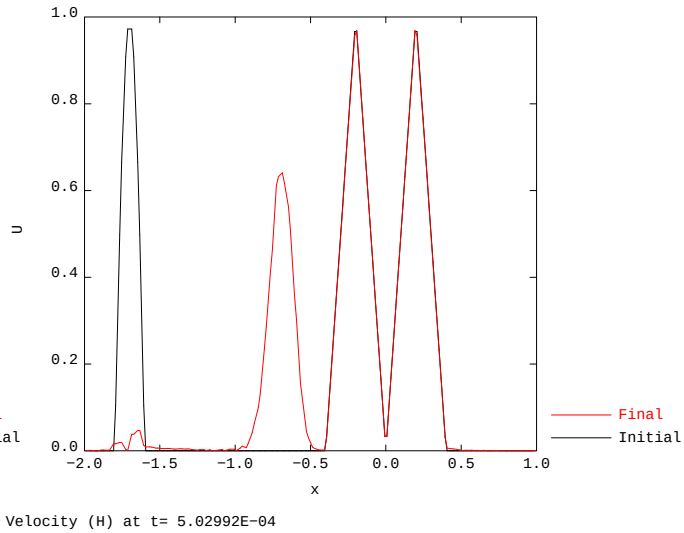

Figure 2.29: Gresho vortex acoustic problem (water): Velocity field comparison on horizontal projection line, on QUAD (left) and TRI (right) meshes, $M_{max} = 5.0 \times 10^{-4}$, $t_f = 1.5 \times 10^{-3}$ s (0.12% of a complete revolution). Second order in space HLLCDL (with limiter) and second order in time with 2-stage RK method, $CFL = 0.45$

Conclusion for the Gresho vortex acoustic problem:

The numerical experiments in this section show that:

- The standard compressible schemes have no problem in capturing the (fast) acoustic wave but, as already mentioned, display difficulties in computing (slow) fluid scale.
- The low-Mach correction schemes yield inaccurate solutions for the acoustic wave on QUAD meshes while the use of TRI meshes allows to obtain satisfactory results.

2.4 1D low-Mach shock tube problem

Observing that the low-mach correction method introduces problems with wave propagation, we decide to return to the elementary shock tube test for stiffened gas. This test case involves a left rarefaction wave and a right shock wave, the strengths of which are functions of a reference Mach number. Denoting (from left to right) the states on each side of the left-running and right-running waves as:

$$\mathbf{U_L}, \mathbf{U_L^*}, \mathbf{U_R^*}, \mathbf{U_R},$$

we impose that $\mathbf{U_L^*} = \mathbf{U_R^*}$. Moreover, we use the acoustic formula to determine the left state as function of the right state and the reference Mach number M_{ref}. We choose p_R^* and ρ_R^* such that:

$$p_L^* = p_R^* \approx p_R + \rho_R M_{\text{ref}} c_R^2$$

$$\rho_L^* = \rho_R^* \approx \rho_R + \frac{p_R^* - p_R}{c_R^2} = \rho_R(1 + M_{\text{ref}})$$

$$c_R^* = c_L^* \approx \sqrt{\frac{p_R^* - p_R}{\rho_R^* - \rho_R}} = \sqrt{\frac{\rho_R M_{\text{ref}} c_R^2}{\rho_R M_{\text{ref}}}} \approx c_R$$

$$p_L \approx p_L^* + \rho_L^* M_{\text{ref}} c_L^{*2} \approx p_R + 2\rho_R M_{\text{ref}} c_R^2$$

$$\rho_L \approx \rho_L^*(1 + M_{\text{ref}}) = \rho_R(1 + 2M_{\text{ref}} + M_{\text{ref}}^2) \approx \rho_R(1 + 2M_{\text{ref}})$$

We consider water described using the SG-EOS with material properties taken from [Ivings et al., 1998].

Material properties		
	Left	Right
γ	7.15	7.15
p_∞ (Pa)	3.0×10^8	3.0×10^8

The computations are realized for $M_{\text{ref}} = 10^{-1}$, $M_{\text{ref}} = 10^{-2}$ and $M_{\text{ref}} = 10^{-3}$. For instance, for $M_{\text{ref}} = 10^{-1}$ we obtain the following values.

Initial conditions		
	Left	Right
ρ (kg/m^3)	1200.0	1000.
p (Pa)	$14.292\,43 \times 10^8$	1×10^5
u (m/s)	0.0	0.0

We insert the left state in the High Pressure region and the right state in Low Pressure region:

HP	LP

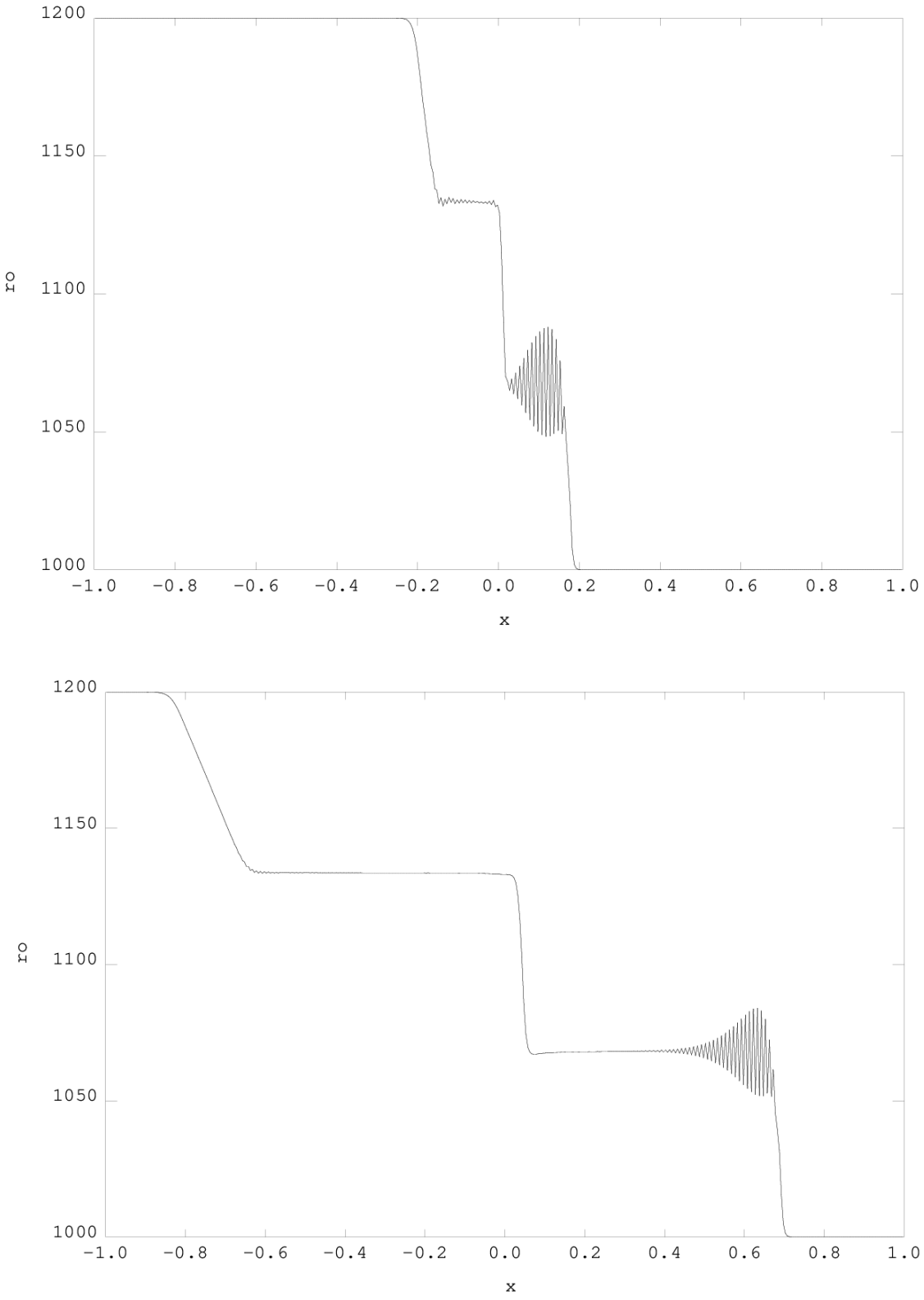

Figure 2.30: Computed density distribution for the 1D low-Mach shock tube problem. $M_{\text{ref}} = 1 \times 10^{-1}$. 400x1 elements. Quadrangular mesh. HLLCDL. Limited second order reconstruction in space, second order in time. Top $t = 1 \times 10^{-4}$. Bottom $t = 4 \times 10^{-4}$.

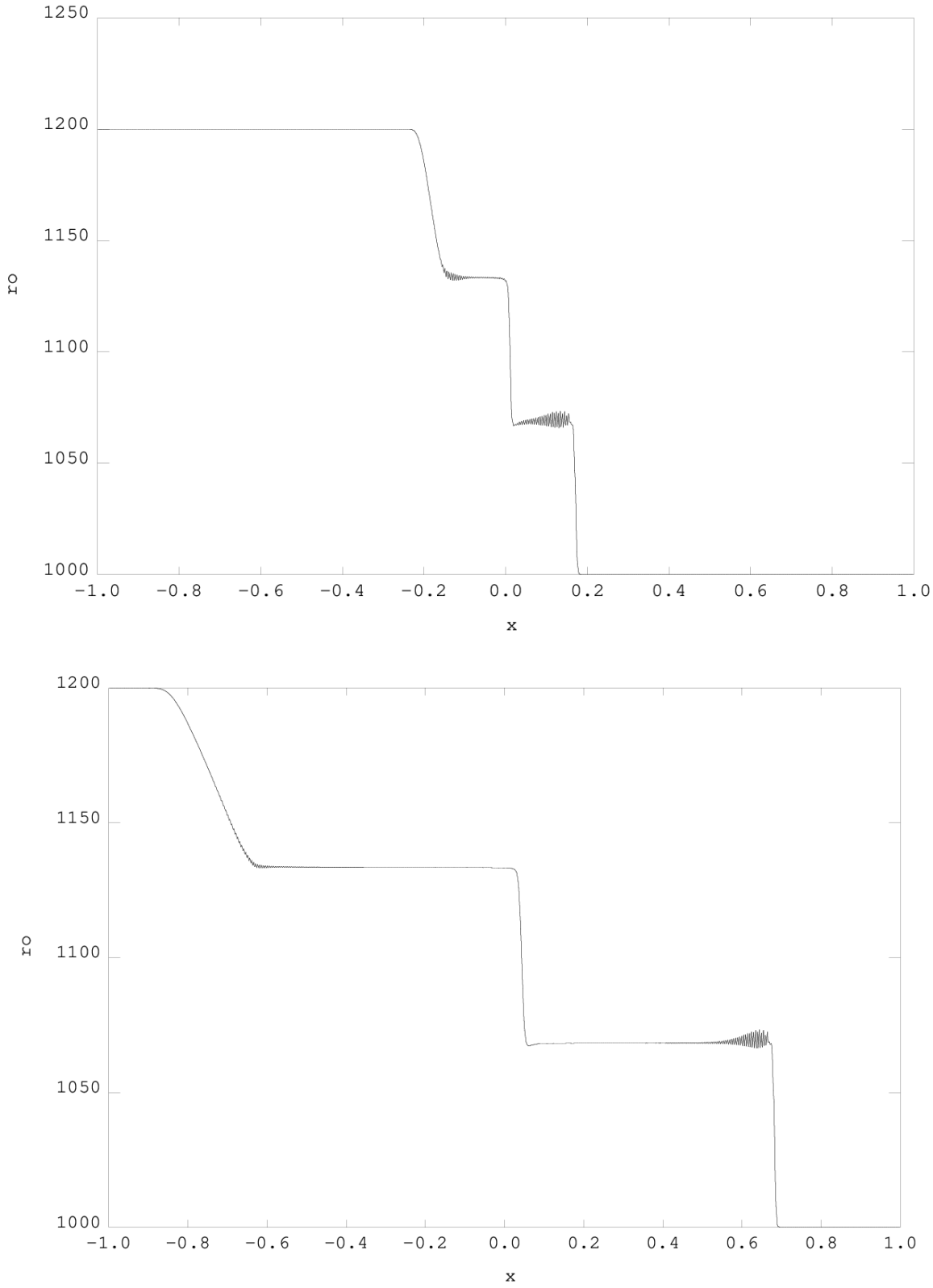

Figure 2.31: Computed density distribution for the 1D low-Mach shock tube problem. $M_{\text{ref}} = 1 \times 10^{-1}$. 4x(400x1) elements. Triangular mesh. HLLCDL. Limited second order reconstruction in space, second order in time. Top $t = 1 \times 10^{-4}$. Bottom $t = 4 \times 10^{-4}$.

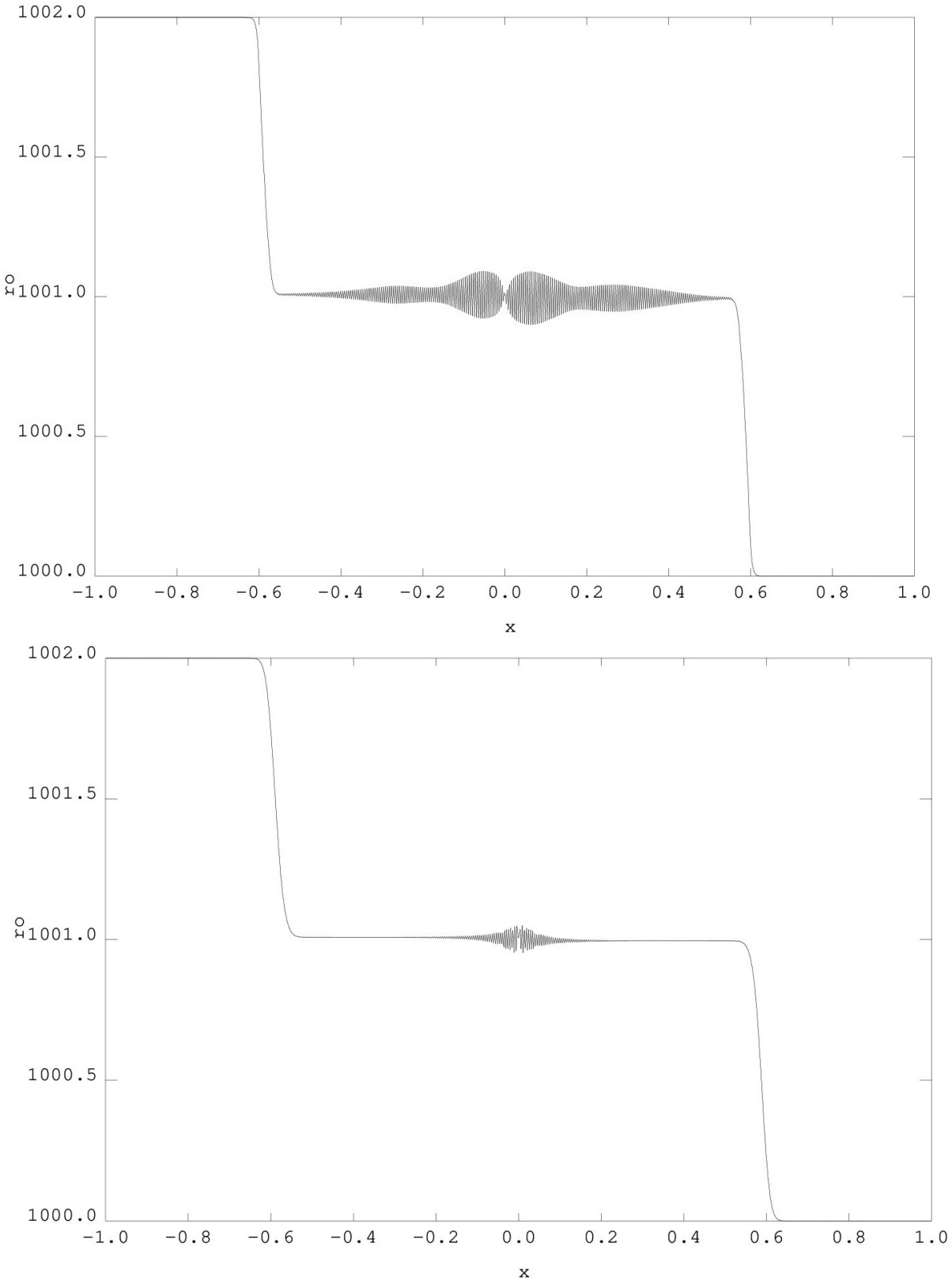

Figure 2.32: Computed density distribution for the 1D low-Mach shock tube problem. $M_{\text{ref}} = 1 \times 10^{-3}$. 4x(400x1) elements. Quadrangular mesh (top). Triangular mesh (bottom). HLLCDL. Limited second order reconstruction in space, second order in time. $t = 4 \times 10^{-4}$.

On a quadrangular mesh with low-Mach correction, oscillations appear near the shock and (less significantly) in the rarefaction region (on the density and the speed only, the pressure is not affected). Their maximum amplitude does not decrease when reducing the mesh size or the CFL (or when increasing the final time). The case with $M_{\text{ref}} = 10^{-1}$ is represented in Figure 2.30 for HLLCDL on the same mesh.
In Figure 2.32 is the solution for the case with $M_{\text{ref}} = 10^{-3}$. We observe that oscillations on the rarefaction and on the shock waves tends to be equal to each other in that case. This is expected since rarefaction and shock waves become both acoustic waves in the low-Mach limit.
In Figure 2.31 we compute the same problem using the triangular mesh. Each quadrangle has been split into four triangles. As one can see, oscillation amplitudes are much less important than in quadrangular case. It seems that transverse numerical diffusion (due to the "triangular split") contributes to damp the numerical oscillations appearing on acoustic waves.

Remarks:

- One can observe that in Figures 2.30 and 2.31 $\rho_L^* \neq \rho_R^*$. We point out that their difference decreases as M_{ref} does and becomes almost invisible for the value 1×10^{-3}. This is due to the use of acoustic formula to compute the shock and the rarefaction (formula that tends to be correct for very low Mach numbers).

- In several articles devoted to low-Mach number computations, see for instance [Dellacherie et al., 2016] or [Li and Gu, 2013], the Sod shock tube is considered and computed using the low-Mach correction schemes. Only very little oscillations are visible in that case when using a compressible scheme with low-Mach correction. This shows the interest of the present shock tube problem which allows to better discriminate the numerical behavior in the low-Mach number regime.

Conclusion for the 1D low-Mach shock tube problem:

The results for this test case show that the low-Mach correction schemes on QUAD cannot give correct solutions for wave-propagating problems. However, the use of TRI mesh helps to fix the issue.

Conclusion

A range of test problems has been numerically investigated in this chapter using standard approximate Riemann solvers and corrected versions of these schemes for the low-Mach region. The observed results can be summarized as follows:

- The piston test problem in section 2.1 show that the acoustic scale c is well-computed by the standard schemes.

- The Gresho vortex problem in section 2.2 shows that the optimal solution for computing (slow) fluid scale can be obtained with the low-Mach correction schemes on TRI meshes.

- The Gresho vortex acoustic test in section 2.3 shows that the low-Mach correction schemes on QUAD mesh are unable to give correct solutions for the acoustic scale and the use of TRI mesh can give a better solution.

- The 1D low-Mach shock tube test confirms the wrong solutions for the wave propagation problems using low-Mach correction schemes on QUAD mesh and the use of TRI mesh is useful in obtaining a good solution.

These various observations made on low-Mach single-phase (liquid) flows lead us to conclude that *the optimal accuracy for capturing both fast and slow scales is obtained by using the low-Mach correction schemes on TRI meshes*. This is however far from being a satisfactory conclusion from a practical viewpoint for at

least two reasons. Firstly, even though inviscid flow calculations could be performed using systematically 2D triangular grids or 3D tetrahedral grids, it is not desirable to depend so strongly on mesh topology. It is clearly preferable to be able to also make use of quadrangular or hexahedral cells. Secondly, and this is probably the strongest argument, we have been exclusively focused up to now on the low-Mach accuracy issue and have disregarded the efficiency issue raised by low-Mach calculations and also described in the previous chapter. While the low-Mach correction methods considered in this part may fix the low-Mach accuracy problem, their lack of efficiency remains an issue and motivates the quest for an efficient way to compute low-Mach flows (while keeping the flow accuracy). When devising such a novel method, we set a constraint which is to be able to apply or adapt the existing numerical solvers in Europlexus to the numerical treatment associated with a novel numerical strategy for low-Mach two-phase flows. This leads us to develop a novel artificial compressibility method which is the main topic of the second part of this thesis.

Part II

Development of a novel artificial compressibility method for low-Mach two-phase flows

3

Artificial compressibility (AC) method: application to the 1D single-phase piston problem

Contents

Introduction

The single-phase test problems solved in chapter 2 show that the efficiency problem in the low-Mach number regime remains when using an exact or approximate Riemann solver including a low-Mach correction to fix the accuracy issue. As a result, the purpose of this chapter is to look for a method allowing to accelerate low-Mach computations without degrading the accuracy of solutions for single-phase flow problems, in a first stage.

In this chapter, we pay attention in particular to the strategy of combining the artificial compressibility (AC) method with the asymptotic system (cf. section 1.2). The AC method is the guideline for the efficiency enhancement since it is suited for the EUROPLEXUS environment which is an explicit code for hyperbolic systems. A quick review of some classical AC-type approaches for single-phase flow is presented

in section 3.1. A classical AC-asymptotic strategy is then evaluated through a simple 1D closed piston problem in section 3.2 so as to demonstrate the advantages and drawbacks of such an approach. The drawbacks are fixed by a new method proposed in sections 3.3, 3.4. Some verification tests for the new method are performed in sections 3.5 through the piston problems.

3.1 Some classical AC-type models for single-phase flow problems

The original AC method of [Chorin, 1967] was developed to find a stationary solution for the incompressible Navier-Stokes equations in an **open domain**. The divergence free constraint is modified by adding an artificial term (which becomes zero in the stationary state) and the whole new system becomes hyperbolic if the physical viscosity is neglected. This method is also called the single time-stepping approach.
From an incompressible viewpoint, one can state that the incompressible system is extended to a weakly compressible regime and the new system contains an artificial acoustic wave with negligible amplitude propagating with its own acoustic speed:

$$\begin{aligned} \frac{1}{c_{AC}^2}\frac{\partial p'}{\partial t} &+ \nabla\cdot\mathbf{v} &&= 0 \\ \frac{\partial \mathbf{v}}{\partial t} &+ \mathbf{v}\cdot\nabla\mathbf{v} &&= -\frac{1}{\rho}\nabla p' + \nu\Delta\mathbf{v} \end{aligned} \tag{3.1}$$

where the constants ρ, ν are respectively the density and the kinematic viscosity of the flow. The system (3.1) can also be compared with the equations of motion of a compressible fluid in a small physical Mach number. One can state that the (fast) physical acoustic wave is replaced by the (slow and negligible amplitude) artificial acoustic wave. When computing a flow governed by the above system using an explicit solver, the stability time step is greatly enhanced as:

$$\Delta t_{AC} = \frac{CFL\cdot\Delta x}{c_{AC}} >> \frac{CFL\cdot\Delta x}{c} = \Delta t \tag{3.2}$$

Many developments for the original AC approach have been observed. For example, a dual time-stepping AC approach to study transient problems (see for instance [Drikakis and Rider, 2005]). In this approach, for each time step $t = t_1 \to t_2$, we iterate our system for the dual time τ until the convergence is found on the divergence free equation:

$$\begin{aligned} \frac{1}{c_{AC}^2}\frac{\partial p'}{\partial \tau} &+ \nabla\cdot\mathbf{v} &&= 0 \\ \frac{\partial \mathbf{v}}{\partial \tau} + \frac{\partial \mathbf{v}}{\partial t} &+ \mathbf{v}\cdot\nabla\mathbf{v} &&= -\frac{1}{\rho}\nabla p' + \nu\Delta\mathbf{v} \end{aligned} \tag{3.3}$$

This strategy allows to extend in a rigorous way the AC approach to unsteady flow problems. Note that in [Clausen, 2013], the single time-stepping approach is used to solve the unsteady incompressible system. The errors caused by the artificial term are allowed meaning $\nabla\cdot\mathbf{v} \neq 0$. It is shown that the solutions obtained are nonetheless satisfactory in the low-Mach number limit.
In a **closed domain**, instead of having a divergence free constraint, one has an isentropic compression/-expansion due to mobile boundaries. The ideas of the AC method can be extended for the asymptotic system (1.19) as:

$$\begin{aligned} \frac{\partial \rho}{\partial t} &+ \nabla\cdot(\rho\mathbf{v}) &&= 0 \\ \frac{\partial(\rho\mathbf{v})}{\partial t} &+ \nabla\cdot(\rho\mathbf{v}\otimes\mathbf{v}) &&= -\nabla p' \\ \frac{1}{c_{AC}^2}\frac{\partial p'}{\partial t} &+ \nabla\cdot\mathbf{v} &&= -\frac{1}{\rho c^2}\frac{dP}{dt} \end{aligned} \tag{3.4}$$

With the purpose of clarifying the physical meaning of system (3.4), we consider a simple 1D single-phase piston problem (see Figure 3.1). The piston is pushed into the fluid initially at rest from left to right at a (slow) constant speed V_p. An acoustic wave propagates inside the cylinder and is reflected by rigid walls. On the right of Figure 3.1, we present the qualitative pressure solutions given by different approaches at the wall-end extremity indicated on the left of Figure 3.1:

- The black curve represents the fully compressible solution. The first impact of the acoustic wave with the wall is identified by a jump in pressure at $t_{comp} = L_0/c$, where L_0 and c are the initial length of the cylinder and the physical acoustic speed respectively. The first jump can be approximated in the low-Mach number regime by the Joukowski formula as [Joukowski, 1900]: $\Delta p = 2\rho_{init} c_{init} V_p$.
- The red curve represents the isentropic compression due to the moving piston obtained by solving analytically the asymptotic system (1.19) in one dimension. As discussed, the asymptotic method filters the waves and replaces the compression by these waves with a global compression due to the boundaries. The pressure solution is therefore homogeneous: $P = P(t)$.
- The blue curve represents the solution for the artificial acoustic wave only. The resolved system is of AC type without the physical viscosity. The first impact is identified by a jump in pressure at a much longer time compared to the fully compressible case since the artificial sound speed is chosen to be much smaller than the physical one: $t_{AC} = L_0/c_A >> t_{comp}$. The pressure jump is very small compared to the fully compressible solution and can be approximated in the low-Mach number case as: $\Delta p' = 2\rho_{init} c_{AC} V_p$.

From these qualitative solutions, we can state that:

- The asymptotic solution P is not correct at the beginning of the piston motion since acoustic waves are filtered in this model. However, in long time computations, such a solution represents correctly the loads on a structure since waves become (numerically and physically) diffused and the fully compressible solution tends to the asymptotic one. The diffusive behavior is much more important in the multidimensional case as observed through the 2D cylindrical piston problem in section 2.1.
- The AC approach originally developed for an open domain when applied for a closed domain (with unsteady evolution) yields a wrong pressure solution since the compression due to the artificial acoustic wave p' is negligible with respect to the fully compressible one. An AC system which contains this wave only could lead to a significant underestimation of loads on a structure.

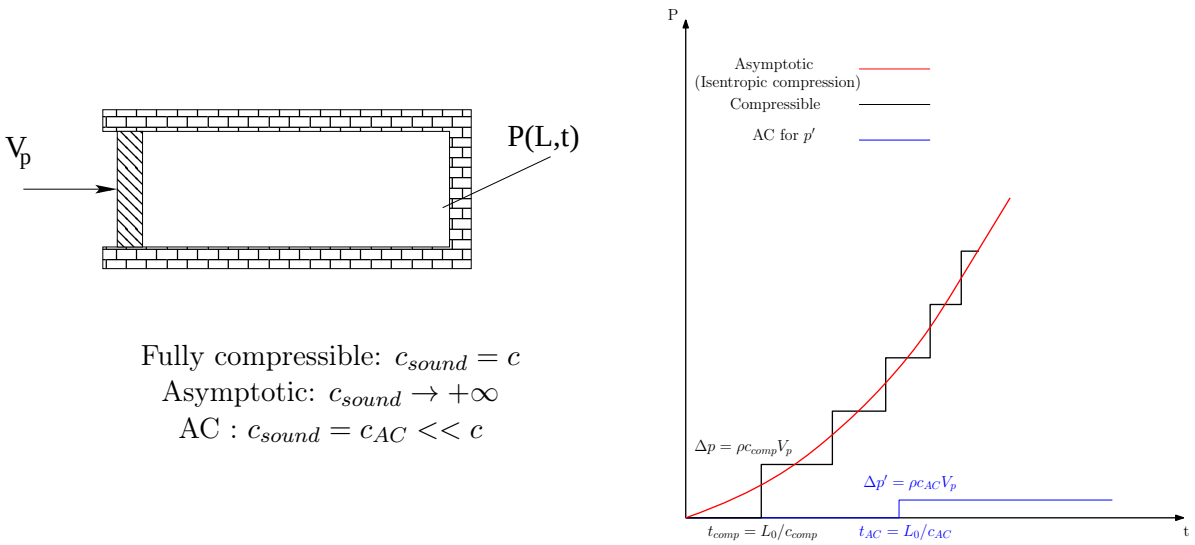

Figure 3.1: Configuration for the 1D planar piston problem (left) and qualitative pressure solution at the wall-end extremity (right).

Consequently, the asymptotic system when combined with the AC approach (3.4) could guarantee a satisfactory estimate of the loads applied on a structure. Moreover, the computational cost is reduced since the stability time step is determined by the artificial acoustic speed c_{AC}.

$$p_{AC,total} = P + p' \approx P$$

3.2 A classical AC-asymptotic model for the 1D planar piston problem

In this section, we solve analytically the aforementioned 1D planar piston problem (Figure 3.1) by considering the system (3.5). Such system is of AC type and is combined with the isentropic compression equation from the asymptotic model. In the literature, the AC part (that is the first three equations of system (3.5)) is often referred as the pseudocompressibility approach (see for instance [Nourgaliev et al., 2004]). This approach is of interest since it is similar, to some extent, to the system (3.4) but it is easier to solve. We denote the system (3.5) as the AC-asymptotic model:

$$\begin{aligned} \frac{\partial \rho}{\partial t} + \frac{\partial (\rho u)}{\partial x} &= 0 \\ \frac{\partial (\rho u)}{\partial t} + \frac{\partial (\rho u^2 + p')}{\partial x} &= 0 \\ p' &= c_{AC}^2 (\rho - \rho_0) \\ (P + p_\infty) L^\gamma &= \text{const} \end{aligned} \tag{3.5}$$

The initial condition for the density ρ_0 as well as for the pressure and velocity are specified in Table 3.2. The dimension of the problem, the artificial sound speed and the material properties are specified in Tables 3.1 and 3.3. The computational domain is bounded by fixed walls except for the moving piston.

Material properties	
γ	4.4
P_∞ (Pa)	6.0×10^8

Table 3.1: 1D planar piston problem: Material properties

Initial conditions	
ρ (kg/m^3)	1000.0
P (Pa)	1×10^5
u (m/s)	0.0

Table 3.2: 1D planar piston problem: Initial conditions

Dimension and parameters	
L_0 (m)	1.0
V_p (m/s)	1.0 ($M_p \approx 6.0 \times 10^{-4}$)
c_{AC} (m/s)	325 ($\approx c/5$)

Table 3.3: 1D planar piston problem: Dimension and parameters

In Figures 3.2, 3.3, 3.4, we compare the fully compressible solution and the asymptotic solution with the one obtained by solving system (3.5). In contrast to the Figure 3.1, we note that the water is compressed by the piston moving from right to left with speed V_p.

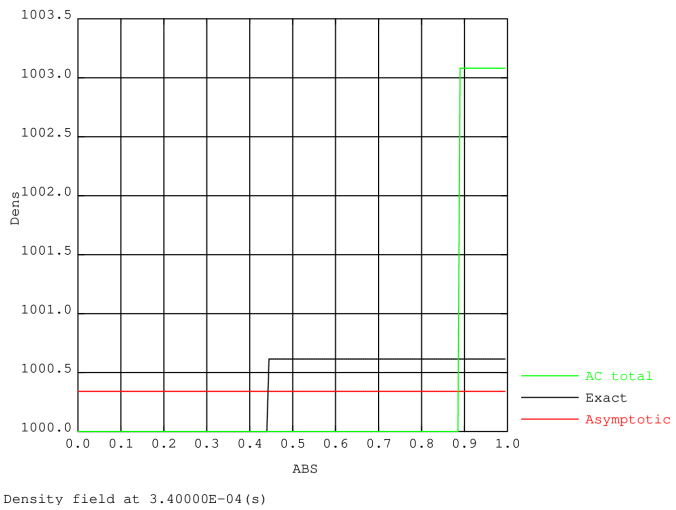

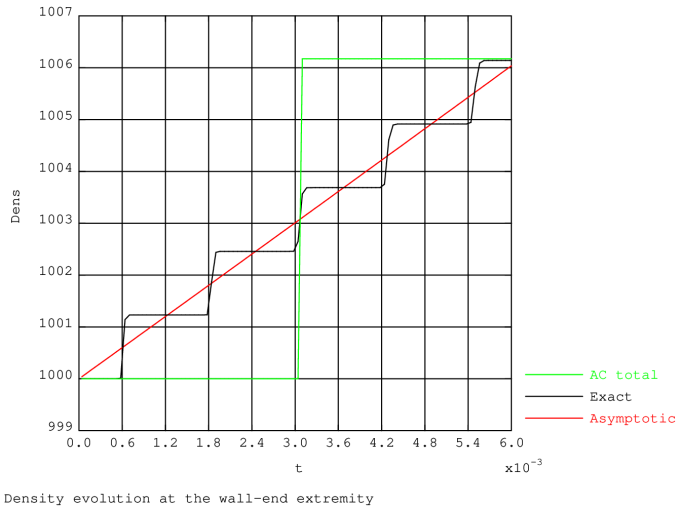

Figure 3.2: 1D planar piston problem. Comparison for the density field for the whole domain at $t = 3.4 \times 10^{-4}$ s (left) and at the wall-end extremity (right).

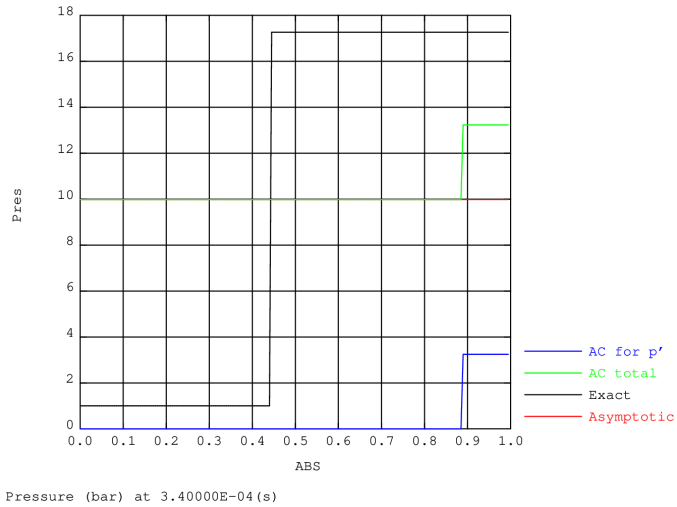

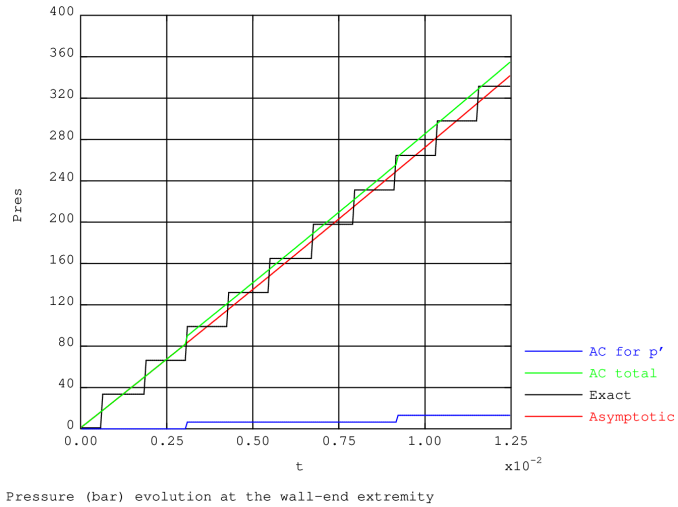

Figure 3.3: 1D planar piston problem. Comparison for the pressure field for the whole domain at $t = 3.4 \times 10^{-4}$ s (left) and at the wall-end extremity (right).

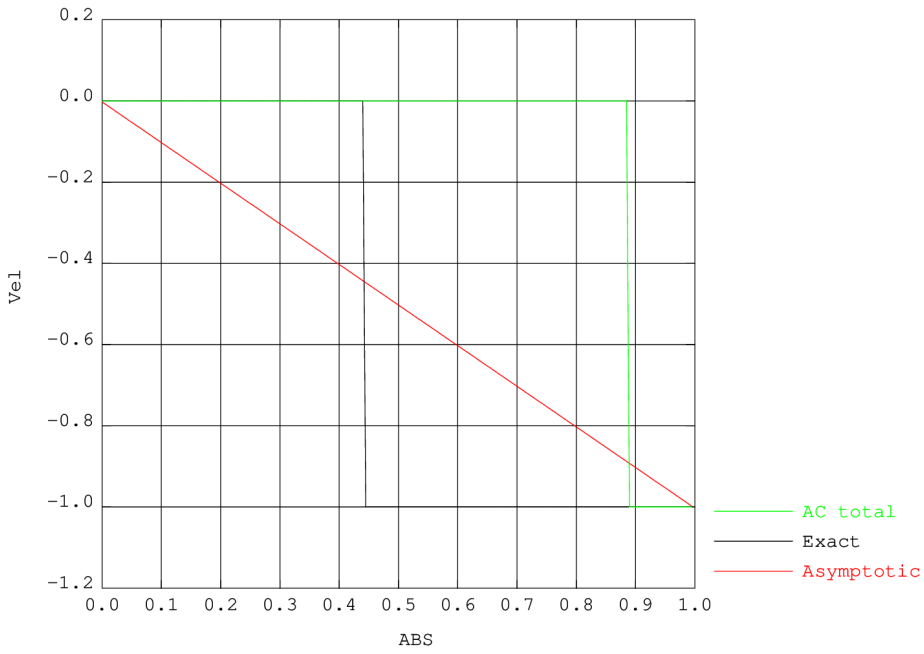

Figure 3.4: 1D planar piston problem. Comparison for the velocity field for the whole domain at $t = 3.4 \times 10^{-4}$ s.

We perform the comparisons at $t = 3.4 \times 10^{-4} s$ corresponding to the instant where no wave reflections occur when solving the fully compressible as well as the AC-asymptotic models. The ratio between the distance covered by waves in each model corresponds to the ratio of sound speed $c/c_{AC} = 5$ (or $M_{p,AC}/M_p = 5$) with M_p the piston Mach number.
In Figure 3.2, a (very small) density jump of 0.6 kg/m^3 for the fully compressible solution can be identified since we are in the low-Mach number regime and moreover water changes very little its volume when being compressed. The asymptotic density increases isentropically, as the pressure, to conserve mass. The density jump in the AC-asymptotic model is much higher compared to the fully compressible one. The ratio of density between the fully compressible and AC models can be demonstrated to be equal to the ratio of the sound speed (or Mach number):

$$\frac{\Delta\rho_{AC}}{\Delta\rho} = \frac{c}{c_{AC}} = \frac{M_{p,AC}}{M_p} > 1 \tag{3.6}$$

This relation can be explained thanks the mass conservation equation in the acoustic wave frame using the Rankine-Hugoniot condition. Let 1, 2 being the states before and behind the wave respectively; $C_{s,AC}$, C_s being the propagating speed of waves in the AC-asymptotic and the fully compressible models respectively. We then have:

$$\rho_{2,AC} = \rho_{1,AC}\frac{C_{s,AC}}{C_{s,AC} - V_p} \rightarrow \Delta\rho_{AC} = \rho_{1,AC}\frac{V_p}{C_{s,AC} - V_p} \approx \rho_{1,AC} M_{p,AC}$$

$$\rho_2 = \rho_1\frac{C_s}{C_s - V_p} \rightarrow \Delta\rho = \rho_1\frac{V_p}{C_s - V_p} \approx \rho_1 M_p$$

As $\rho_1 = \rho_{AC,1}$, relation (3.6) can be recovered. We note that a larger value of the Mach ratio $M_{p,AC}/M_p$ leads to a larger value of the density jump ratio.

In Figure 3.3, the dynamic pressure jump $\Delta p'$ is small compared to the fully compressible solution. This jump in dynamic pressure can be determined by Joukowski formula and is found to decrease as the ratio

M/M_{AC} increases:

$$\Delta p' \approx \rho_{1,AC} c_{AC} V_p = \rho_{1,AC} c_{AC}^2 M_{p,AC} = \rho_{1,AC} c^2 M_p \frac{M_p}{M_{p,AC}}$$

In Figure 3.4, the velocity profile in the asymptotic model is linear as $\nabla \cdot u = -\frac{1}{\rho c^2}\frac{dP}{dt} = f(t)$, connecting $-V_p$ and 0 corresponding to the boundary conditions. In the fully compressible and AC-asymptotic models, waves propagating with different speeds induce behind them the low-Mach motion of water of velocity $-V_p$.

Concluding remarks

The AC-asymptotic system (3.5) has the following advantages:

- The computational cost is reduced and is dependent on the the ratio of the sound speed c_{AC}/c (or M_{AC}/M). The parameter c_{AC} is chosen to be much smaller than the physical sound speed c.
- A smaller value of c_{AC}/c leads to a smaller jump of the dynamic pressure $\Delta p'$. Since we are interested in the asymptotic solution, this guarantees that the total pressure solution is approximately equal to the asymptotic one. For a closed domain like the above piston problem, a small value of c_{AC}/c is important since the negligible amplitude of the dynamic pressure at the beginning of the calculation could become significant in long time computations after several reflections.

However, the approach has a main drawback in producing an incorrect solution for the density. A small value of c_{AC}/c makes the AC density solution far from the fully compressible solution as well as the asymptotic one as explained in (3.6).

3.3 New AC approach for Low-Mach flows (AC-LM): physical model

In section 3.2, we have observed the main drawback of the AC-asymptotic system (3.5) in solving closed domain problems: the excessive jump of density due to the mass conservation. As a result, a new method is proposed in this section and denoted as the AC-LM since it relies on the artificial compressibility approach in solving low-Mach flows.
The physical model of the AC-LM method can be derived starting from the Euler system of conservation equations, in particular in its primitive form which can be written as:

$$\begin{aligned}
\frac{\partial \rho}{\partial t} &+ \mathbf{v}\cdot\nabla\rho &+ \rho\nabla\cdot\mathbf{v} &= 0\\
\frac{\partial \mathbf{v}}{\partial t} &+ \mathbf{v}\cdot\nabla\mathbf{v} &+ \frac{1}{\rho}\nabla p &= 0\\
\frac{\partial p}{\partial t} &+ \mathbf{v}\cdot\nabla p &+ \rho c^2\nabla\cdot\mathbf{v} &= 0
\end{aligned} \tag{3.7}$$

By adding and subtracting the same quantity $\rho c_{AC}^2 \nabla\cdot\mathbf{v}$ in the pressure evolution equation $(3.7)_3$, we obtain:

$$\begin{aligned}
\frac{\partial \rho}{\partial t} &+ \mathbf{v}\cdot\nabla\rho &+ \rho\nabla\cdot\mathbf{v} &= 0\\
\frac{\partial \mathbf{v}}{\partial t} &+ \mathbf{v}\cdot\nabla\mathbf{v} &+ \frac{1}{\rho}\nabla p &= 0\\
\frac{\partial p}{\partial t} &+ \mathbf{v}\cdot\nabla p &+ \rho c_{AC}^2\nabla\cdot\mathbf{v} &= -(\rho c^2 - \rho c_{AC}^2)\nabla\cdot\mathbf{v}
\end{aligned} \tag{3.8}$$

In (3.8), the parameter c_{AC} is called the artificial sound speed. Since our purpose is to extend the standard compressible solvers in the low-Mach number regime such as implemented and available in Europlexus,

we add the conservation of total energy equation into the system (3.8) in order to ensure that the existing structure of the computational code is least modified when implementing the newly proposed strategy. The final system of equations takes the form (3.9):

$$\begin{array}{lllll}
\dfrac{\partial \rho}{\partial t} & + \mathbf{v}\cdot\nabla\rho & = 0 & -\rho\nabla\cdot\mathbf{v} \\
\dfrac{\partial \mathbf{v}}{\partial t} & + \mathbf{v}\cdot\nabla\mathbf{v} + \dfrac{1}{\rho}\nabla p & = 0 & \\
\dfrac{\partial p}{\partial t} & + \mathbf{v}\cdot\nabla p & = -\rho c_{AC}^2\nabla\cdot\mathbf{v} & -(\rho c^2 - \rho c_{AC}^2)\nabla\cdot\mathbf{v} \\
\dfrac{\partial (\rho e^t)}{\partial t} & + \mathbf{v}\cdot\nabla(\rho e^t + p) & = \underbrace{0}_{\text{Part I}} & \underbrace{-(\rho e^t + p)\nabla\cdot\mathbf{v}}_{\text{Part II}}
\end{array} \tag{3.9}$$

and it can be divided into two parts:

- Part I, analyzed in section 3.3.1, corresponds to the convective mechanism with fast acoustic waves filtered through the use of the artificial sound speed. Part I gives the wrong solutions for the artificial wave but is efficient since the computational cost is significantly reduced.
- Part II, detailed in section 3.3.2, serves to correct the density and pressure field by considering the isentropic transformations through the speed divergence term $\nabla\cdot\mathbf{v}$.

3.3.1 Part I: convective mechanism

In part I, we solve the following system:

$$\begin{array}{llllll}
\dfrac{\partial \rho}{\partial t} & + \mathbf{v}\cdot\nabla\rho & & & = & 0 \\
\dfrac{\partial \mathbf{v}}{\partial t} & + \mathbf{v}\cdot\nabla\rho & + \dfrac{1}{\rho}\nabla p & & = & 0 \\
\dfrac{\partial p}{\partial t} & + \mathbf{v}\cdot\nabla p & + \rho c_{AC}^2\nabla\cdot\mathbf{v} & & = & 0 \\
\dfrac{\partial (\rho e^t)}{\partial t} & + \mathbf{v}\cdot\nabla(\rho e^t + p) & & & = & 0
\end{array} \tag{3.10}$$

System (3.10) has the following characteristics:

- It does not conserve the mass and the total energy. The mass conservation equation is replaced by the transport equation for the density $(3.10)_1$ to avoid the undesirable jump in the density solution observed in the 1D planar piston problem.
- The convective mechanism of the fast acoustic wave at speed c is replaced by the propagation of the slower artificial acoustic wave at speed c_{AC}. This parameter is normally chosen to be much smaller than the physical sound speed: $c_{AC} << c$ (typically $c_{AC} \approx c/10$, see [Madsen and Schäffer, 2006]).

System (3.10) can be written in a more conservative form as:

$$\begin{array}{llll}
\dfrac{\partial \rho}{\partial t} & + \nabla\cdot(\rho\mathbf{v}) & = & \rho\nabla\cdot\mathbf{v} \\
\dfrac{\partial (\rho\mathbf{v})}{\partial t} & + \nabla\cdot(\rho\mathbf{v}\otimes\mathbf{v} + p\mathcal{I}) & = & \rho\mathbf{v}\nabla\cdot\mathbf{v} \\
\dfrac{\partial p}{\partial t} & + \nabla\cdot(p\mathbf{v}) & = & (p - \rho c_{AC}^2)\nabla\cdot\mathbf{v} \\
\dfrac{\partial (\rho e^t)}{\partial t} & + \nabla\cdot((\rho e^t + p)\mathbf{v}) & = & (\rho e^t + p)\nabla\cdot\mathbf{v}
\end{array} \tag{3.11}$$

In compact form, system (3.11) writes:

$$\frac{\partial \mathbf{a}}{\partial t} + \nabla \cdot \mathbf{f} = \mathbf{b} \nabla \cdot \mathbf{v} \tag{3.12}$$

where:

$$\mathbf{a} = \begin{pmatrix} \rho \\ \rho \mathbf{v} \\ p \\ \rho e^t \end{pmatrix}, \ \mathbf{f} = \begin{pmatrix} \rho \mathbf{v} \\ \rho \mathbf{v} \otimes \mathbf{v} + p\mathcal{I} \\ p\mathbf{v} \\ (\rho e^t + p)\mathbf{v} \end{pmatrix}, \ \mathbf{b} = \begin{pmatrix} \rho \\ \rho \mathbf{v} \\ p - \rho c_{AC}^2 \\ \rho e^t + p \end{pmatrix}$$

We must clarify at this stage that the system (3.11) or (3.12) is actually advanced without using the evolution equation for the total energy. Expressing the system with the total energy equation included in the set of conservation laws is done to minimize the modification of the existing computational code when implementing the new strategy. Compared to the original Euler equations, system (3.11) displays one extra equation for the pressure and source terms in the right-hand-side of (3.11) or (3.12).The updated value of the total energy is computed from the updated values of velocity and internal energy, with the internal energy computed from the pressure and the density using the EOS, after solving part II as will be described in section 3.4.2.

Hyperbolicity, eigenvalues, eigenvectors

System (3.10) in 1D can be rewritten in compact form as:

$$\frac{\partial \mathcal{W}}{\partial t} + A(\mathcal{W}) \frac{\partial \mathcal{W}}{\partial x} = 0 \tag{3.13}$$

with

$$\mathcal{W} = \begin{pmatrix} \rho \\ u \\ p \\ \rho e^t \end{pmatrix}, \ A(\mathcal{W}) = \begin{pmatrix} u & 0 & 0 & 0 \\ 0 & u & 1/\rho & 0 \\ 0 & \rho c_{AC}^2 & u & 0 \\ 0 & 0 & u & u \end{pmatrix}$$

The above system is hyperbolic since the matrix A has 4 real eigenvalues:

$$\lambda_1 = u - c_{AC}, \ \lambda_2 = \lambda_3 = u, \ \lambda_4 = u + c_{AC}$$

and the corresponding right eigenvectors are linearly independent:

$$\mathbf{K}^{(1)} = \begin{pmatrix} 0 \\ 1 \\ -\rho c_{AC} \\ \rho u \end{pmatrix}, \ \mathbf{K}^{(2)} = \begin{pmatrix} 1 \\ 0 \\ 0 \\ 1 \end{pmatrix}, \ \mathbf{K}^{(3)} = \begin{pmatrix} 1 \\ 0 \\ 0 \\ -1 \end{pmatrix}, \ \mathbf{K}^{(4)} = \begin{pmatrix} 0 \\ 1 \\ \rho c_{AC} \\ \rho u \end{pmatrix}$$

Moreover, the $K^{(2)}, K^{(3)}$-characteristic fields are linearly degenerate and the $K^{(1)}$, $K^{(3)}$-characteristic fields are genuinely non-linear. Indeed:

$$\nabla \lambda_1 \cdot K^{(1)} = (0,1,0,0) \cdot \begin{pmatrix} 0 \\ 1 \\ -\rho c_{AC} \\ \rho u \end{pmatrix} \neq 0, \quad \nabla \lambda_3 \cdot K^{(4)} = (0,1,0,0) \cdot \begin{pmatrix} 0 \\ 1 \\ \rho c_{AC} \\ \rho u \end{pmatrix} \neq 0$$

$$\nabla \lambda_2 \cdot K^{(2)} = (0,1,0,0) \cdot \begin{pmatrix} 1 \\ 0 \\ 0 \\ 1 \end{pmatrix} = 0, \quad \nabla \lambda_2 \cdot K^{(3)} = (0,1,0,0) \cdot \begin{pmatrix} 1 \\ 0 \\ 0 \\ -1 \end{pmatrix} = 0$$

From the eigenvectors, we state that:

- The density is constant across λ_1, λ_4 waves. The jumps in the velocity and the pressure across these waves are non-trivial:
$$\rho = \text{const}$$
- The density and the total energy jump across λ_2, λ_3 waves. The velocity and the pressure are constant across these waves:
$$u = \text{const}, \; p = \text{const}$$

3.3.2 Part II: isentropic transformation

In part II, we take into account the filtering of the fast acoustic waves of the system (3.14):

$$\begin{aligned} \frac{\partial \rho}{\partial t} &= -\rho \nabla \cdot \mathbf{v} \\ \frac{\partial \mathbf{v}}{\partial t} &= 0 \\ \frac{\partial p}{\partial t} &= -(\rho c^2 - \rho c_{AC}^2) \nabla \cdot \mathbf{v} \\ \frac{\partial \rho e^t}{\partial t} &= -(\rho e^t + p) \nabla \cdot \mathbf{v} \end{aligned} \tag{3.14}$$

by imposing that the divergence of the velocity $\nabla \cdot \mathbf{v}$ is a function of time only. This comes from the asymptotic system discussed in section 1.2 for a closed domain in which the compability condition reads:

$$\nabla \cdot \mathbf{v} = -\frac{1}{\rho c^2} \frac{dP}{dt} = f(t) \tag{3.15}$$

The calculation of $\nabla \cdot \mathbf{v}$ is the key step in solving (3.14) since the other variables in the RHS of (3.14) are in general known from the output of part I.

3.4 New AC approach for Low-Mach flows (AC-LM): numerical treatment

In this section, we discretise the physical model previously described. As discussed, the method consists of two steps. The first step involves discretising the hyperbolic part (part I). Let $\mathbb{L}_h^{\Delta t}$ be the hyperbolic operator, we find the solution after a time step Δt by:

$$\mathbf{A}_i^{n+1,*} = \mathbb{L}_h^{\Delta t} \mathbf{A}_i^n$$

The method takes into account the moving mesh using the ALE approach and will be discussed thoroughly in section 3.4.1.
The second step corrects the solution of part I by considering the isentropic transformation. Let $\mathbb{L}_{is}$ be the isentropic operator, we find the solution at the new instant by:

$$\mathbf{A}_i^{n+1} = \mathbb{L}_{is} \mathbf{A}_i^{n+1,*}$$

3.4.1 Part I: Discretization

For the sake of simplicity, we consider the 1D case. By integrating system (3.12) over a finite control volume with moving boundaries $C_i(t) = [x_{i-1/2}(t), x_{i+1/2}(t)]$ and over time $[t^n, t^{n+1}]$, we obtain:

$$\int_{t^n}^{t^{n+1}} \int_{x_{i-1/2}}^{x_{i+1/2}} \frac{\partial \mathbf{a}}{\partial t} dt dx + \int_{t^n}^{t^{n+1}} \int_{x_{i-1/2}}^{x_{i+1/2}} \frac{\partial \mathbf{f}}{\partial x} dt dx = \int_{t^n}^{t^{n+1}} \int_{x_{i-1/2}}^{x_{i+1/2}} \mathbf{b} \frac{\partial u}{\partial x} dx dt \tag{3.16}$$

The integration for the type of equation in the L.H.S of (3.16) has been performed in section 1.3.3 considering the ALE approach. The integration for source term in the R.H.S of (3.16) needs approximation:

$$\int_{t^n}^{t^{n+1}} \int_{x_{i-1/2}}^{x_{i+1/2}} \mathbf{b}\frac{\partial u}{\partial x} dx dt \approx \mathbf{b}_i^n \int_{t^n}^{t^{n+1}} \int_{x_{i-1/2}}^{x_{i+1/2}} \frac{\partial u}{\partial x} dx dt = \mathbf{b}_i^n (u_{i+1/2} - u_{i-1/2})\Delta t$$

We then obtain the first order scheme:

$$\mathbf{A}_i^{n+1,*} = \mathbf{A}_i^n \frac{\Delta x_i^n}{\Delta x_i^{n+1}} - \frac{\Delta t}{\Delta x_i^{n+1}}(\mathbf{F}_{i+1/2}^{ALE} - \mathbf{F}_{i-1/2}^{ALE}) + \frac{\Delta t}{\Delta x_i^{n+1}} \mathbf{b}_i^n (u_{i+1/2} - u_{i-1/2}) \tag{3.17}$$

where:

- $\mathbf{A}_i^n, \mathbf{A}_i^{n+1,*}$ are the cell averages of $\mathbf{a}$ at time t^n, t^{n+1}.

$$\mathbf{A}_i^n = \frac{1}{\Delta x^n} \int_{x_{i-1/2}^n}^{x_{i+1/2}^n} \mathbf{a}(x, t^n) dx, \quad \mathbf{A}_i^{n+1} = \frac{1}{\Delta x^{n+1}} \int_{x_{i-1/2}^{n+1}}^{x_{i+1/2}^{n+1}} \mathbf{a}(x, t^{n+1}) dx$$

- $\mathbf{F}_{i\pm1/2}^{ALE}$ is the numerical ALE flux vectors approximating the average of the physical ALE fluxes.

$$\mathbf{F}_{i\pm1/2}^{ALE} \approx \tilde{\mathbf{f}}_{i\pm1/2}^{ALE} = \frac{1}{\Delta t} \int_{t^n}^{t^{n+1}} \left(\mathbf{f}_{i\pm1/2} - u_{i\pm1/2} u_{m,i\pm1/2}\right) dt$$

- $u_{i\pm1/2}$ is the velocity at the cell interfaces.
- Δx_i^{n+1} is the new volume of the cell that can be determined by the DGCL (see section 1.3.3).

It is obvious that solving the RP at the intercell is the key step in finding the solution. In solving the RP, we use the acoustic solver. For each RP with $\mathbf{A}_L$ and $\mathbf{A}_R$ as the left and right states of an intercell respectively, we determine the intermediate states which provide p^* and u^* such that:

$$\begin{aligned} p^* &= p_R + \rho_R c_{AC}(u^* - u_R) \\ p^* &= p_L - \rho_L c_{AC}(u^* - u_L) \end{aligned} \tag{3.18}$$

The system (3.18) can be solved and gives:

$$\begin{aligned} u^* &= \frac{(p_L + \rho_L c_{AC} u_L) - (p_R - \rho_R c_{AC} u_R)}{\rho_L c_{AC} + \rho_R c_{AC}} \\ p^* &= \frac{u_L - u_R}{\frac{1}{\rho_L c_{AC}} + \frac{1}{\rho_R c_{AC}}} + \frac{\frac{1}{\rho_L c_{AC}} p_L + \frac{1}{\rho_R c_{AC}} p_R}{\frac{1}{\rho_L c_{AC}} + \frac{1}{\rho_R c_{AC}}} \end{aligned} \tag{3.19}$$

The numerical fluxes $\mathbf{F}^{ALE}$ can now be computed and their values depend on the relative position of the intercell within the wave systems quantified in (3.20). The full acoustic solutions in terms of the intercell speed ($\lambda_m = x/t = u_m$) are given in Table 3.4.

$$\begin{aligned} \lambda_L &= \min(u_L - c_{AC}, u_L^* - c_{AC}) \\ \lambda_L^* &= \max(u_L - c_{AC}, u_L^* - c_{AC}) \\ \lambda^* &= u^* \\ \lambda_R^* &= \min(u_R + c_{AC}, u_R^* + c_{AC}) \\ \lambda_R &= \max(u_R + c_{AC}, u_R^* + c_{AC}) \end{aligned} \tag{3.20}$$

Wave speed	$x/t < \lambda_L$	$\lambda_L^* < x/t < \lambda^*$	$\lambda^* < x/t < \lambda_R^*$	$\lambda_R < x/t$
Density	ρ_L	ρ_L	ρ_R	ρ_R
Sound speed	c_{AC}	c_{AC}	c_{AC}	c_{AC}
Velocity	u_L	u^*	u^*	u_R
Pressure	p_L	p^*	p^*	p_R

Table 3.4: Acoustic solution for the single-phase Riemann Problem (RP)

The solutions described in Table 3.4 are not complete since the states between λ_L, λ_L^* and λ_R^*, λ_R are unknown (see also Figure 5.1 with $c_{AC,L} = c_{AC,R} = c_{AC}$). We suppose that solutions are linear in these regions and also satisfy the acoustic formula: $\Delta p = \rho c_{AC} \Delta u$.
The method is extended to second order accuracy in space and time with the Barth-Jespersen reconstruction on primitive variables and the two-stage Runge-Kutta method.
In appendix D.1, we provide a verification for the numerical method of part I considering the transport equation for the density.

3.4.2 Part II: Discretization

We recall that in part II, we need to solve the system:

$$\begin{aligned} \frac{\partial \rho}{\partial t} &= -\rho \nabla \cdot \mathbf{v} \\ \frac{\partial \mathbf{v}}{\partial t} &= 0 \\ \frac{\partial p}{\partial t} &= -(\rho c^2 - \rho c_{AC}^2) \nabla \cdot \mathbf{v} \\ \frac{\partial (\rho e^t)}{\partial t} &= -(\rho e^t + p) \nabla \cdot \mathbf{v} \end{aligned} \tag{3.21}$$

where $\nabla \cdot \mathbf{v}$ is, as already mentioned, a homogeneous function. By integrating $(3.21)_1$ over a whole domain $\mathcal{V}$, we obtain:

$$\frac{d}{dt} \int_{\mathcal{V}} \rho dV = - \left(\int_{\mathcal{V}} \rho dV \right) (\nabla \cdot \mathbf{v})$$

Using the first-order forward Euler method, we get:

$$\frac{m^{n+1} - m^{n+1,*}}{\Delta t} = -m^{n+1,*} (\nabla \cdot \mathbf{v})$$

where $m^{n+1,*}$ is the total mass after part I and m^{n+1} is a known quantity, derived from mass conservation. Indeed, in the case of closed domain, the total mass at every instant is equal to the initial mass:

$$m^{n+1} = m^0$$

The divergence of the velocity can therefore be determined as:

$$(\nabla \cdot \mathbf{v}) = -\frac{m^{n+1} - m^*}{m^* \Delta t} \tag{3.22}$$

The density, the pressure and the total energy could be integrally updated by system (3.21) using the first-order method. However, the original EOS is not respected with these solutions. To overcome this issue, the density and the pressure are firstly computed by system (3.21):

$$\begin{aligned} \rho_i^{n+1} &= \rho_i^{n+1,*} - \Delta t \rho_i^{n+1,*} \nabla \cdot \mathbf{v} \\ p_i^{n+1} &= p_i^{n+1,*} - \Delta t \rho_i^{n+1,*} (c^2 - c_{AC}^2) \nabla \cdot \mathbf{v} \end{aligned} \tag{3.23}$$

The computation of the internal energy is performed using the SG-EOS (1.7) and the total energy follows:

$$\begin{aligned} e_i^{n+1} &= \frac{p_i^{n+1} + \gamma p_\infty}{(\gamma - 1)\rho_i^{n+1}} \\ (\rho e^t)_i^{n+1} &= \rho_i^{n+1} e_i^{n+1} + \frac{1}{2}\rho_i^{n+1}(\mathbf{v}_i^n)^2 \end{aligned} \tag{3.24}$$

3.5 Numerical results

3.5.1 1D planar piston problem with acoustic waves

In this section, we assess the properties of the new method by computing the 1D planar piston problem without WPIC. The dimension, parameters, initial conditions and material properties are similar to those previously used (see section 3.2, Tables 3.1, 3.2, 3.3). The new AC method is applied with second order accuracy in space using linear reconstruction for primitive variables, second order accuracy in time using a 2-stage RK method, $CFL = 0.5$. In the following analysis, we present the comparison between the fully compressible (analytical/exact) solution, the asymptotic solution and the solution given by the new AC-LM method.
In Figure 3.5 (left), we present the pressure solution at $t = 4.0 \times 10^{-4}$, prior to any wave impact on fixed walls. Concerning the exact fully compressible solution, we observe that there is a wave propagating from right to left at speed which is approximately equal to the sound speed in water (≈ 1625 m/s). The wave at time $t = 4.0 \times 10^{-4}$ s:

- is located at position $x \approx 1.0 - 1625 \times 4.0 \times 10^{-4} = 0.35$ m
- corresponds to a pressure jump satisfying the Joukowski acoustic formula $\Delta p \approx 1000 \times 1625 \times 1 = 16.25$ bars

Concerning the asymptotic pressure solution, it is as expected homogeneous and evolves isentropically:

$$\begin{aligned} p &= (p_0 + P_\infty)\left(\frac{L_0}{L_0 - V_p \times t}\right)^\gamma - P_\infty \\ &= (1 \times 10^5 + 6 \times 10^8)\left(\frac{1}{1 - 1 \times 4 \times 10^{-4}}\right)^{4.4} - 6 \times 10^8 \\ &= 11.537 \text{ bars} \end{aligned}$$

Concerning the pressure solution given by the AC-LM method, we observe that:

- The artificial acoustic wave is 5 times slower than the physical wave as we have the sound speed ratio $c_{AC}/c = 1/5$ (or $M_{AC}/M = 5$). The wave is located at the position:

$$x \approx 1.0 - 325 \cdot 4.0 \times 10^{-4} = 0.87 \text{ m}$$

- The pressure in the region which is not yet perturbed by the artificial acoustic wave takes a value close to the asymptotic pressure. The jump in the pressure satisfies the Joukowski formula:

$$\Delta p \approx 1000 \cdot 325 \cdot 1 = 3.25 \text{ bars}$$

We emphasize that lowering the artificial sound speed improves the pressure approximation that can be obtained for the asymptotic distribution as the pressure jump will be much smaller. However, due to the dimension of the problem, we present the case where the artificial acoustic wave is only 5 times slower than the physical wave. The case where the artificial acoustic wave is much slower than the physical wave (for example 10 times or more) would require an increase of the piston length and simulation time to observe

wave reflections. Moreover, the compression of water over a much longer time is not physically realistic due to the fluid stiffness and would lead to a very high pressure inside the cylinder.
In Figure 3.5 (right), we present the density solution. Concerning the fully compressible solution, we obtain as expected a density wave propagating from right to left and since we are in the low-Mach number regime, the density jump can be approximated as:

$$\Delta\rho = \frac{\Delta p}{c^2} = \frac{16.25 \times 10^5}{1625^2} = 0.615 \text{ kg/m}^3$$

Concerning the solution with the new method (AC-LM in the Figures), the density is constant in space and evolves isentropically in time as expected.
In Figure 3.6, we present the velocity solution at $t = 4 \times 10^{-4}$ s (left) and $t = 1 \times 10^{-2}$ s (right). In short time at $t = 4 \times 10^{-4}$ s where there is no reflections of waves, the velocity is as expected equal to the piston velocity in the perturbed region. The velocity solution given by the asymptotic model is linear as discussed. In long time at $t = 1 \times 10^{-2}$ s, we can observe that the velocity is slightly lower than the expected value of -1 m/s. This small error is however not well-understood as we solve the momentum equation in part I and do not modify the velocity in the second part of the scheme. The mesh refinement does not help increase the accuracy.
In Figures 3.7 and 3.8, we compare the pressure and density solution at the wall-end extremity. In general, the solutions given by the new method are very close to the asymptotic one. The solutions given by different meshes of 200, 400 cells are very close to each other indicating satisfactory grid convergence.

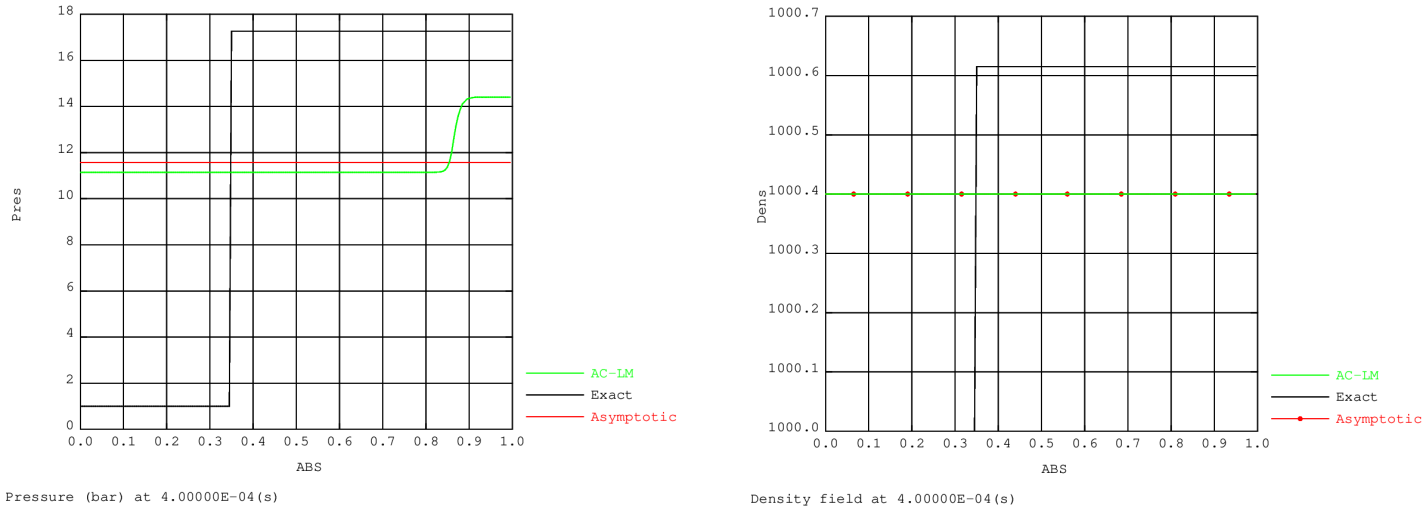

Figure 3.5: 1D planar piston problem. Comparison between the fully compressible solution (black), the asymptotic solution (red) and the new AC (AC-LM, 200 cells, green) solution. Pressure (left) and density (right) fields at $t = 4.0 \times 10^{-4}$ s.

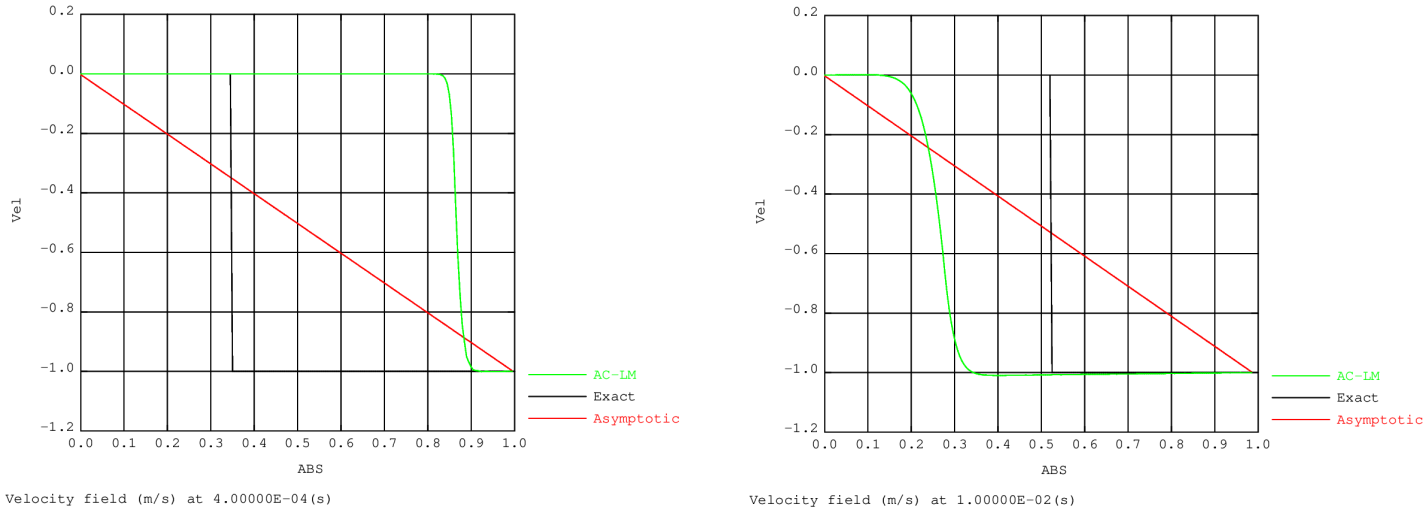

Figure 3.6: 1D planar piston problem. Comparison between the fully compressible solution (black), the asymptotic solution (red) and the new AC (AC-LM, 200 cells, green) solution. Velocity field at $t = 4.0 \times 10^{-4}$ s (left) and $t = 1.0 \times 10^{-3}$ s (right).

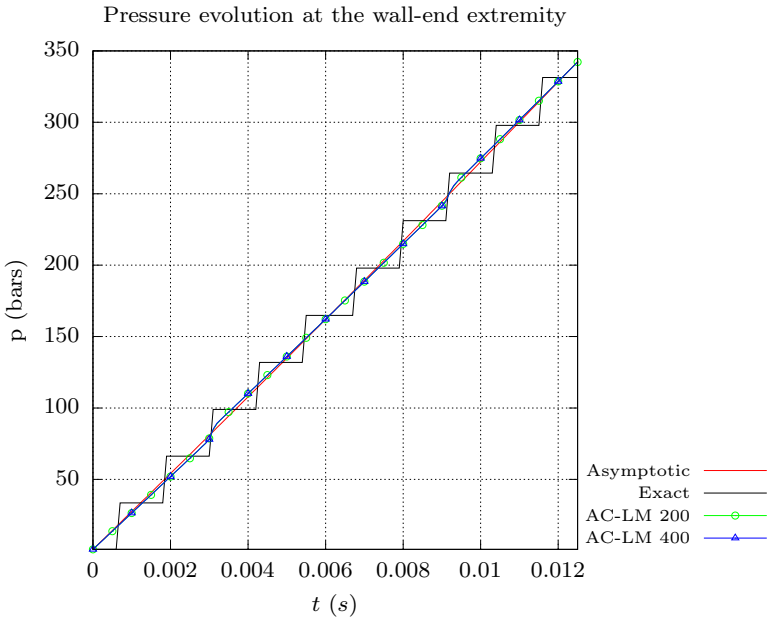

Figure 3.7: 1D planar piston problem. Comparison between the fully compressible solution (black), the asymptotic solution (red) and the new AC (AC-LM, green) solution. Pressure at the wall-end extremity.

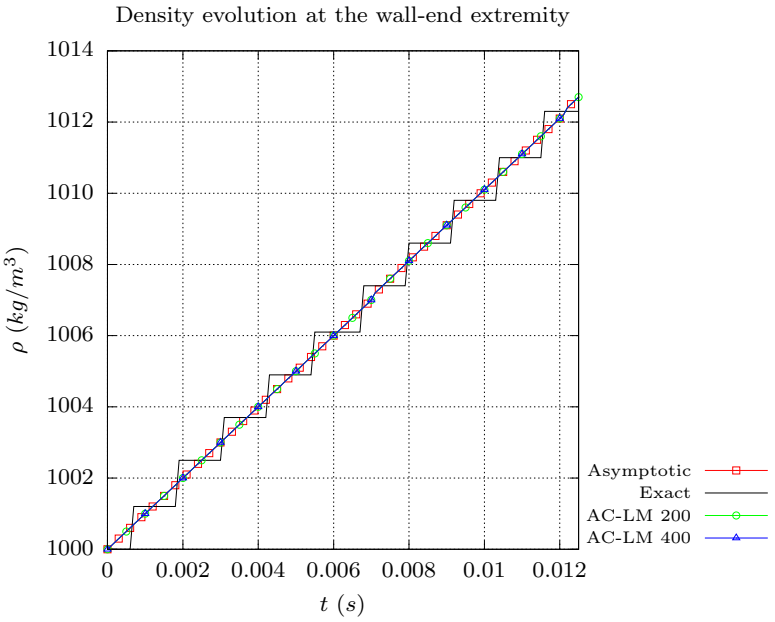

Figure 3.8: 1D planar piston problem. Comparison between the fully compressible solution (black), the asymptotic solution (red) and the new AC (AC-LM, green) solution. Density at the wall-end extremity.

3.5.2 1D axisymmetric cylindrical piston problem with well-prepared initial condition

We perform in this section the 1D axisymmetric cylindrical piston problem with WPIC considering perfect gas as material computed on a 1D domain with the dimension $R_0 = 0.1$ m, $R_{ext} = 1.1$ m. The piston in our case is pushed at a constant speed 1 m/s at the beginning followed by a deceleration from 1 m/s to -1 m/s and is finally pulled at a constant speed -1 m/s:

$$V_p = \begin{cases} 1, & 0 \leq t \leq 0.4 \text{ s} \\ -10t + 5, & 0.4 \text{ s} \leq t \leq 0.6 \text{ s} \\ -1, & 0.6 \text{ s} \leq t \leq 1 \text{ s} \end{cases}$$

3.5.2.1 Reference solution

The solution of the asymptotic system (1.19) is regarded as the reference solution in the low-Mach number regime. By considering the WPIC, the divergence of the velocity field for a closed domain is as discussed a function of time only:

$$\nabla \cdot \mathbf{v} = \frac{1}{r}\frac{\partial (r u_r)}{\partial r} = f(t)$$

The velocity solution at each instant can be obtained by integrating the above relation with the two boundary conditions: $u_r(R_0(t)) = V_p(t)$ and $u_r(R_{ext}) = 0$. It then yields:

$$u_r = \frac{V_p R_0}{R_{ext}^2 - R_0^2}\left(\frac{R_{ext}^2}{r} - r\right) \tag{3.25}$$

The dynamic pressure of the asymptotic system can be deduced by substituting the velocity field into the momentum equation followed by a spatial integration:

$$\rho \frac{\partial u_r}{\partial t} + \rho u_r \frac{\partial u_r}{\partial r} = -\frac{\partial p'}{\partial r}$$

In the following, we decompose the pressure field p' into two parts: one part p'_{acc} is dependent on the acceleration of the piston $\frac{dV_p}{dt}$ and the other part p'_{vel} is dependent on this piston velocity V_p.

$$p'_{acc} = \rho \frac{R_0}{R_{ext}^2 - R_0^2} \left(\frac{dV_p}{dt}\right) \left[\frac{R_0^2}{2}\left(\left(\frac{r}{R_0}\right)^2 - 1\right) - R_{ext}^2 ln\left(\frac{r}{R_0}\right)\right]$$

$$p'_{vel} = -\rho V_p^2 \frac{R_{ext}^2}{(R_{ext}^2 - R_0^2)^2}\left[\frac{R_{ext}^2}{2}\left(\left(\frac{R_0}{r}\right)^2 - 1\right) + (R_0^2 + R_{ext}^2) ln\left(\frac{r}{R_0}\right) - \frac{R_0^2}{2}\left(\left(\frac{r}{R_0}\right)^2 - 1\right)\right]$$

3.5.2.2 Numerical results

We compare the solutions given by the new AC-LM and the standard fully compressible HLLC methods with the reference one. The numerical methods are second order accurate in space using linear reconstruction (without limiter) for primitive variables and second order accuracte in time with the 2-stage RK method. The CFL number is such that $CFL = 0.5$ and $c_{AC} = 10$ m/s for the AC-LM method). Two different types of initial conditions are applied for the numerical computations: case 1 corresponds to an initial constant pressure field while case 2 corresponds to the presence of a dynamic pressure in the initial pressure field. The initial conditions for these two cases are specified in Tables 3.5 and 3.6 and the heat capacity ratio for the perfect gas is set as $\gamma = 1.4$.

Initial conditions	
ρ (kg/m^3)	1.0
p (Pa)	1×10^5
u (m/s)	u_r

Table 3.5: 1D axisymmetric cylindrical piston problem with WPIC. Case 1: Initial conditions with constant pressure.

Initial conditions	
ρ (kg/m^3)	1.0
p (Pa)	1×10^5 $+p'$
u (m/s)	u_r

Table 3.6: 1D axisymmetric cylindrical piston problem with WPIC. Case 2: Initial conditions with dynamic pressure.

Different levels of mesh refinement are considered: coarse, medium and fine meshes contain respectively 40, 80 and 160 cells.

Comparison for case 1

In Figure 3.9, we compare the solutions for the pressure fluctuation. The comparisons are performed at $t = 5.0 \times 10^{-2}$ s with constant piston velocity and therefore the pressure component associated to the piston acceleration (curve "acceleration" remaining equal to zero) does not have any contribution and the total pressure fluctuation for the reference solution, sum of the "acceleration" component p'_{acc} and the "velocity" component p'_{vel} is consequently equal to p'_{vel}, as seen in Figure 3.9 (left). From this figure, we observe that the numerical fully compressible solution computed using HLLC (curve "angle=0") oscillates near the reference solution. The error between the HLLC solution and the exact solution can be considered

as negligible from a practical viewpoint since the pressure fluctuation is very small, of order 1 Pa compared to the homogeneous pressure of order 1.0×10^5 Pa. The use of the AC-LM solver does not help improve the accuracy in this situation as shown in Figure 3.9 (right) where the exact solution is plotted vs the AC-LM solution (curve "angle=0").
In Figure 3.10, we compare the solutions for the velocity at the same instant. We can observe that the solution given by the fully compressible HLLC solver is correct (superimposed with the exact solution) while small errors are recognized when employing the AC-LM solver. This error can be explained by the fact that our physical problem is slightly modified to a higher Mach number regime when reducing the artificial sound speed. The piston Mach number at this instant is $M_{p,AC} = 1/10 = 0.1$.
Figure 3.11 displays a velocity comparison at $t = 0.5$ s where the flow is in its deceleration phase with $V_p = 0$. The exact velocity field u_r is consequently equal to zero (see (3.25)) which is correctly predicted by the HLLC scheme used in the fully compressible solver but is not perfectly satisfied by the AC-LM solution.

Comparison for case 2

We compute next the solutions for the case with small pressure fluctuations present in the initial flowfield. Note that the solutions given by the HLLC solver are qualitatively not very different from the one given in the case 1. This means that the (negligible) pressure fluctuation oscillates about the reference one while the velocity is always correct.
In the following, we focus our comparisons with the exact solution on the AC-LM solver at different instants: $t = 5.0 \times 10^{-2}$ s corresponding the constant phase of the piston velocity and $t = 5.0 \times 10^{-1}$ s corresponding to the deceleration phase. As observed in Figure 3.12 (left), the AC-LM solver has a considerable effect in reducing the oscillations yielding a much better accuracy compared to case 1. However, the pressure solutions during and after the deceleration phase oscillate as observed in Figure 3.12 (right). At $t = 5.0 \times 10^{-1}$ s, we do not have the contribution of the pressure component p'_{vel} as $V_p = 0$.
In Figure 3.13, we compare the velocity solutions at the same instants. We observe that the solution during the zero acceleration phase from the beginning is improved while oscillations are identified during the deceleration phase. The velocity field at 0.5 s is not equal to zero as desired.

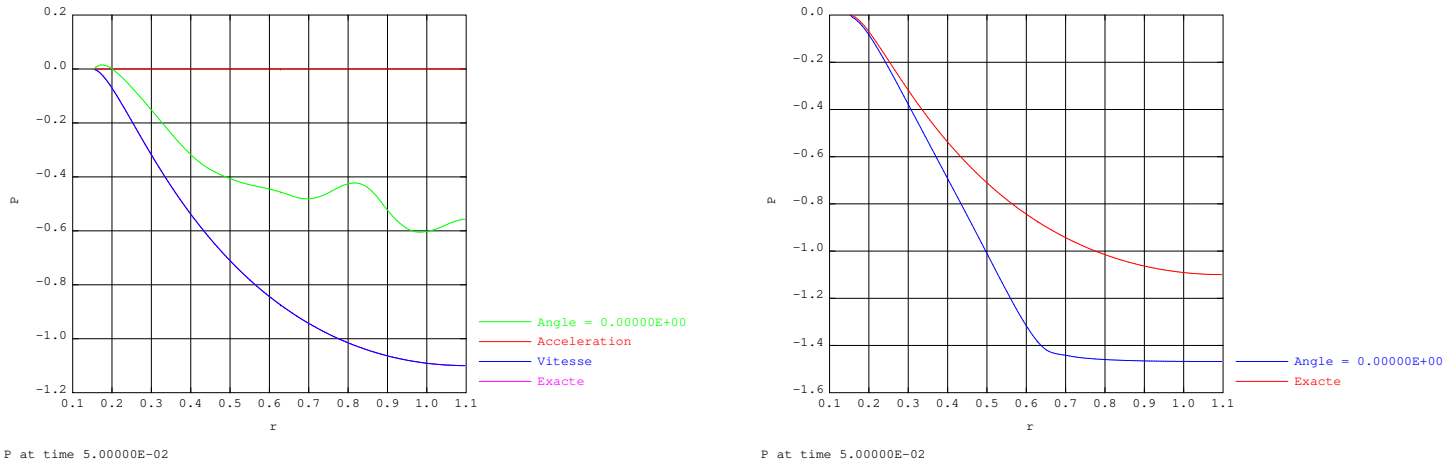

Figure 3.9: 1D axisymmetric cylindrical piston problem with WPIC. Case 1: Pressure solutions $t = 5.0 \times 10^{-2}$ s. HLLC solver on fine QUAD mesh (left), AC-LM solver on fine QUAD mesh (right).

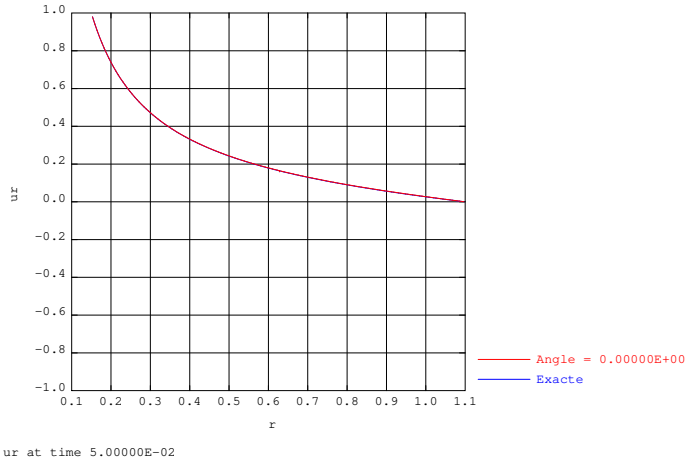

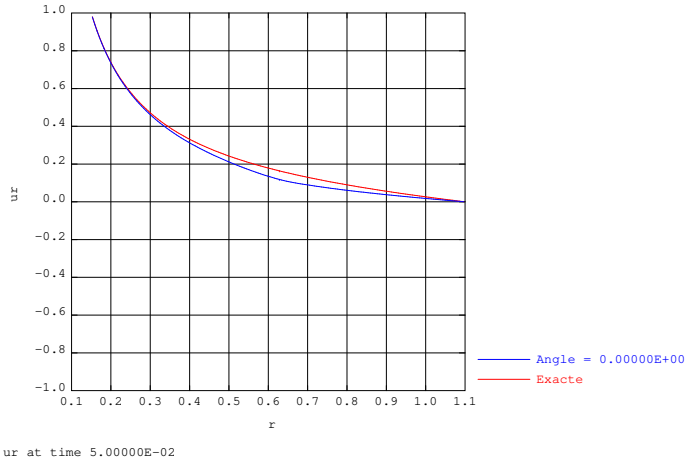

Figure 3.10: 1D axisymmetric cylindrical piston problem with WPIC. Case 1: Velocity solutions $t = 5.0 \times 10^{-2}$ s. HLLC solver on fine QUAD mesh (left), AC-LM solver on fine QUAD mesh (right).

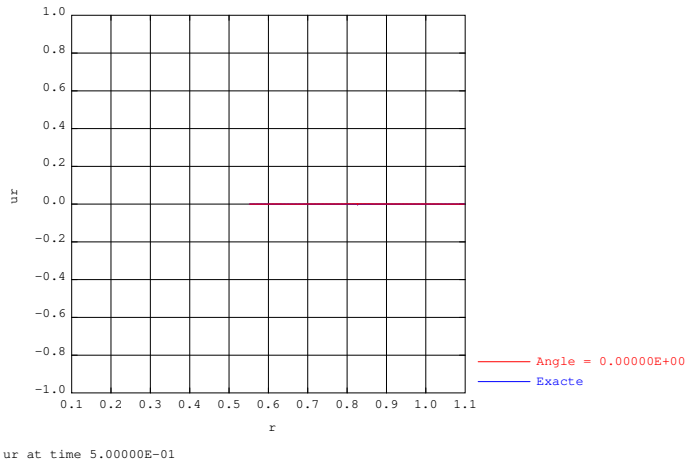

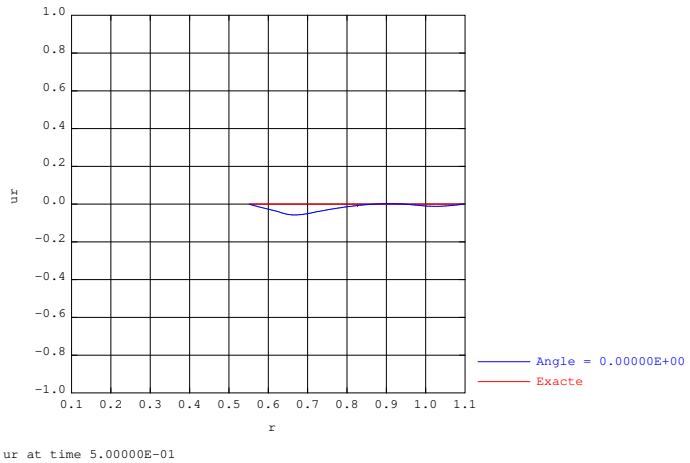

Figure 3.11: 1D axisymmetric cylindrical piston problem with WPIC. Case 1: Velocity solutions at $t = 0.5$ s. HLLC solver on fine QUAD mesh (left), AC-LM solver on fine QUAD mesh (right).

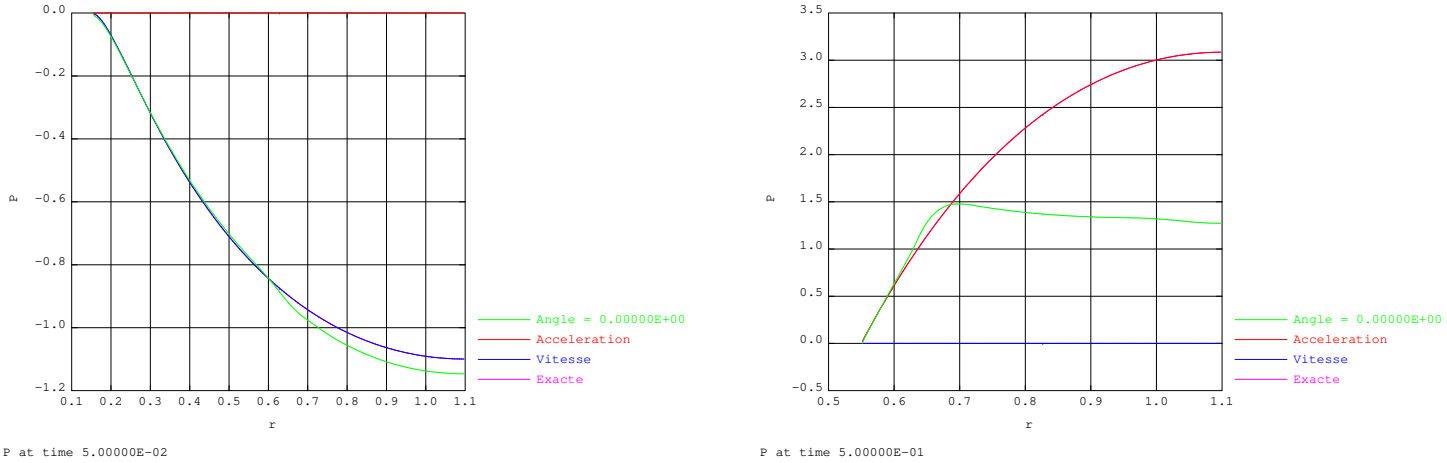

Figure 3.12: 1D axisymmetric cylindrical piston problem with WPIC. Case 2: Pressure solutions at $t = 5.0 \times 10^{-2}$ s (left) and $t = 5.0 \times 10^{-1}$ s (right). AC-LM solver on fine QUAD mesh.

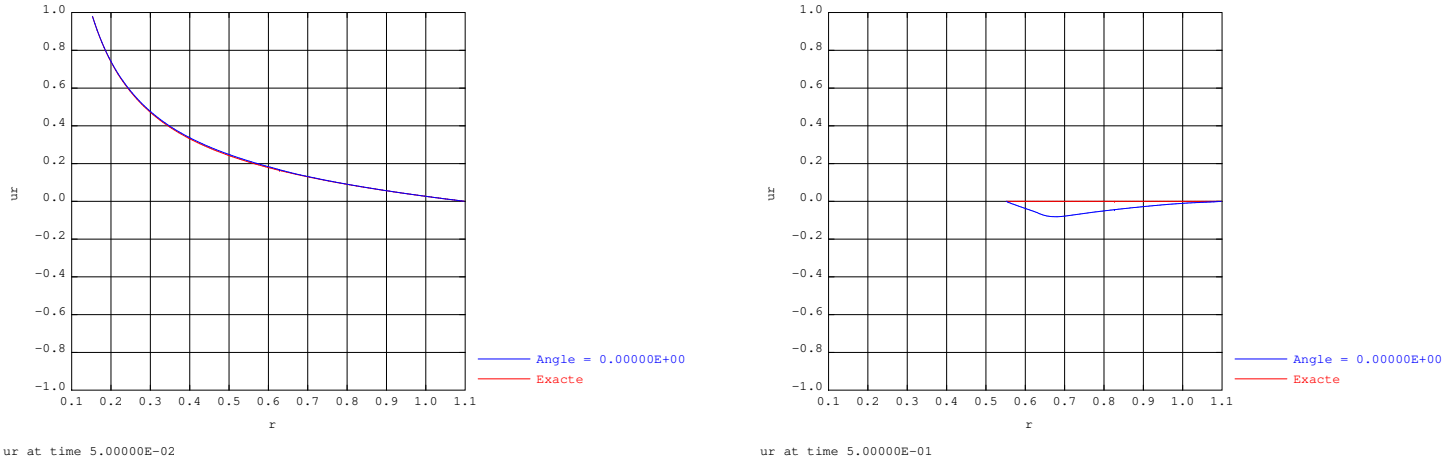

Figure 3.13: 1D axisymmetric cylindrical piston problem with WPIC. Case 2: Velocity solutions at $t = 5.0 \times 10^{-2}$ s (left) and $t = 5.0 \times 10^{-1}$ s (right). AC-LM solver on fine QUAD mesh.

Concluding remarks:

- The HLLC solver always gives good correct solutions for the velocity in all cases.
- The HLLC solver gives oscillating solutions for the pressure in all cases. These errors are negligible if compared with the thermodynamic pressure of order 1.0×10^5 Pa.
- The AC-LM does not give a better pressure solution in case 1 (constant initial pressure field). It does give a better pressure solution in case 2 (with presence of initial pressure fluctuation) only for the first constant phase of the piston velocity. The same conclusions are drawn for the velocity field.
- Mesh refinement does not improve the accuracy of the AC-LM solutions during and after the deceleration phase of the piston.

- Despite presenting small errors in some situations, the AC-LM still gives satisfactory results.

3.5.3 2D axisymmetric cylindrical piston problem with well-prepared initial condition

We perform in this section two-dimensional computations for the piston problem presented in the previous section. The initial conditions are well-prepared as already specified in Tables 3.5 and 3.6 and they are projected on two-dimensional unstructured meshes. The first type of mesh contains mainly quadrangular cells (see Figure 2.3) and the second one has only triangular cells. The numerical methods are similar to the ones presented in section 3.5.2.
Despite having two-dimensional meshes, we however expect the numerical solution demonstrating the one-dimensional behavior as the problem in consideration is axisymmetric.

3.5.3.1 Numerical results

Different mesh refinement levels are considered:

- Coarse and medium QUAD meshes with mainly quadrangular cells (see Figure 3.14 (left)). Each radial direction has 40, 80 cells and iso-spatial step size on each side of the geometry so as not to favor any computational directions.
- Coarse and medium TRI meshes with only triangular cells (see Figure 3.14 (right)). Each radial direction has 40, 80 cells with iso-spatial step size on each side of the geometry with the same purpose.

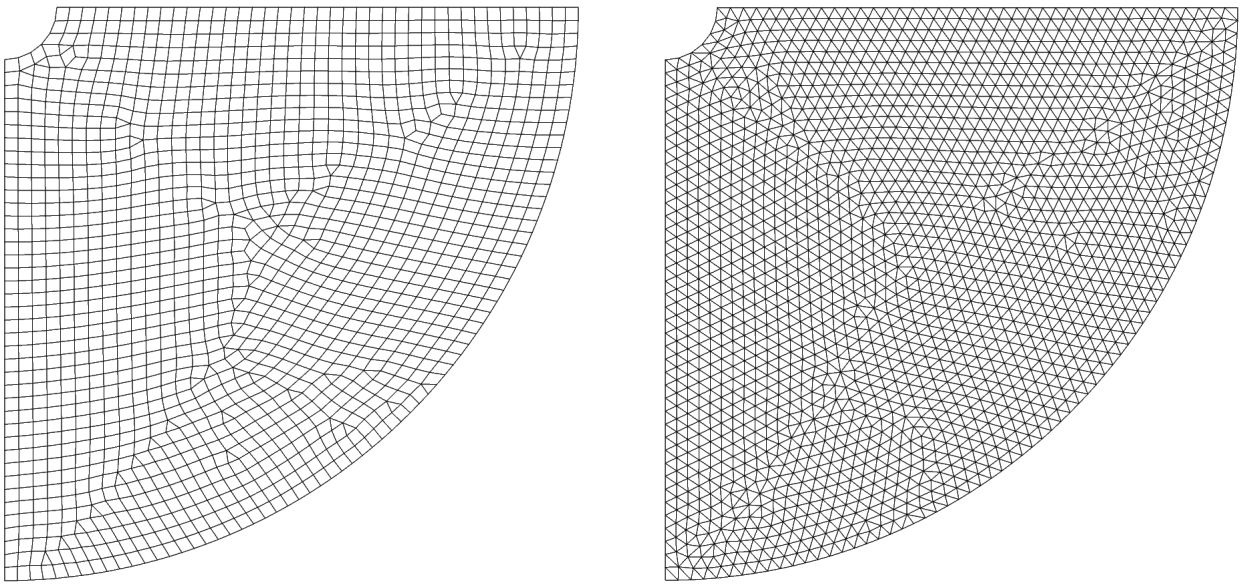

Figure 3.14: 2D axisymmetric cylindrical piston problem with WPIC. Example of coarse meshes: mainly quadrangular cells mesh (left), triangular mesh (right).

Comparison for case 1

In Figure 3.15, we compare the computed velocity field on different meshes using the HLLC (fully compressible solution) and AC-LM solvers at $t = 0.35$ s. It is clearly observed that the low-Mach accuracy problem is present for the computations using the HLLC solver on QUAD meshes. By reducing the physical sound speed and replacing the compression due to physical waves by an isentropic transformation, we recover the satisfactory one-dimensional behavior.

The TRI mesh, when computation is performed with the AC-LM method, also yields a good result. Figure 3.17 displays the AC-LM solutions computed on TRI meshes along three selected lines from the 2D mesh, respectively at angles of -22.5, -45 and -67.5 degrees with respect to the horizontal line. As in the 1D case, small errors are observed during the zero acceleration phase (Figure 3.17, left) and an oscillating behavior is identified during and after the deceleration phase (Figure 3.17, right).
In Figure 3.16, we compare the projected pressure solution at the same instant $t = 3.5 \times 10^{-1}$ s. Similarly to the 1D computations, the pressure solution on QUAD mesh with the HLLC solver oscillates about the reference one. The use of AC-LM solver does not help improve the accuracy on both QUAD and TRI meshes as observed in the 1D case.

Comparison for case 2

In Figures 3.18 - 3.20, we compare the solutions with pressure fluctuations present in the initial flowfield. In Figure 3.18, the computed pressures with the AC-LM solver on QUAD mesh are shown at two instants corresponding to the zero acceleration phase $t = 3.5 \times 10^{-1}$ s and the deceleration phase $t = 5.0 \times 10^{-1}$ s. Similarly to the 1D case, the pressure solution has a better accuracy compared to case 1 at the beginning of the evolution but presents an oscillating behavior about the reference one when the piston begins decelerating. The computed results on the TRI mesh shown in Figure 3.20 (left) have qualitatively the same behavior. Once again, we emphasize that the errors in the pressure fluctuation can be considered as negligible when compared to the thermodynamic pressure of order 1.0×10^5 Pa.
Figure 3.19 display the velocities computed with the AC-LM method on QUAD mesh at the same two instants. The velocity is correctly computed at $t = 3.5 \times 10^{-1}$ s but presents small errors at $t = 5.0 \times 10^{-1}$ s, similarly to the 1D situation. The computed results on TRI mesh shown in Figure 3.20 (right) display a similar behavior.

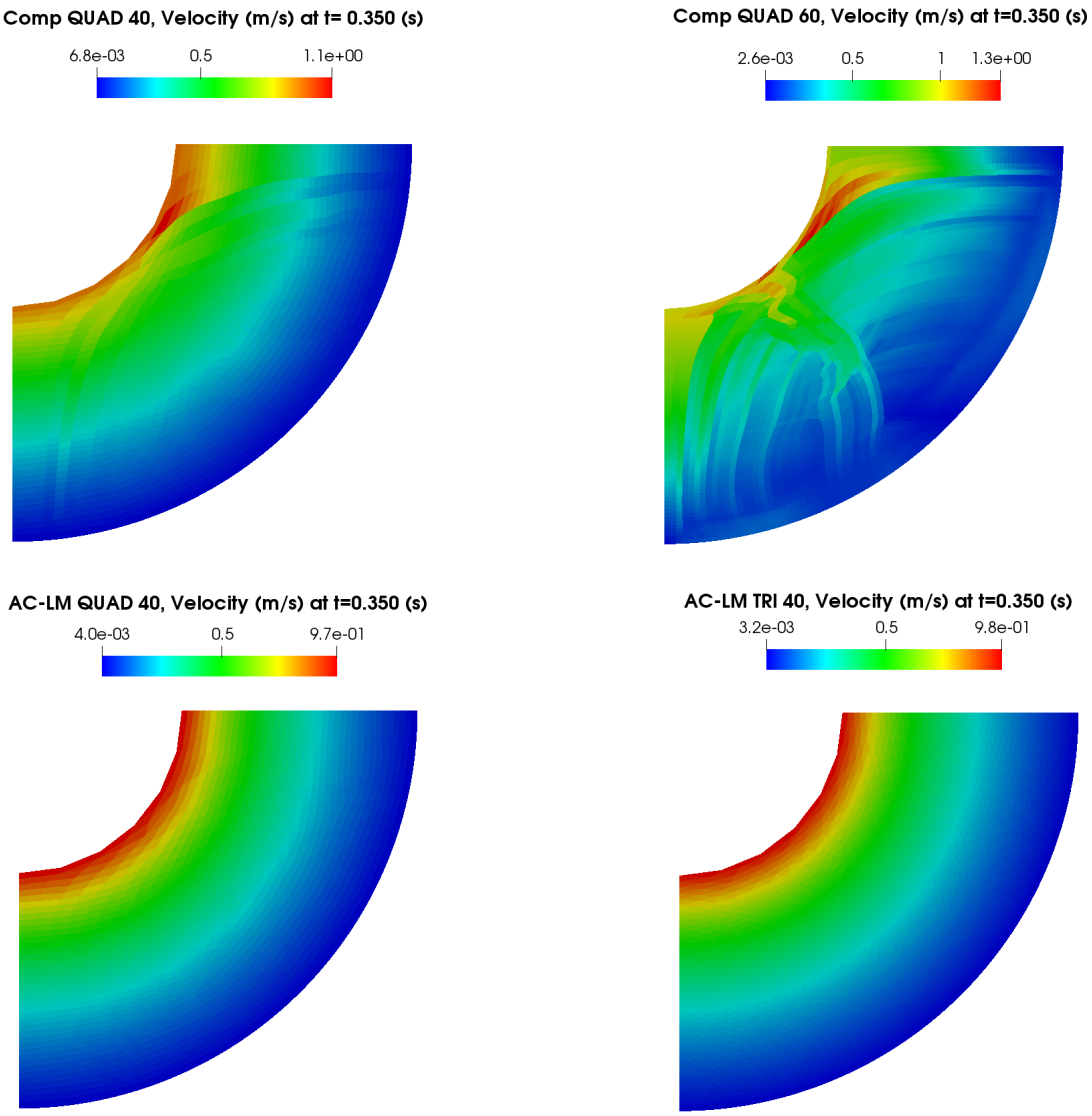

Figure 3.15: 2D axisymmetric cylindrical piston problem with WPIC. Case 1: Velocity solutions at $t = 0.35$ s, $CFL = 0.5$. HLLC solver on coarse QUAD mesh (top, left), HLLC solver on medium QUAD mesh (top, right), AC-LM solver on coarse QUAD mesh (bottom, left), AC-LM solver on coarse TRI mesh (bottom, right).

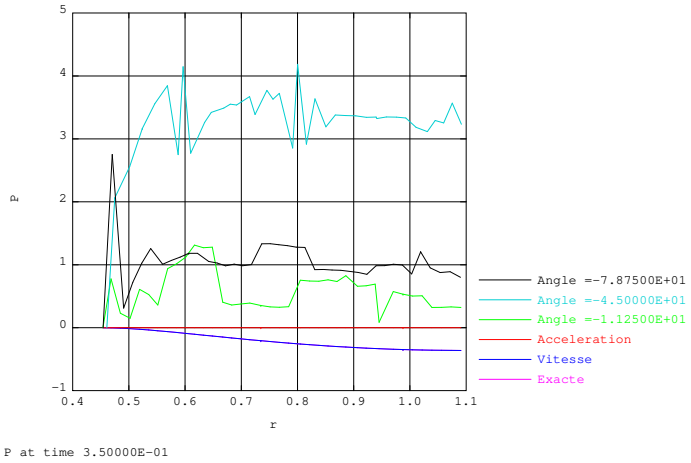

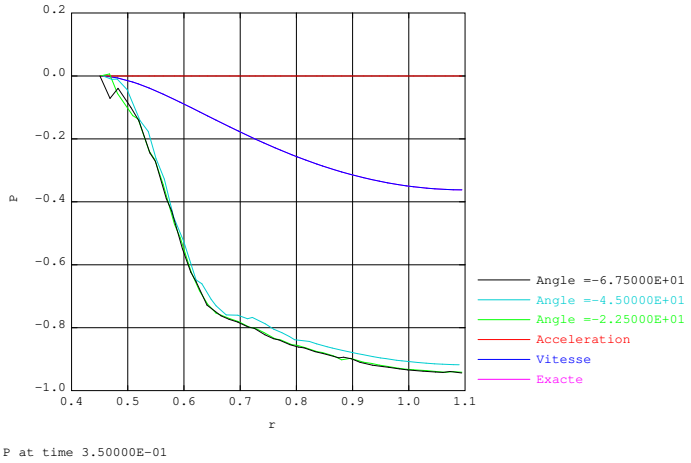

Figure 3.16: 2D axisymmetric cylindrical piston problem with WPIC. Case 1: Projected pressure solutions. HLLC solver on coarse QUAD mesh (left), AC-LM solver on coarse TRI mesh (right).

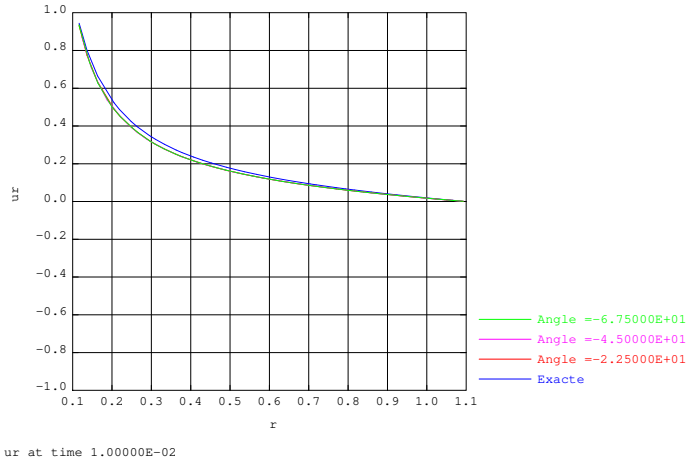

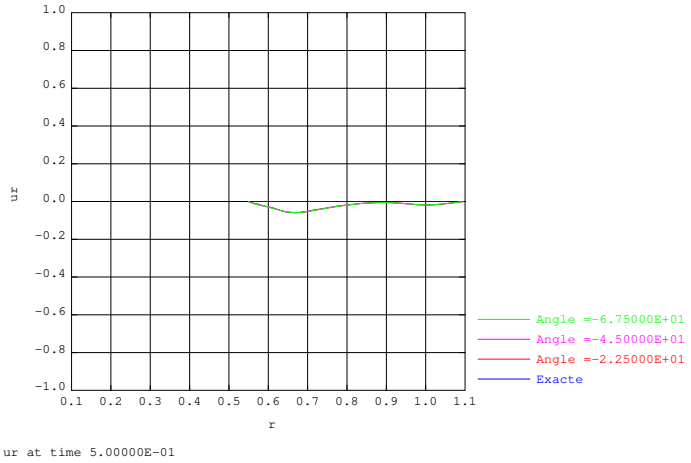

Figure 3.17: 2D axisymmetric cylindrical piston problem with WPIC. Case 1: Projected velocity solutions. AC-LM solver on coarse TRI mesh at $t = 1.0 \times 10^{-2}$ s (left), AC-LM solver on coarse TRI mesh at $t = 5.0 \times 10^{-1}$ s (right).

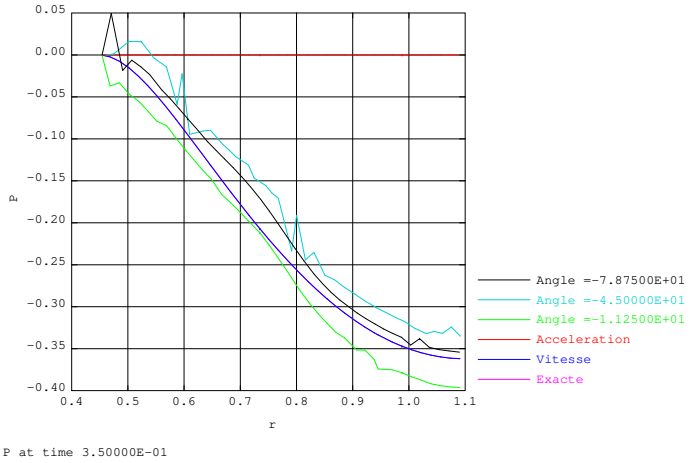

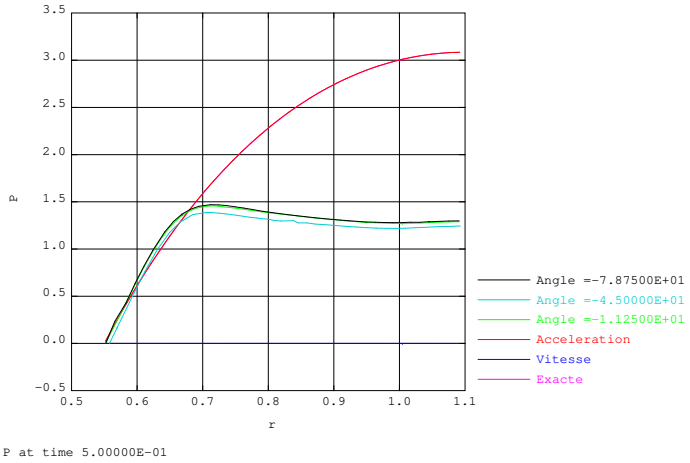

Figure 3.18: 2D axisymmetric cylindrical piston problem with WPIC. Case 2: Projected pressure solutions at $t = 3.5 \times 10^{-1}$ s (left) and $t = 5.0 \times 10^{-1}$ s (right). AC-LM solver on coarse QUAD mesh.

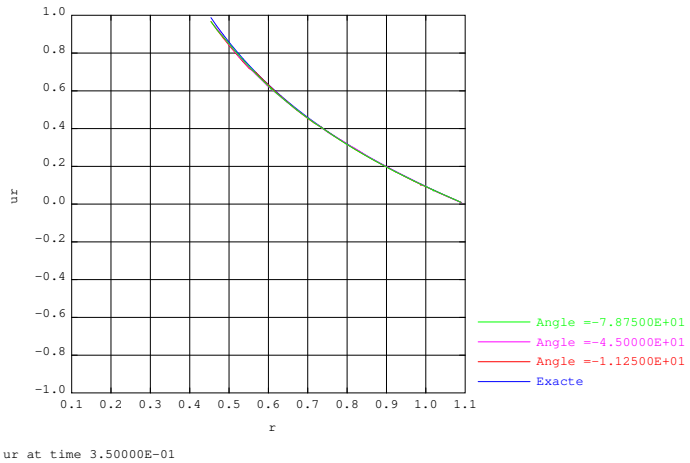

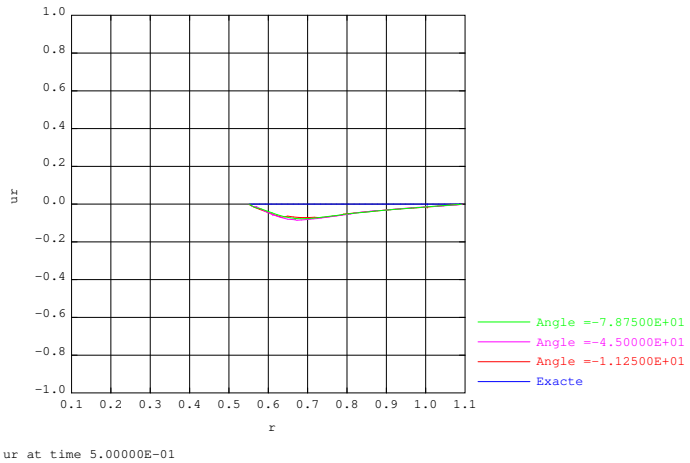

Figure 3.19: 2D axisymmetric cylindrical piston problem with WPIC. Case 2: Projected velocity solutions at $t = 3.5 \times 10^{-1}$ s (left) and $t = 5.0 \times 10^{-1}$ s (right). AC-LM solver on coarse QUAD mesh.

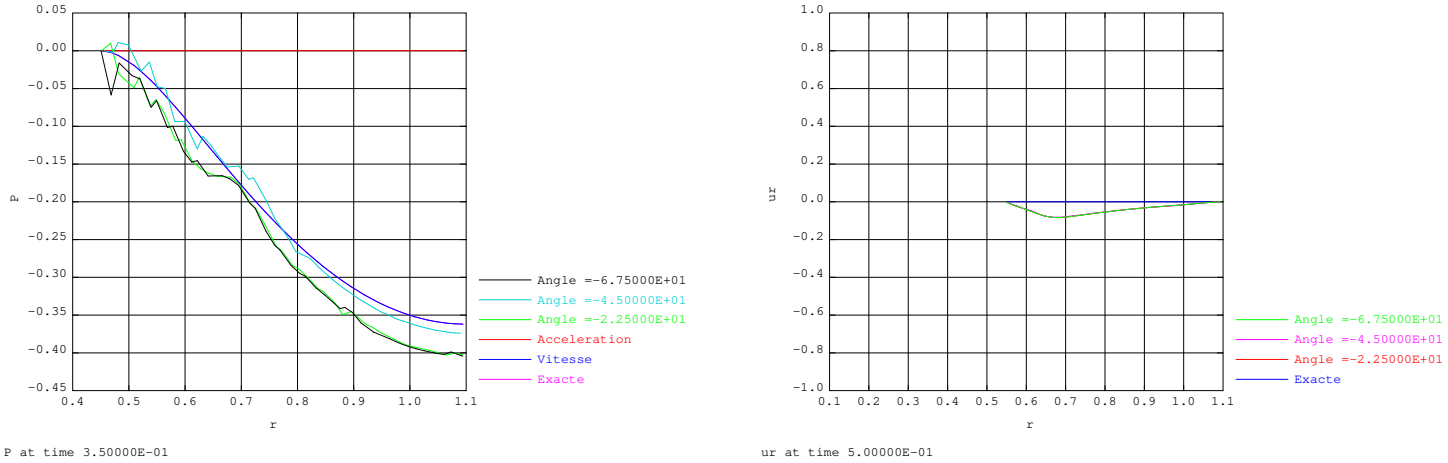

Figure 3.20: 2D axisymmetric cylindrical piston problem with WPIC. Case 2: Projected pressure solutions at $t = 3.5 \times 10^{-1}$ s (left) and velocity solutions at $t = 5.0 \times 10^{-1}$ s (right). AC-LM solver on coarse TRI mesh.

Concluding remarks:

- The HLLC solver exhibits the low-Mach accuracy problem on QUAD meshes as expected.
- The AC-LM solver with QUAD mesh does not yield a better pressure solution in case 1 (constant initial pressure field). It does however provide a better pressure solution in case 2 (with presence of initial pressure fluctuation) only for the first constant phase of the piston velocity. The same conclusions are drawn for the velocity field.
- The AC-LM solver with TRI mesh does not reduce the errors observed during and after the deceleration phase of the piston.
- Mesh refinement does not improve the accuracy of the AC-LM solutions during and after the deceleration phase and of the piston.
- Despite presenting small errors in some situations, the AC-LM still gives satisfactory results.

3.5.4 Computational cost

Table 3.7 compares the computational cost between the HLLC method with the AC-LM for the 1D axisymmetric cylindrical piston problem discussed in section 3.5.2. It can be seen from the table the great advantage of the new method from an efficiency viewpoint with a reduction of (almost) 25 times the CPU time consumption for a computation on our fine mesh. This efficiency enhancement is related to the choice of the stability time step which depends on the artificial sound speed c_{AC} for the new method in stead of the physical sound speed c for the standard compressible solvers.

	HLLC	AC-LM
	TCPU (s)	TCPU (s)
Coarse	23.4	1.4
Medium	91.6	4
Fine	347.5	13.5

Table 3.7: 1D axisymmetric cylindrical piston problem with WPIC. Computational cost: HLLC vs AC-LM solvers for case 1.

Conclusion

In this chapter, we have presented in section 3.1 some classical AC methods to enhance the numerical efficiency of low-Mach flow computations and observed their drawbacks via the 1D planar piston problem in section 3.2. As a result, a new method for computing low-Mach single-phase flows has been introduced in sections 3.3 and 3.4 to circumvent the difficulties by combining the AC and the asymptotic approaches. This new method has shown its great benefits in:

- Accelerating the computations of the 1D planar piston problem with presence of acoustic waves (or with IC which is not well-prepared) in section 3.5.1. It gives not only a good density solution (which is wrongly computed using the classical AC methods) but also yields the expected solution for the pressure field.
- Accelerating the computations of the 1D/2D cylindrical piston problems using the well-prepared initial condition defined in sections 3.5.2 and 3.5.3. The accuracy, which is lost in using standard compressible solvers, is kept thanks to the double effect of the new scheme: the amplitude of the wrongly computed pressure fluctuation analyzed in chapter 1 is greatly reduced via the efficiency enhancement mechanism in part I and the expected isentropic transformation is recovered in part II.

However, the new method presented in this chapter is limited to the single-phase case. In the following chapters, we will extend the current method to two-phase low-Mach problems.

4

DEM: Discrete Equation Method - application to the 1D bubble expansion problem

Contents

Introduction

In chapter 3, we have shown that the asymptotic model is a good approximation for single-phase flow computations in the low-Mach number regime. A new method has also been proposed by combining this model with the AC approach in order to reduce the computational cost.
Since our final purpose is to compute efficiently two-phase problems involving bubble expansion phenomena (e.g the MARA problem), we would like to extend the aforementioned strategy to the computation of low-Mach two-phase flow problems. However, it is important to check first, before making further developments, whether the asymptotic model remains a good approximation for two-phase flow computations

in the low-Mach number regime.
Consequently, we investigate in section 4.3 the behavior of a so-called bubble model via a simple 1D (two-phase) bubble expansion problem. The bubble model is in fact the asymptotic model with further approximations for water as an incompressible material (section 4.3.2). The solutions given by this model are compared with the ones given by the two-phase fully compressible seven-equation DEM model (Discrete Equation Method) [Abgrall and Saurel, 2003]. The DEM approach, available in the Europlexus code, is indeed our reference method for compressible two-phase flows. We hope to improve the efficiency of low-Mach two-phase flows by using a two-phase version of the AC-LM model, while preserving the accuracy. A quick review of the DEM method as well as its physical model is presented for both the Eulerian and the ALE case in sections 4.1, 4.2.

4.1 Physical model for two-phase flow problems

4.1.1 Conservation equations

The two-fluid model in the original DEM method considers each phase separately and thus an inviscid two-phase flow is governed by two sets of Euler equations as presented in section 1.1.1. In EUROPLEXUS, the DEM method has been augmented by adding extra transport equations for the mass fraction Y_k of species k. In conservative form, the system can be written as:

$$\begin{aligned}
\frac{\partial \rho_k}{\partial t} &+ \nabla \cdot (\rho_k \mathbf{v}_k) &&= 0 \\
\frac{\partial (\rho_k \mathbf{v}_k)}{\partial t} &+ \nabla \cdot (\rho_k \mathbf{v}_k \otimes \mathbf{v}_k + p_k \mathcal{I}) &&= 0 \\
\frac{\partial (\rho_k e_k^t)}{\partial t} &+ \nabla \cdot ((\rho_k e_k^t + p_k)\mathbf{v}_k) &&= 0 \\
\frac{\partial (\rho_k \mathbf{Y}_k)}{\partial t} &+ \nabla \cdot (\rho_k \mathbf{Y}_k \mathbf{v}_k) &&= 0
\end{aligned} \tag{4.1}$$

with the index k denoting the phase indicator. For a system involving two phases (typically liquid and gas for the applications of interest in this work), $k = 1$ would denote for instance the liquid properties while $k = 2$ would denote the gas properties.
System (4.1) can be recast in the following compact form:

$$\frac{\partial (\alpha_k \mathcal{U}_k)}{\partial t} + \nabla \cdot \mathbf{f}_k = 0 \tag{4.2}$$

with:

$$\mathcal{U}_k = \begin{pmatrix} \rho_k \\ \rho \mathbf{v}_k \\ \rho_k e_k^t \\ \rho_k \mathbf{Y}_k \end{pmatrix}, \quad \mathbf{f}_k = \begin{pmatrix} \rho_k \mathbf{v}_k \\ \rho_k \mathbf{v}_k \otimes \mathbf{v}_k + p_k \mathcal{I} \\ (\rho_k e_k^t + p_k)\mathbf{v}_k \\ \rho_k \mathbf{Y}_k \mathbf{v}_k \end{pmatrix}$$

The above system is closed by the so-called equation of state (EOS). As indicated in section 1.1.3, the SG-EOS is considered in this work since it is valid for both liquid and gas phases. The SG-EOS for each phase reads:

$$p_k(\rho_k, e_k) = (\gamma_k - 1)\rho_k e_k - \gamma_k P_{\infty,k} \tag{4.3}$$

with parameters γ_k and $P_{\infty,k}$ different for each phase.

4.1.2 Phase characteristic function X_k and volume fraction α_k

The DEM method requires defining the phase characteristic function and the corresponding volume fraction. The so-called characteristic function is defined as [Drew and Passman, 1999]:

$$X_k\left(\mathbf{x}, t, \sum\nolimits_k\right) = \begin{cases} 1, & \text{if } \mathbf{x} \text{ lies in phase } \sum_k \text{ at } t \\ 0, & \text{otherwise} \end{cases} \tag{4.4}$$

The function X_k satisfies the topological equation describing the evolution of the phase interface:

$$\frac{\partial X_k}{\partial t} + \sigma \cdot \nabla X_k = 0 \tag{4.5}$$

In (4.5), σ represents the velocity of the interface between two phases. If we look at a point that is not on the interface, by definition $X_k = 0$ or $X_k = 1$ and the L.H.S of (4.5) vanishes. If we look for a point on the interface of two phases, it moves with the interface velocity σ.
[Drew and Passman, 1999] considers the average procedure $< \cdot >$ applied to the topological equation (4.5) which gives (see [Tang, 2012] and references therein):

$$\frac{\partial \alpha_k}{\partial t} + < \sigma \cdot \nabla X_k >= 0$$

Following [Perrier, 2007], the term $< \sigma \cdot \nabla X_k >$ can be expressed as the sum of the average term $\mathbf{v}_I \cdot \nabla \alpha_k$ and a fluctuation term which will be neglected in this work:

$$< \sigma \cdot \nabla X_k > \approx \mathbf{v}_I \cdot \nabla \alpha_k \tag{4.6}$$

Finally, the topological equation (4.5) thus becomes the averaged topological equation (4.7):

$$\frac{\partial \alpha_k}{\partial t} + \mathbf{v}_I \cdot \nabla \alpha_k = 0 \tag{4.7}$$

4.1.3 Balance equations of two-fluid model for interfaces

The balance equations for each phase can be derived by coupling the system (4.2) with the averaged topological equation (4.5) and yields (see e.g [Tang, 2012] and references therein for more details):

$$\frac{\partial (\alpha_k \mathcal{U}_k)}{\partial t} + \nabla \cdot (\alpha_k \mathbf{f}_k) = \mathbf{f}_{k,I}^{Lag} \cdot \nabla \alpha_k \tag{4.8}$$

where the term $\mathbf{f}_{k,I}^{Lag} = \mathbf{f}_{k,I} - \mathbf{v}_I \mathcal{U}_k$ is called the Lagrangian flux and should only be defined on the interface since it is the only location where the gradient of the volume fraction does not vanish (see [Abgrall and Saurel, 2003]):

$$\mathbf{f}_{k,I}^{Lag} = \begin{pmatrix} \rho_{k,I}(\mathbf{v}_{k,I} - \mathbf{v}_I) \\ \rho_k \mathbf{v}_{k,I}(\mathbf{v}_{k,I} - \mathbf{v}_I) + p_{k,I} \\ \rho_k e_{k,I}^t (\mathbf{v}_{k,I} - \mathbf{v}_I) + p_{k,I} \mathbf{v}_{k,I} \\ \rho_{k,I} \mathbf{Y}_{k,I} (\mathbf{v}_{k,I} - \mathbf{v}_I) \end{pmatrix} \tag{4.9}$$

In case of impermeable interfaces (without chemical reaction or phase change), we obtain $\mathbf{v}_{k,I} = \mathbf{v}_I$, $p_{k,I} = p_I$. The Lagrangian flux (4.9) becomes (see also [Tang, 2012]):

$$\mathbf{f}_{k,I}^{Lag} = \begin{pmatrix} 0 \\ p_I \mathcal{I} \\ p_I \mathbf{v}_I \\ 0 \end{pmatrix} \tag{4.10}$$

where p_I and $\mathbf{v}_I$ are the average interface pressure and velocity respectively.
The system (4.8) together with the averaged topological equation (4.7) form the physical model where each phase has its own pressure and velocity.
In conclusion, the two-fluid model to be solved for impermeable interfaces reads:

$$\begin{array}{lcll}
\dfrac{\partial \alpha_k}{\partial t} & + & \mathbf{v}_I \cdot \nabla \alpha_k & = 0 \\
\dfrac{\partial (\alpha_k \rho_k)}{\partial t} & + & \nabla \cdot (\alpha_k \rho_k \mathbf{v}_k) & = 0 \\
\dfrac{\partial (\alpha_k \rho_k \mathbf{v}_k)}{\partial t} & + & \nabla \cdot (\alpha_k (\rho_k \mathbf{v}_k \otimes \mathbf{v}_k + p_k \mathcal{I})) & = p_I \nabla \alpha_k \\
\dfrac{\partial (\alpha_k \rho_k e_k^t)}{\partial t} & + & \nabla \cdot (\alpha_k (\rho_k e_k^t + p_k) \mathbf{v}_k) & = p_I \mathbf{v}_I \cdot \nabla \alpha_k \\
\dfrac{\partial (\alpha_k \rho_k \mathbf{Y}_k)}{\partial t} & + & \nabla \cdot (\alpha_k \rho_k \mathbf{Y}_k \mathbf{v}_k) & = 0 \\
p_k(\rho_k, e_k) & = & (\gamma_k - 1)\rho_k e_k - \gamma_k P_{\infty,k} &
\end{array} \tag{4.11}$$

This model needs to be closed and therefore requires, in addition to the SG-EOS (4.3) for each phase, to determine p_I and $\mathbf{v}_I$ in function of the other variables of the model. The determination of these quantities in the non-reacting case can be done by considering the Riemann problem involving two different phases. It is well known that the solution of the Riemann problem for the Euler system consists of three waves: shock or rarefaction waves of speed $u \pm c$ depending on the initial conditions separated by a contact wave. The corresponding contact surface is the interface between two fluids. Thus, the interfacial pressure and velocity are naturally defined as the intermediate solution p^*_{2P} and u^*_{2P} given by solving the two-phase RP (c.f. section 4.2.2). In this way, one can profit from the numerical data and avoid the difficult task of modeling for the interfacial pressure and velocity [Abgrall and Saurel, 2003, Saurel and Abgrall, 1999].

4.2 Overview of the DEM method

4.2.1 Partition of intercell boundaries

As will be seen further in this section, the DEM method is based on solving many Riemann Problems (RP) at the intercell boundaries involving the same or different phases. As a result, it is necessary to define the so-called partition of intercell boundaries to indicate the RP in consideration. Since the presence of each phase inside a control volume is described by its volume fraction, the concept of the partition of intercell boundaries is based on this quantity and is expressed graphically using Figure 4.1.
In general, we distinguish three partitions at the intercell:

- $S^{(11)}_{i-1/2}$: the partition involves the phase Σ_1 to the left and the phase Σ_1 to the right of the intercell:

$$S^{(11)}_{i-1/2} = \min(\alpha_{1,i-1}, \alpha_{1,i}) = 1 - \max(\alpha_{2,i-1}, \alpha_{2,i})$$

- $S^{(22)}_{i-1/2}$: the partition involves the phase Σ_2 to the left and the phase Σ_2 to the right of the intercell:

$$S^{(22)}_{i-1/2} = 1 - \max(\alpha_{1,i-1}, \alpha_{1,i}) = \min(\alpha_{2,i-1}, \alpha_{2,i})$$

- $S^{(12)}_{i-1/2}$ (or $S^{(21)}_{i-1/2}$): the partition involves the phase Σ_1 (or phase Σ_2) to the left and the phase Σ_2 (or phase Σ_1) to the right of the intercell:

$$S^{(12)}_{i-1/2} = \max(0, \alpha_{1,i-1} - \alpha_{1,i}) = \max(0, \alpha_{2,i} - \alpha_{2,i-1})$$

$$S_{i-1/2}^{(21)} = \max(0, \alpha_{1,i} - \alpha_{1,i-1}) = \max(0, \alpha_{2,i-1} - \alpha_{2,i})$$

In the particular case considered in Figure 4.1, we obtain:

$$\begin{aligned} S_{i-1/2}^{(11)} &= \alpha_{1,i} \\ S_{i-1/2}^{(22)} &= 1 - \alpha_{1,i-1} \\ S_{i-1/2}^{(12)} &= \alpha_{1,i-1} - \alpha_{1,i} \\ S_{i-1/2}^{(21)} &= 0 \end{aligned}$$

The sum of the partitions is equal to unity:

$$S_{i-1/2}^{(11)} + S_{i-1/2}^{(22)} + S_{i-1/2}^{(12)} + S_{i-1/2}^{(21)} = 1$$

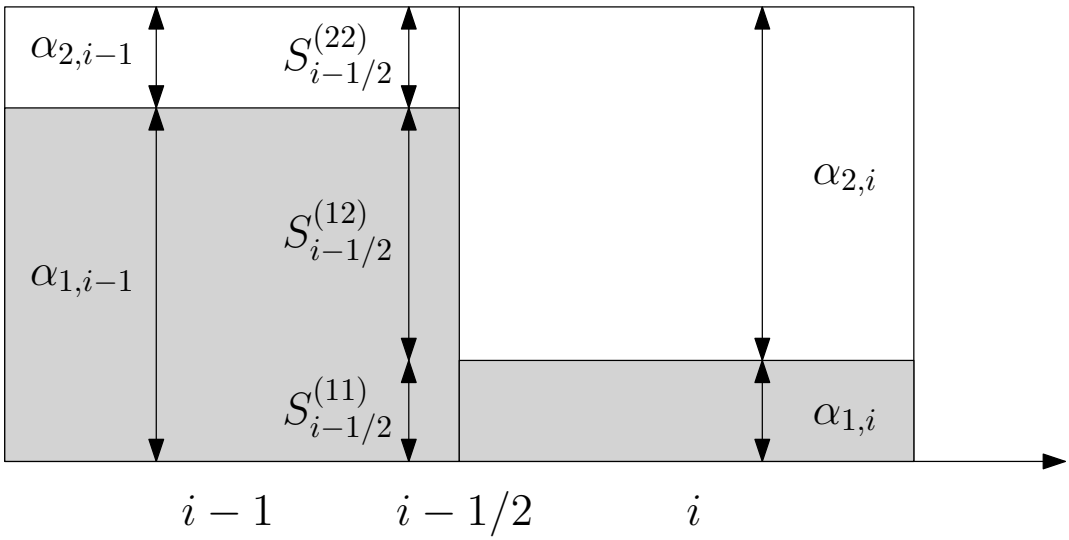

Figure 4.1: Partition of the intercell boundaries.

4.2.2 Local Riemann problem for two-fluid system

At each intercell, the DEM method considers three local RPs corresponding to three intercell partitions presented in section 4.2.1. For the particular case in Figure 4.2, the three RPs in consideration at the intercell $i-1/2$ with $\mathbf{U}_{k,i-1}^n, \mathbf{U}_{k,i}^n$ as the cell average of conservative variables are:

- RP11($\mathbf{U}_{1,i-1}^n$, $\mathbf{U}_{1,i}^n$): the local RP corresponds to the intercell partition $S_{i-1/2}^{(11)}$ involving the phase Σ_1 to the left and the phase Σ_1 to the right of the intercell.
- RP22($\mathbf{U}_{2,i-1}^n$, $\mathbf{U}_{2,i}^n$): the local RP corresponds to the intercell partition $S_{i-1/2}^{(22)}$ involving the phase Σ_2 to the left and the phase Σ_2 to the right of the intercell.
- RP12($\mathbf{U}_{1,i-1}^n$, $\mathbf{U}_{2,i}^n$): the local RP corresponds to the intercell partition $S_{i-1/2}^{(12)}$ involving the phase Σ_1 to the left and the phase Σ_1 to the right of the intercell.
- RP21 is not taken into account since the corresponding intercell partition $S_{i-1/2}^{(21)} = 0$.

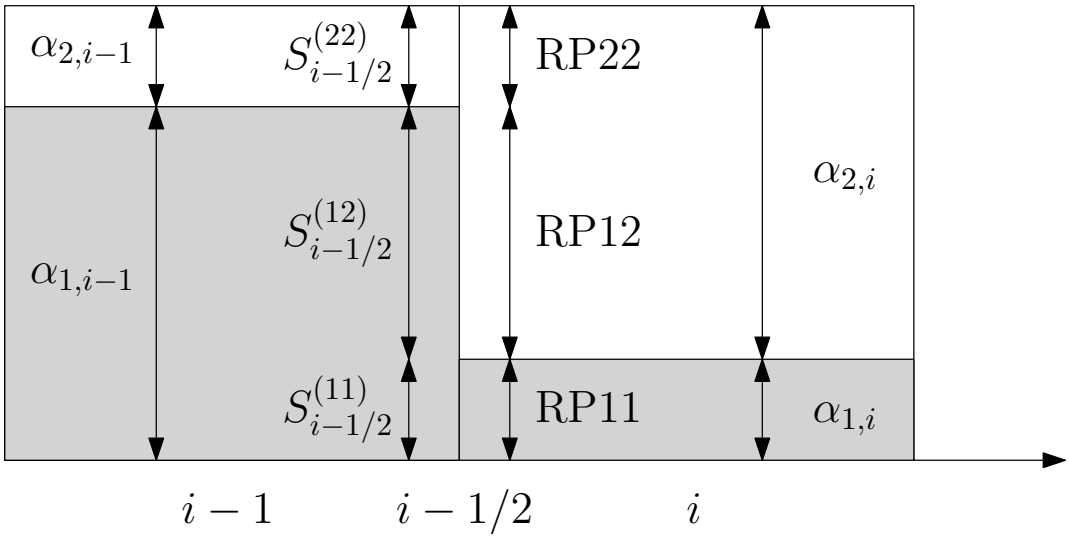

Figure 4.2: The local RPs corresponding to the partitions at the intercell.

4.2.3 Eulerian case: general formulation

In this section, we briefly derive the general formulation of the numerical scheme. For the sake of simplicity, let us recast system (4.8) into the following one-dimensional form:

$$\frac{\partial(\alpha_k \mathcal{U}_k)}{\partial t} + \frac{\partial(\alpha_k \mathbf{f}_k)}{\partial x} = \mathbf{f}_k^{Lag} \frac{\partial \alpha_k}{\partial x} \tag{4.12}$$

According to [Drew and Passman, 1999], the non-conservative term $\mathbf{f}_k^{Lag} \frac{\partial \alpha_k}{\partial x}$ can be rewritten as:

$$\mathbf{f}_k^{Lag} \frac{\partial \alpha_k}{\partial x} = \frac{\partial(\alpha_k \mathbf{f}_k^{Lag})}{\partial x} - \alpha_k \frac{\partial \mathbf{f}_k^{Lag}}{\partial x}$$

The system (4.12) can therefore be rewritten in the form:

$$\frac{\partial(\alpha_k \mathcal{U}_k)}{\partial t} + \frac{\partial(\alpha_k \mathbf{f}_k)}{\partial x} = \frac{\partial(\alpha_k \mathbf{f}_k^{Lag})}{\partial x} - \alpha_k \frac{\partial \mathbf{f}_k^{Lag}}{\partial x} \tag{4.13}$$

By integrating (4.13) over cell $C_i = [x_{i-1/2}, x_{i+1/2}]$ and time $[t^n, t^{n+1}]$, we obtain:

$$\begin{aligned} &\int_{t^n}^{t^{n+1}} \int_{x_{i-1/2}}^{x_{i+1/2}} \frac{\partial(\alpha_k \mathcal{U}_k)}{\partial t} dx dt + \int_{t^n}^{t^{n+1}} \int_{x_{i-1/2}}^{x_{i+1/2}} \frac{\partial(\alpha_k \mathbf{f}_k)}{\partial x} dx dt \\ &= \int_{t^n}^{t^{n+1}} \int_{x_{i-1/2}}^{x_{i+1/2}} \frac{\partial(\alpha_k \mathbf{f}_k^{Lag})}{\partial x} dx dt - \int_{t^n}^{t^{n+1}} \int_{x_{i-1/2}}^{x_{i+1/2}} \alpha_k \frac{\partial \mathbf{f}_k^{Lag}}{\partial x} dx dt \end{aligned} \tag{4.14}$$

The conservative terms in (4.14) can be discretized using the standard finite volume method:

$$\int_{t^n}^{t^{n+1}} \int_{x_{i-1/2}}^{x_{i+1/2}} \frac{\partial(\alpha_k \mathbf{f}_k)}{\partial x} dx dt = (\alpha_{k,i+1/2} \mathbf{F}_{k,i+1/2} - \alpha_{k,i-1/2} \mathbf{F}_{k,i-1/2}) \Delta t$$

$$\int_{t^n}^{t^{n+1}} \int_{x_{i-1/2}}^{x_{i+1/2}} \frac{\partial(\alpha_k \mathbf{f}_k^{Lag})}{\partial x} dx dt = (\alpha_{k,i+1/2} \mathbf{F}_{k,i+1/2}^{Lag} - \alpha_{k,i-1/2} \mathbf{F}_{k,i-1/2}^{Lag}) \Delta t$$

and the non-conservative term can be discretized as follows:

$$\int_{t^n}^{t^{n+1}} \int_{x_{i-1/2}}^{x_{i+1/2}} \alpha_k \frac{\partial \mathbf{f}_k^{Lag}}{\partial x} dx dt = \alpha_{k,i}^n (\mathbf{F}_{k,i+1/2}^{Lag} - \mathbf{F}_{k,i-1/2}^{Lag}) \Delta t$$

where $\mathbf{F}$ is the numerical flux approximating the physical one.
Concerning the time-derivative term, we can simply employ the first order forward Euler method:

$$\int_{t^n}^{t^{n+1}} \int_{x_{i-1/2}}^{x_{i+1/2}} \frac{\partial (\alpha_k \mathcal{U}_k)}{\partial t} dx dt = \Delta x \left[(\alpha \mathbf{U})_{k,i}^{n+1} - (\alpha \mathbf{U})_{k,i}^n \right]$$

We thus obtain the first order DEM scheme (4.15) for the two-fluid model:

$$\begin{aligned} &\frac{(\alpha \mathbf{U})_{k,i}^{n+1} - (\alpha \mathbf{U})_{k,i}^n}{\Delta t} + \frac{(\alpha \mathbf{F})_{k,i+1/2} - (\alpha \mathbf{F})_{k,i-1/2}}{\Delta x} \\ &= \frac{\mathbf{F}_{k,i+1/2}^{Lag} (\alpha_{k,i+1/2} - \alpha_{k,i}^n) - \mathbf{F}_{k,i-1/2}^{Lag} (\alpha_{k,i-1/2} - \alpha_{k,i}^n)}{\Delta x} \end{aligned} \tag{4.15}$$

From (4.15), we observe that the computation of $\mathbf{U}_{k,i}^{n+1}$ requires:

- $\alpha_{k,i}^{n+1}$: volume fraction at time $t = t^{n+1}$.
- $\alpha_{k,i\pm1/2}$: volume fraction at the intercell associated to the Lagrangian fluxes.
- $(\alpha \mathbf{F})_{k,i+1/2}$, $(\alpha \mathbf{F})_{k,i-1/2}$: numerical conservative fluxes at the intercells.
- $\mathbf{F}_{k,i+1/2}^{Lag}$, $\mathbf{F}_{k,i-1/2}^{Lag}$: numerical Lagrangian fluxes.

In section 4.2.4, we will present the method to compute $\alpha_{k,i}^{n+1}$. Concerning the numerical fluxes $\mathbf{F}$ at the intercell, they can be computed considering a RP problem solved with the exact or any alternative approximate Riemann solvers. In section 4.2.5, we provide more details on the contribution of different numerical fluxes corresponding to different RPs.

4.2.4 Eulerian case: volume fraction

The update of the volume fraction in each cell can be done by discretizing the averaged topological equation (4.7). In 1D, it can be written as:

$$\frac{\partial \alpha_k}{\partial t} + u_I \frac{\partial \alpha_k}{\partial x} = 0$$

which can be recast in the form:

$$\frac{\partial \alpha_k}{\partial t} + \frac{\partial (\alpha_k u_I)}{\partial x} = \alpha_k \frac{\partial u_I}{\partial x} \tag{4.16}$$

We notice that (4.16) can be obtained by letting $\mathcal{U}_k = 1$ and $\mathbf{f}_k = 0$ in (4.13) which then yields $\mathbf{f}_k^{Lag} = -u_I$. Consequently, the discretization of the averaged topological equation is included in (4.15) by letting $\mathbf{U}_{k,i}^{n+1} = \mathbf{U}_{k,i}^n = 1$, $\mathbf{F}_{k,i\pm1/2} = 0$ and $\mathbf{F}_{k,i\pm1/2}^{Lag} = -u_{I,i\pm1/2}$.
We thus obtain the first order scheme for computing the volume fraction deduced from (4.15):

$$\alpha_{k,i}^{n+1} = \alpha_{k,i}^n + \frac{\Delta t}{\Delta x} \left[u_{I,i-1/2} (\alpha_{k,i-1/2} - \alpha_{k,i}^n) - u_{I,i+1/2} (\alpha_{k,i+1/2} - \alpha_{k,i}^n) \right] \tag{4.17}$$

In (4.17), the volume fractions $\alpha_{k,i\pm1/2}$ are the volume fractions associated to the Lagrangian fluxes determined by the upwind strategy:

$$\alpha_{k,i-1/2} = \begin{cases} \alpha_{k,i-1}^n, \text{ if } u_{I,i-1/2} > 0 \\ \alpha_{k,i}^n, \text{ if } u_{I,i-1/2} < 0 \end{cases}$$

In Figure 4.5, we present a verification for the computation of the volume fraction supposing $\alpha^n_{1,i-1} > \alpha^n_{1,i}$ and the phase Σ_1 of the cell $i-1$ enters the cell i. If we neglect the contribution at the intercell $i+1/2$, the volume fraction of phase $\alpha^{n+1}_{1,i}$ can be computed using (4.17) as:

$$\alpha^{n+1}_{1,i} = \alpha^n_{1,i} + \frac{(\alpha^n_{1,i-1} - \alpha^n_{1,i})u_{I,i-1/2}\Delta t}{\Delta x}$$

Each term of the above formula is expressed graphically using Figure 4.5 for the Eulerian case of fixed cell boundary $u_{m,i-1/2} = 0$. The graphical interpretation says that the variation of the volume fraction of cell i is due to the added part S_{ADEB} when phase Σ_1 enters cell i from cell $i-1$.

$$\alpha^{n+1}_{1,i} = \alpha^n_{1,i} + \frac{S_{ADEB}}{\Delta x}$$

4.2.5 Eulerian case: quantitative contribution of different Riemann problems

In this section, we evaluate the numerical fluxes in (4.15). The conservative fluxes $(\alpha\mathbf{F})_{k,i+1/2}$, $(\alpha\mathbf{F})_{k,i-1/2}$, as observed in Figure 4.2, are the sum of different fluxes involving different local RPs between the same/different phases.

$$(\alpha\mathbf{F})_{k,i-1/2} = (\alpha\mathbf{F})_{k,i-1/2,1P} + (\alpha\mathbf{F})_{k,i-1/2,2P}$$

In the above relation, $(\alpha\mathbf{F})_{k,i-1/2,1P}$ denotes the single-phase flux involving the RPs between the same phases (RP11 and RP22). On the other hand, $(\alpha\mathbf{F})_{k,i-1/2,2P}$ implies the two-phase flux involving the RP between different phases (RP12 or RP21). The conservative fluxes in the DEM method can be thus determined by (4.18) using the concept of the partition of intercell boundaries introduced in section 4.2.1 (see also [Tang, 2012]):

$$(\alpha\mathbf{F})_{k,i-1/2} = \begin{cases} S^{(kk)}_{i-1/2}\mathbf{F}^{(kk)}_{k,i-1/2} + S^{(kk')}_{i-1/2}\mathbf{F}^{(kk')}_{k,i-1/2}, & \text{if } u_{I,i-1/2} > 0 \\ S^{(kk)}_{i-1/2}\mathbf{F}^{(kk)}_{k,i-1/2} + S^{(k'k)}_{i-1/2}\mathbf{F}^{(k'k)}_{k,i-1/2}, & \text{if } u_{I,i-1/2} < 0 \end{cases} \tag{4.18}$$

With the restriction the exact Riemann solver and the approximate Riemann solvers taking into account the contact wave (e.g. the HLLC solver), the Lagrangian fluxes, which concern only the two-phase RP, can be computed as:

$$\mathbf{F}^{Lag}_{k,i-1/2} = \mathbf{F}^{Lag}_{i-1/2} = \begin{pmatrix} 0 \\ p_{I,i-1/2} \\ p_{I,i-1/2}u_{I,i-1/2} \\ 0 \end{pmatrix}$$

From (4.18), we notice that the numerical fluxes strongly depend on the moving direction of the phase interface. For the purpose of constructing a solution for the numerical fluxes, it is sufficient to consider the four possibilities described in Figure 4.3:

- *IN* Σ_1: Phase Σ_1 goes in the cell i. This case only occurs when $\alpha^n_{1,\ell} > \alpha^n_{1,i}1$ with ℓ is an adjacent cell of cell i.
- *OUT* Σ_1: Phase Σ_1 goes out the cell i. This case only occurs when $\alpha^n_{1,\ell} < \alpha^n_{1,i}1$ with ℓ is an adjacent cell of cell i.
- *IN* Σ_2: Phase Σ_2 goes in the cell i. This case only occurs when $\alpha^n_{1,\ell} < \alpha^n_{1,i}1$ with ℓ is an adjacent cell of cell i.
- *OUT* Σ_2: Phase Σ_2 goes out the cell i. This case only occurs when $\alpha^n_{1,\ell} > \alpha^n_{1,i}$ with ℓ is an adjacent cell of cell i.

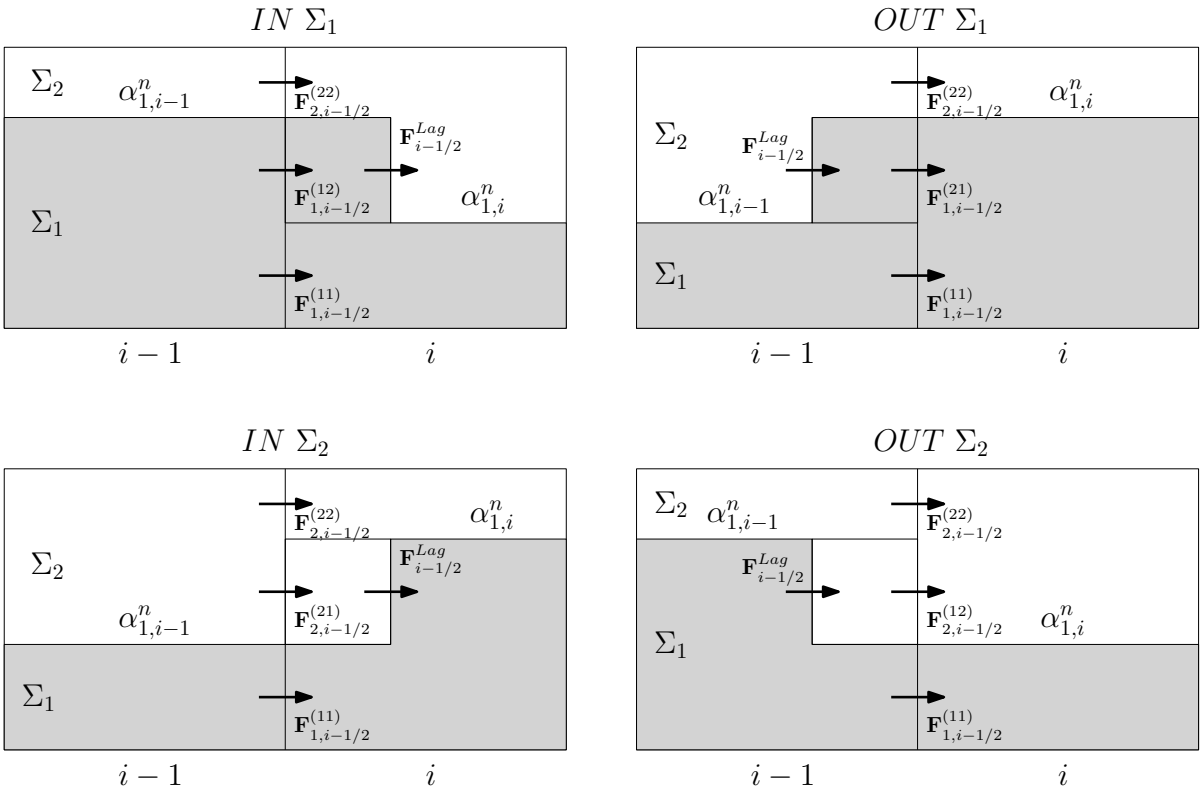

Figure 4.3: Four possibilities illustrated in the intercell frame of velocity u_m ($u_m = 0$: the Eulerian case, $u_m \neq 0$: the ALE case).

Any situation is the combination of these four possibilities. In Figure 4.4, we illustrate a particular case with $\alpha^n_{1,i-1} > \alpha^n_{1,i} > \alpha^n_{1,i+1}$. The direction of motion of the phase interfaces generates four subcases:

- *IN* Σ_1, *OUT* Σ_1: phase Σ_1 from the cell $i-1$ goes in the cell i via the intercell $i-1/2$; phase Σ_1 from the cell i goes out the cell i via the intercell $i+1/2$.
- *IN* Σ_1, *IN* Σ_2: phase Σ_1 from the cell $i-1$ goes in the cell i via the intercell $i-1/2$; phase Σ_2 from the cell $i+1$ goes in the cell i via the intercell $i+1/2$.
- *OUT* Σ_2, *IN* Σ_2: phase Σ_2 from the cell i goes out the cell i via the intercell $i-1/2$; phase Σ_2 from cell $i+1$ goes in cell i via the intercell $i+1/2$.
- *OUT* Σ_2, *OUT* Σ_1: phase Σ_2 from the cell i goes out the cell i via the intercell $i-1/2$; phase Σ_1 from the cell i goes out the cell i via the intercell $i+1/2$.

In the following sections 4.2.5.1 - 4.2.5.5, we detail the computation of the numerical fluxes for the four possibilities illustrated in Figure 4.3.

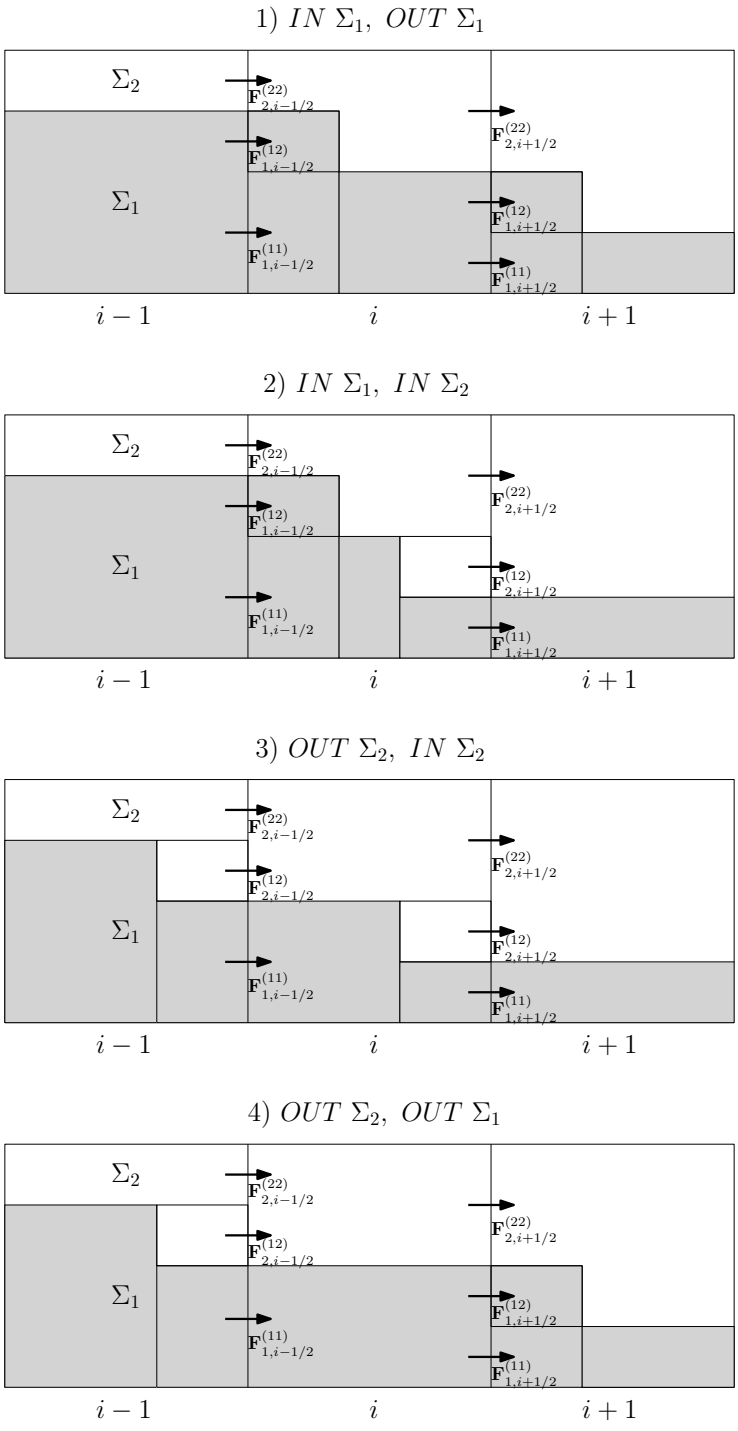

Figure 4.4: Four possibilities. A particular case with $\alpha^n_{1,i-1} > \alpha^n_{1,i} > \alpha^n_{1,i+1}$

4.2.5.1 Two-phase Riemann problem: $IN\ \Sigma_1$

The case $IN\ \Sigma_1$ illustrated in Figure 4.3 is characterized by the RP12.
Contribution of the conservative flux:

$$\begin{aligned}(\alpha\mathbf{F})_{1,i-1/2,2P} &= (\alpha^n_{1,i-1} - \alpha^n_{1,i})\mathbf{F}^{(12)}_{1,i-1/2}(\mathbf{U}^n_{1,i-1}, \mathbf{U}^n_{2,i}) \\ (\alpha\mathbf{F})_{2,i-1/2,2P} &= 0\end{aligned}$$

Contribution of the Lagrangian flux:

$$(\alpha_{k,i-1/2} - \alpha_{k,i})\mathbf{F}^{Lag}_{i-1/2} = (\alpha^n_{1,i-1} - \alpha^n_{1,i})\mathbf{F}^{Lag}_{i-1/2} = -(\alpha^n_{2,i-1} - \alpha^n_{2,i})\mathbf{F}^{Lag}_{i-1/2}$$

4.2.5.2 Two-phase Riemann problem: *OUT* Σ_1

The case *OUT* Σ_1 illustrated in Figure 4.3 is characterized by the RP21.
Contribution of the conservative flux:

$$\begin{aligned}(\alpha\mathbf{F})_{1,i-1/2,2P} &= (\alpha^n_{1,i} - \alpha^n_{1,i-1})\mathbf{F}^{(21)}_{1,i-1/2}(\mathbf{U}^n_{2,i-1}, \mathbf{U}^n_{1,i}) \\ (\alpha\mathbf{F})_{2,i-1/2,2P} &= 0\end{aligned}$$

Contribution of the Lagrangian flux:

$$(\alpha_{k,i-1/2} - \alpha_{k,i})\mathbf{F}^{Lag}_{i-1/2} = (\alpha^n_{2,i} - \alpha^n_{2,i})\mathbf{F}^{Lag}_{i-1/2} = 0$$

4.2.5.3 Two-phase Riemann problem: *IN* Σ_2

The case *IN* Σ_1 illustrated in Figure 4.3 is characterized by the RP21.
Contribution of the conservative flux:

$$\begin{aligned}(\alpha\mathbf{F})_{1,i-1/2,2P} &= 0 \\ (\alpha\mathbf{F})_{2,i-1/2,2P} &= (\alpha^n_{1,i} - \alpha^n_{1,i-1})\mathbf{F}^{(21)}_{2,i-1/2}(\mathbf{U}^n_{2,i-1}, \mathbf{U}^n_{1,i})\end{aligned}$$

Contribution of the Lagrangian flux:

$$(\alpha_{k,i-1/2} - \alpha_{k,i})\mathbf{F}^{Lag}_{i-1/2} = (\alpha^n_{2,i-1} - \alpha^n_{2,i})\mathbf{F}^{Lag}_{i-1/2} = -(\alpha^n_{1,i-1} - \alpha^n_{1,i})\mathbf{F}^{Lag}_{i-1/2}$$

4.2.5.4 Two-phase Riemann problem: *OUT* Σ_2

The case *OUT* Σ_2 illustrated in Figure 4.3 is characterized by the RP12.
Contribution of the conservative flux:

$$\begin{aligned}(\alpha\mathbf{F})_{1,i-1/2,2P} &= 0 \\ (\alpha\mathbf{F})_{2,i-1/2,2P} &= (\alpha^n_{1,i-1} - \alpha^n_{1,i})\mathbf{F}^{(12)}_{2,i-1/2}(\mathbf{U}^n_{1,i-1}, \mathbf{U}^n_{2,i})\end{aligned}$$

Contribution of the Lagrangian flux:

$$(\alpha_{k,i-1/2} - \alpha_{k,i})\mathbf{F}^{Lag}_{i-1/2} = (\alpha^n_{1,i} - \alpha^n_{1,i})\mathbf{F}^{Lag}_{i-1/2} = 0$$

4.2.5.5 Single-phase Riemann problem

The single-phase RP involves only the conservative flux taking the left and right states of the same phases as the initial conditions. For the particular configuration in Figure 4.3, the conservative numerical fluxes are computed with by:

$$\begin{aligned}(\alpha\mathbf{F})_{1,i-1/2,1P,IN\ \Sigma_1} = (\alpha\mathbf{F})_{1,i-1/2,1P,OUT\ \Sigma_2} &= \alpha^n_{1,i}\mathbf{F}^{(11)}_{1,i-1/2}(\mathbf{U}^n_{1,i-1}, \mathbf{U}^n_{1,i}) \\ (\alpha\mathbf{F})_{1,i-1/2,1P,OUT\ \Sigma_1} = (\alpha\mathbf{F})_{1,i-1/2,1P,IN\ \Sigma_2} &= \alpha^n_{1,i-1}\mathbf{F}^{(11)}_{1,i-1/2}(\mathbf{U}^n_{1,i-1}, \mathbf{U}^n_{1,i}) \\ (\alpha\mathbf{F})_{2,i-1/2,1P,IN\ \Sigma_1} = (\alpha\mathbf{F})_{2,i-1/2,1P,OUT\ \Sigma_2} &= \alpha^n_{2,i-1}\mathbf{F}^{(22)}_{2,i-1/2}(\mathbf{U}^n_{2,i-1}, \mathbf{U}^n_{2,i}) \\ (\alpha\mathbf{F})_{2,i-1/2,1P,OUT\ \Sigma_1} = (\alpha\mathbf{F})_{2,i-1/2,1P,IN\ \Sigma_2} &= \alpha^n_{2,i}\mathbf{F}^{(22)}_{2,i-1/2}(\mathbf{U}^n_{2,i-1}, \mathbf{U}^n_{2,i})\end{aligned}$$

4.2.6 ALE case: general formulation

The numerical scheme derived in formula (4.15) is no longer valid when considering a cell with moving boundaries using the Reynolds transport theorem. For the sake of completeness, we describe the extension of the previous formulation to the ALE framework. By integrating (4.8) over cell $C_i = [x_{i-1/2}(t), x_{i+1/2}(t)]$, we obtain:

$$\frac{d}{dt}\int_{x_{i-1/2}(t)}^{x_{i+1/2}(t)} \alpha_k \mathcal{U}_k dx + \int_{x_{i-1/2}(t)}^{x_{i+1/2}(t)} \frac{\partial(\alpha_k \mathbf{f}_k^{ALE})}{\partial x} dx = \int_{x_{i-1/2}(t)}^{x_{i+1/2}(t)} \mathbf{f}_k^{Lag} \frac{\partial \alpha_k}{\partial x} dx \tag{4.19}$$

where $\mathbf{f}_k^{ALE} = \mathbf{f}_k - u_m \mathcal{U}_k$ is called the ALE flux and u_m is the velocity of the intercell.

$$\mathbf{f}_k^{ALE} = \begin{pmatrix} \rho_k(u_k - u_m) \\ \rho_k u_k(u_k - u_m) + p_k \\ \rho_k e_k^t(u_k - u_m) + p_k u_k \\ \rho_k \mathbf{Y}_k(u_k - u_m) \end{pmatrix}$$

The conservative flux is computed using the classical finite volume technique:

$$\int_{x_{i-1/2}(t)}^{x_{i+1/2}(t)} \frac{\partial(\alpha_k \mathbf{f}_k^{ALE})}{\partial x} dx = \alpha_{k,i+1/2} \mathbf{f}_{k,i+1/2}^{ALE} - \alpha_{k,i-1/2} \mathbf{f}_{k,i-1/2}^{ALE} \tag{4.20}$$

The integration of (4.20) over time $[t^n, t^{n+1}]$ gives:

$$\int_{t^n}^{t^{n+1}} \int_{x_{i-1/2}(t)}^{x_{i+1/2}(t)} \frac{\partial(\alpha_k \mathbf{f}_k^{ALE})}{\partial x} dx dt = \Delta t(\alpha_{k,i+1/2} \mathbf{F}_{k,i+1/2}^{ALE} - \alpha_{k,i-1/2} \mathbf{F}_{k,i-1/2}^{ALE})$$

where $\mathbf{F}_{k,i\pm1/2}^{ALE}$ denote the numerical ALE fluxes approximating the corresponding physical ones $\mathbf{f}_{k,i\pm1/2}^{ALE}$ during an interval of time Δt:

$$\mathbf{F}_{k,i\pm1/2}^{ALE} \approx \frac{1}{\Delta t}\int_{t^n}^{t^{n+1}} \mathbf{f}_{k,i\pm1/2}^{ALE} dt$$

Concerning the Lagrangian term, as in the case of fixed mesh, it can be rewritten as:

$$\mathbf{f}_k^{Lag} \frac{\partial \alpha_k}{\partial x} = \frac{\partial(\alpha_k \mathbf{f}_k^{Lag})}{\partial x} - \alpha_k \frac{\partial \mathbf{f}_k^{Lag}}{\partial x}$$

The integration of the conservative term associated to the Lagrangian flux gives:

$$\int_{t^n}^{t^{n+1}} \int_{x_{i-1/2}(t)}^{x_{i+1/2}(t)} \frac{\partial(\alpha_k \mathbf{f}_k^{Lag})}{\partial x} dx dt = \Delta t(\alpha_{k,i+1/2} \mathbf{F}_{k,i+1/2}^{Lag} - \alpha_{k,i-1/2} \mathbf{F}_{k,i-1/2}^{Lag})$$

The integration of the non-conservative term associated to the Lagrangian flux is approximated:

$$\int_{t^n}^{t^{n+1}} \int_{x_{i-1/2}(t)}^{x_{i+1/2}(t)} \alpha_k \frac{\partial \mathbf{f}_k^{Lag}}{\partial x} dx dt \quad = \quad \Delta t \alpha_{k,i}^n (\mathbf{F}_{k,i+1/2}^{Lag} - \mathbf{F}_{k,i-1/2}^{Lag})$$

In the above formulas, the volume fraction $\alpha_{k,i\pm1/2}$ associated to the Lagrangian fluxes are evaluated using the upwind strategy.

$$\alpha_{k,i-1/2} = \begin{cases} \alpha_{k,i-1}^n, \text{ if } u_{I,i-1/2} - u_{m,i-1/2} > 0 \\ \alpha_{k,i}^n, \text{ if } u_{I,i-1/2} - u_{m,i-1/2} < 0 \end{cases} \tag{4.21}$$

The numerical Lagrangian fluxes $\mathbf{F}_{k,i\pm1/2}^{Lag}$ approximate the corresponding physical ones $\mathbf{f}_{k,i\pm1/2}^{Lag}$ during an interval of time Δt:

$$\mathbf{F}_{k,i\pm1/2}^{Lag} \approx \frac{1}{\Delta t}\int_{t^n}^{t^{n+1}} \mathbf{f}_{k,i\pm1/2}^{Lag} dt$$

Concerning the time-derivative term in (4.19), its integration over time $[t^n, t^{n+1}]$ yields:

$$\begin{aligned}\int_{t^n}^{t^{n+1}} \left(\frac{d}{dt} \int_{x_{i-1/2}(t)}^{x_{i+1/2}(t)} \alpha_k \mathcal{U}_k dx \right) dt &= \int_{x_{i-1/2}(t^{n+1})}^{x_{i+1/2}(t^{n+1})} \alpha_k \mathcal{U}_k dx - \int_{x_{i-1/2}(t^n)}^{x_{i+1/2}(t^n)} \alpha_k \mathcal{U}_k dx \\ &= \Delta x_i^{n+1} (\alpha \mathbf{U})_{k,i}^{n+1} - \Delta x_i^n (\alpha \mathbf{U})_{k,i}^n\end{aligned}$$

We thus obtain the first order DEM scheme for the ALE case:

$$\begin{aligned}(\alpha \mathbf{U})_{k,i}^{n+1} &= \frac{\Delta x_i^n}{\Delta x_i^{n+1}} (\alpha \mathbf{U})_{k,i}^n - \frac{\Delta t}{\Delta x_i^{n+1}} \left[(\alpha \mathbf{F}^{ALE})_{k,i+1/2} - (\alpha \mathbf{F}^{ALE})_{k,i-1/2} \right] \\ &+ \frac{\Delta t}{\Delta x_i^{n+1}} \left[\mathbf{F}_{k,i+1/2}^{Lag} (\alpha_{k,i+1/2} - \alpha_{k,i}^n) - \mathbf{F}_{k,i-1/2}^{Lag} (\alpha_{k,i-1/2} - \alpha_{k,i}^n) \right]\end{aligned} \tag{4.22}$$

In general, the computation of $\mathbf{U}_{k,i}^{n+1}$ requires:

- Δx_i^{n+1}, $\alpha_{k,i}^{n+1}$: volume and volume fraction at time $t = t^{n+1}$.
- $\alpha_{k,i\pm1/2}$: volume fraction at the intercell associated to the Lagrangian fluxes.
- $(\alpha \mathbf{F}^{ALE})_{k,i+1/2}$, $(\alpha \mathbf{F}^{ALE})_{k,i-1/2}$: numerical conservative ALE fluxes.
- $\mathbf{F}_{k,i+1/2}^{Lag}$, $\mathbf{F}_{k,i-1/2}^{Lag}$: numerical Lagrangian fluxes.

We can clearly observe from (4.22) that the ALE case introduces the variation of cell volumes which gives a supplementary contribution to the cell volume fraction comparing to the case of fixed mesh. The variation of a cell volume can be taken into account by using the DGCL as discussed in section 1.3.3 and the variation of the volume fraction will be addressed in section 4.2.7. The volume fractions at the intercell associated to the Lagrangian fluxes are determined by the upwind strategy (4.21). The numerical conservative ALE fluxes can be computed in a way similar to the fixed mesh case using the concept of partition of cell boundaries.

4.2.7 ALE case: volume fraction

The update of the volume fraction can be done by discretizing the averaged topological equation (4.7). In 1D, it can be written as:

$$\frac{\partial \alpha_k}{\partial t} + u_I \frac{\partial \alpha_k}{\partial x} = 0$$

which can be recast as follows:

$$\frac{\partial \alpha_k}{\partial t} + \frac{\partial (\alpha_k u_I)}{\partial x} = \alpha_k \frac{\partial u_I}{\partial x}$$

By integrating the above equation over cell $C_i = [x_{i-1/2}(t), x_{i+1/2}(t)]$, we obtain the semi-discrete form:

$$\frac{d}{dt} \int_{x_{i-1/2}(t)}^{x_{i+1/2}(t)} \alpha_k dx + \int_{x_{i-1/2}(t)}^{x_{i+1/2}(t)} \frac{\partial (\alpha_k (u_I - u_m))}{\partial x} dx = \int_{x_{i-1/2}(t)}^{x_{i+1/2}(t)} \alpha_k \frac{\partial u_I}{\partial x} dx \tag{4.23}$$

Similarly to the Eulerian case, we notice that (4.23) can be obtained by letting $\mathcal{U}_k = 1$ and $\mathbf{f}_k = 0$ in (4.19) which then yields $\mathbf{f}_k^{Lag} = -u_I$ and $\mathbf{f}_k^{ALE} = -u_m$. Consequently, the discretization of the averaged topological equation in the ALE case is included in (4.22) by letting $\mathbf{U}_{k,i}^{n+1} = \mathbf{U}_{k,i}^n = 1$, $\mathbf{F}_{k,i\pm1/2} = 0$,

$\mathbf{F}^{Lag}_{k,i\pm1/2} = -u_{I,i\pm1/2}$ and $\mathbf{F}^{ALE}_{k,i\pm1/2} = -u_{m,i\pm1/2}$. The numerical scheme for computing the volume fraction deduced from (4.22) is:

$$\begin{aligned}\alpha_{k,i}^{n+1} = \frac{\Delta x_i^n}{\Delta x_i^{n+1}}\alpha_{k,i}^n \quad &+ \quad \frac{\Delta t}{\Delta x_i^{n+1}}[u_{I,i-1/2}(\alpha_{k,i-1/2} - \alpha_{k,i}^n) - \alpha_{k,i-1/2}u_{m,i-1/2}] \\ &- \quad \frac{\Delta t}{\Delta x_i^{n+1}}[u_{I,i+1/2}(\alpha_{k,i+1/2} - \alpha_{k,i}^n) - \alpha_{k,i+1/2}u_{m,i+1/2}]\end{aligned} \tag{4.24}$$

Figure 4.5 displays a verification for the computation of the volume fraction supposing $\alpha^n_{1,i-1} > \alpha^n_{1,i}$ and also assuming, for the sake of simplicity, the variation of the volume fraction inside the cell i is only due to the intercell $i-1/2$. We also suppose the phase Σ_1 of the cell $i-1$ enters the cell i and the intercell moves with velocity $0 < u_{m,i-1/2} < u^*$. The quantity $\alpha^{n+1}_{1,i}$ can be computed using (4.24):

$$\alpha_{1,i}^{n+1} = \frac{1}{\Delta x_i^{n+1}}\left[\Delta x_i^n \alpha_{1,i}^n + (\alpha_{1,i-1}^n - \alpha_{1,i}^n)u_{I,i-1/2}\Delta t - \alpha_{1,i-1}^n u_{m,i-1/2}\Delta t\right]$$

Each term of the above formula is expressed graphically using Figure 4.5. The graphical interpretation says that the variation of the volume fraction of cell i is due to the added part S_{ADEB} (when phase Σ_1 enters cell i from cell $i-1$) and the subtracted part $S_{AA'C'C}$ by the moving intercell of velocity $u_{m,i-1/2}$.

$$\alpha_{1,i}^{n+1} = \frac{1}{\Delta x_i^{n+1}}(S_{BFGC} + S_{ADEB} - S_{AA'C'C})$$

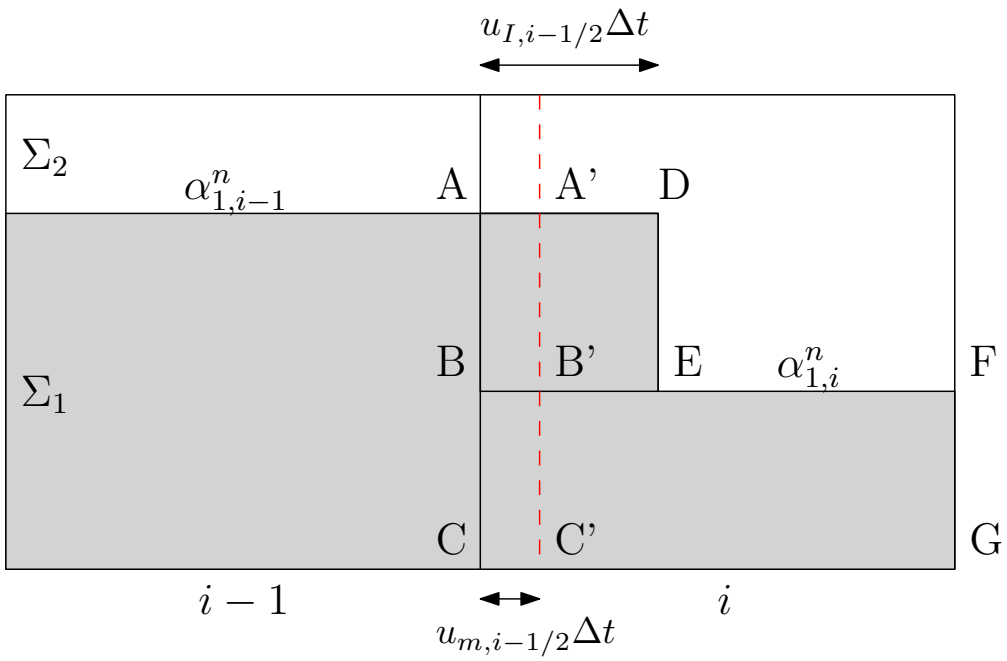

Figure 4.5: Graphical presentation for the computation of the volume fraction. In ALE case: $u_{m,i-1/2} > 0$. In the Eulerian case: $u_{m,i-1/2} = 0$.

4.3 1D bubble expansion problem

4.3.1 Presentation of the problem

In this section, we consider the so-called 1D bubble expansion problem, the configuration of which is presented in Figure 4.6. The purpose of this test problem is to evaluate a specific analytical model under

low-Mach hypothesis (bubble model) when computing this two-phase problem. The bubble solutions will be presented in section 4.3.2 and evaluated in section 4.3.3 by comparison with the fully compressible two-phase DEM solver of EUROPLEXUS [Europlexus, 2020]. The DEM method includes by default an instantaneous relaxation procedure for the pressure and velocity (see [Saurel and Abgrall, 1999], [Tang, 2012]-Appendix C, see also Appendix E).

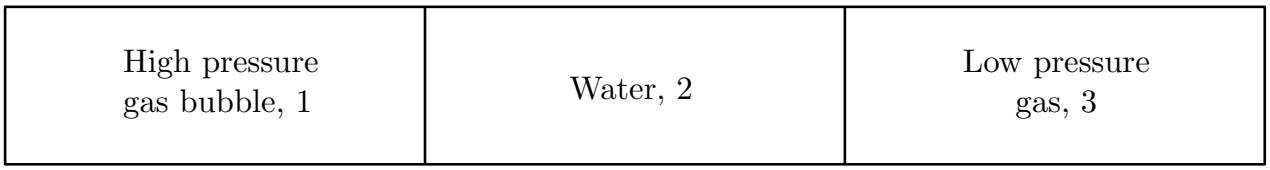

Figure 4.6: Bubble expansion problem. Configuration

The system under consideration is isolated and consists of a high-pressure gas bubble (region 1, denoted by B), a low-pressure column of water (region 2, denoted by W) and a low-pressure gas (region 3, denoted by A). The gas bubble due to its high initial pressure expands and pushes the liquid water rightward, which increases the pressure of the low-pressure gas region. The low-pressure gas is thus compressed and then behaves like the gas bubble at the beginning of the scenario when it is at its maximum level of compression. The initial lengths of the regions 1, 2, 3 are 3m, 6m, 3m consecutively. Note these 3 regions of the 1D problem are representative of an application such as the MARA problem, with a high pressure gas bubble expanding in the liquid filling a vessel but with a sky of gas on top of the vessel (see chapter 6).
When computing this problem, we consider two different sets of initial conditions corresponding to different levels of initial energy inside the high-pressure bubble region. The distinct regions are filled with gases and liquid governed by the SG-EOS. The initial conditions and the material properties are specified in the following tables:

	Region 1	Region 2	Region 3
ρ (kg/m^3)	26.827	1000.0	1.0
P (Pa)	1×10^7	1×10^5	1×10^5
u (m/s)	0.0	0.0	0.0

Table 4.1: Initial conditions for the **strong bubble expansion** problem (100 bars in high-pressure bubble)

	Region 1	Region 2	Region 3
ρ (kg/m^3)	5.1795	1000.0	1.0
P (Pa)	1×10^6	1×10^5	1×10^5
u (m/s)	0.0	0.0	0.0

Table 4.2: Initial conditions for the **weak bubble expansion** problem (10 bars in high-pressure bubble)

Material properties			
	Region 1	Region 2	Region 3
γ	1.4	4.4	1.4
P_∞ (Pa)	0.0	6.0×10^8	0.0

Comments

- The value of the initial density of the bubble region is obtained by supposing that it is made of perfect gas which is isentropically compressed:

From 1 to 100 bars:

$$\rho_{B,0} = \left(\frac{P_{B,0}}{P_{A,0}}\right)^{1/\gamma_B} \rho_{A,0} = \left(\frac{1\times 10^7 \text{Pa}}{1\times 10^5 \text{Pa}}\right)^{1/1.4} 1.0 \text{ kg/m}^3 \approx 26.827 \text{ kg/m}^3$$

From 1 to 10 bars:

$$\rho_{B,0} = \left(\frac{P_{B,0}}{P_{A,0}}\right)^{1/\gamma_B} \rho_{A,0} = \left(\frac{1\times 10^6 \text{Pa}}{1\times 10^5 \text{Pa}}\right)^{1/1.4} 1.0 \text{ kg/m}^3 \approx 5.1795 \text{ kg/m}^3$$

- The speed of sound in the water column is

$$c_W = \left(\gamma_W \frac{p_W + P_\infty}{\rho_W}\right)^{0.5} \approx \left(4.4 \times \frac{6.0\times 10^8}{1000.0}\right)^{0.5} \approx 1625 \text{ m/s}$$

- In order to avoid the formation of negative pressure in the liquid water, we suppose that there is initially a small volume fraction of residual gas which is at mechanical equilibrium with the liquid. This volume fraction is set to $\alpha_{res,gas} = 10^{-5}$.

4.3.2 Bubble model

In this section we investigate an analytical model for the bubble expansion problem. We firstly emphasize that it is possible to compute analytically the fully compressible solution in short time; conversely, when considering long time (several reflections of shocks and rarefaction waves on the domain boundaries), finding a reference solution becomes quite difficult, despite the geometric simplicity of the problem with respect to problems considered in industrial cases. However, in the low-Mach number regime, the shock and rarefaction waves can be considered as (weak) acoustic waves and therefore we can avoid their computations and just evaluate the kinetic energy of the water and the average pressure in different gas regions. These quantities are particularly important since they are representative of the loads applied on a structure. The fully compressible system can be simplified relying on the following considerations:

- Since we are in the low-Mach number limit, all the phenomena can be considered as isentropic and all the waves can be filtered.
- The liquid water can be considered as incompressible since the volume of liquid changes very little, especially in low-Mach number flows.

In this way, the governing equations describing the problem become:
For gas regions:

$$\begin{aligned} \frac{\partial \rho}{\partial t} + u\frac{\partial \rho}{\partial x} + \rho\frac{\partial u}{\partial x} &= 0 \\ \rho\frac{\partial u}{\partial t} + \rho u\frac{\partial u}{\partial x} + \frac{\partial p'}{\partial x} &= 0 \\ \frac{dP}{dt} + \rho c^2 \frac{\partial u}{\partial x} &= 0, \quad P = P(t) \end{aligned} \tag{4.25}$$

This is the asymptotic system as already discussed for a compressible material (see section 1.2.2). The dynamic and thermodynamic pressures are denoted as p' and P respectively.
For water region:

$$\begin{aligned} \frac{\partial u}{\partial x} &= 0 \\ \rho\frac{\partial u}{\partial t} + \frac{\partial p}{\partial x} &= 0 \end{aligned} \tag{4.26}$$

As we can see, the bubble model is nothing but the asymptotic model with incompressible assumption for the water column.
The solution of systems (4.25), (4.26) is computed as follows:

For gases:

$$\begin{aligned} P_B l_B^\gamma &= P_{B,0} l_{B,0}^\gamma \\ P_A l_A^\gamma &= P_{A,0} l_{A,0}^\gamma \\ \rho_B l_B &= \rho_{B,0} l_{B,0} \\ \rho_A l_A &= \rho_{A,0} l_{A,0} \\ u_B &= \frac{u_{B,W}}{l_B} x,\ 0 \le x \le l_B \\ u_A &= \frac{u_{A,W}}{l_A}(l-x),\ l_A \le x \le l \end{aligned} \tag{4.27}$$

The dynamic pressure is very small compared to the thermodynamic pressure and is therefore negligible in the solutions: $p' << P$.

For water:

$$\begin{aligned} p_W &= \frac{P_B - P_A}{l_B - l_A}(x - l_B) + P_B,\ l_A \le x \le l_B \\ u_W &= u_W(t) = u_{A,W} = u_{B,W} \end{aligned} \tag{4.28}$$

where:

- $l_{B,0},\ l_{A,0}$ are the initial lengths of regions 1 and 3. l is the total length of the three regions.
- $l_B,\ l_A$ are the current lengths of regions 1 and 3 and are functions of time only.
- $P_{B,0},\ P_{A,0},\ \rho_{B,0},\ \rho_{A,0}$ are the initial pressures and densities of regions 1 and 3.
- $P_B,\ P_A,\ \rho_B,\ \rho_A$ are the pressures and densities of regions 1, 3 and are functions of time only.
- $u_{B,W},\ u_{A,W}$ are the velocity at the interfaces between regions 1-2 and 2-3.
- $u_B,\ u_A$ are the velocity in regions 1 and 3. They are functions depending on time and linear in space.
- p_W is the pressure in region 2. It is a function depending on time and linear in space.
- u_W is the velocity in region 2 and is a function time only.

We now investigate the problem from the energetic point of view by introducing the concepts of equilibrium pressure and exergy, which will be useful to analyze the quality of the computed numerical solutions (in section 4.3.3) with respect to the bubble model solutions detailed in this section.
We consider first the continuous bubble model (without considering the numerical treatment). For an isolated system, the total energy is conserved and is the sum of the internal and kinetic energies. By neglecting the contribution of the kinetic energy of gases and under the hypothesis that the internal energy of the liquid does not vary, the total energy of our system writes:

$$E_{tot} = \frac{1}{\gamma - 1}\int_{l_B} p dl + \frac{1}{\gamma - 1}\int_{l_A} p dl + \underbrace{\frac{1}{2}\int_{l_W} \rho_W u_w^2 dl}_{K_W} \tag{4.29}$$

or

$$E_{tot} = \frac{P_B l_B}{\gamma - 1} + \frac{P_A l_A}{\gamma - 1} + K_W$$

In other words, the total energy can be regarded as the sum of the amounts of energy that can be and cannot be integrally converted into the kinetic energy.
For a thermodynamic process, the exergy can be defined as "the amount of work obtainable when some matter is brought to a state of thermodynamic equilibrium with the common components of the natural surroundings by means of reversible processes" [Szargut et al., 1988]. In the case considered here, we can define the exergy E_{exe} as the amount of energy which can be integrally converted into kinetic energy under the hypothesis of isentropic processes. The amount of energy that cannot be integrally converted into kinetic energy is defined as the anergy E_{an} of the system:

$$E_{tot} = E_{an} + E_{exe}$$

Concerning the equilibrium pressure, it corresponds to the state at which the pressure levels of the two gas regions are equal ($P_A = P_B = P_e$). At this state, the acceleration of the liquid column is zero and its kinetic energy is maximum meaning that no more energy can be converted into kinetic energy (with the anergy the amount of energy that cannot be converted anymore into kinetic energy):

$$E_{tot} = \frac{P_e l_{B,e}}{\gamma - 1} + \frac{P_e l_{A,e}}{\gamma - 1} + K_{W,max} = E_{an} + K_{W,max}$$

where:

$$E_{an} = \frac{P_e l_{B,e}}{\gamma - 1} + \frac{P_e l_{A,e}}{\gamma - 1} = \frac{P_e l_{A+B,e}}{\gamma - 1} = \frac{P_e l_{A+B}}{\gamma - 1} = \frac{P_e l_B}{\gamma - 1} + \frac{P_e l_A}{\gamma - 1}$$

and $l_{A,e}$, $l_{B,e}$ are the lengths of low-pressure gas and bubble regions at the equilibrium state.
The exergy is finally the difference between the total energy and the anergy:

$$E_{exe} = E_{tot} - E_{an} = \frac{1}{\gamma - 1}(P_A - P_e) l_A + \frac{1}{\gamma - 1}(P_B - P_e) l_B + K_W$$

In computing the exergy of the system, one needs to determine the equilibrium pressure P_e. The solutions for P_e, as P_A and P_B, satisfy:

$$\begin{array}{lcll} P_e l_{B,e}^{\gamma} & = & P_B l_B^{\gamma} & = & P_{B,0} l_{B,0}^{\gamma} \\ P_e l_{A,e}^{\gamma} & = & P_A l_A^{\gamma} & = & P_{A,0} l_{A,0}^{\gamma} \\ l_{A,e} + l_{B,e} & = & l_{A+B,e} & = & l_{A+B} = l_{A+B,0} \end{array}$$

which gives:

$$l_{A,e} = \frac{l_{A+B}}{1 + \left(\frac{P_B}{P_A}\right)^{1/\gamma} \frac{l_B}{l_A}} = \frac{l_{A+B,0}}{1 + \left(\frac{P_{B,0}}{P_{A,0}}\right)^{1/\gamma} \frac{l_{B,0}}{l_{A,0}}}$$

$$P_e = P_A \left(\frac{1 + \left(\frac{P_B}{P_A}\right)^{1/\gamma} \frac{l_B}{l_A}}{\frac{l_{A+B}}{l_A}} \right)^{\gamma} = P_{A,0} \left(\frac{1 + \left(\frac{P_{B,0}}{P_{A,0}}\right)^{1/\gamma} \frac{l_{B,0}}{l_{A,0}}}{\frac{l_{A+B,0}}{l_{A,0}}} \right)^{\gamma} \tag{4.30}$$

From these solutions, we can state that exergy, anergy and equilibrium pressure for the bubble model take constant values over time.

We now consider the case of a numerical solution for the bubble model. In general, all numerical approaches produce numerical entropy which, as the physical entropy, degrades the quality of the solution: part of the initial energy is not transformed into kinetic energy for the liquid phase but is numerically converted into heat. The equilibrium pressure, anergy and exergy are not constant in time for this reason. However, the total energy is always conserved and equation (4.29) is still valid since the kinetic energy of gases and

the variation of water internal energy are negligible in the low-Mach regime.
In order to compute the equilibrium pressure and exergy of a numerical solution, the steps described in the (continuous) bubble case are followed. The non-homogeneous pressure in (4.29) can be averaged as:

$$P_B = \frac{1}{l_B} \int_{l_B} p(x,t) dl \tag{4.31}$$

$$P_A = \frac{1}{l_A} \int_{l_A} p(x,t) dl \tag{4.32}$$

Moreover, we use the time-dependent arguments instead of initial values to compute for example the equilibrium pressure (see (4.30)) so that its temporal evolution can be observed. We also notice that (4.30) is an approximation in the discrete situation since in general $l_{A+B,e} \neq l_{A+B}$ due to the negligible variation in the computed volume of the incompressible material.
Figures 4.7 and 4.8 display the bubble model solutions for the case of 100 bars and 10 bars in high-pressure gas bubble. We describe the main physical phenomena of the 100 bars case (the 10 bars case is qualitatively similar):

- From 0-63 ms: the gas bubble (region 1) is in expansion and the low-pressure gas (region 3) is in compression ($P_B > P_A$). The water column accelerates.
- At around 63 ms: The pressures in gas regions are equal and the equilibrium state of the system is established: $P_B = P_A = P_e$. The water column reaches its maximum speed.
- From 63 - 67 ms: Region 1 continues to expand and region 3 continues to be compressed due to inertia. However, the water column decelerates since the pressure gradient is inverted $P_B > P_A$.
- At around 67 ms: The water column stops moving and begins to change its direction. Region 3 (region 1) reaches its limit of compression (expansion). Region 3 begins to expand and push the water column leftward to compress the gas bubble.

In the next section, we will compare these bubble model solutions with the fully compressible solutions given by the DEM solver in order to assess the relevance of the low-Mach bubble model. If this comparison is conclusive, we will then proceed to develop a numerical treatment for this low-Mach model (which will be the two-phase DEM extension of the AC-LM treatment introduced in the previous chapter for single-phase low-Mach flows).

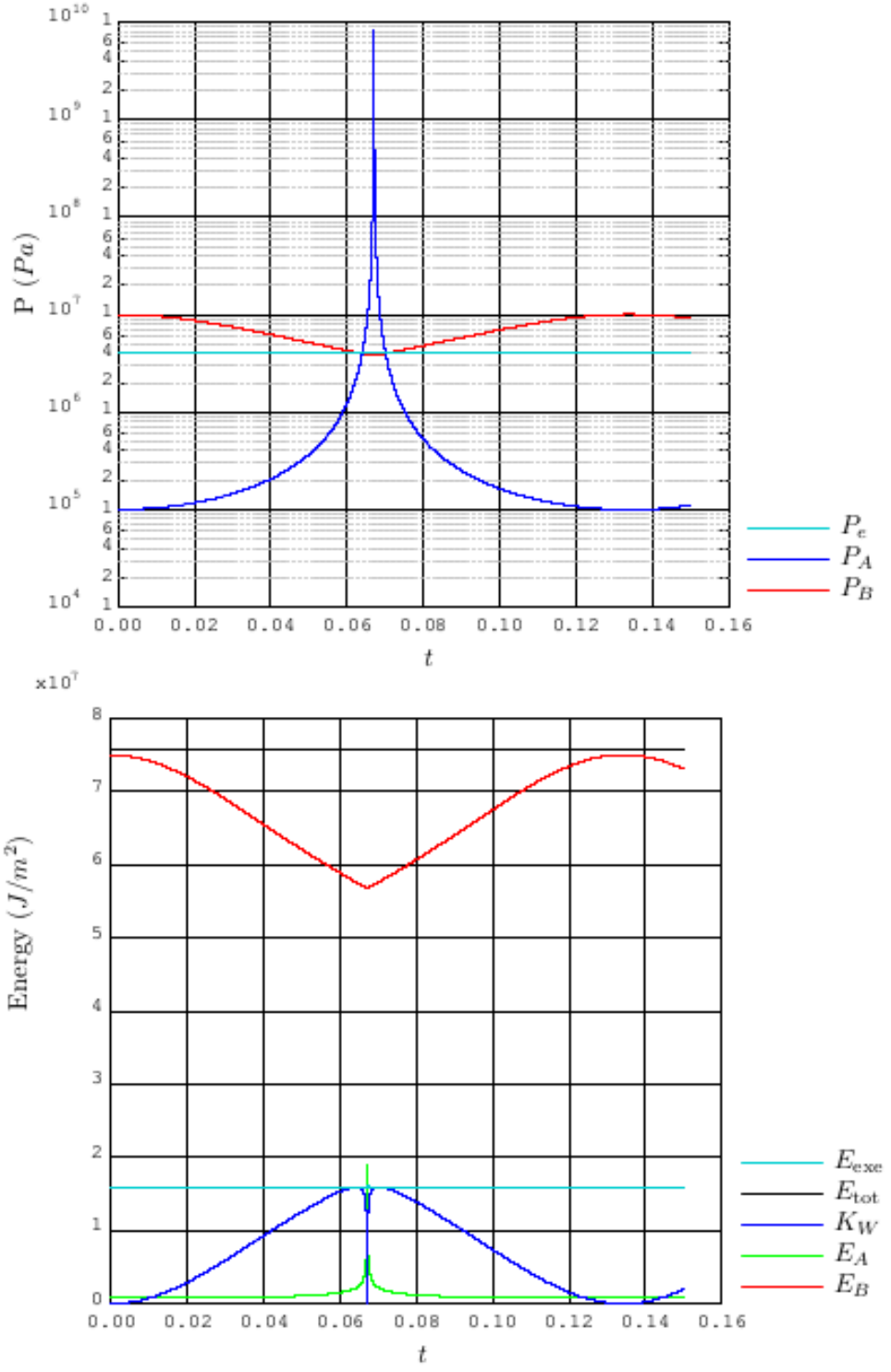

Figure 4.7: Strong bubble expansion problem (100 bars). "Bubble model" solution. On the top, ("equilibrium", low-pressure gas and bubble regions) pressures as function of time. On the bottom, energies per unit surface (1D problem): the exergy, the total energy, the kinetic energy of the liquid water, the internal energy of the low-pressure gas and the bubble regions. SI units.

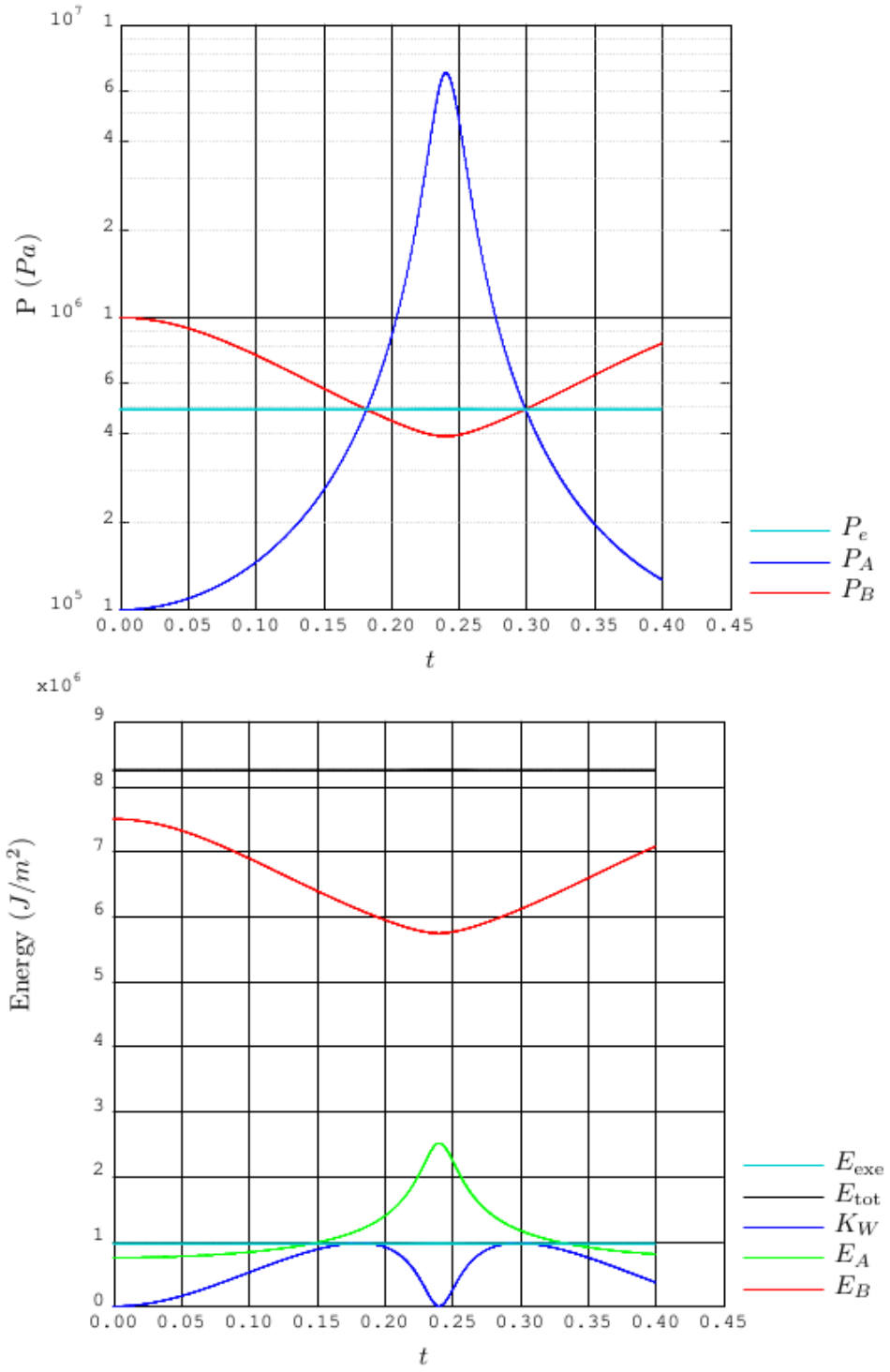

Figure 4.8: Weak bubble expansion problem (10 bars). "Bubble model" solution. On the top, ("equilibrium", low-pressure gas and bubble regions) pressures as function of time. On the bottom, energies per unit surface (1D problem): the exergy, the total energy, the kinetic energy of the liquid water, the internal energy of the low-pressure gas and the bubble regions. SI units.

4.3.3 Numerical results

In this section, we compare the fully compressible solutions (given by DEM solver) with the bubble model solutions. The DEM method is characterized by the following features:

- second order accuracy in space using the limited linear reconstruction on primitive variables.
- second order accuracy in time using 2-stage RK method
- instantaneous relaxation procedure of [Saurel and Abgrall, 1999, Tang, 2012] for the pressure and velocity.
- anti-diffusive UDCS approach for the volume fraction [Tang et al., 2014a, Tang et al., 2014b, Tang, 2012].
- $CFL = 0.5$.

Different levels of mesh refinement are considered:

- the coarsest (uniforme) mesh is composed of 48 elements in region 1 (one fourth of the initial total domain, which means 192 cells for the whole domain).
- the medium mesh is composed of 96 cells in the initial region 1 (384 cells in total).
- the finest mesh is composed of 192 cells in the initial region 1 (768 cells all over the domain).

4.3.3.1 Strong bubble expansion problem (100 bars)

The numerical solution presented in this section corresponds to the case of 100 bars in the high-pressure gas bubble (see Table 4.1).
In Figure 4.9, we present the initial stage ($t = 4\,ms$) of the problem. For the compressible model, we can clearly see waves propagating inside the liquid region. In particular, at the beginning of the evolution, the interface between the high-pressure gas bubble (region 1) and liquid water (region 2) defines a RP and the solution consists of:

- A (weak) right-propagating shock wave with the pressure which is very close to the initial pressure of the bubble.
- A left-propagating rarefaction with the purpose of decreasing the pressure in the bubble.
- A right-propagating contact wave.

The speed of the liquid column in the region perturbed by the shock wave can be approximated by the Joukowski formula:

$$u \approx \frac{P_{B,0} - P_{W,0}}{\rho_{W,0} c_{W,0}} = \frac{99 \times 10^5}{1000 \times 1625} \approx 6.1\ m/s$$

This shock wave when arriving at the interface between water and the low-pressure gas region generates: a (weak) right-propagating shock wave (to increase the pressure in the low-pressure gas region), a left-propagating rarefaction and a right-propagating contact wave. We can clearly see that the compressible solution is far from the bubble model solution (low-Mach red curve in Figure 4.9) in this initial stage.

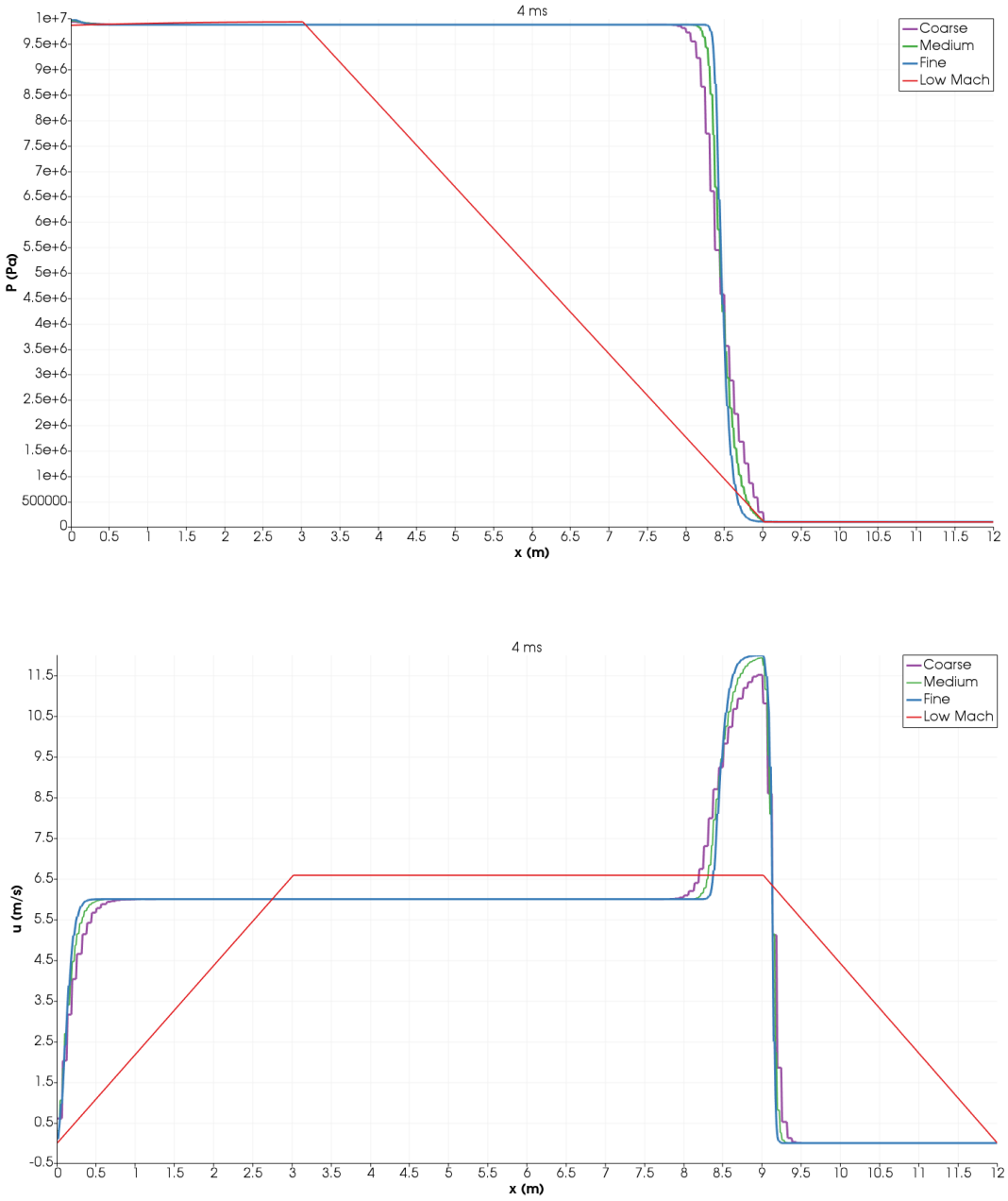

Figure 4.9: Strong bubble expansion problem (100 bars). Comparison between DEM and bubble (low-Mach) model. Pressure and velocity fields at 4 ms. Limited linear space reconstruction for primitive variables and 2-stage Runge-Kutta time discretization, $CFL = 0.5$.

At later times, the waves of the whole domain are reflected on the wall boundaries, interact with each other and then form a complex system despite the geometric simplicity of the problem.
Figure 4.10 displays the instant ($t = 43\,ms$) where the fully compressible solutions have a qualitatively low-Mach behavior. We notice that the medium and coarse meshes solutions are close to the bubble model one while significant oscillations are observed on the solutions with the fine mesh. Such behavior is expected since waves with high frequency are better computed on the fine mesh. The coarse mesh, which is known to yield more diffused solutions, artificially filters waves and therefore is closer to the bubble model solutions compared to other more refined meshes.

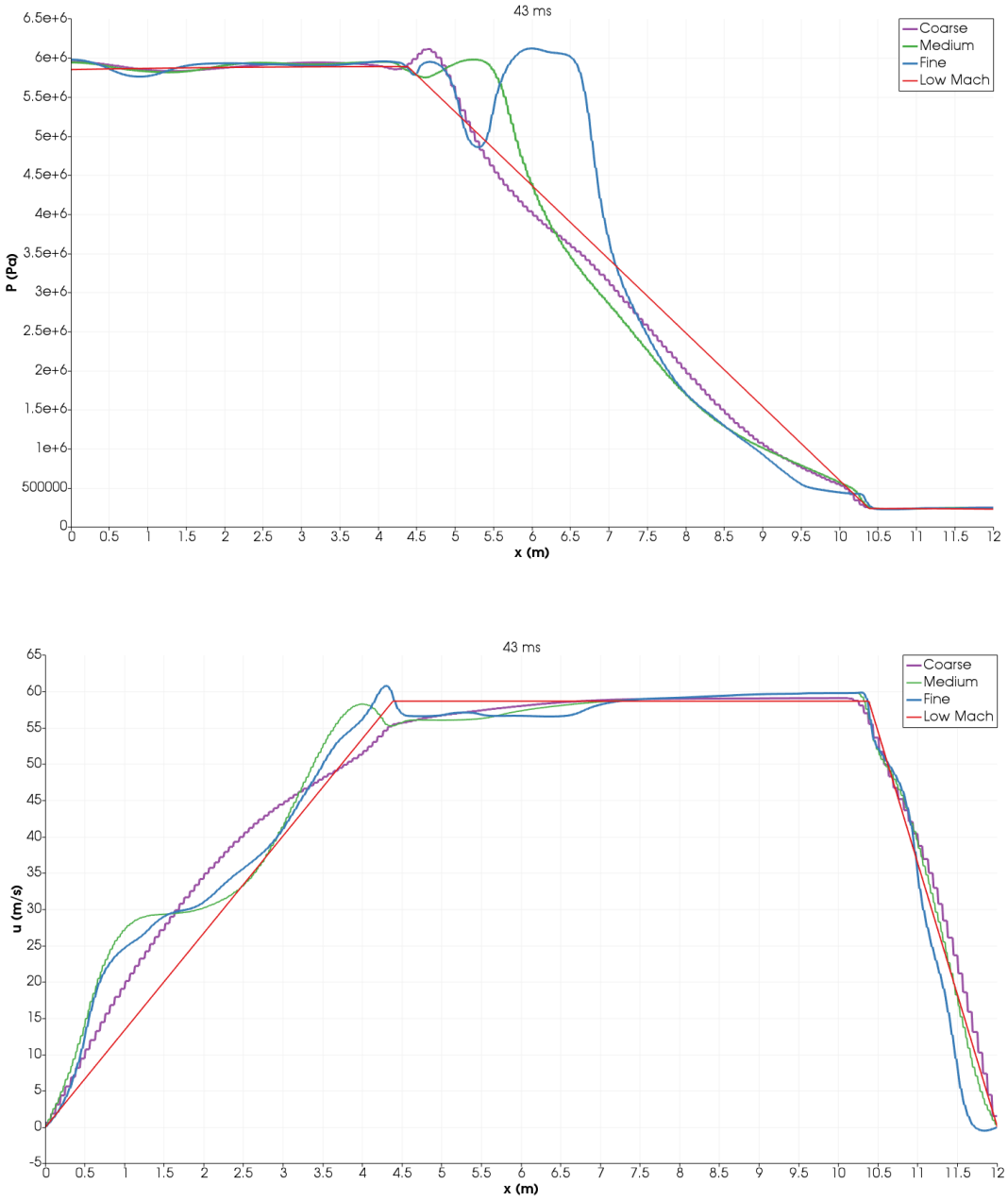

Figure 4.10: Strong bubble expansion problem (100 bars). Comparison between DEM and bubble (low-Mach) model. Pressure and velocity fields at 43 ms. Limited linear space reconstruction for primitive variables and 2-stage Runge-Kutta time discretization, $CFL = 0.5$.

Figure 4.11 displays the instant where the water column in the bubble model just inverts its motion and region 3 begins to expand. The water column in the compressible solutions has not yet changed its direction and region 3 is close to its maximum limit of compression. This time-shift between the compressible and bubble model solutions is linked to the difference in sound speed of the models. While the water column in the bubble model accelerates, decelerates and inverts its motion in a uniform and immediate way because the sound speed tends to infinity, the water column in the compressible model accelerates, decelerates and inverts its motion in a progressive way due to the finite-speed acoustic wave.

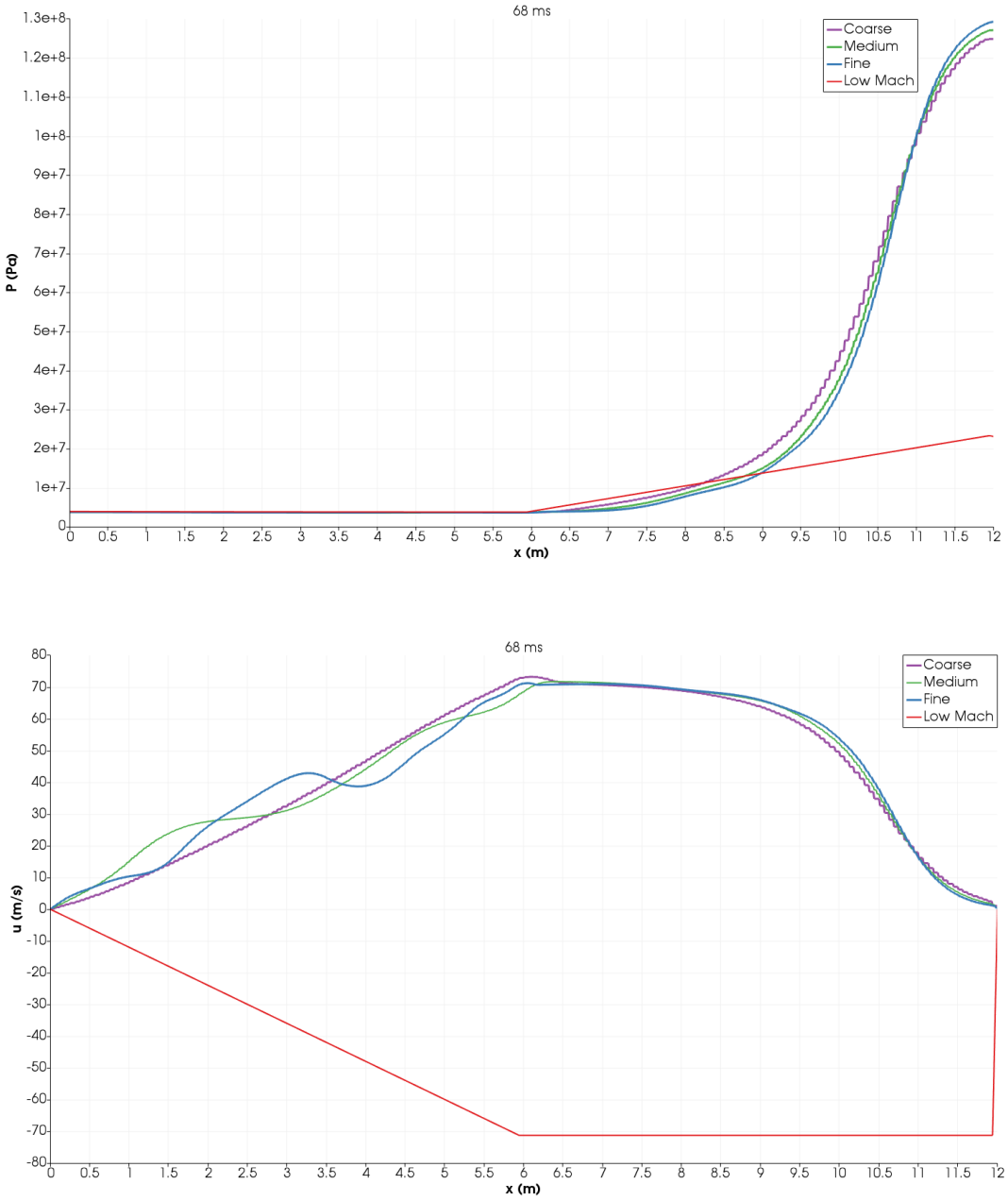

Figure 4.11: Strong bubble expansion problem (100 bars). Comparison between DEM and bubble (low-Mach) model. Pressure and velocity fields at 68 ms. Limited linear space reconstruction for primitive variables and 2-stage Runge-Kutta time discretization, $CFL = 0.5$.

As previously mentioned, since we are in the low-Mach number regime, the (weak) shock and rarefaction waves can be considered as acoustic waves. Consequently, the average pressure in gas regions and the kinetic energy of water represent the main loads applied on a structure. In Figure 4.12, we present the average pressures in the bubble, in the low-pressure gas regions and the "equilibrium" pressure P_e. In Figure 4.13, we compare the exergy of the system and the kinetic energy of liquid water (which is almost equal to the total kinetic energy of the whole system). As one can see, before the water column inverts its motion, the average pressures in regions 1 and 3 computed from the compressible model (formulas (4.31), (4.32)) are close to the bubble model solutions. However, the maximum average pressure of the region 3 given by the bubble model is much higher than the pressure given by the DEM model. The solutions

are clearly shifted in time and, as already explained, this is related to the sound speed of the different models. Because of the finite speed of propagation for the acoustic waves in the compressible calculation, the minimum bubble pressure (region 1) or absorber peak pressure (region 3) is reached slightly later (hence the large pressure difference previously observed in Figure 4.11). Another consequence is the much larger peak of pressure observed in the absorber (region 3) for the low-Mach solution with respect to the compressible solution. The finite value of the sound speed is indeed responsible for the weaker momentum variation of the liquid column in the compressible solutions.
It is clear that some of the low-Mach assumptions are violated around the moment when the water changes its direction. The analysis of the "equilibrium" pressure P_e and the exergy justifies this point.
In the bottom of Figure 4.12, we can see that after the inversion time, the DEM-computed equilibrium pressure in the fine mesh shows less error compared to other meshes (with the bubble model solution taken as reference). This is expected since it is directly related to the anergy of the system, which increases with the production of (numerical and physical) entropy (the finest mesh giving the least numerical entropy production).
In the same manner the exergy of the system and the kinetic energy of the water are presented in Figure 4.13. The solutions before the liquid column inverts its motion is satisfactory but differences between them are observed after this instant. In general, they increase with the mesh refinement since less initial energy is (numerically) converted into heat. The time-shift phenomenon is also observed.

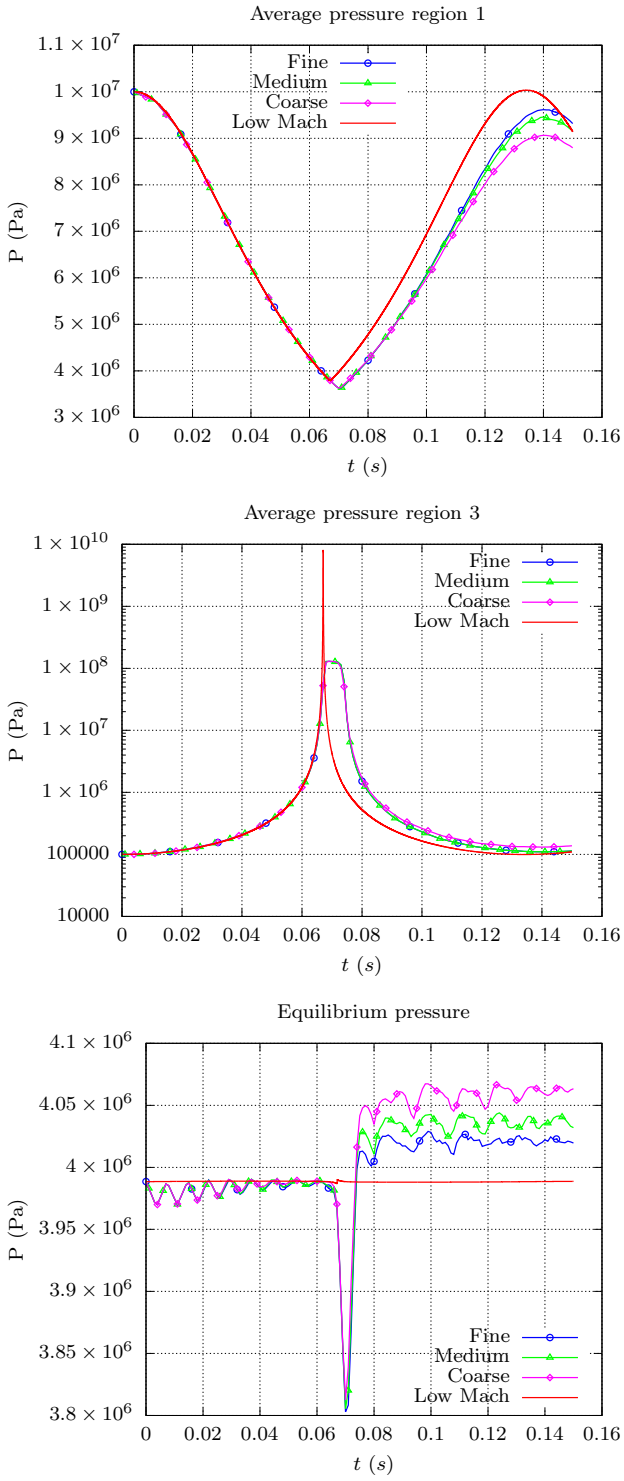

Figure 4.12: Strong bubble expansion problem (100 bars). Comparison between DEM and bubble (low-Mach) model. Average pressures in the regions 1, 3 and the "equilibrium" pressure P_e. Limited linear space reconstruction for primitive variables and 2-stage Runge-Kutta time discretization, $CFL = 0.5$.

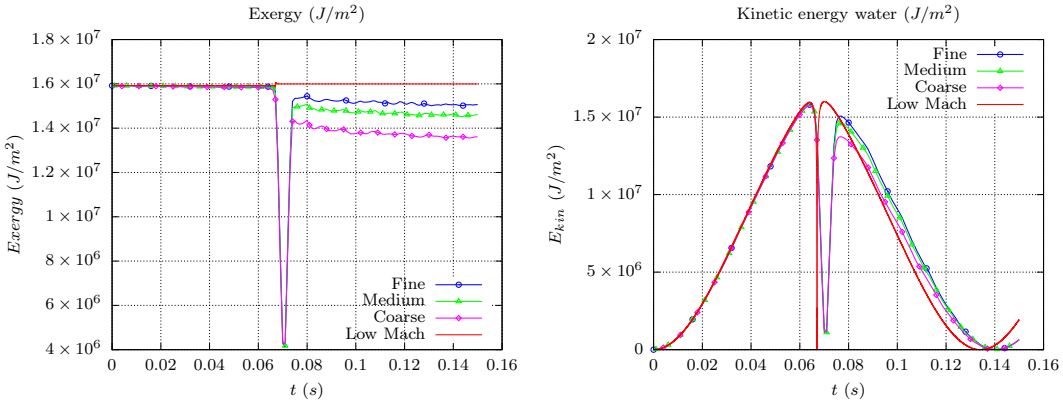

Figure 4.13: Strong bubble expansion problem (100 bars). Comparison between DEM and bubble (low-Mach) model. The exergy E_{exe} (J/m^2) and the kinetic energy of water (J/m^2). Limited linear space reconstruction for primitive variables and 2-stage Runge-Kutta time discretization, $CFL = 0.5$.

4.3.3.2 Weak bubble expansion problem (10 bars)

We repeat the computations with the new initial conditions specified in Table 4.2. The mesh resolution is the same as in the 100 bars case. The compressible results at different successive times are presented in Figures 4.14 - 4.18 along with the bubble model solution (low-Mach).
Figure 4.14 displays the initial stage ($t = 5\,ms$) of the problem. The solution structure is similar to the case of 100 bars. The bubble-water interface generates: a (weak) right-propagating shock wave, a left-propagating rarefaction and a right-propagating contact wave. The speed of the liquid column in the region perturbed by the shock wave the contact wave can be easily approximated by the Joukowski formula:

$$u \approx \frac{p_{B,0} - p_{W,0}}{\rho_{W,0} c_{W,0}} = \frac{9 \times 10^5}{1000 \times 1625} \approx 0.55\ m/s$$

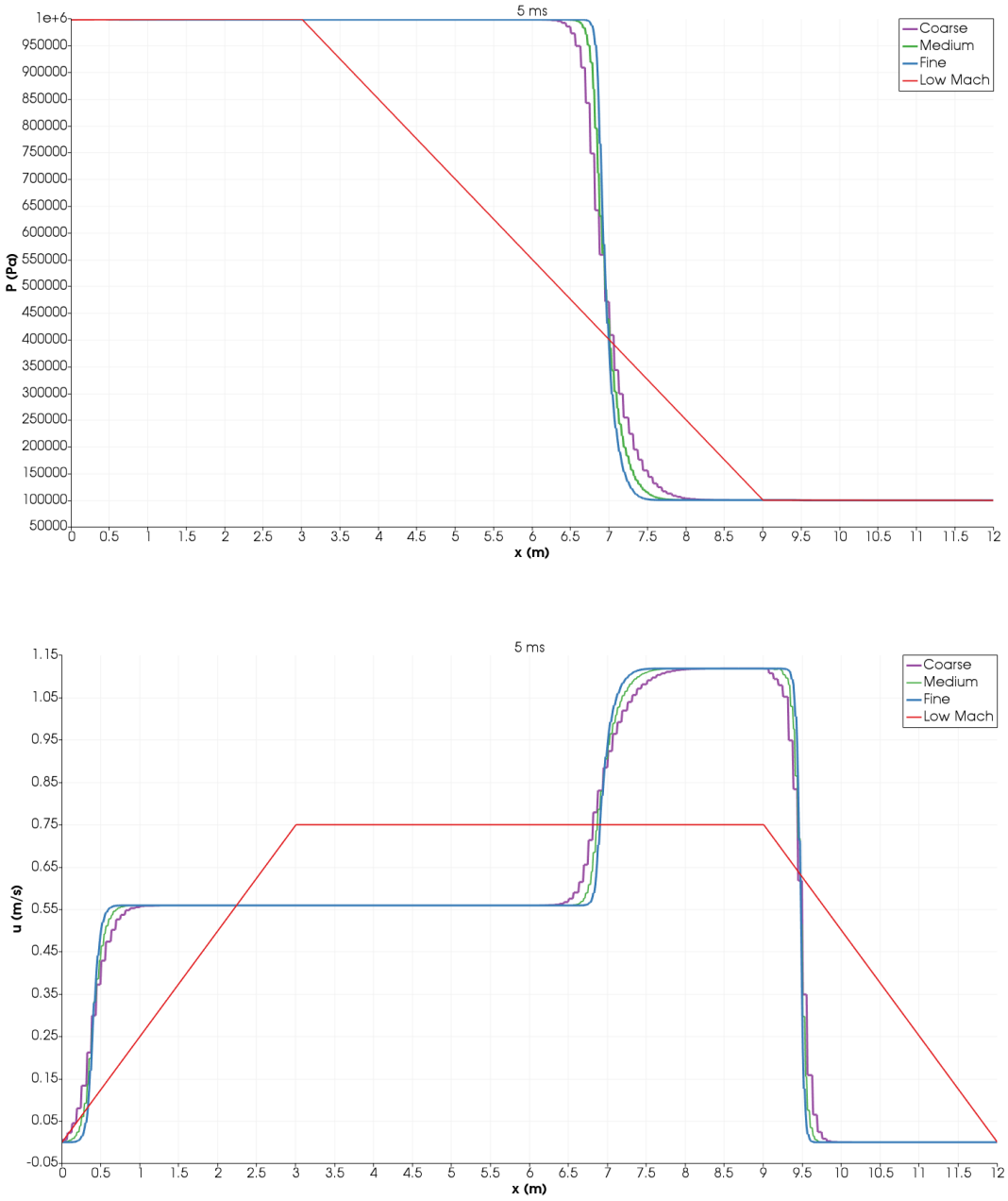

Figure 4.14: Weak bubble expansion problem (10 bars). Comparison between DEM and bubble (low-Mach) model. Pressure and velocity fields at 5 ms. Limited linear space reconstruction for primitive variables and 2-stage Runge-Kutta time discretization, $CFL = 0.5$.

Figure 4.15 displays the early stage of the low-Mach behavior of the compressible solutions ($t = 150\,ms$). As we can see, these DEM-computed compressible solutions show a rather good agreement with the bubble model reference solution. The mesh refinement effect on the compressible solution is still visible on the pressure distribution but quite limited for the velocity distribution.

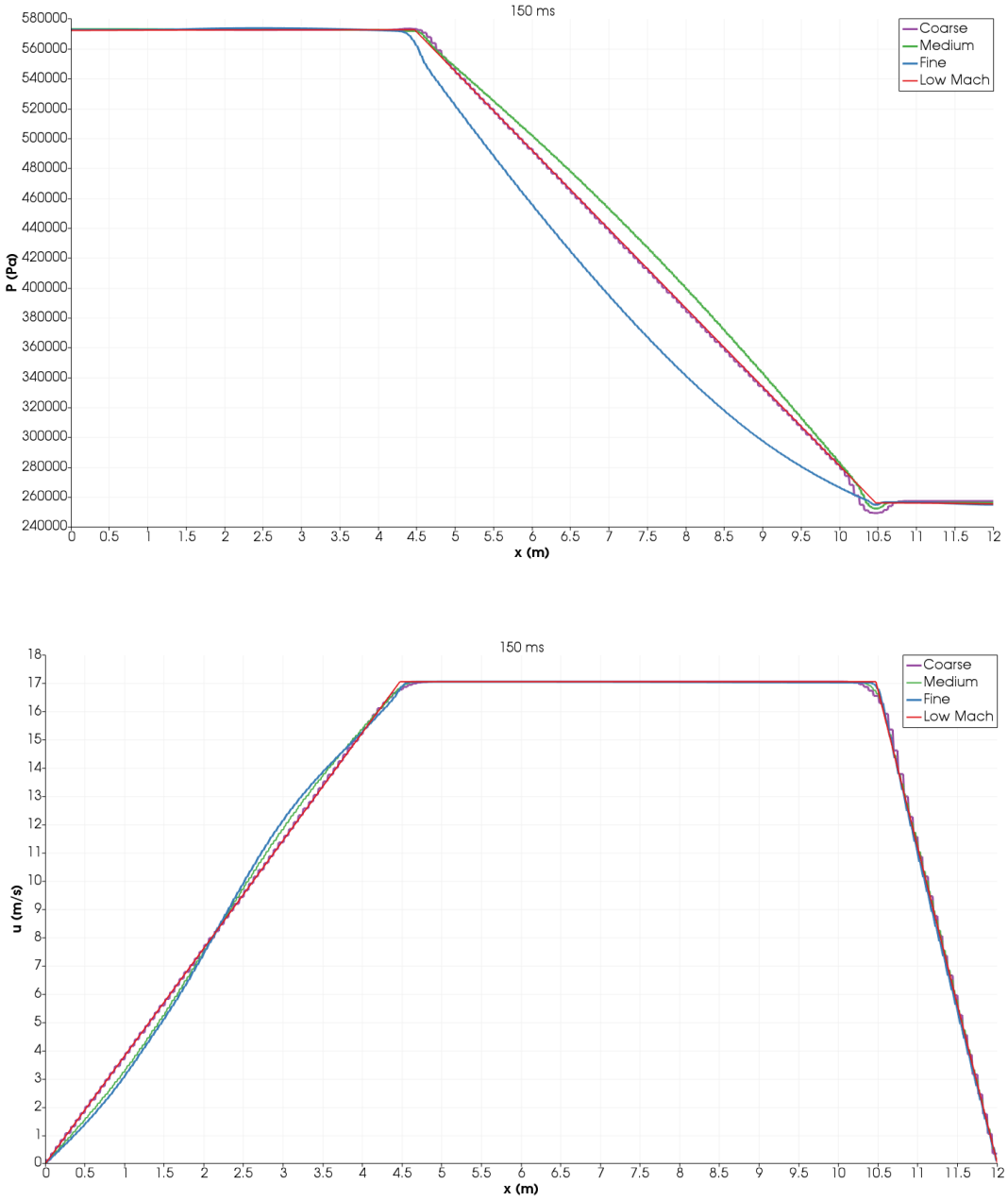

Figure 4.15: Weak bubble expansion problem (10 bars). Comparison between DEM and bubble (low-Mach) model. Pressure and velocity fields at 150 ms. Limited linear space reconstruction for primitive variables and 2-stage Runge-Kutta time discretization, $CFL = 0.5$.

Figures 4.16, 4.17 display the instants before and after the water column in the bubble model reverts its motion. The time-shift phenomenon can only be identified by the velocity in the bubble region. While the velocity of the bubble is (already) negative in the bubble model (due to the boundary condition at the bubble-water interface), that velocity in the compressible model is still positive since the flow is decelerated by finite-speed waves. The column water in the compressible model changes its direction at (almost) the same time as in the bubble model.

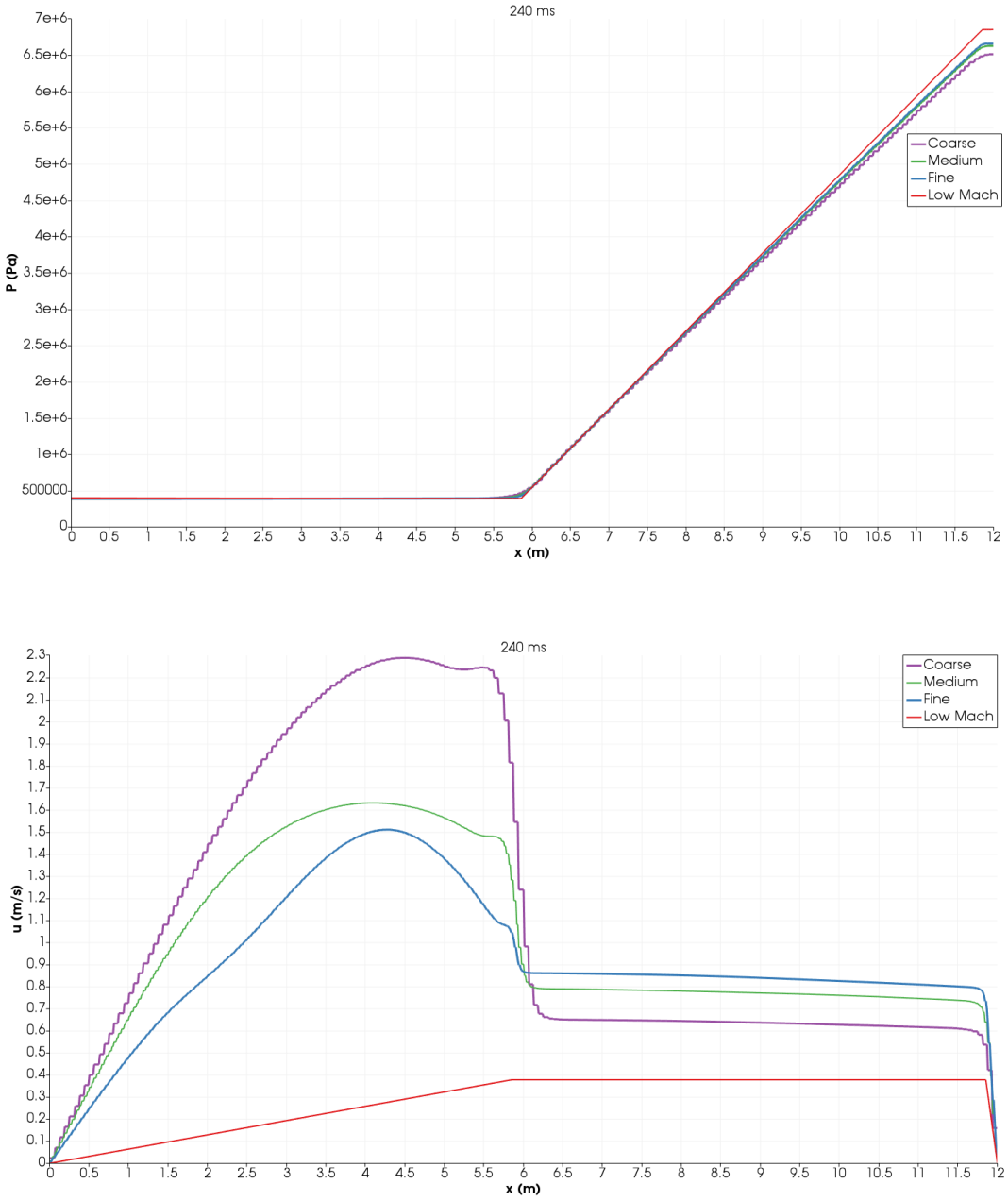

Figure 4.16: Weak bubble expansion problem (10 bars). Comparison between DEM and bubble (low-Mach) model. Pressure and velocity fields at 240 ms. Limited linear space reconstruction for primitive variables and 2-stage Runge-Kutta time discretization, $CFL = 0.5$.

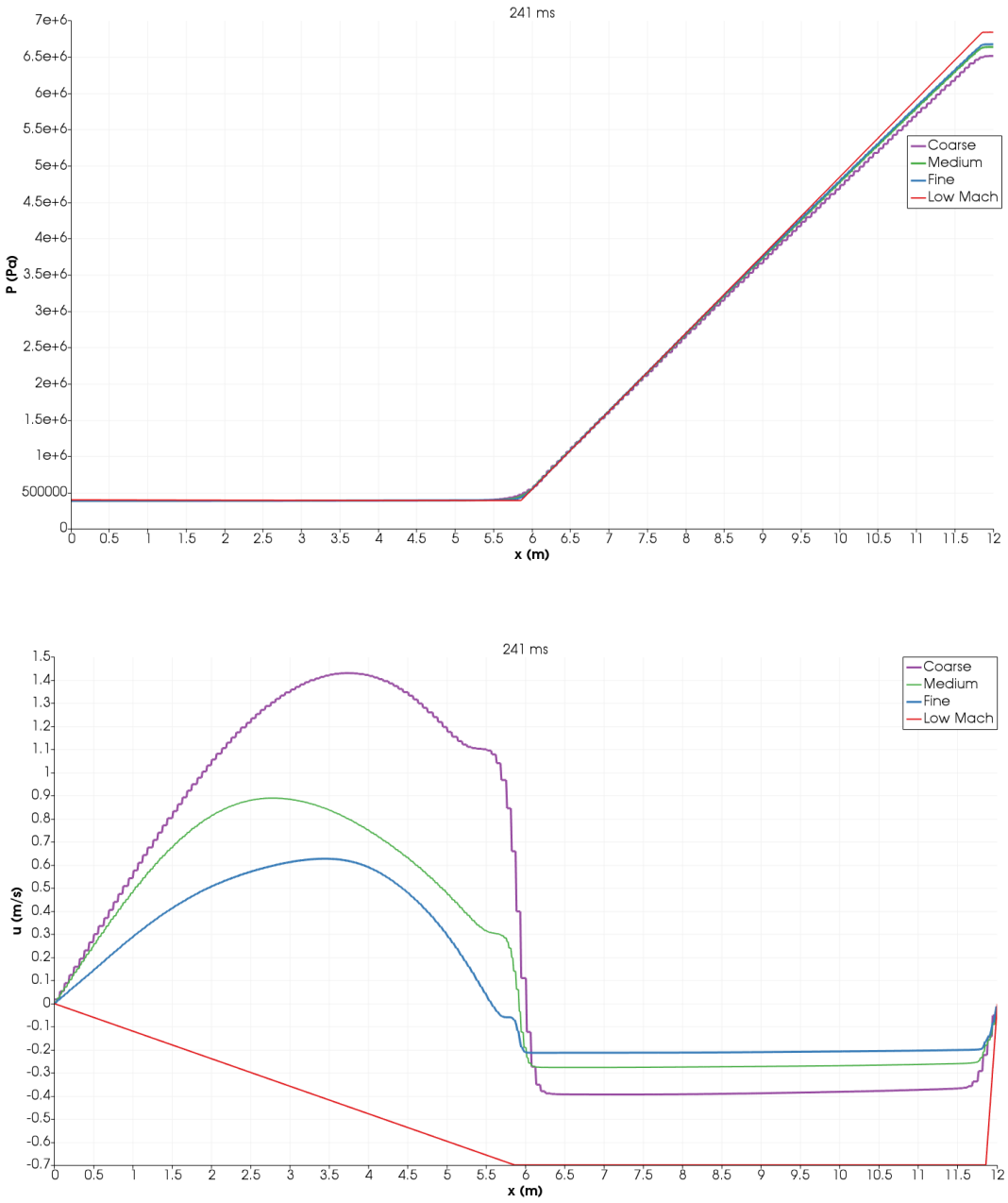

Figure 4.17: Weak bubble expansion problem (10 bars). Comparison between DEM and bubble (low-Mach) model. Pressure and velocity fields at 241 ms. Limited linear space reconstruction for primitive variables and 2-stage Runge-Kutta time discretization, $CFL = 0.5$.

In Figure 4.18, we present the solution after ($t = 270\,ms$) the inversion time of the water column: the bubble is in the compression phase and region 3 is in expansion. The low-Mach behavior of the compressible solutions is clearly recovered.

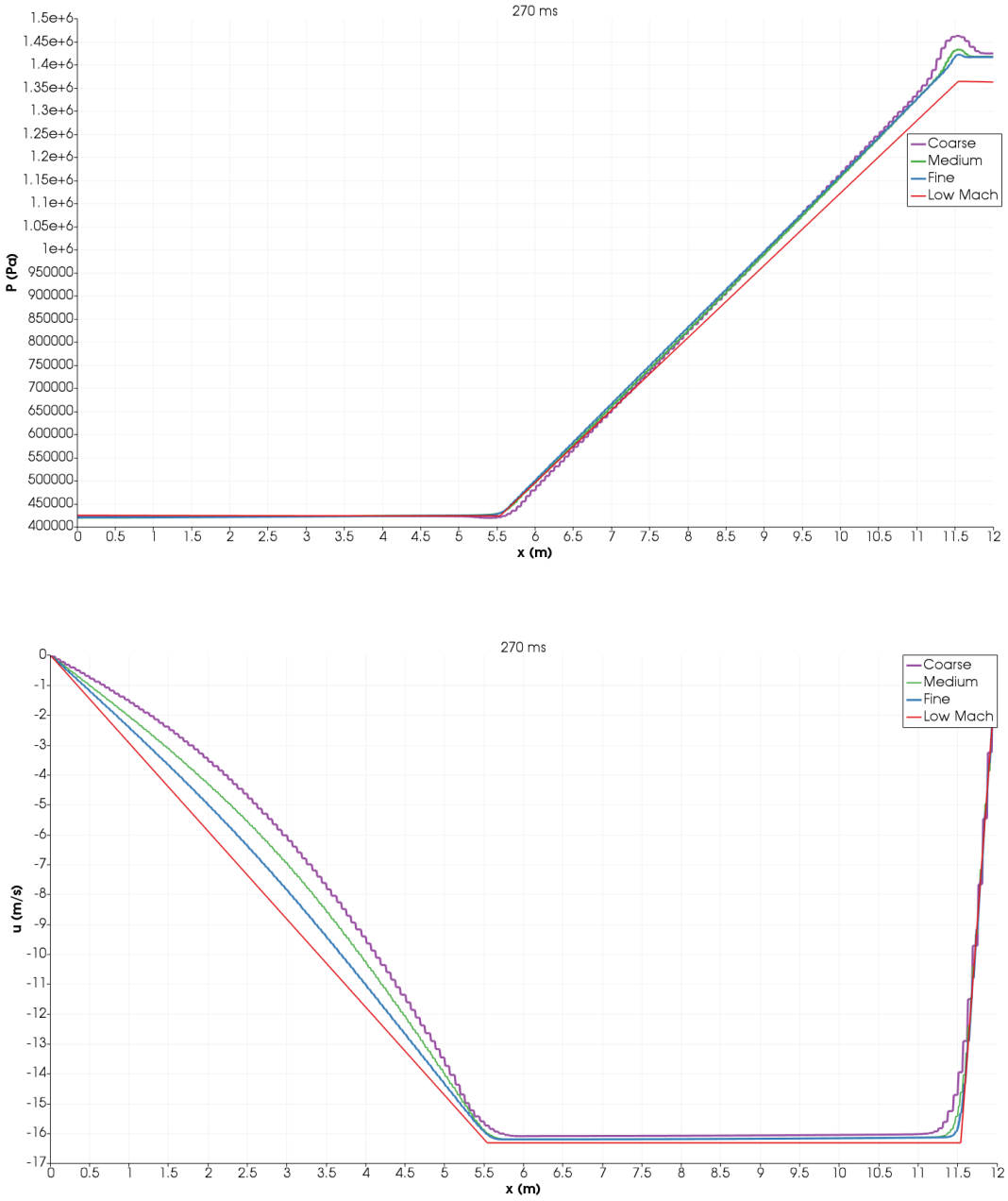

Figure 4.18: Weak bubble expansion problem (10 bars). Comparison between DEM and bubble (low-Mach) model. Pressure and velocity fields at 270 ms. Limited linear space reconstruction for primitive variables and 2-stage Runge-Kutta time discretization, $CFL = 0.5$.

In Figure 4.19, we compare the average pressure of gases and the equilibrium pressure. The average pressures of gases before and after the water column changes its direction are very close to each other and the time-shift phenomenon is negligible. The error in the computed equilibrium pressure with respect to the bubble reference solution decreases as expected with the mesh refinement.
In Figure 4.20, we compare the kinetic energy of water and the exergy of the system. The computed exergies are very close to each other and follow the same tendency as in the 100 bars case. The kinetic energies do not present much difference and the time-shift phenomenon is negligible.
It can be stated from this test case that the compressible solutions are very close to the bubble model solution at the low-Mach number limit (except for some very specific time instants, at the beginning of the

flow evolution or when the water inverts its direction). The bubble model estimates correctly the average pressure in gas regions, the kinetic energy of water and the time-shift phenomenon is negligible. This is expected since the characteristic time associated with the physical phenomena for this weak bubble case is much larger than the previous strong bubble case. Moreover, a lower initial energy level inside the bubble results in less high-frequency and high-amplitude waves compared to the strong case (which is justified in Figure 4.15 where the solution on the fine mesh does not show important oscillations and is very close to the bubble model one). The water column in the bubble model accelerates, decelerates and inverts its motion in a much more progressive way and at much lower speed and therefore in a certain way similar to the compressible model where the progressive motion of water is induced by finite-speed waves.

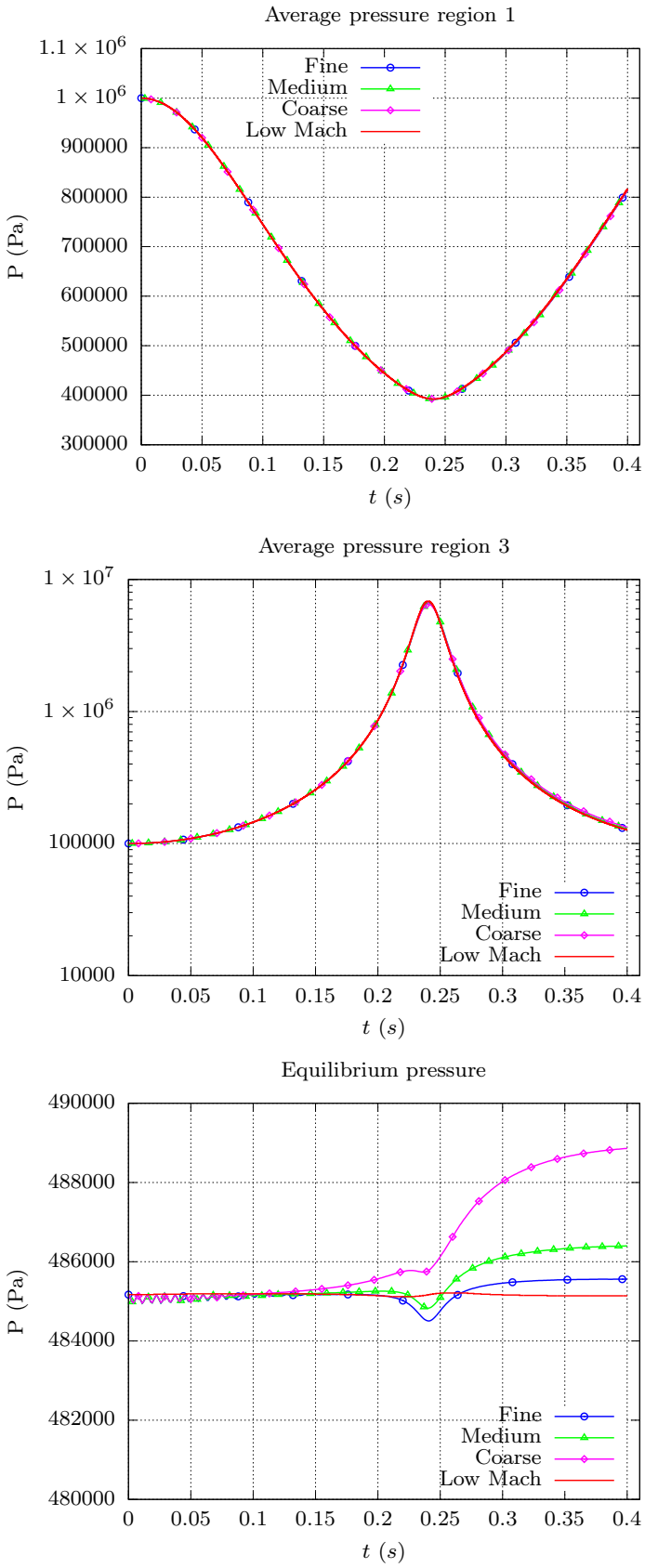

Figure 4.19: Weak bubble expansion problem (10 bars). Comparison between DEM and bubble (low-Mach) model. Average pressures in the regions 1, 3 and the "equilibrium" pressure P_e. Limited linear space reconstruction for primitive variables and 2-stage Runge-Kutta time discretization, $CFL = 0.5$.

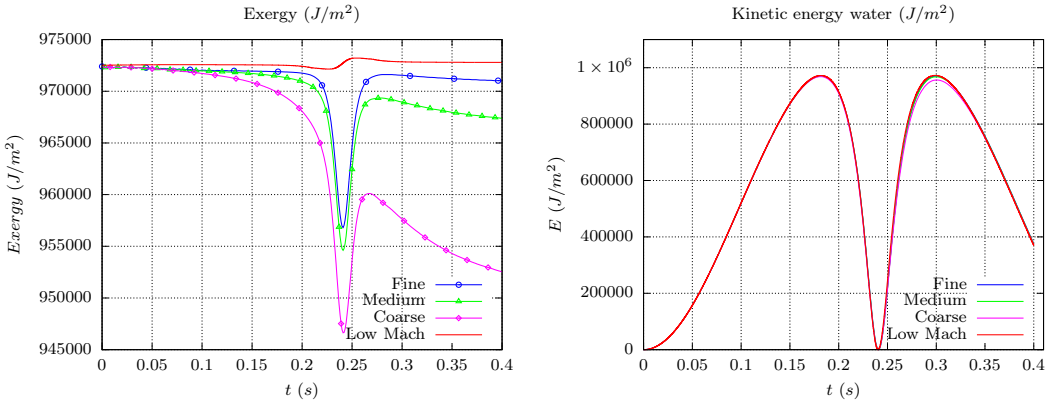

Figure 4.20: Weak bubble expansion problem (10 bars). Comparison between DEM and bubble (low-Mach) model. The exergy E_{exe} (J/m^2) and the kinetic energy of water (J/m^2). Limited linear space reconstruction for primitive variables and 2-stage Runge-Kutta time discretization, $CFL = 0.5$.

Conclusion

In this chapter, we have first briefly reviewed the DEM method for computing compressible two-fluid problems in both the Eulerian case and the ALE case. We have derived next a so-called bubble model for a simplified 1D low-Mach bubble expansion which corresponds to a particular case of the asymptotic model. The idea is to assess the relevance of this two-phase low-Mach asymptotic model with respect to fully compressible numerical solutions. Performing the analysis for a simplified 1D bubble expansion problem allowed to derive an exact analytical solution of the low-Mach asymptotic model. The numerical experiments performed in this chapter with the DEM compressible solutions compared with the low-Mach analytical solution show that the bubble model derived is indeed a good approximation of the DEM method in computing two-phase problems in the low-Mach number regime. More precisely, it was shown the agreement between both approaches is very good for a weak bubble expansion problem and remains satisfactory even for a strong bubble expansion problem. Consequently, the asymptotic model can be used as a starting point for the extension of the AC-LM method to the efficient computation of low-Mach two-phase flows. The development of a low-Mach extension of the DEM method built on a two-step AC approach will be presented in chapter 5 with the purpose of reducing the computational cost while preserving accuracy for the physical features of interest.

5

DEM-LM: Discrete Equation Method in the Low-Mach number regime

Contents

Introduction

In this chapter, we present an original method to efficiently compute low-Mach two-phase flow problems without degrading the accuracy level of the physical prediction. This new method combines the DEM principles for computing two-phase flow problems and the Artificial Compressibility (AC) approach introduced in sections 3.3 and 3.4 to deal with low-Mach single-phase flows. The novel method developed and applied in this chapter could have been denoted DEM-AC-LM to make this combination as explicit as possible but we opted for the shorter denomination DEM-LM.
The organization of the chapter is as follows. In section 5.1, we present the physical model at the basis of the DEM-LM method, which is a generalization of the simplified bubble model introduced in the previous chapter. In section 5.2, we present the discretization of this physical model and in section 5.3, we show the performance of the DEM-LM approach for numerically computing the low-Mach bubble expansion problem.

5.1 Physical model

The two-fluid model in development considers each phase separately and thus the inviscid flow is governed by two sets of Euler equations. In the low-Mach number regime, we can write the system of Euler equations in primitive form for phase k as:

$$\begin{array}{lllll}
\dfrac{\partial \rho_k}{\partial t} & + \ \mathbf{v}_k \cdot \nabla \rho_k & + \ \rho_k \nabla \cdot \mathbf{v}_k & = & 0 \\
\dfrac{\partial \mathbf{v}_k}{\partial t} & + \ \mathbf{v}_k \cdot \nabla \mathbf{v}_k & + \ \dfrac{1}{\rho_k} \nabla p_k & = & 0 \\
\dfrac{\partial p_k}{\partial t} & + \ \mathbf{v}_k \cdot \nabla p_k & + \ \rho_k c_k^2 \nabla \cdot \mathbf{v}_k & = & 0 \\
\dfrac{\partial (\rho_k e_k^t)}{\partial t} & + \ \mathbf{v}_k \cdot \nabla (\rho_k e_k^t + p_k) & + \ (\rho_k e_k^t + p_k) \nabla \cdot \mathbf{v}_k & = & 0 \\
\dfrac{\partial (\rho_k \mathbf{Y}_k)}{\partial t} & + \ \mathbf{v}_k \cdot \nabla (\rho_k \mathbf{Y}_k) & + \ (\rho_k \mathbf{Y}_k) \nabla \cdot \mathbf{v}_k & = & 0
\end{array} \tag{5.1}$$

We notice that the total energy conservation equation and the transport equations for the mass fractions are maintained in (5.1) so that the structure of the EUROPLEXUS computational code is least modified when adapted to the DEM-LM method. Adding and subtracting the same quantity $\rho_k c_{AC,k}^2 \nabla \cdot \mathbf{v}_k$ in the pressure evolution equation $(5.1)_3$, we obtain:

$$\begin{array}{llllll}
\dfrac{\partial \rho_k}{\partial t} & + \ \mathbf{v}_k \cdot \nabla \rho_k & = & 0 & -\rho_k \nabla \cdot \mathbf{v}_k \\
\dfrac{\partial \mathbf{v}_k}{\partial t} & + \ \mathbf{v}_k \cdot \nabla \mathbf{v}_k + \dfrac{1}{\rho_k} \nabla p_k & = & 0 & \\
\dfrac{\partial p_k}{\partial t} & + \ \mathbf{v}_k \cdot \nabla p_k & = & -\rho_k c_{AC,k}^2 \nabla \cdot \mathbf{v}_k & -(\rho_k c_k^2 - \rho_k c_{AC,k}^2) \nabla \cdot \mathbf{v}_k \\
\dfrac{\partial (\rho_k e_k^t)}{\partial t} & + \ \mathbf{v}_k \cdot \nabla (\rho_k e_k^t + p_k) & = & 0 & -(\rho_k e_k^t + p_k) \nabla \cdot \mathbf{v}_k \\
\dfrac{\partial (\rho_k \mathbf{Y}_k)}{\partial t} & + \ \mathbf{v}_k \cdot \nabla (\rho_k \mathbf{Y}_k) & = & \underbrace{0}_{\text{Part I}} & \underbrace{-(\rho_k \mathbf{Y}_k) \nabla \cdot \mathbf{v}_k}_{\text{Part II}}
\end{array} \tag{5.2}$$

The parameter $c_{AC,k}$ in (5.2) corresponds to the artificial sound speed which is now defined for each phase. Moreover, we can observe that system (5.2) is divided into two parts (in a way similar to the one adopted for the single-phase AC-LM method). Part I, which will be studied in section 5.1.1, corresponds to the convective mechanism with fast acoustic waves filtered through the use of the artificial sound speed. Part II, which will be studied in section 5.1.2, considers the isentropic transformation through the velocity divergence term $\nabla \cdot \mathbf{v}_k$.

5.1.1 Part I: convective mechanism

Part I of system (5.2) describes the convective mechanism of the slow artificial pressure waves of small amplitudes:

$$\begin{array}{lcll}
\dfrac{\partial \rho_k}{\partial t} & + & \mathbf{v}_k \cdot \nabla \rho_k & = 0 \\
\dfrac{\partial \mathbf{v}_k}{\partial t} & + & \mathbf{v}_k \cdot \nabla \mathbf{v}_k + \dfrac{1}{\rho_k} \nabla p_k & = 0 \\
\dfrac{\partial p_k}{\partial t} & + & \mathbf{v}_k \cdot \nabla p_k & = -\rho_k c_{AC,k}^2 \nabla \cdot \mathbf{v}_k \\
\dfrac{\partial (\rho_k e_k^t)}{\partial t} & + & \mathbf{v}_k \cdot \nabla (\rho_k e_k^t + p_k) & = 0 \\
\dfrac{\partial (\rho_k \mathbf{Y}_k)}{\partial t} & + & \mathbf{v}_k \cdot \nabla (\rho_k \mathbf{Y}_k) & = 0
\end{array} \tag{5.3}$$

Some key characteristics of system (5.3) can be underlined:

- The system does not conserve the mass and the total energy. The density (as well the mass fraction) is transported by velocity $\mathbf{v}_k$. In this way, we avoid the undesirable density jump when reducing the sound speed (see section 3.2).
- The convective mechanism of the fast acoustic wave at speed c is replaced by the propagation of the slower artificial acoustic wave at speed c_{AC}. This parameter is normally chosen to be much smaller than the physical sound speed: $c_{AC} << c$ (normally chosen $c_{AC} \approx c/10$, see [Madsen and Schäffer, 2006]).

In a more conservative form, system (5.3) can be recast as:

$$\begin{array}{lcll}
\dfrac{\partial \rho_k}{\partial t} & + & \nabla \cdot (\rho_k \mathbf{v}_k) & = \rho_k \nabla \cdot \mathbf{v}_k \\
\dfrac{\partial (\rho_k \mathbf{v}_k)}{\partial t} & + & \nabla \cdot (\rho_k \mathbf{v}_k \otimes \mathbf{v}_k + p_k \mathcal{I}) & = (\rho_k \mathbf{v}_k) \nabla \cdot \mathbf{v}_k \\
\dfrac{\partial p_k}{\partial t} & + & \nabla \cdot (p_k \mathbf{v}_k) & = (p_k - \rho_k c_{AC,k}^2) \nabla \cdot \mathbf{v}_k \\
\dfrac{\partial (\rho_k e_k^t)}{\partial t} & + & \nabla \cdot ((\rho_k e_k^t + p_k) \mathbf{v}_k) & = (\rho_k e_k^t + p_k) \nabla \cdot \mathbf{v}_k \\
\dfrac{\partial (\rho_k \mathbf{Y}_k)}{\partial t} & + & \nabla \cdot (\rho_k \mathbf{Y}_k \mathbf{v}_k) & = (\rho_k \mathbf{Y}_k) \nabla \cdot \mathbf{v}_k
\end{array} \tag{5.4}$$

and in compact form, system (5.4) is expressed as:

$$\frac{\partial \mathbf{a}_k}{\partial t} + \nabla \cdot \mathbf{f}_k = \mathbf{b}_k \nabla \cdot \mathbf{v}_k \tag{5.5}$$

with

$$\mathbf{a}_k = \begin{pmatrix} \rho_k \\ \rho_k \mathbf{v}_k \\ p_k \\ \rho_k e_k^t \\ \rho_k \mathbf{Y}_k \end{pmatrix}, \quad \mathbf{f}_k = \begin{pmatrix} \rho_k \mathbf{v}_k \\ \rho_k \mathbf{v}_k \otimes \mathbf{v}_k + p_k \mathcal{I} \\ p_k \mathbf{v}_k \\ (\rho_k e_k^t + p_k) \mathbf{v}_k \\ \rho_k \mathbf{Y}_k \mathbf{v}_k \end{pmatrix}, \quad \mathbf{b}_k = \begin{pmatrix} \rho_k \\ \rho_k \mathbf{v}_k \\ p_k - \rho_k c_{AC,k}^2 \\ \rho_k e_k^t + p_k \\ \rho_k \mathbf{Y}_k \end{pmatrix}$$

Following the DEM method described in section 4.1 (see also [Abgrall and Saurel, 2003, Tang, 2012]), system (5.5) is coupled with the averaged topological equation (4.7):

$$\frac{\partial \alpha_k}{\partial t} + \mathbf{v}_I \cdot \nabla \alpha_k = 0$$

Multiplying the volume fraction α_k to both sides of (5.5), we obtain:

$$\alpha_k \frac{\partial \mathbf{a}_k}{\partial t} + \alpha_k \nabla \cdot \mathbf{f}_k = \alpha_k \mathbf{b}_k \nabla \cdot \mathbf{v}_k$$

which can then be rewritten in the form:

$$\frac{\partial (\alpha \mathbf{a})_k}{\partial t} + \nabla \cdot (\alpha \mathbf{f})_k \quad = \quad \mathbf{f}_k^{Lag} \cdot \nabla \alpha_k + (\alpha \mathbf{b})_k \nabla \cdot \mathbf{v}_k \tag{5.6}$$

Similarly to the DEM method, the term $\mathbf{f}_k^{Lag} = \mathbf{f}_{k,I} - \mathbf{a}_{k,I}\mathbf{v}_I$ is called the Lagrangian flux and needs only to be defined on the interface between phases:

$$\mathbf{f}_k^{Lag} = \begin{pmatrix} \rho_{k,I}(\mathbf{v}_{k,I} - \mathbf{v}_I) \\ \rho_k \mathbf{v}_{k,I}(\mathbf{v}_{k,I} - \mathbf{v}_I) + p_{k,I} \\ p_{k,I}(\mathbf{v}_{k,I} - \mathbf{v}_I) \\ \rho_k e^t_{k,I}(\mathbf{v}_{k,I} - \mathbf{v}_I) + p_{k,I}\mathbf{v}_{k,I} \\ \rho_{k,I}\mathbf{Y}_{k,I}(\mathbf{v}_{k,I} - \mathbf{v}_I) \end{pmatrix} \tag{5.7}$$

In case of impermeable interfaces, the Lagrangian flux (5.7) reduces to (see (4.10), see also [Tang, 2012]):

$$\mathbf{f}_k^{Lag} = \begin{pmatrix} 0 \\ p_I \mathcal{I} \\ 0 \\ p_I \mathbf{v}_I \\ 0 \end{pmatrix} \tag{5.8}$$

It is clearly observed that system (5.6) displays one extra equation compared to the physical two-fluid model described in the DEM method (4.8). This extra equation corresponds to the evolution of the pressure field. Moreover, we have the contribution of the source term $\alpha_k \mathbf{b}_k \nabla \cdot \mathbf{v}_k$ in the R.H.S of (5.6). As a result, the computation of this term is the main ingredient in part I of the DEM-LM method. System (5.6) is closed by the SG-EOS (4.3) and by the determination of the interface variables p_I and $\mathbf{v}_I$ obtained by solving the two-phase RP at the intercell boundaries.
In conclusion, part I of the two-fluid model involving impermeable interfaces in the low-Mach number regime can be written as:

$$\begin{array}{lcll}
\dfrac{\partial \alpha_k}{\partial t} & + & \mathbf{v}_I \cdot \nabla \alpha_k & = \quad 0 \\
\dfrac{\partial (\alpha_k \rho_k)}{\partial t} & + & \nabla \cdot (\alpha_k \rho_k \mathbf{v}_k) & = \quad (\alpha_k \rho_k) \nabla \cdot \mathbf{v}_k \\
\dfrac{\partial (\alpha_k \rho_k \mathbf{v}_k)}{\partial t} & + & \nabla \cdot (\alpha_k (\rho_k \mathbf{v}_k \otimes \mathbf{v}_k + p_k \mathcal{I})) & = \quad (\alpha_k \rho_k \mathbf{v}_k) \nabla \cdot \mathbf{v}_k + p_I \nabla \alpha_k \\
\dfrac{\partial (\alpha_k p_k)}{\partial t} & + & \nabla \cdot (\alpha_k p_k \mathbf{v}_k) & = \quad \left(\alpha_k (p_k - \rho_k c^2_{AC,k}) \right) \nabla \cdot \mathbf{v}_k \\
\dfrac{\partial (\alpha_k \rho_k e^t_k)}{\partial t} & + & \nabla \cdot \left(\alpha_k (\rho_k e^t_k + p_k) \mathbf{v}_k \right) & = \quad \left(\alpha_k (\rho_k e^t_k + p_k) \right) \nabla \cdot \mathbf{v}_k \\
 & & & \quad + p_I \mathbf{v}_I \nabla \alpha_k \\
\dfrac{\partial (\alpha_k \rho_k \mathbf{Y}_k)}{\partial t} & + & \nabla \cdot (\alpha_k \rho_k \mathbf{Y}_k \mathbf{v}_k) & = \quad (\alpha_k \rho_k \mathbf{Y}_k) \nabla \cdot \mathbf{v}_k
\end{array} \tag{5.9}$$

Note that system (5.9) can be solved without actually computing the evolution equation for the total energy (since the pressure equation is available). Indeed, we prefer not to solve this equation but rather compute the total energy from the internal energy and velocity and obtain the internal energy from the

pressure and the density using the EOS after solving part II of the physical model. This point will be addressed in section 5.2.4. We emphasize again that the presence of the total energy equation in system 5.9 is retained to reflect the actual minimal modifications brought to the EUROPLEXUS computational code when implementing the DEM-LM approach. When compared to the original DEM model (available for the fully compressible model), system (5.9) introduces, as already emphasized, one extra equation for the pressure and source terms in the R.H.S of (5.9).

5.1.2 Part II: isentropic transformation

In part II, we take into account the filtering of the fast acoustic waves of system (5.10):

$$\begin{aligned}
\frac{\partial \rho_k}{\partial t} &= -\rho_k \nabla \cdot \mathbf{v}_k \\
\frac{\partial \mathbf{v}_k}{\partial t} &= 0 \\
\frac{\partial p_k}{\partial t} &= -(\rho_k c_k^2 - \rho_k c_{AC,k}^2) \nabla \cdot \mathbf{v}_k \\
\frac{\partial (\rho_k e_k^t)}{\partial t} &= -(\rho_k e_k^t + p_k) \nabla \cdot \mathbf{v}_k \\
\frac{\partial (\rho_k \mathbf{Y}_k)}{\partial t} &= -\rho_k \mathbf{Y}_k \nabla \cdot \mathbf{v}_k
\end{aligned} \tag{5.10}$$

by imposing that the divergence of the velocity $\nabla \cdot \mathbf{v}_k$ is a function of time only. This comes from the asymptotic system discussed in section 1.2 for a closed domain in which the compability condition for each phase reads:

$$\nabla \cdot \mathbf{v}_k = -\frac{1}{\rho_k c_k^2} \frac{dP_k}{dt} = f(t) \tag{5.11}$$

It can be seen from (5.10) that the determination of $\nabla \cdot \mathbf{v}_k$ is the key step in finding the solution at the new instant since the other variables in the R.H.S of (5.10) are in general known from the output of part I.

5.2 DEM-LM: Discrete Equation Method in the Low-Mach number regime

In this section, the physical model previously described is discretized using a two-step method, each step corresponding to each part of the model. The first step involves discretising the hyperbolic part (part I). Let $\mathbb{L}_h^{\Delta t}$ be the hyperbolic operator, we find the solution after a time step Δt by:

$$\mathbf{A}_{k,i}^{n+1,*} = \mathbb{L}_h^{\Delta t} \mathbf{A}_{k,i}^{n}$$

The second step corrects the solutions of part I by considering the isentropic transformation. Let $\mathbb{L}_{is}$ be the isentropic operator, we find the solution at the new instant by:

$$\mathbf{A}_{k,i}^{n+1} = \mathbb{L}_{is} \mathbf{A}_{k,i}^{n+1,*}$$

5.2.1 Part I: General formulation

For the sake of simplicity, let us now recast (5.6) in one-dimensional form:

$$\frac{\partial (\alpha_k \mathbf{a}_k)}{\partial t} + \frac{\partial (\alpha_k \mathbf{f}_k)}{\partial x} = \mathbf{f}_k^{Lag} \frac{\partial \alpha_k}{\partial x} + \alpha_k \mathbf{b}_k \frac{\partial u_k}{\partial x} \tag{5.12}$$

As in DEM, the Lagrangian flux can be written in the form:

$$\mathbf{f}_k^{Lag}\frac{\partial \alpha_k}{\partial x} = \frac{\partial(\alpha_k \mathbf{f}_k^{Lag})}{\partial x} - \alpha_k \frac{\partial \mathbf{f}_k^{Lag}}{\partial x}$$

System (5.12) thus becomes:

$$\frac{\partial(\alpha_k \mathbf{a}_k)}{\partial t} + \frac{\partial(\alpha_k \mathbf{f}_k)}{\partial x} = \frac{\partial(\alpha_k \mathbf{f}_k^{Lag})}{\partial x} - \alpha_k \frac{\partial \mathbf{f}_k^{Lag}}{\partial x} + \alpha_k \mathbf{b}_k \frac{\partial u_k}{\partial x} \tag{5.13}$$

Let us directly derive the general ALE formulation. By integrating (5.13) over a cell $C_i = [x_{i-1/2}(t), x_{i+1/2}(t)]$ and using the Reynolds transport theorem, we obtain the semi-discrete form:

$$\begin{aligned} \frac{d}{dt}\int_{x_{i-1/2}(t)}^{x_{i+1/2}(t)} \alpha_k \mathbf{a}_k dx + \int_{x_{i-1/2}(t)}^{x_{i+1/2}(t)} \frac{\partial(\alpha_k \mathbf{f}_k^{ALE})}{\partial x} dx &= \int_{x_{i-1/2}(t)}^{x_{i+1/2}(t)} \mathbf{f}_k^{Lag}\frac{\partial \alpha_k}{\partial x} dx \\ &+ \int_{x_{i-1/2}(t)}^{x_{i+1/2}(t)} \alpha_k \mathbf{b}_k \frac{\partial u_k}{\partial x} \end{aligned} \tag{5.14}$$

where the ALE flux is defined by $\mathbf{f}_k^{ALE} = \mathbf{f}_k - u_m \mathbf{a}_k$ and u_m is the velocity of the intercell.

$$\mathbf{f}_k^{ALE} = \begin{pmatrix} \rho_k(u_k - u_m) \\ \rho_k u_k(u_k - u_m) + p_k \\ p_k(u_k - u_m) \\ \rho_k e_k^t(u_k - u_m) + p_k u_k \\ \rho_k \mathbf{Y}_k(u_k - u_m) \end{pmatrix}$$

The non-conservative term $\mathbf{f}_k^{Lag}\frac{\partial \alpha_k}{\partial x}$ can be decomposed similarly as in DEM:

$$\mathbf{f}_k^{Lag}\frac{\partial \alpha_k}{\partial x} = \frac{\partial(\alpha_k \mathbf{f}_k^{Lag})}{\partial x} - \alpha_k \frac{\partial \mathbf{f}_k^{Lag}}{\partial x}$$

By integrating the terms containing the ALE and Lagrangian fluxes in the system (5.14) over the time interval $[t^n, t^{n+1}]$, we obtain:

$$\int_{t^n}^{t^{n+1}} \int_{x_{i-1/2}(t)}^{x_{i+1/2}(t)} \frac{\partial(\alpha_k \mathbf{f}_k^{ALE})}{\partial x} dx dt = \Delta t(\alpha_{k,i+1/2}\mathbf{F}_{k,i+1/2}^{ALE} - \alpha_{k,i-1/2}\mathbf{F}_{k,i-1/2}^{ALE})$$

$$\int_{t^n}^{t^{n+1}} \int_{x_{i-1/2}(t)}^{x_{i+1/2}(t)} \frac{\partial(\alpha_k \mathbf{f}_k^{Lag})}{\partial x} dx dt = \Delta t(\alpha_{k,i+1/2}\mathbf{F}_{k,i+1/2}^{Lag} - \alpha_{k,i-1/2}\mathbf{F}_{k,i-1/2}^{Lag})$$

$$\int_{t^n}^{t^{n+1}} \int_{x_{i-1/2}(t)}^{x_{i+1/2}(t)} \alpha_k \frac{\partial \mathbf{f}_k^{Lag}}{\partial x} dx dt = \Delta t \alpha_{k,i}^n(\mathbf{F}_{k,i+1/2}^{Lag} - \mathbf{F}_{k,i-1/2}^{Lag})$$

Concerning the time-derivative term in (5.14), we get by integrating over time $[t^n, t^{n+1}]$:

$$\begin{aligned} \int_{t^n}^{t^{n+1}} \left(\frac{d}{dt}\int_{x_{i-1/2}(t)}^{x_{i+1/2}(t)} \alpha_k \mathbf{a}_k dx\right) dt &= \int_{x_{i-1/2}(t^{n+1})}^{x_{i+1/2}(t^{n+1})} \alpha_k \mathbf{a}_k dx - \int_{x_{i-1/2}(t^n)}^{x_{i+1/2}(t^n)} \alpha_k \mathbf{a}_k dx \\ &= \Delta x_i^{n+1}(\alpha \mathbf{A})_{k,i}^{n+1} - \Delta x_i^n (\alpha \mathbf{A})_{k,i}^n \end{aligned}$$

The integration of the source term associated to the divergence of velocity $\alpha_k \mathbf{b}_k \dfrac{\partial u_k}{\partial x}$ depends on the moving direction of the phase interface. Let $\mathbf{B}_{k,i}$ be its discrete form, we thus obtain the first order general ALE formulation for the DEM-LM:

$$\begin{aligned}(\alpha\mathbf{A})_{k,i}^{n+1} &= \frac{\Delta x_i^n}{\Delta x_i^{n+1}}(\alpha\mathbf{A})_{k,i}^n - \frac{\Delta t}{\Delta x_i^{n+1}}\left[(\alpha\mathbf{F}^{ALE})_{k,i+1/2} - (\alpha\mathbf{F}^{ALE})_{k,i-1/2}\right] \\ &+ \frac{\Delta t}{\Delta x_i^{n+1}}\left[\mathbf{F}^{Lag}_{k,i+1/2}(\alpha_{k,i+1/2} - \alpha_{k,i}^n) - \mathbf{F}^{Lag}_{k,i-1/2}(\alpha_{k,i-1/2} - \alpha_{k,i}^n)\right] \\ &+ \frac{\Delta t}{\Delta x_i^{n+1}}\mathbf{B}_{k,i}\end{aligned} \tag{5.15}$$

By setting the mesh velocity $u_m = 0$, one can obtain the Eulerian formulation. In such case, the ALE fluxes reduce to the Eulerian fluxes and there is no difference between the size of a cell at two consecutive time steps ($\Delta x_i^n = \Delta x_i^{n+1}$). By further setting the source term $B_{k,i} = 0$, one can recover the general formulation for the DEM method (except for an extra equation for the pressure).
In general, the computation of $\mathbf{A}_{k,i}^{n+1}$ requires:

- Δx_i^{n+1}, $\alpha_{k,i}^{n+1}$: volume and volume fraction at time $t = t^{n+1}$.
- $\alpha_{k,i\pm1/2}$: volume fraction at the intercell associated to the Lagrangian fluxes.
- $(\alpha\mathbf{F}^{ALE})_{k,i+1/2}$, $(\alpha\mathbf{F}^{ALE})_{k,i-1/2}$: numerical conservative ALE fluxes.
- $\mathbf{F}^{Lag}_{k,i+1/2}$, $\mathbf{F}^{Lag}_{k,i-1/2}$: numerical Lagrangian fluxes.
- The source term $\mathbf{B}_{k,i}$ depends on the moving direction of the phase interface and the intercell speed.

The variation of a cell volume can be taken into account by using the DGCL as discussed in section 1.3.3 and the variation of the volume fraction has been addressed in section 4.2.7. The volume fractions at the intercell associated to the Lagrangian fluxes are determined by the upwind strategy (4.21). The determination of the numerical fluxes and source term will be discussed in section 5.2.2.

5.2.2 Part I: Numerical fluxes and source term

Similarly to the DEM method, the conservative fluxes $(\alpha\mathbf{F}^{ALE})_{k,i+1/2}$, $(\alpha\mathbf{F}^{ALE})_{k,i-1/2}$ are the sum of several fluxes involving different local RPs between same and different phases.

$$(\alpha\mathbf{F}^{ALE})_{k,i-1/2} = (\alpha\mathbf{F}^{ALE})_{k,i-1/2,1P} + (\alpha\mathbf{F}^{ALE})_{k,i-1/2,2P}$$

which can be rewritten in terms of the partition of cell boundaries as:

$$(\alpha\mathbf{F}^{ALE})_{k,i-1/2} = \begin{cases} S_{i-1/2}^{(kk)}\mathbf{F}_{k,i-1/2}^{(kk)} + S_{i-1/2}^{(kk')}\mathbf{F}_{k,i-1/2}^{(kk')}, & \text{if } u_{I,i-1/2} - u_{m,i-1/2} > 0 \\ S_{i-1/2}^{(kk)}\mathbf{F}_{k,i-1/2}^{(kk)} + S_{i-1/2}^{(k'k)}\mathbf{F}_{k,i-1/2}^{(k'k)}, & \text{if } u_{I,i-1/2} - u_{m,i-1/2} < 0 \end{cases}$$

With the restriction the Riemann solvers taking into account the contact wave, the Lagrangian fluxes, which concern only the two-phase RP, can be computed as:

$$\mathbf{F}^{Lag}_{k,i-1/2} = \mathbf{F}^{Lag}_{i-1/2} = \begin{pmatrix} 0 \\ p_{I,i-1/2} \\ 0 \\ p_{I,i-1/2}u_{I,i-1/2} \\ 0 \end{pmatrix}$$

The numerical fluxes can be computed by solving the RP. For each RP involving the same or two different phases with $\mathbf{A}_L$ and $\mathbf{A}_R$ as respectively the left and right states of an intercell, we determine the intermediate states p^* and u^* are such that:

$$\begin{aligned} p^* &= p_R + \rho_R c_{AC,R}(u^* - u_R) \\ p^* &= p_L - \rho_L c_{AC,L}(u^* - u_L) \end{aligned} \tag{5.16}$$

System (5.16) can be solved to obtain:

$$\begin{aligned} u^* &= \frac{(p_L + \rho_L c_{AC,L} u_L) - (p_R - \rho_R c_{AC,R} u_R)}{\rho_L c_{AC,L} + \rho_R c_{AC,R}} \\ p^* &= \frac{u_L - u_R}{\dfrac{1}{\rho_L c_{AC,L}} + \dfrac{1}{\rho_R c_{AC,R}}} + \frac{\dfrac{1}{\rho_L c_{AC,L}} p_L + \dfrac{1}{\rho_R c_{AC,R}} p_R}{\dfrac{1}{\rho_L c_{AC,L}} + \dfrac{1}{\rho_R c_{AC,R}}} \end{aligned} \tag{5.17}$$

The numerical fluxes can now be computed and their values depend on the relative position of the intercell within the wave systems quantified in (5.18). The full acoustic solutions in terms of the intercell speed ($\lambda_m = x/t = u_m$) are given in Table 5.1.

$$\begin{aligned} \lambda_L &= \min(u_L - c_{AC,L}, u^* - c_{AC,L}) \\ \lambda_L^* &= \max(u_L - c_{AC,L}, u^* - c_{AC,L}) \\ \lambda^* &= u^* \\ \lambda_R^* &= \min(u_R + c_{AC,R}, u^* + c_{AC,R}) \\ \lambda_R &= \max(u_R + c_{AC,R}, u^* + c_{AC,R}) \end{aligned} \tag{5.18}$$

Wave speed	$\lambda_m < \lambda_L$	$\lambda_L^* < \lambda_m < \lambda^*$	$\lambda^* < \lambda_m < \lambda_R^*$	$\lambda_R < \lambda_m$
Density	ρ_L	ρ_L	ρ_R	ρ_R
Sound speed	$c_{AC,L}$	$c_{AC,L}$	$c_{AC,R}$	$c_{AC,R}$
Velocity	u_L	u^*	u^*	u_R
Pressure	p_L	p^*	p^*	p_R
Mass fraction	Y_L	Y_L	Y_R	Y_R

Table 5.1: Acoustic solution for the two-phase Riemann problem

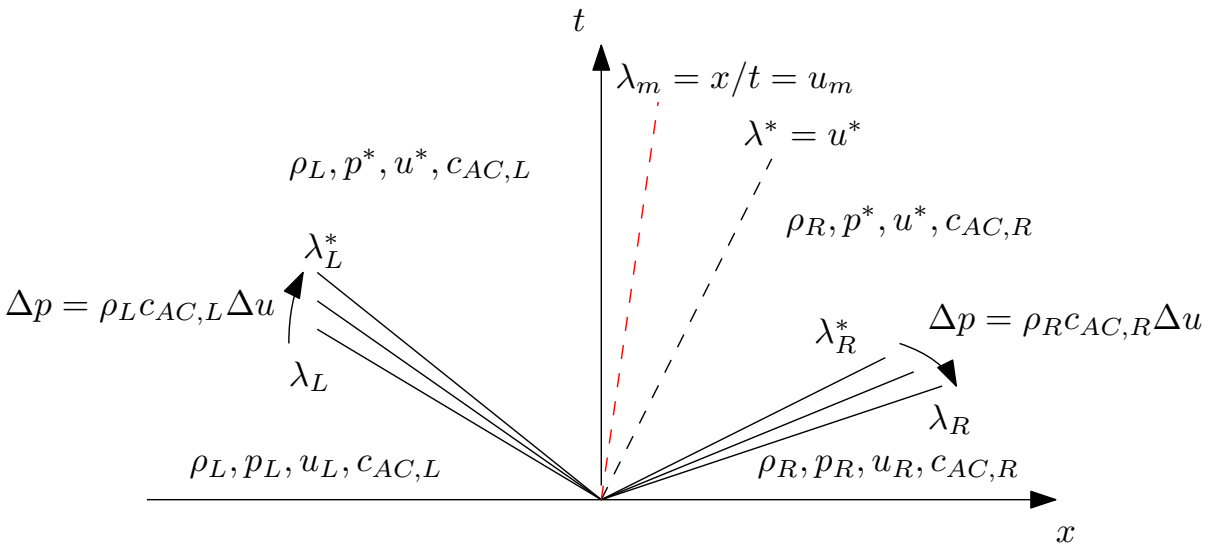

Figure 5.1: Acoustic solutions supposing the wave structure: $\lambda_L < \lambda_L^* < \lambda_m < \lambda^* < \lambda_R^* < \lambda_R$ ($\lambda_m = 0$ in the Eulerian case). The solutions at the intercell are $\rho_L, p^*, u^*, c_{AC,L}$

.

As observed in Figure 5.1, the solutions described in Table 5.1 are not complete since the state between λ_L, λ_L^* and λ_R^*, λ_R remain unknown. We suppose that solutions are linear in these regions and that the acoustic formula is satisfied: $\Delta p = \rho c_{AC} \Delta u$.
Concerning the term $\mathbf{B}_{k,i}$, its computation can be decomposed similarly into several contributions involving the single-phase and two-phase problems:

$$\mathbf{B}_{k,i} = \mathbf{B}_{k,i,1P} + \mathbf{B}_{k,i,2P}$$

In the following sections 5.2.2.1-5.2.2.5, we quantify the contribution of several fluxes and the source term $\mathbf{B}_{k,i}$ for the four main possibilities described in Figure 5.2 using the partition of cell boundaries. For the sake of simplicity, we consider only the contribution from the intercell $i - 1/2$ for phase Σ_1. A similar procedure can be applied for phase Σ_2. The following notations for the velocities are adopted in our description:

u_m : intercell velocity. $u_m = 0$ in the Eulerian case.

u_{2P}^* : Two-phase RP velocity on the contact discontinuity.

u_{2P}^0 : Two-phase RP velocity on $x/t = u_m$.

u_{1P}^* : Single-phase RP velocity on the contact discontinuity.

u_{1P}^0 : Single-phase RP velocity on $x/t = u_m$.

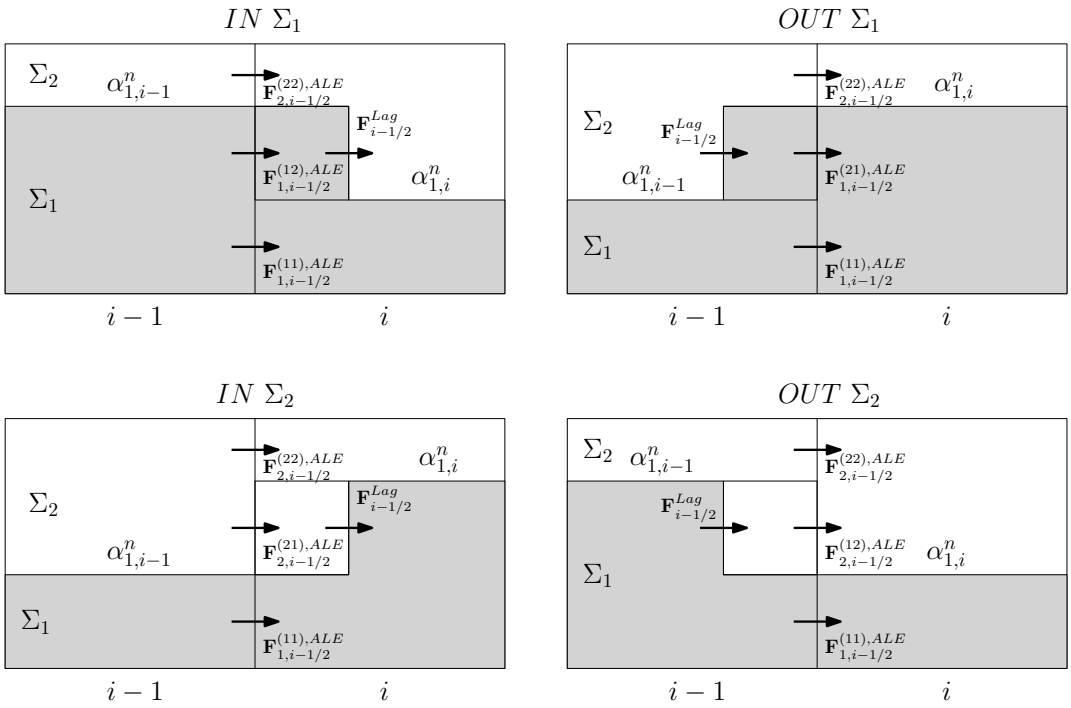

Figure 5.2: Four possibilities illustrated in the intercell frame of velocity u_m ($u_m = 0$: the Eulerian case, $u_m \neq 0$: the ALE case).

5.2.2.1 Two-phase Riemann problem: $IN\ \Sigma_1$

The case $IN\ \Sigma_1$ illustrated in Figure 5.2 is characterized by the RP12.
Contribution of the conservative flux:

$$(\alpha \mathbf{F}^{ALE})_{1,i-1/2,2P} \quad = \quad (\alpha^n_{1,i-1} - \alpha^n_{1,i}) \mathbf{F}^{(12),ALE}_{1,i-1/2}(\mathbf{A}^n_{1,i-1}, \mathbf{A}^n_{2,i})$$

Contribution of the Lagrangian flux:

$$(\alpha_{k,i-1/2} - \alpha_{k,i}) \mathbf{F}^{Lag}_{i-1/2} = (\alpha^n_{1,i-1} - \alpha^n_{1,i}) \mathbf{F}^{Lag}_{i-1/2} = -(\alpha^n_{2,i-1} - \alpha^n_{2,i}) \mathbf{F}^{Lag}_{i-1/2}$$

Contribution of the source term:

$$\mathbf{B}_{1,i,2P} = (\alpha^n_{1,i-1} - \alpha^n_{1,i}) \mathbf{b}^n_{1,i-1} (u^*_{i-1/2,2P} - u^0_{i-1/2,2P})$$

5.2.2.2 Two-phase Riemann problem: $OUT\ \Sigma_1$

The case $OUT\ \Sigma_1$ illustrated in Figure 5.2 is characterized by the RP21.
Contribution of the conservative flux:

$$(\alpha \mathbf{F}^{ALE})_{1,i-1/2,2P} \quad = \quad (\alpha^n_{1,i} - \alpha^n_{1,i-1}) \mathbf{F}^{(21),ALE}_{1,i-1/2}(\mathbf{A}^n_{2,i-1}, \mathbf{A}^n_{1,i})$$

Contribution of the Lagrangian flux:

$$(\alpha_{k,i-1/2} - \alpha_{k,i}) \mathbf{F}^{Lag}_{i-1/2} = (\alpha^n_{2,i} - \alpha^n_{2,i}) \mathbf{F}^{Lag}_{i-1/2} = 0$$

Contribution of the source term:

$$\mathbf{B}_{1,i,2P} = (\alpha^n_{1,i} - \alpha^n_{1,i-1}) \mathbf{b}^n_{1,i} (-u^0_{i-1/2,2P})$$

5.2.2.3 Two-phase Riemann problem: $IN\ \Sigma_2$

The case $IN\ \Sigma_1$ illustrated in Figure 4.3 is characterized by the RP21.
Contribution of the conservative flux:

$$(\alpha\mathbf{F}^{ALE})_{1,i-1/2,2P} = 0$$

Contribution of the Lagrangian flux:

$$(\alpha_{k,i-1/2} - \alpha_{k,i})\mathbf{F}^{Lag}_{i-1/2} = (\alpha^n_{2,i-1} - \alpha^n_{2,i})\mathbf{F}^{Lag}_{i-1/2} = -(\alpha^n_{1,i-1} - \alpha^n_{1,i})\mathbf{F}^{Lag}_{i-1/2}$$

Contribution of the source term:

$$\mathbf{B}_{1,i,2P} = (\alpha^n_{1,i} - \alpha^n_{1,i-1})\mathbf{b}^n_{1,i}(-u^*_{i-1/2,2P})$$

5.2.2.4 Two-phase Riemann problem: $OUT\ \Sigma_2$

The case $OUT\ \Sigma_2$ illustrated in Figure 4.3 is characterized by the RP12.
Contribution of the conservative flux:

$$(\alpha\mathbf{F}^{ALE})_{1,i-1/2,2P} = 0$$

Contribution of the Lagrangian flux:

$$(\alpha_{k,i-1/2} - \alpha_{k,i})\mathbf{F}^{Lag}_{i-1/2} = (\alpha^n_{1,i} - \alpha^n_{1,i})\mathbf{F}^{Lag}_{i-1/2} = 0$$

Contribution of the source term:

$$\mathbf{B}_{1,i,2P} = 0$$

5.2.2.5 Single-phase Riemann problem

The single-phase RP involves only the conservative flux taking the left and right states of the same phases as initial conditions. For the particular configuration displayed in Figure 5.2, the conservative numerical fluxes are computed by:

$$\begin{aligned}
(\alpha\mathbf{F}^{ALE})_{1,i-1/2,1P,IN\ \Sigma_1} = (\alpha\mathbf{F}^{ALE})_{1,i-1/2,1P,OUT\ \Sigma_2} &= \alpha^n_{1,i}\mathbf{F}^{(11),ALE}_{1,i-1/2}(\mathbf{A}^n_{1,i-1}, \mathbf{U}^n_{1,i}) \\
(\alpha\mathbf{F}^{ALE})_{1,i-1/2,1P,OUT\ \Sigma_1} = (\alpha\mathbf{F}^{ALE})_{1,i-1/2,1P,IN\ \Sigma_2} &= \alpha^n_{1,i-1}\mathbf{F}^{(11),ALE}_{1,i-1/2}(\mathbf{A}^n_{1,i-1}, \mathbf{A}^n_{1,i}) \\
(\alpha\mathbf{F}^{ALE})_{2,i-1/2,1P,IN\ \Sigma_1} = (\alpha\mathbf{F}^{ALE})_{2,i-1/2,1P,OUT\ \Sigma_2} &= \alpha^n_{2,i-1}\mathbf{F}^{(22),ALE}_{2,i-1/2}(\mathbf{A}^n_{2,i-1}, \mathbf{A}^n_{2,i}) \\
(\alpha\mathbf{F}^{ALE})_{2,i-1/2,1P,OUT\ \Sigma_1} = (\alpha\mathbf{F}^{ALE})_{2,i-1/2,1P,IN\ \Sigma_2} &= \alpha^n_{2,i}\mathbf{F}^{(22),ALE}_{2,i-1/2}(\mathbf{A}^n_{2,i-1}, \mathbf{A}^n_{2,i})
\end{aligned}$$

Contribution of the source term:

$$\mathbf{B}_{1,i,1P,IN\ \Sigma_1} = \mathbf{B}_{1,i,1P,OUT\ \Sigma_1} = \mathbf{B}_{1,i,1P,IN\ \Sigma_2} = \mathbf{B}_{1,i,1P,OUT\ \Sigma_2} = \alpha^n_{1,i}(-u^0_{i-1/2,1P})$$

In appendix D.2, we perform a verification for the numerical method of part I considering the transport equation for the quantity $\alpha\rho$.

5.2.3 Part I: Investigation on the artificial sound speed

The DEM-LM in this work considers each phase with its own artificial sound speed. The choice of the artificial sound speeds is of particular importance as it will affect the efficiency, the accuracy and the stability of our numerical scheme.
Without loss of generality, we consider two adjacent cells with the left one occupied by gas and the right one occupied by liquid. The initial values are qualitatively illustrated in Figure 5.3 in the (p, u) diagram.

In the low-Mach regime, the (physical) intermediate state (u^*, p^*) is determined by intersecting the line of slope $\rho_L c_L$ passing through point (u_L, p_L) and the line of slope $-\rho_G c_G$ passing through point (u_G, p_G). The slope is also called the acoustic impedance taking very high values for both phases but the acoustic impedance of liquid is much higher than that of gas. For instance at 1 atm, the acoustic impedance of water is of order 1.625×10^6, approximately 4300 times much higher than that of air. As a result, the line passing through (u_G, p_G) can be regarded as almost perpendicular to the very steep line passing through (u_L, p_L). The intermediate velocity u^* (or the velocity of the contact wave) is therefore very close to that of the liquid u_L. The liquid is therefore under a very weak compression due to small divergence of velocity in the compressible models.

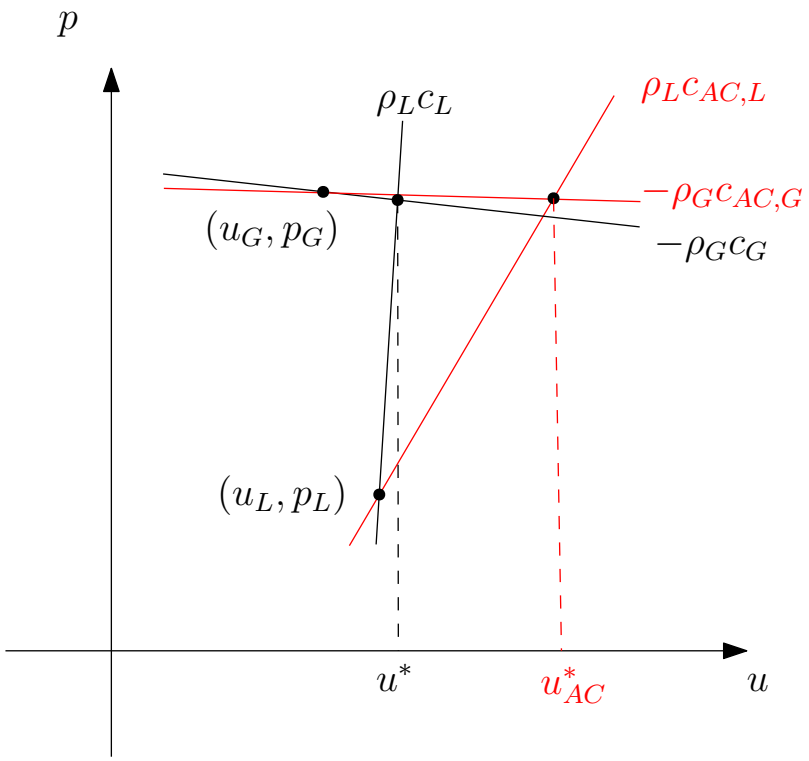

Figure 5.3: Investigation on the artificial sound speed.

When reducing the sound speed in the DEM-LM method, we obtain less steep lines whose intersection gives the intermediate velocity u^*_{AC}. As observed, the velocity of the intermediate state is no longer close to the velocity of liquid and the divergence of the velocity is consequently much more important than in the physical case. This could lead to a numerical stability problem since the liquid is under a higher level compression than expected. The numerical stability (and the accuracy) of the DEM-LM approach is therefore strongly dependent on the choice of the artificial sound speed. For these reasons, these parameters should be set in such a way that the value of u^*_{AC} though much higher than the physical value u^* remains very small compared to the artificial sound speeds, meaning $M_{AC} << 1$.

5.2.4 Part II: Discretization

We recall that in part II, we need to solve the system:

$$\begin{aligned}
\frac{\partial \rho_k}{\partial t} &= -\rho_k \nabla \cdot \mathbf{v}_k \\
\frac{\partial \mathbf{v}_k}{\partial t} &= 0 \\
\frac{\partial p_k}{\partial t} &= -(\rho c_k^2 - \rho c_{k,AC}^2) \nabla \cdot \mathbf{v}_k \\
\frac{\partial (\rho_k e_k^t)}{\partial t} &= -(\rho_k e_k^t + p_k) \nabla \cdot \mathbf{v}_k \\
\frac{\partial (\rho_k \mathbf{Y}_k)}{\partial t} &= -\rho_k \mathbf{Y}_k \nabla \cdot \mathbf{v}_k
\end{aligned} \tag{5.19}$$

where $\nabla \cdot \mathbf{v}_k$ is, as previously discussed, an imposed homogeneous function. Moreover, the equations $(5.19)_1$ and $(5.19)_5$ can be combined and yield $\frac{\partial \mathbf{Y}_k}{\partial t} = 0$ which implies that the mass fraction $\mathbf{Y}_k$, similarly to the velocity $\mathbf{v}_k$, does not vary in time.
In our physical problem, each phase can contain several species. For instance, the gaseous phase in the bubble expansion problem contains two species: the gas in the bubble (region 1) and the gas in the low-pressure region (region 3). Since $\nabla \cdot \mathbf{v}_k$ is a homogeneous function, we suppose that it is also true for the divergence of velocity for each species $\nabla \cdot \mathbf{v}_{k,e}$. The mass fraction equation for each species e deduced from $(5.19)_5$ reads:

$$\frac{\partial (\rho_k Y_{k,e})}{\partial t} = -\rho_k Y_{k,e} \nabla \cdot \mathbf{v}_{k,e} \tag{5.20}$$

By integrating (5.20) over the whole volume containing phase $\mathcal{V}_k$, we obtain:

$$\frac{d}{dt} \int_{\mathcal{V}_k} \rho_k Y_{k,e} dV_k = -\left(\int_{\mathcal{V}_k} \rho_k Y_{k,e} dV_k \right) (\nabla \cdot \mathbf{v}_{k,e})$$

Using the first-order forward Euler method, we get:

$$\frac{m_{k,e}^{n+1} - m_{k,e}^{n+1,*}}{\Delta t} = -m_{k,e}^{n+1,*} (\nabla \cdot \mathbf{v}_{k,e})$$

where $m_{k,e}^{n+1,*}$ is the total mass after part I and $m_{k,e}^{n+1}$ is a known quantity obtained from mass conservation. Indeed, in the case of closed domain, the total mass at every instant is equal to the initial mass:

$$m_{k,e}^{n+1} = m_{k,e}^{0}$$

The divergence of the velocity for each phase k can be determined as:

$$\nabla \cdot \mathbf{v}_k = \sum_e Y_{k,e} \nabla \cdot \mathbf{v}_{k,e} \tag{5.21}$$

As discussed in Chapter 3, the density, the pressure and the total energy computed directly from system (5.19) do not satisfy the original SG-EOS (1.7). The computation of these quantities will be therefore performed similarly as in the single-phase situation. We compute first the density and the pressure from system (5.19):

$$\begin{aligned}
\rho_{k,i}^{n+1} &= \rho_{k,i}^{n+1,*} - \Delta t \rho_{k,i}^{*} \nabla \cdot \mathbf{v}_k \\
p_{k,i}^{n+1} &= p_{k,i}^{n+1,*} - \Delta t \rho_{k,i}^{n+1,*} (c_k^2 - c_{k,AC}^2) \nabla \cdot \mathbf{v}_k
\end{aligned} \tag{5.22}$$

The internal energy is computed next using the SG-EOS (1.7) and the total energy is computed from the internal enery, density and velocity:

$$\begin{aligned} e_{i,k}^{n+1} &= \frac{p_{i,k}^{n+1} + \gamma_k p_{\infty,k}}{(\gamma_k - 1)\rho_{i,k}^{n+1}} \\ (\rho e^t)_{i,k}^{n+1} &= \rho_{i,k}^{n+1} e_{i,k}^{n+1} + \frac{1}{2}\rho_{i,k}^{n+1}(\mathbf{v}_{i,k}^{n})^2 \end{aligned} \tag{5.23}$$

5.3 Low-Mach 1D bubble expansion problem

5.3.1 Presentation of the problem

The problem solved in this section to assess the DEM-LM method applied to low-Mach number problems is similar to the one previously discussed in section 4.3. The main difference with the previous 1D bubble expansion test problem (representative of the HCDA configuration studied in the next final chapter) lies in the initial conditions. They are modified to obtain a low-Mach test case (see Table 5.2). Moreover, we also investigate the influence of the so-called efficiency parameter (eff) which corresponds to the choice of artificial sound speeds the in liquid and gas phases (see Table 5.3). The artificial sound speed in each phase is computed by dividing by the factor eff the initial physical sound speed associated to each phase. With the initial conditions defined in Table 5.2, the initial (physical) soundspeed in the liquid region is equal to $1625\,m/s$ so that using for instance eff $= 3.25$ the artificial soundspeed in the liquid region is set equal to $500\,m/s$. The artificial soundspeed in the gas region is similarly defined. Note this scaling parameter for the artificial soundspeeds is called eff because it determines directly the computational speed-up which is expected from the DEM-LM approach with respect to the fully compressible DEM approach, thanks to the choice of the time-step. The material properties for the test problem remain those defined in section 4.3.

	Region 1	Region 2	Region 3
ρ (kg/m^3)	1.64067	1000.0	1.0
P (Pa)	2×10^5	1×10^5	1×10^5
u (m/s)	0.0	0.0	0.0

Table 5.2: Low Mach bubble expansion problem. Initial conditions.

Artificial sound speed		
	$c_{AC,water}$ (m/s)	$c_{AC,gas}$ (m/s)
eff $= 3.25$	500	100
eff $= 4$	406	93
eff $= 4.5$	361.09	83.15
eff $= 5$	325	75
eff $= 16.25$	100	20

Table 5.3: Low Mach bubble expansion problem. Artificial sound speed.

Comments

- The value of the initial density of the bubble region is obtained by supposing that it is made of perfect gas which is isentropically compressed:
  From 1 to 2 bars:

$$\rho_{B,0} = \left(\frac{P_{B,0}}{P_{A,0}}\right)^{1/\gamma_B} \rho_{A,0} = \left(\frac{2 \times 10^5 \text{Pa}}{1 \times 10^5 \text{Pa}}\right)^{1/1.4} 1.0 \text{ kg/m}^3 \approx 1.64067 \text{ kg/m}^3$$

- In each region, we suppose that there are initially two phases (gas and liquid) but with a small initial volume fraction for the so-called residual phase which is at mechanical equilibrium with the other - in regions 1 and 3, the residual phase is the liquid while it is the gas in region 2. These residual volume fractions are set equal to $\alpha_{res} = 10^{-6}$.

5.3.2 Numerical results

In this section, we compare the DEM-LM numerical solutions with the DEM fully compressible numerical solutions and the bubble model analytical solution (referred as "Low Mach" in the following plots). In section 5.3.2.1, we first investigate the DEM-LM without the instantaneous relaxation procedure briefly described in appendix E and which applies to both pressure and velocity. In section 5.3.2.2 we investigate the DEM-LM using this instantaneous relaxation for velocity only. The DEM and DEM-LM methods share the following characteristic features:

- Second order accuracy in space using the limited linear reconstruction on primitive variables
- Second order accuracy in time using 2-stage RK method
- Instantaneous relaxation procedure of [Saurel and Abgrall, 1999, Tang, 2012] for pressure and velocity for DEM. When applying DEM-LM this relaxation procedure is either not applied or applied for velocity only.
- Anti-diffusive UDCS approach for the volume fraction [Tang et al., 2014a, Tang et al., 2014b, Tang, 2012].
- $CFL = 0.5$.

We emphasize that the SG-EOS (1.7) allows the pressure of liquid to obtain a negative value as long as the sound speed is positive, meaning $p > -p_\infty$. This situation occurs for instance with the presence of strong rarefaction waves in the flow. Consequently, the application of the relaxation procedure for both velocity and pressure is necessary when it is possible (case of the DEM solver). However, the application of the full procedure (for both velocity and pressure) to the DEM-LM solver and for the test case in investigation makes our computation explode and the problem is till the present not well understood.
The use of the relaxation procedure is not obligatory in our situation since the low-Mach test case under investigation, by our numerical experiments, creates only negative pressure in the residual phase. As a result, the global numerical solutions with or without the relaxation process should not be much different from each other.
In the following test cases, different levels of mesh refinement are considered:

- The coarsest mesh considered is composed of 100 elements in region 1 (one fourth of the initial total domain, which means 400 cells for the whole domain).
- The medium mesh is composed of 200 cells in region 1 (800 cells in total).
- The finest mesh is composed of 400 cells in region 1 (1600 cells all over the domain).

5.3.2.1 Case without instantaneous relaxation for velocity and pressure (DEM-LM)

Similarly to the test cases presented in section 4.3, the numerical solutions given by the DEM-LM present artificial acoustic waves with small amplitudes. These artificial acoustic waves propagate inside the domain and are reflected when impacting on rigid walls. The interaction of reflected waves form a complex flow pattern. The numerical solutions of the DEM-LM model are not expected to match the bubble model solution since the acoustic waves are filtered in the bubble model. The following comparison will not be

limited to the space distributions of velocity and pressure in the computational domain but will also focus on the prediction of global variables of practical interest: average pressures, kinetic energy of water, etc.

In Figure 5.4, we display the comparisons between DEM-LM, DEM and the bubble model at 100 ms with a choice eff = 3.25 to define the artificial soundspeeds used in DEM-LM. As observed, all the numerical results begin to exhibit their asymptotic (or low Mach) behavior. The pressure levels in gas regions are very close to each other while the pressure in water presents oscillations due to a much more important acoustic impedance. The velocity distributions have nearly the same order of magnitude. It can be also observed that the DEM-LM solutions display more (spurious) oscillations compared to the DEM solutions which is expected since the DEM-LM model has less numerical viscosity and a larger time step with respect to the DEM model, a consequence of reducing the sound speed. This results in less numerical diffusion to help damping the oscillations.

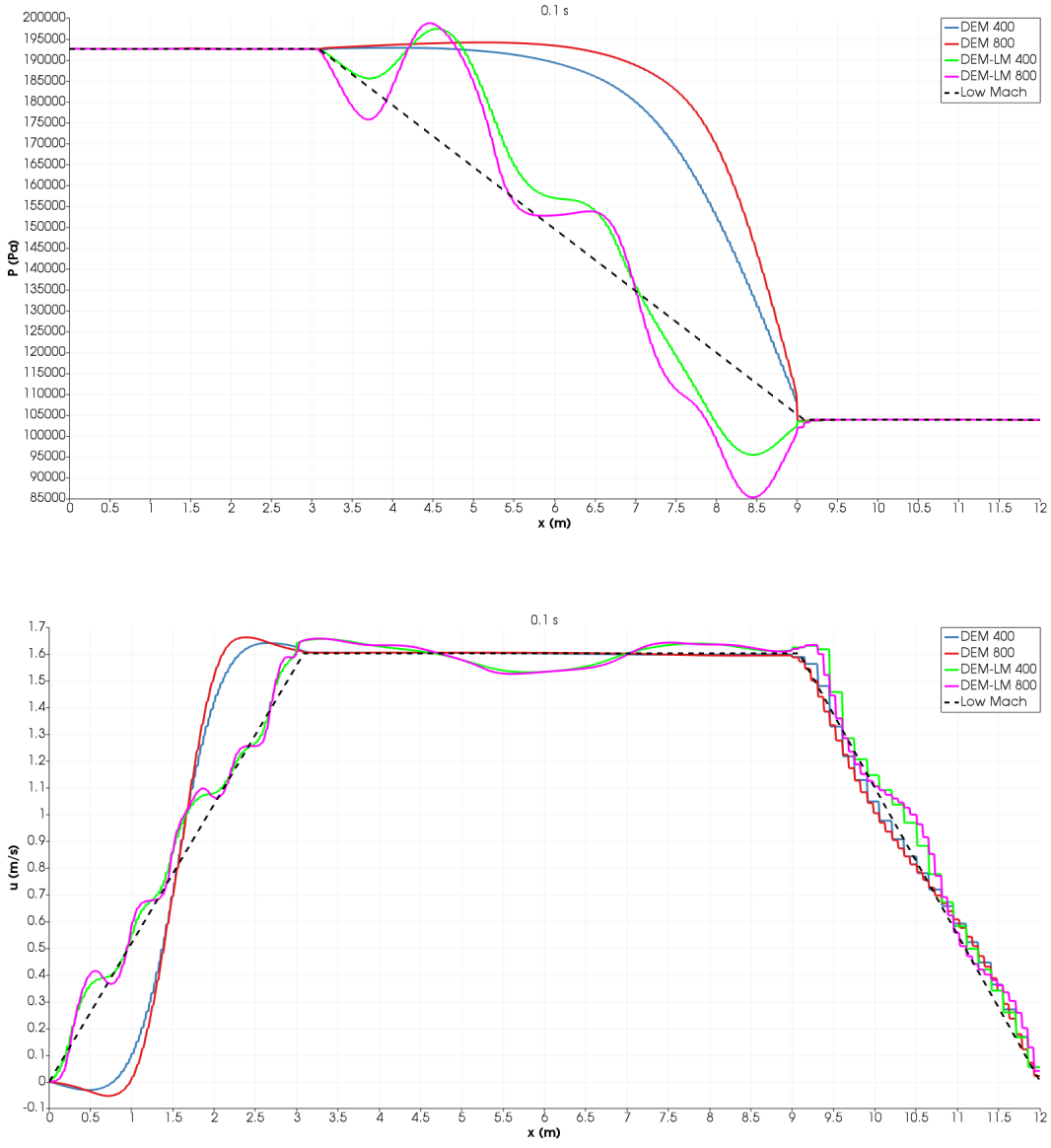

Figure 5.4: Low Mach bubble expansion problem. Comparison between DEM, DEM-LM (no relaxation, eff = 3.25) and bubble (low Mach) models. Pressure and velocity fields at 100 ms.

In Figure 5.5, we display the comparison at 200 ms which shows a much clearer low-Mach behavior for the DEM and DEM-LM numerical solutions. The DEM-LM model still produces significant oscillations for the pressure in the water region. The magnitude of the pressure oscillations is higher with the mesh refinement since the finer mesh is able to capture higher frequency waves.

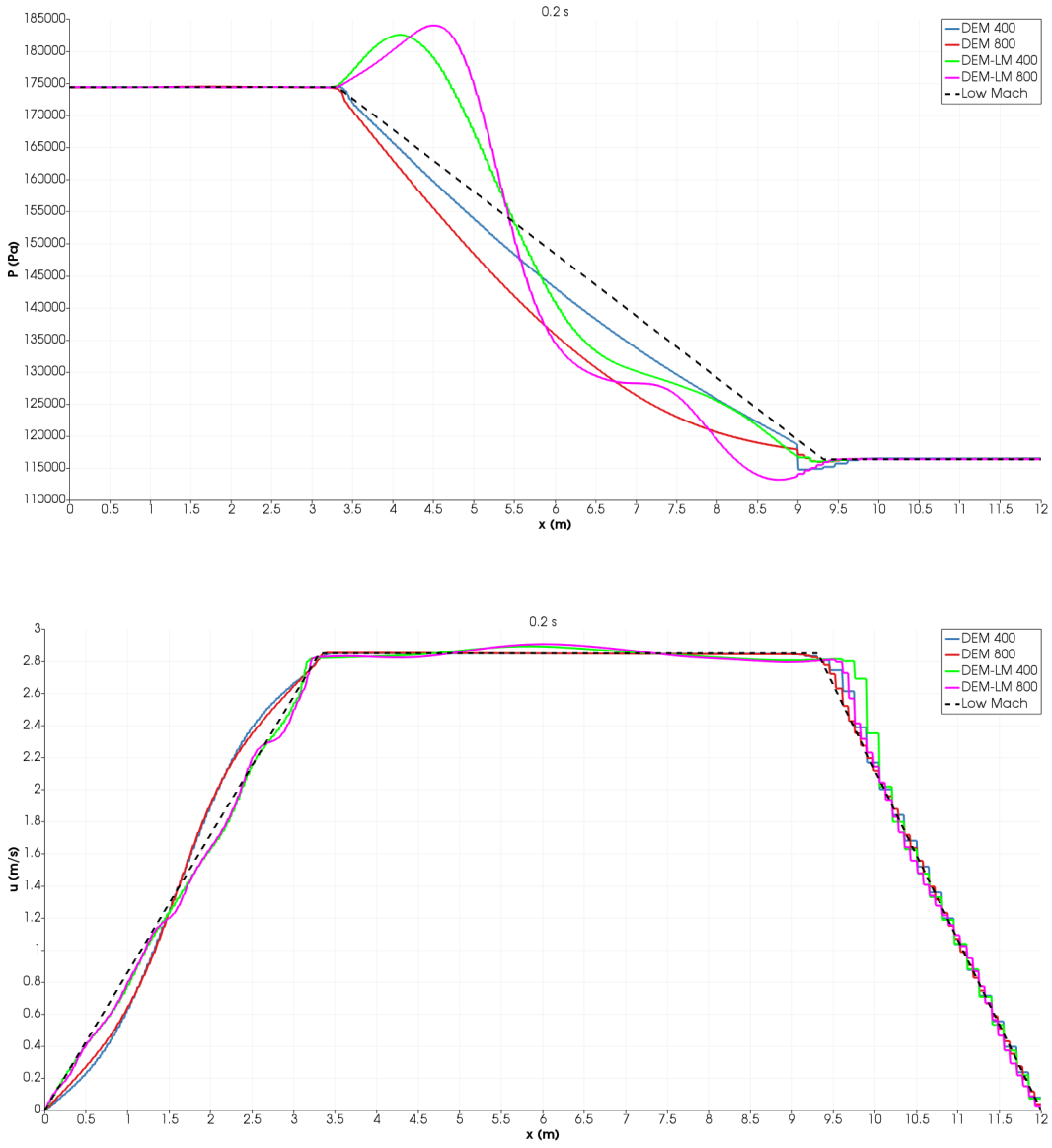

Figure 5.5: Low Mach bubble expansion problem. Comparison between DEM, DEM-LM (no relaxation, eff = 3.25) and bubble (low Mach) models. Pressure and velocity fields at 200 ms.

In Figure 5.6, we display the comparisons at 800 ms corresponding to the instant where the gas bubble is in the phase of compression, meaning the water column is displacing to the right. As observed, the numerical solutions are in a good agreement with the reference one.
As previously discussed, we are particulary interested in the average pressures in gas regions and the kinetic energy of water since they are representative of the main loads applying on a structure. In Figure 5.7, we compare the numerical predictions for these quantities with the reference analytical values. As seen, the numerical solutions and the reference values are almost superimposed.

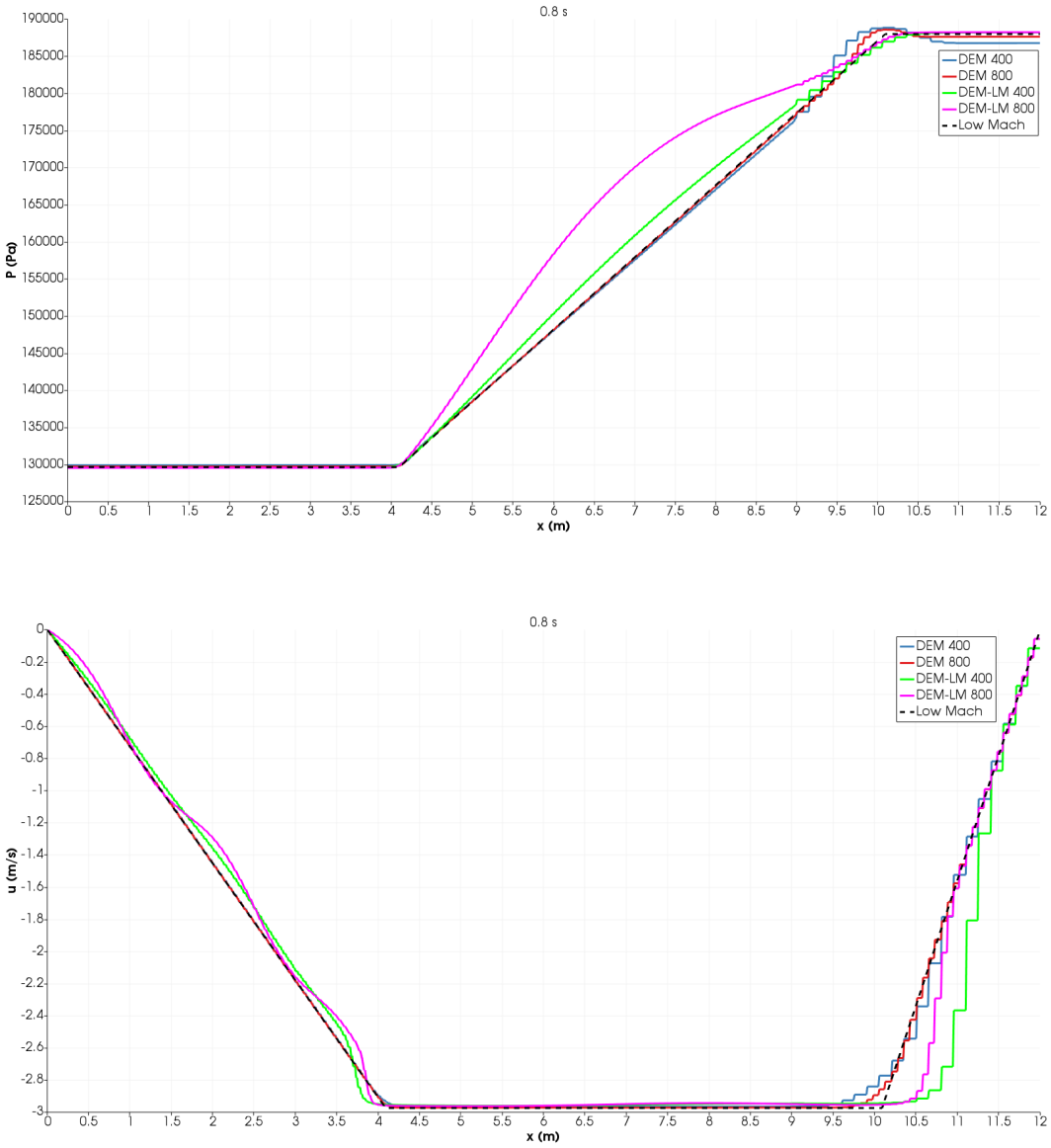

Figure 5.6: Low Mach bubble expansion problem. Comparison between DEM, DEM-LM (no relaxation, eff = 3.25) and bubble (low Mach) models. Pressure and velocity fields at 800 ms.

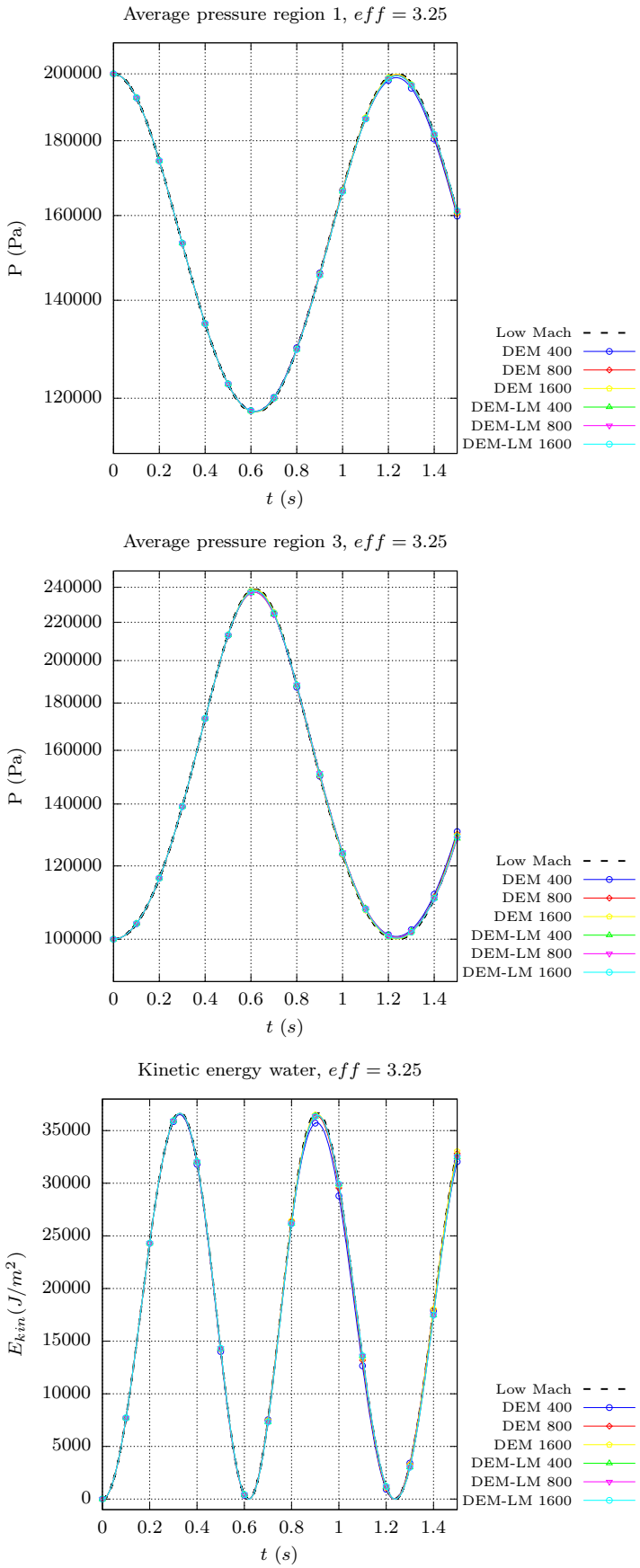

Figure 5.7: Low Mach bubble expansion problem. Comparison between DEM, DEM-LM (no relaxation, eff = 3.25) and bubble (low Mach) models. Average pressures in the regions 1, 3 and the kinetic energy.

In Figure 5.8, we present the temporal evolution of the internal energies of gases, the kinetic energy of water computed with the DEM-LM method; the total energy is the sum of these quantities. We note that the internal energy of water and the kinetic energy of gases are negligible. Although the total energy is not strictly conserved in the DEM-LM model, we still obtain in practice a rather good conservation of this quantity.

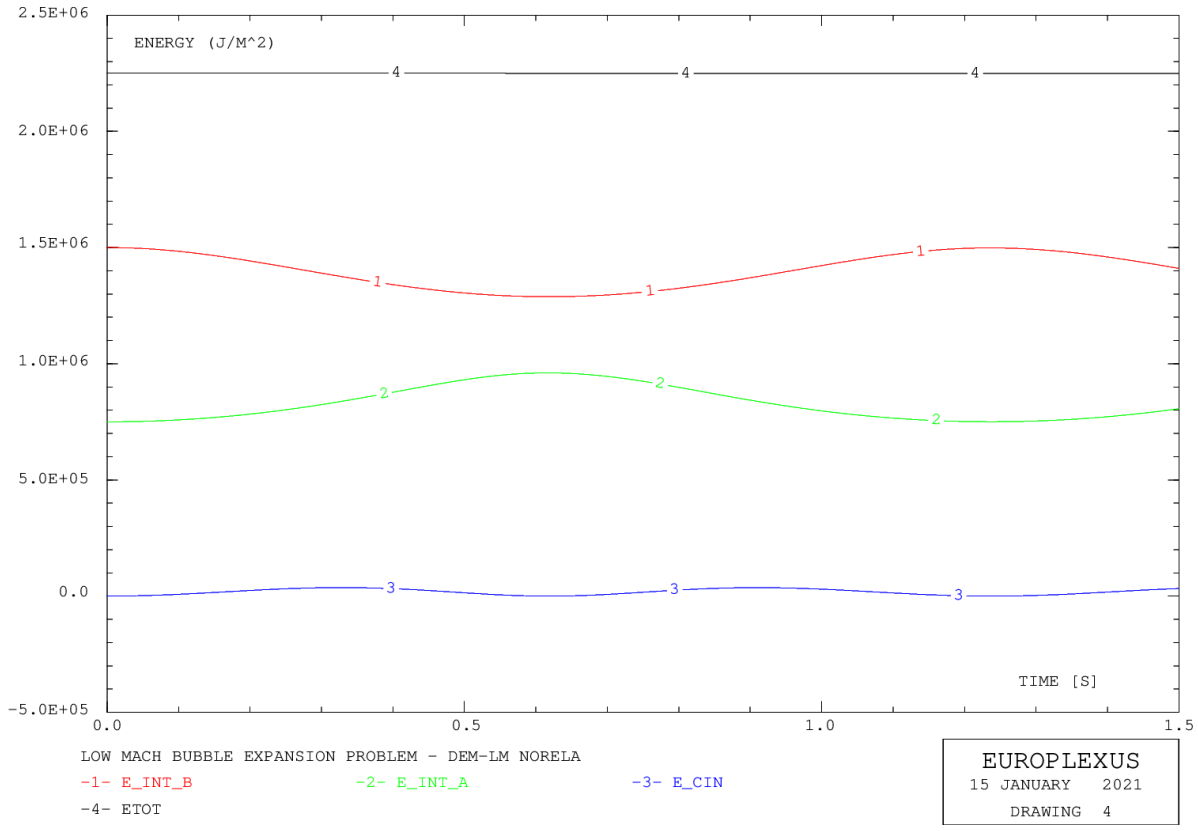

Figure 5.8: Low Mach bubble expansion problem. The DEM-LM solutions (no relaxation, eff = 3.25) for the internal energy of regions 1 and 3, the kinetic energy of water and the total energy.

Limit of efficiency enhancement for the DEM-LM no relaxation case.

The above discussion shows that the DEM-LM method gives satisfactory solutions while the computational cost is reduced by almost 3.25 times, as expected from the choice of the time-step. Note that details on the actual computational cost will be provided in Section 5.3.3. Supplementary numerical experiments were performed with increased values of the parameter eff (to achieve a larger speed-up with DEM-LM). It was found that beyond a value of eff = 4 the DEM-LM simulation provides numerical solutions displaying a loss of accuracy. In Figure 5.9, we compare the solutions given by DEM and DEM-LM models with different level of efficiency: eff $= 4, 4.5, 5$. The computations are performed on a mesh of 400 cells. It can be observed the DEM-LM method with eff = 4 gives satisfactory solutions when compared with the DEM ones. In contrast, we cannot keep the accuracy for the DEM-LM solutions with the efficiency factors eff = 4.5, 5. Wrongly computed average pressures and kinetic energy as well as a phase shift in the kinetic energy are clearly identified, especially with the case eff = 5. It is shown in Figure 5.10 that the computed DEM-LM entropy displays an important variation which violates the underlying assumption of the DEM-LM approach. A further investigation and explanation will be given in the following section. We conclude at this stage that the efficiency of the DEM-LM approach applied without instantaneous relaxation remains limited to a factor of approximately 4 (CPU gain with respect to DEM, with comparable accuracy).

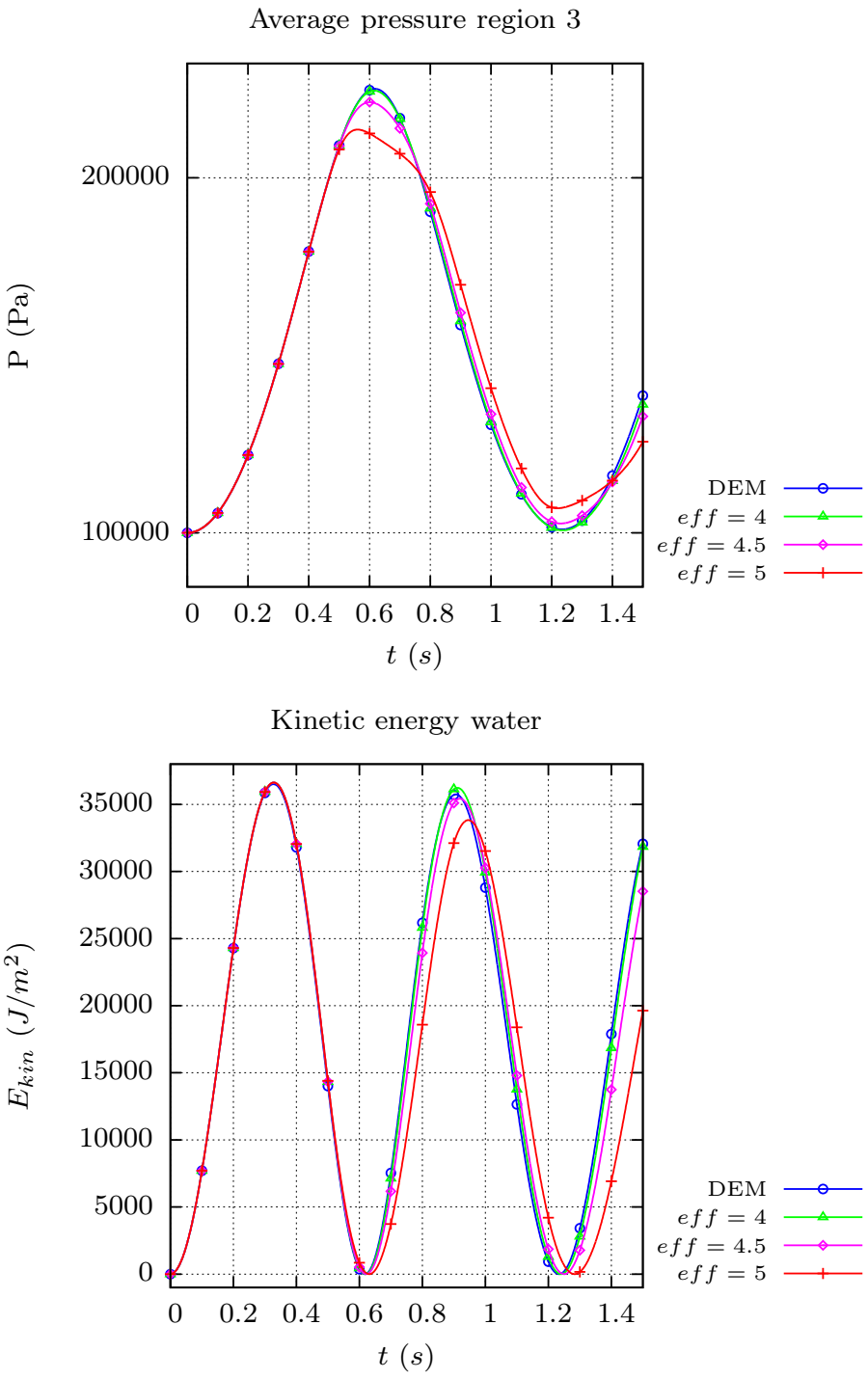

Figure 5.9: Low Mach bubble expansion problem. Limit of efficiency. Comparison between DEM, DEM-LM (no relaxation). From the top to the bottom, average pressure in the region 3 and kinetic energy of water.

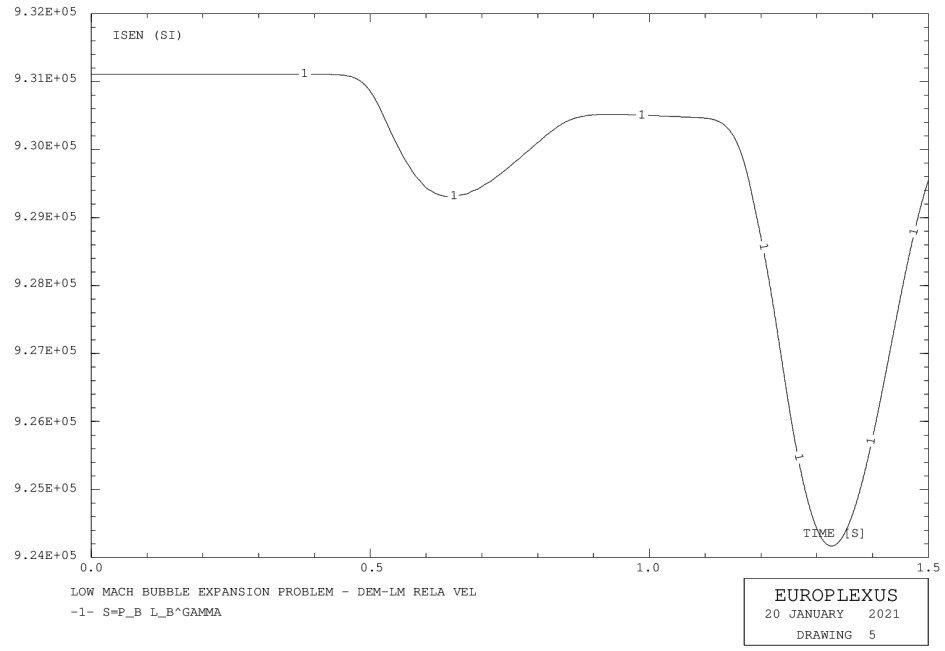

Figure 5.10: Low Mach bubble expansion problem. Limit of efficiency for the no relaxation case. The computed entropy with DEM-LM for region 1 ($s = P_B l_b^{\gamma_B}$, eff $= 5$).

5.3.2.2 Case with instantaneous relaxation only for velocity for (DEM-LM)

The DEM-LM method without the instantaneous relaxation procedure for velocity and pressure can only accelerate the computations by nearly 4 times. The reasons for this limit may reside in the residual phase. In fact, we have observed that the velocity for the residual gas in the liquid is very high. For example, in the case eff $= 5$ ($c_{AC,water} = 325, c_{AC,gas} = 75$ m/s), the maximum gas velocity in the water column can reach up to $u_{max,gas} = 470$ m/s. We emphasize that though the gas velocity in the liquid is very high, the total velocity $u = \sum_k \alpha_k u_k$ changes very little since the gas occupies only a tiny volume in the liquid.
In order to circumvent this situation, an instantaneous relaxation procedure is applied for the velocity only. The average pressures of gas regions and the kinetic energy of water are given by the DEM-LM with a level of efficiency of 16.25 in Figure 5.11. It is observed that the DEM, DEM-LM and reference (low-Mach) solutions are very close to each other which demonstrate the use of an instantaneous relaxation procedure for velocity fixes the accuracy issue previously observed for eff beyond 4 and does so for an efficiency factor which can be as large as 16.25.
In Figure 5.12, we display the internal energy of gases, the kinetic energy of water and the total energy. As before, the total energy is (almost) constant in practice despite not ensuring a strict conservation from a theoretical viewpoint.

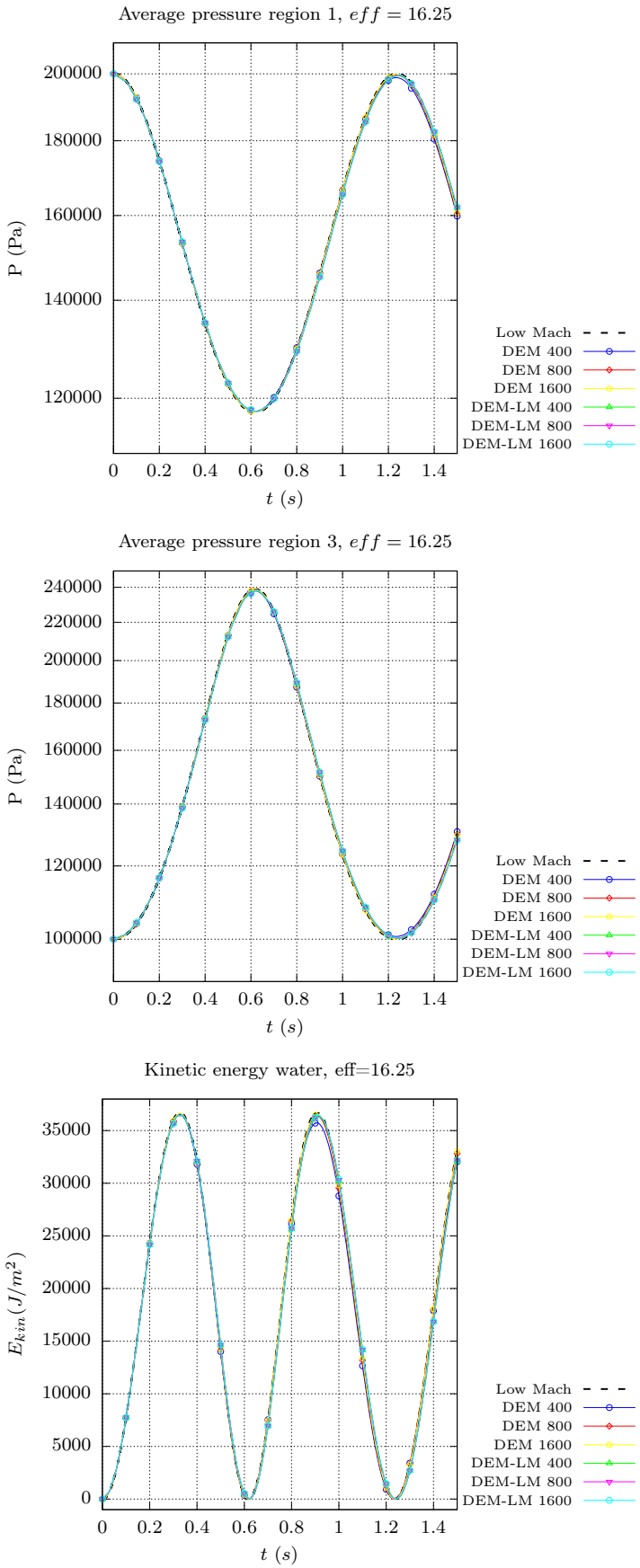

Figure 5.11: Low Mach bubble expansion problem. Comparison between DEM, DEM-LM (with relaxation for the velocity only, eff = 16.25) and bubble (low Mach) models. Average pressures in the regions 1, 3 and the kinetic energy.

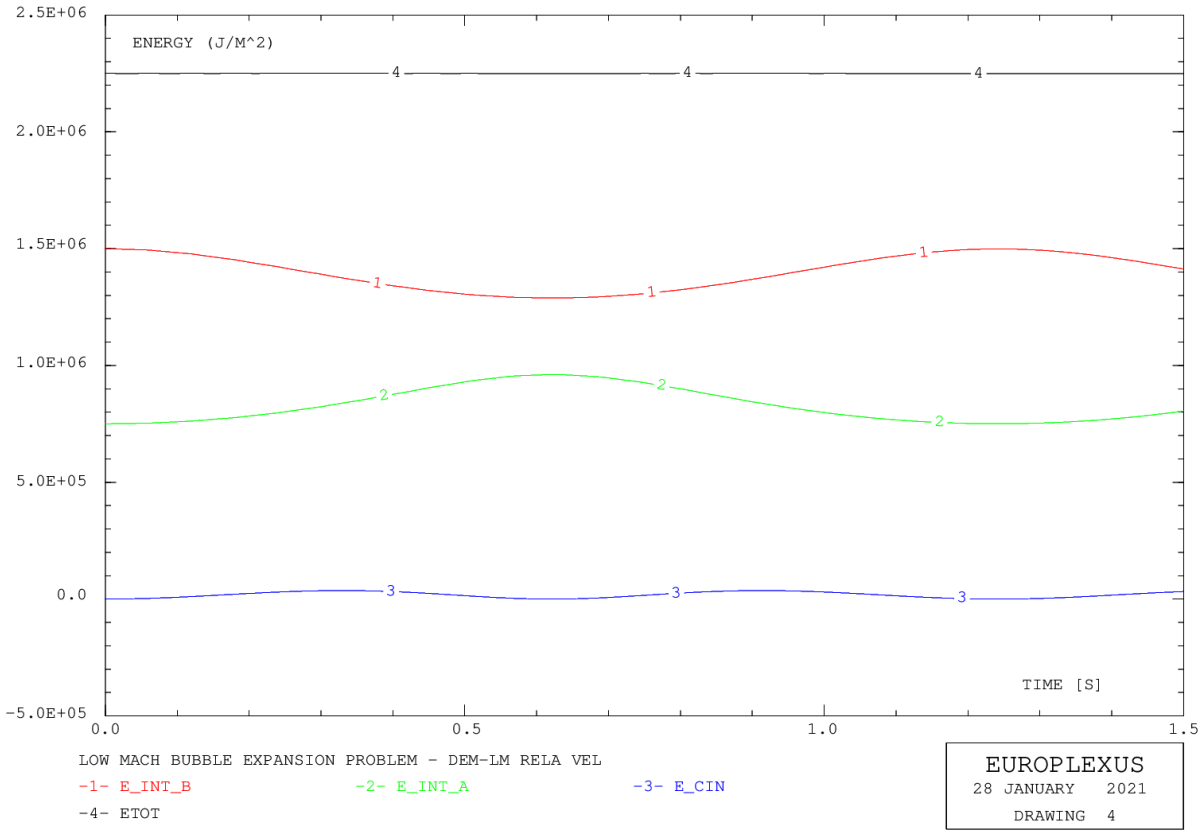

Figure 5.12: Low Mach bubble expansion problem. The DEM-LM solutions (with relaxation for the velocity only, eff = 16.25) for the internal energy of regions 1 and 3, the kinetic energy of water and the total energy.

5.3.3 Computational cost

All the test cases in section 5.3.2 have been performed with sequential computations on an Intel(R) Core(TM) i3-3110M CPU @ 2.40GHz. The CPU time consumption $TCPU$(s) and the corresponding number of time steps n needed to reach the same final physical time are presented in Table 5.4.
It is obvious that the computational cost is greatly reduced by DEM-LM with respect to DEM, while the accuracy remains guaranteed when employing the DEM-LM method with instantaneous velocity relaxation. Instead of spending 17641.41(s) (or nearly 5 hours) for a DEM computation on a 1D fine mesh with 1600 cells, the same computation can be performed using the DEM-LM method with relaxation for the velocity only and produce similar solutions while taking only 1459.81s (or nearly 24 minutes). For multi-dimensional problems, the computational efficiency is expected to be further enhanced.

	DEM		DEM-LM, eff = 3.25		DEM-LM, eff = 16.25	
	TCPU (s)	n	TCPU (s)	n	TCPU (s)	n
400	1182.45	163500	343.77	51000	80.57	10500
800	4267.80	326229	1420.71	101220	322.74	21000
1600	17641.41	651732	5774.62	201723	1459.81	41805

Table 5.4: Low Mach bubble expansion problem. Computational cost: DEM vs DEM-LM

Conclusion

The new numerical method developed in chapter 3 to efficiently and accurately compute low-Mach single-phase flows has been successfully extended in this chapter for two-phase flows in the general framework of the DEM approach. The two-phase low-Mach physical model as well as the corresponding new DEM-LM numerical scheme have been presented in section 5.1 and section 5.2. DEM-LM consists of two parts: part I describes the convective mechanism for artificial acoustic waves of negligible amplitude while an isentropic correction is applied in part II. The solutions given by the DEM-LM method have been compared in section 5.3 with the DEM fully compressible solutions as well as the analytical solution of the bubble model. For this 1D low-Mach bubble expansion problem (representative of the HCDA problem which will be tackled in the following final chapter), the DEM-LM method displayed its great advantage in significantly reducing computational cost while keeping a good accuracy.
Note however, a main drawback of DEM-LM was also identified regarding its range of validity. Indeed, since a (linear) acoustic solver is used, the physical problem in consideration must be (almost) linear. The Mach number in the computed flowfield must remain very low to overcome the robustness problem of the new solver. For example, in the 1D low-Mach bubble expansion problem, the new DEM-LM method suffers from a robustness problem when setting the initial pressure of the bubble above 5 bars. Future numerical developments (precise suggestions will be provided in the general conclusion) should allow to fix these issues so as to extent the range of applicability of the DEM-LM method to flow problems with increasing non-linearities.

6 Application to an industrial case: the 2D MARA test problem

Contents

Introduction

This final chapter evaluates the numerical methods developed in the previous chapters when applied to the computation of the industrial multi-dimensional MARA problem mentioned in the introduction of the manuscript and which motivates the present work, along with other nuclear safety problems involving the low-Mach expansion of gas bubbles. For this purpose, we first perform in section 6.1 acomparison between the solutions given by the DEM fully compressible model and the experimental results available for the MARA problem with a very high initial level of energy released from the gas bubble. The simulation involves the deformation of the structure, which is taken into account by the fluid-structure coupling procedure available in the EUROPLEXUS code.
The DEM method is able to produce correct solutions but found to be computationally expensive. Consequently, we perform next in section 6.2 a low-Mach MARA problem in which we compare the solutions given by the DEM and the DEM-LM methods. As will be shown, the DEM-LM method demonstrates a great advantage in computational cost compared to DEM while maintaining a good accuracy. Note that the comparison between DEM and DEM-LM cannot yet be performed for the original MARA problem because of a lack of robustness for DEM-LM when dealing with strong compressions.

6.1 The MARA problem

6.1.1 Presentation of the problem

The aim of the MARA test rig is to assess the performance of fluid-structure coupling strategies developed in various codes (SIRIUS, CASTEM-PLEXUS, EUROPLEXUS) (see [Robbe et al., 2003a] [Robbe et al., 2003b]) used to study and control the dimension of the containment of the reactor following the so-called hypothetical core disruptive accident (HCDA). The MARA program involved 10 tests of increasing complexity with additional internal deformable structures gradually accounted for: from MARA 1 and 2 considering a plain vessel with a rigid roof [Acket et al., 1981] to MARA 10 including the core support structures and the above core structures [Louvet et al., 1987] (see Figure 6.1). As presented in the introductory chapter, the physical phenomena of the HCDA can be interpreted as the expansion of a high-pressure bubble of vaporized materials in liquid after the interaction between the combustible at a very high temperature with the liquid as coolant. The flow thus involves (first stage) shock waves propagating in the liquid phase which generate the motion of the liquid itself, the impact of which (second stage) can damage the containment and the mechanical devices therein. As a result, the main focus of this test is on studying the overall behavior of the containment (loading, displacements and deformation of the vessel and the slab[1]).
The MARA set of experiments was carried out by CEA in the 1980s on a 1/30-scale model of the Superphenix reactor (which corresponds approximately to a vessel diameter of 700 mm and a total height of 551 mm) in order to provide reference measurements (pressure at transducers, structure deformation) to be used for validation of the codes applied to the HCDA fluid-structure interaction problem. Thanks to the axisymmetric property, we consider in our computation a geometry with reduced dimension as illustrated in Figure 6.2. In the experiments, water replaces the liquid sodium cooling the reactor core (yellow region in Figure 6.2) and the cover gas below the reactor roof of 43 mm height (blue region in Figure 6.2) is air instead of argon; the explosion is triggered by an explosive charge (red region in Figure 6.2) placed on the axis of symmetry and 330 mm below the slab. In the computations, the red region is actually a high pressure gas bubble.

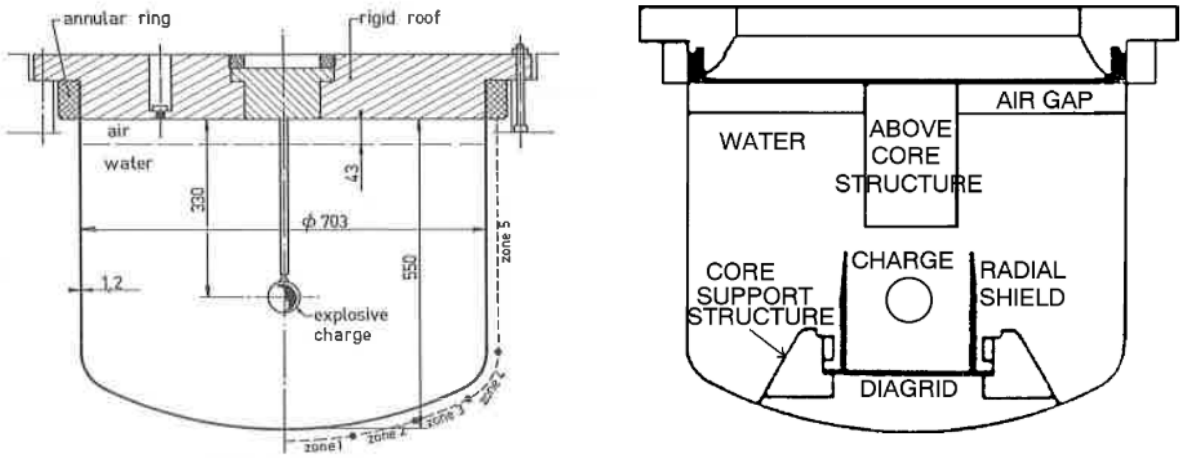

Figure 6.1: Left : schematic view of the MARA 1/2 configuration taken from [Fiche et al., 1985]. The charge creating the gas bubble is located at the center of the liquid domain; the layer of air below the vessel cover is also visible. Right : schematic view of the MARA 10 configuration taken from [Robbe and Casadei, 2004] displaying the added structures included in the fluid-structure interaction.

[1] Vessel and slab are "cuve" and "dalle" in french, respectively

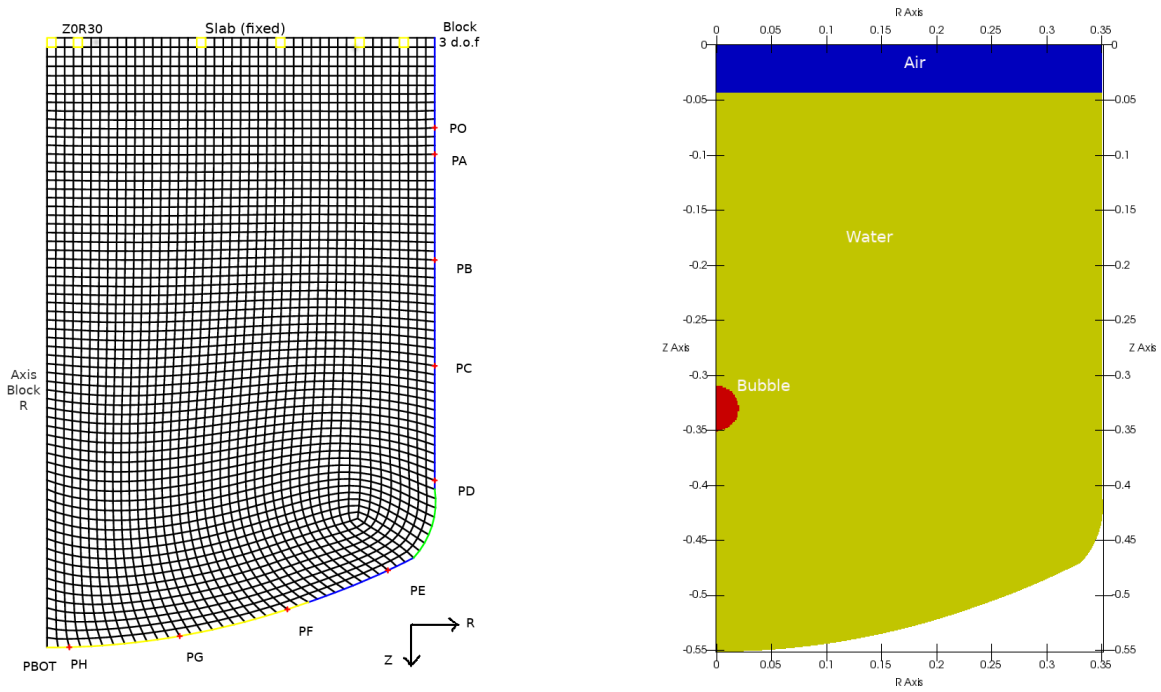

Figure 6.2: MARA problem. Mesh and initial configuration.

6.1.2 Material: fluid and structure

6.1.2.1 Fluid

We compute the MARA problem using the DEM method with the same initial conditions of fluid specified in the MARA test rig. The initial conditions and the material properties of the SG-EOS are specified for different regions in Tables 6.1, 6.2:

	Region 1 (bubble)	Region 2 (water)	Region 3 (air)
ρ (kg/m^3)	1350	998.3	1.206
P (Pa)	6.25×10^8	1×10^5	1×10^5
u (m/s)	0.0	0.0	0.0

Table 6.1: Initial conditions for the MARA test case

Material properties			
	Region 1 (bubble)	Region 2 (water)	Region 3 (air)
γ	1.24	3.99669	1.4
P_∞ (Pa)	0.0	6.0×10^8	0.0

Table 6.2: Material properties for the MARA test case

Comments:

- The speed of sound in the water is

$$c_W = \left(\gamma_W \frac{p_W + P_\infty}{\rho_W}\right)^{0.5} \approx \left(3.99669 \times \frac{6.0 \times 10^8}{1000.0}\right)^{0.5} \approx 1550 \text{ m/s}$$

- In order to avoid the numerical difficulty in the two-phase DEM model, we suppose that there is initially a small volume fraction of residual phase which is at mechanical equilibrium with the other

phase. These volume fractions are specified in Table 6.3. As seen, the mixture density does not vary much with respect to the initial density.

Volume fractions			
	Region 1 (bubble)	Region 2 (water)	Region 3 (air)
α_{liquid}	1.0×10^{-3}	0.999	1.0×10^{-6}
α_{gas}	0.999	1.0×10^{-3}	0.999999
$\rho_{mixture}$ (kg/m^3)	1349.6483	997.3	1.207

Table 6.3: Volume fraction for the MARA test case

6.1.2.2 Structure

The structure properties for our computations are taken from [Galon, 2002]. The fluid in the MARA test rig is bounded by the vessel made of 316L stainless steel. It consists of a cylindrical shell connected to the bottom by welding technique. It is then closed by a very thick slab/roof which can be assumed to be perfectly rigid (see Figure 6.1, left).
When modeling the vessel for computations, we have encountered a particular difficulty: the bottom of the vessel is manufactured by a cold metal spinning process which leads to a significant initial work hardening and to significant variations in the initial thickness which must be taken into account in the computations.

Static behavior and material properties:

With the effort of best representing the behavior of the structure, the vessel is divided into four zones (A, B, C, D) of different thicknesses to which we associate four laws of behavior corresponding to different initial states of hardening.
The thicknesses e associated to the four zones are thus defined as:

- Zone A: $0 \leq |Z| \leq 40$cm, $e = 1.275$mm.
- Zone B: $40 \leq |Z| \leq 47$cm, $e = 0.96$mm.
- Zone C: $47 \leq |Z| \leq 51$cm, $e = 1.119$mm.
- Zone D: $51 \leq |Z| \leq 55$cm, $e = 1.245$mm.

The material's behavior is elastoplastic under von Mises criterion. The characteristics for 316 L stainless steel are:

- Young's modulus: $E = 192$ GPa.
- Poisson's ratio: $\nu = 0.3$.
- Density: $\rho = 7800$ kg/m^3.

The "static" curves corresponding to the four zones are given in Tables 6.4 - 6.7.

Zone A:

Stress (MPa)	Strain (in percent)
220	0.1146
249	0.2
315	1
425	5
863	41

Table 6.4: MARA problem. Static curve for zone A [Galon, 2002].

Zone B:

Stress (MPa)	Strain (in percent)
730	0.38
750	0.5
800	19

Table 6.5: MARA problem. Static curve for zone B [Galon, 2002].

Zone C:

Stress (MPa)	Strain (in percent)
580	0.3
630	5
695	19

Table 6.6: MARA problem. Static curve for zone C [Galon, 2002].

Zone D:

Stress (MPa)	Strain (in percent)
450	0.234
500	5
590	19

Table 6.7: MARA problem. Static curve for zone D [Galon, 2002].

Dynamic behavior:

From uni-axial tensile tests carried out on 316 L steel for different strain rates, the strain hardening is taken into account by introducing the following law:

$$\sigma(\dot{\epsilon}, \epsilon) = \sigma(\dot{\epsilon} = 0, \epsilon) \left[1 + \left(\frac{\dot{\epsilon}}{k} \right)^n \right] \tag{6.1}$$

where:

- $\sigma(\dot{\epsilon}, \epsilon)$ is the dynamic stress.
- $\sigma(\dot{\epsilon} = 0, \epsilon)$ is the static stress.
- k, n are the parameters of the constitutive law.

The experimental curves established for different strain rates made it possible to determine the k and n coefficients for 316L steel by means of least squares adjustments and in our case give the following values:

$$k = e^{\dfrac{a + b\epsilon}{1 + c\epsilon}} \tag{6.2}$$

with $a = 6.388,\ b = 86.215,\ c = 6.457$ and

$$n = 0.233.$$

6.1.3 Fluid-structure interaction

The fluid-structure interaction plays an important role in the MARA experiment and should therefore be taken into account in the numerical simulation. The MARA simulation in this thesis computes the fluid evolution using a cell-centered finite volume technique combined with the ALE formulation while the structure is modeled with a finite element method using the Lagrangian description. The fluid variables are discretized at the centers of the control volumes, so that when transferring information from the fluid to the structure, the pressure of the fluid must be projected onto the nodes of the structure grid at the fluid-structure interface. Note that the influence of the structure motion on the fluid is also taken into account in the EUROPLEXUS calculation. The detailed governing equations at the base of the transient explicit formulation applied for the fluid-structure interaction are presented in [Casadei and Halleux, 2009] (see for instance section 2 and references therein for more detail) but not detailed here as our focus will be on the fluid solution method.
A practical implementation of the ALE description requires that an automatic mesh displacement algorithm be supplied. The method of [Giuliani, 1982] serves for this purpose and provides the ALE approach in EUROPLEXUS with an automatic and continuous rezoning algorithm, calculating the velocities of the nodes based on the fluid velocities. The algorithm preserves, as much as possible, the regularity of the computational mesh when computing fluid-structure interaction problems. For this purpose, it relies on a numerical remeshing coefficient γ_m which is user-specified in the range $0 \leq \gamma_m \leq 1$ and requires an expert tuning in order to ensure the robustness of the computations, as could be observed in our own numerical experiments.

6.1.4 Boundary conditions and sensors

The boundary conditions applied for the present MARA simulations are displayed in Figure 6.2. In particular, we allow the nodes on the axis of symmetry to move freely in the Z direction (except for the common point with the slab) but we block the movement in the R direction as well as the rotation around this axis. For the slab, we block the movement in the Z direction since the the slab is considered as perfectly rigid in the MARA2 test rig. The nodes on the vessel are the Lagrangian ones allowing the structure to deform. We also block three degrees of freedom for the common point of the vessel and the slab.
In the MARA problem, the deformation of the structure is assessed by measuring the displacement at ten points denoted from PO to PBOT and which are reported in Figure 6.2. The initial coordinates of these points, before structure deformation takes place, are given in Table 6.8. Moreover, the pressure under the slab is also measured via the sensors highlighted in yellow cells. The radial distances between these sensors and the origin of coordinates (placed at the top-left corner of the domain) are approximately $R = 0,\ 30,\ 140,\ 210,\ 280,\ 325$ mm.

	R (mm)	Z (mm)
PO	350	-78.71
PA	350	-99.95
PB	350	-200.87
PC	350	-301.78
PD	350	-397.38
PE	305.22	-482.51
PF	217.02	-516.49
PG	113.17	-541.77
PH	20.06	-550.71
PBOT	0.0	-551.0

Table 6.8: MARA problem. Coordinates of points for measuring the displacement on the vessel for the coarse mesh.

6.1.5 Numerical results

In order to numerically study HCDA problems, a dedicated model has been developed in EUROPLEXUS. This so-called ADCR model (where ADCR stands for "Accident de Dimension du Confinement pour des Réacteurs") is described in the Appendix B. In the first stage of the present analysis, we wish to compare the results obtained using the (fully compressible) DEM approach, such as described in the previous chapters, with the numerical results provided by ADCR and the available measurements from the MARA experiments, taken from [Galon, 2002]. We emphasize the ADCR and DEM calculations make use of the same numerical strategy to account for the fluid-structure interaction phenomena and differ only by the solution process applied to the fluid simulation. The DEM method used in the following computations is second-order accurate in space using a limited linear reconstruction on primitive variables and in time using a 2-stage RK method. It also makes use of the instantaneous relaxation procedure of [Saurel and Abgrall, 1999, Tang, 2012] for the pressure and velocity and of the anti-diffusive UDCS approach for the volume fraction [Tang et al., 2014a, Tang et al., 2014b, Tang, 2012]. Regarding the CFL number, most of the ADCR simulations were performed with $CFL = 0.1$ to ensure a stable evolution for both the fluid and the structure in the MARA simulations. Depending on the mesh used (see below), the DEM method could be run with a CFL number up to $CFL = 0.5$ but $CFL = 0.1$ will be also used (for instance to allow for a comparison between ADCR and DEM with the same time-accuracy). Note that, as already mentioned, the remeshing coefficient γ_m has also a significant influence on the robustness of the numerical simulations. It must be carefully adjusted to avoid the generation of strongly deformed elements or cells when the mesh rezoning procedure is applied.
Different levels of mesh refinement are considered:

- The coarse mesh is composed of 6522 elements with the smallest spatial size of an element of order $\Delta = 4.74$mm.
- The medium mesh is composed of 25956 elements with the smallest spatial size of an element of order $\Delta = 2.32$mm.

Figure 6.3 displays the computed solutions with the DEM method on the coarse mesh. The high pressure gas bubble of 6.25 kbars when expanding from its initial radius of 2 cm generates a shock wave inside the confinement building. The density, velocity and pressure field are presented in Figure 6.3 at $t = 10 \times 10^{-5}$ s corresponding to a shock wave propagating radially without yet any impact with the vessel. The pressure peak at this instant decreases rapidly from the initial state due to the multi-dimensional effect and reaches about 440 bars. The maximum velocity of the flow at this instant can locally reach 180 m/s. From our numerical results, this maximum value can locally reach up to 380 m/s meaning the flow under investigation is not in the low-Mach regime. The density inside the bubble at $t = 10 \times 10^{-5}$ s

is of order 120 kg/m^3 which is much lower than its initial state of 1350 kg/m^3 due to the expansion of the bubble. Since water is (almost) incompressible, its density in the region perturbed by the shock wave changes very little. Later on the shock will impact the structure and cause structural deformation: the displacement field of the vessel at $t = 10$ ms is displayed in Figure 6.3 (bottom right plot). It is clearly observed that the structure is significantly deformed, forming a bulge under the slab but also with a strong deformation of the containment bottom. The maximum displacement at $t = 10\ ms$ is in fact found at the lowest point on the axis of symmetry (bottom point) and is approximately equal to 45 mm.

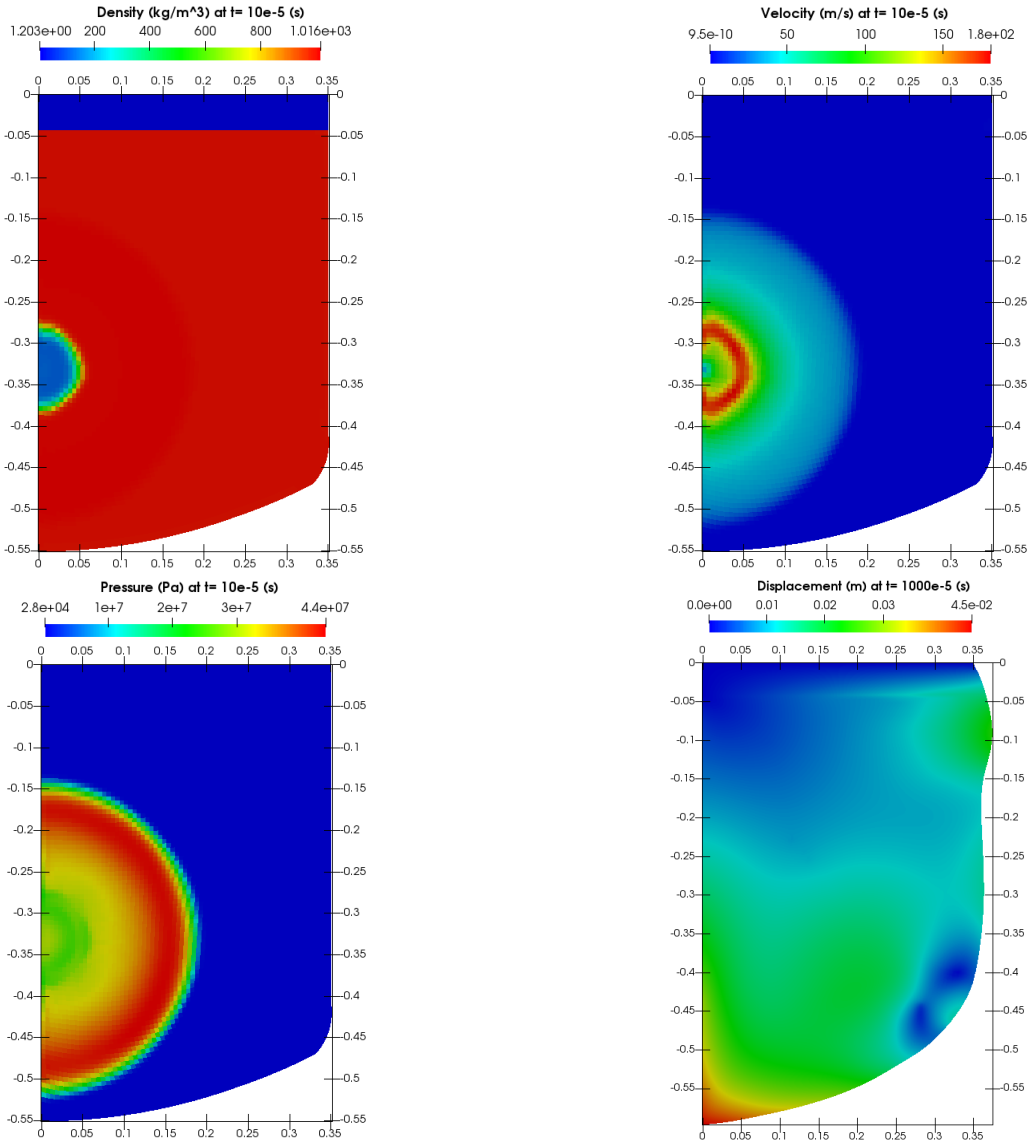

Figure 6.3: MARA problem. Density (top left), velocity (top right) and pressure (bottom left) fields at $t = 10 \times 10^{-5}$ s computed using the DEM method ($CFL = 0.5$) on the coarse mesh. Computed displacement at $t = 10$ ms (bottom right).

Figures 6.4 and 6.5 display the pressure evolution at the sensor $R = 30$ mm, that is the second sensor away from the symmetry axis under the slab (see Figure 6.2). The numerical solutions are computed with differently refined meshes, different remeshing coefficient γ_m and CFL numbers. It is clearly observed in Figure 6.4 (bottom plot) that the peak of pressure obtained in the experiment is much higher than in the calculations (of the order of 250 bars against 130 bars for DEM medium mesh). This may be

due in particular to the fact the initial high pressure bubble defined in the simulation does not allow to faithfully account for the actual charge explosion performed in the experiment. Note that this difference in the pressure peak between the numerical and experimental results is not a significant issue, as the impulse associated with this peak of order 0.2 ms from 1.9 ms to 2.1 ms remains actually low with respect to the global force transmitted by the fluid to the slab (see also [Galon, 2002] for the comparison of the impulse given by the experiments and the finite element methods applied for both fluid and structure).

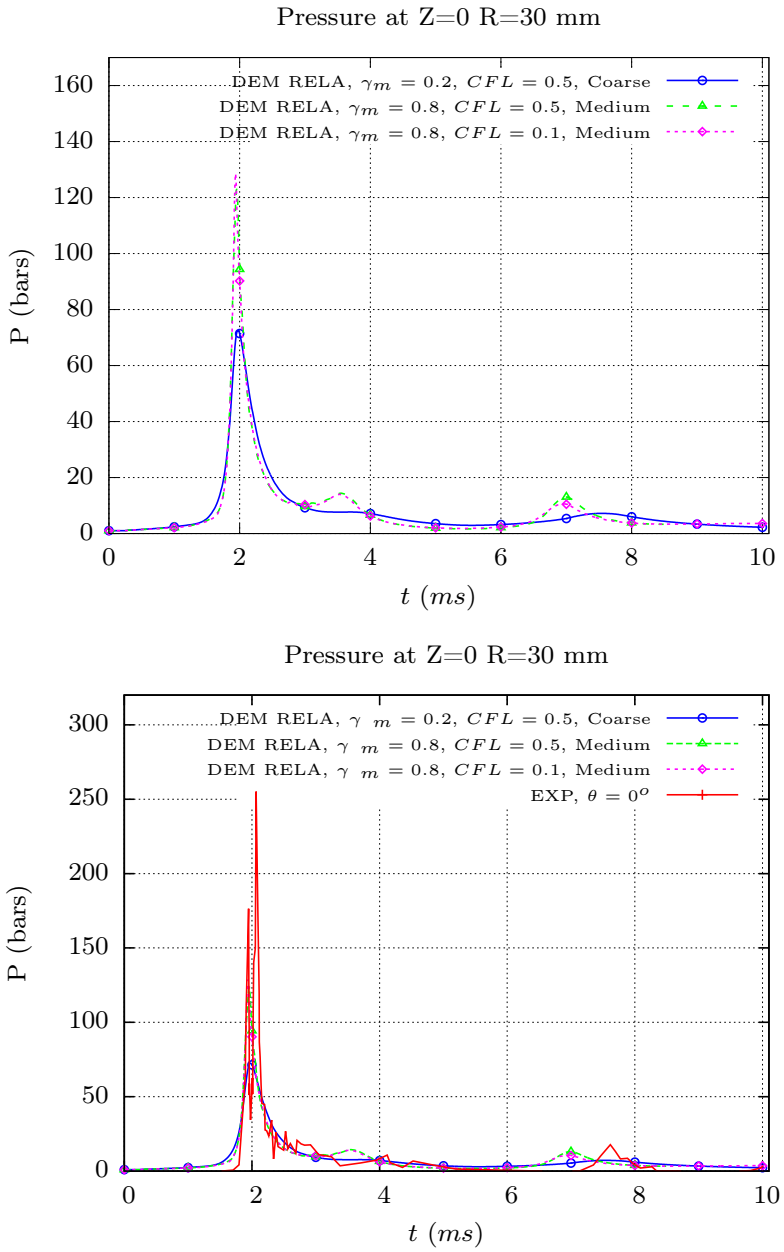

Figure 6.4: MARA problem. Evolution of the pressure under the slab at $Z = 0, R = 30$ mm. Top: verification and validation for the DEM results (influence of mesh resolution, γ_m, CFL). Bottom: comparison between DEM and EXP.

The study of the influence of numerical parameters (mesh resolution, remeshing coefficient γ_m and CFL) (see Figure 6.4 (top plot)) indicates the prediction of the pressure peak is quite sensitive to the grid

resolution. The DEM results in the medium grid depend only weakly on the CFL number (or physical time-step). Note the remeshing parameter γ_m needs to be adjusted to the grid resolution in order to ensure the stability of the simulation. The comparison between DEM results and experiments in Figure 6.4 (bottom plot) shows the dynamics of the fluid-structure problem is correctly captured by the simulation (at least for the pressure sensor under consideration, other measurements will be exploited next). Finally, Figure 6.5 displays a comparison between the best DEM results and the ADCR results (the experimental results are not reported on purpose as they would prevent a clear comparison between the two numerical evolutions). Local differences can be observed between both predictions but they will not be commented in detail in this work as the main purpose of this ADCR / DEM comparison in the context of this thesis is to establish that the DEM numerical strategy can be applied to the MARA problem and provides a numerical solution which is consistent with the reference numerical strategy applied up to now for this problem, namely ADCR. It should be emphasized the present DEM results represent the first application of this numerical strategy to the very challenging MARA problem.

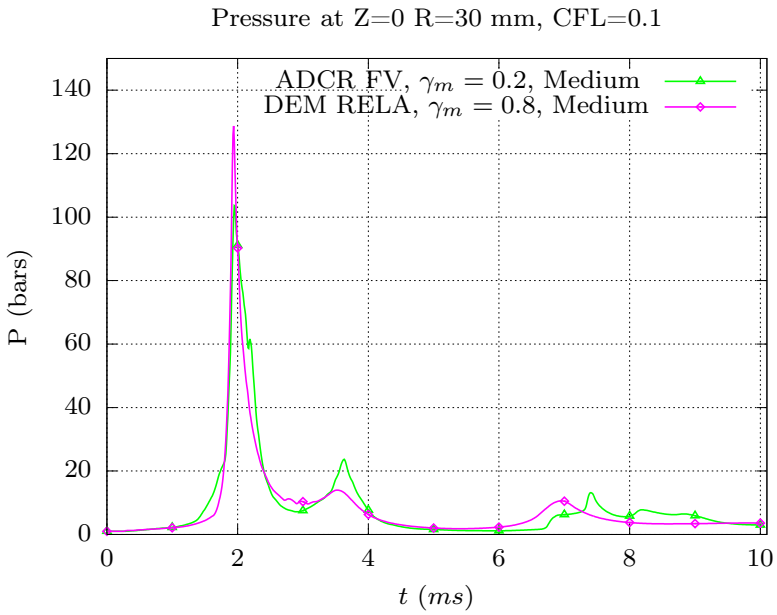

Figure 6.5: MARA problem. Evolution of the pressure under the slab at $Z = 0, R = 30$ mm. Comparison between DEM and ADCR.

Figure 6.6 and 6.7 display the pressure evolution at the sensor located under the slab at 140 mm from the axis of symmetry, that is the third sensor away from the symmetry axis under the slab (see Figure 6.2). Note that in fact two measurements have been performed at the same altitude and the same radial distance from the vessel axis but for two different azimuthal positions in order to assess the actual axisymmetry of the configuration. It can first be observed on the bottom plot of Figure 6.6 that both sensors provide time-evolution for the pressure at $Z = 0$, $R = 140\,mm$ which are not identical. A second observation is the pressure peaks observed experimentally and numerically computed are closer at this location: between 205 and 190 bars for the experiment against approximately 170 bars for the DEM calculation in the medium mesh. On the top plot of Figure 6.6, the grid sensitivity of the numerical simulation is evidenced: the coarse grid yields an underestimated pressure peak but correctly accounts for the remainder of the pressure time-evolution.

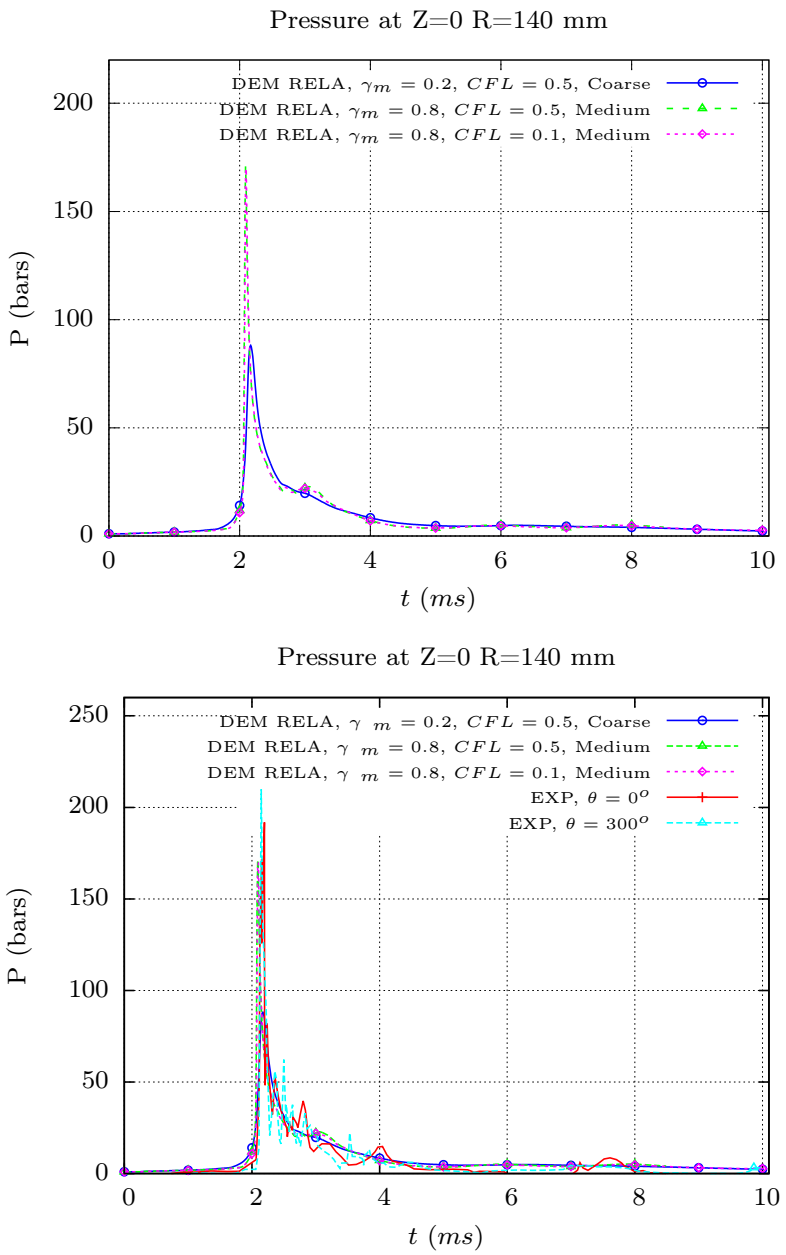

Figure 6.6: MARA problem. Evolution of the pressure under the slab at $Z = 0, R = 140$ mm. Top: verification and validation for the DEM results (influence of mesh resolution, γ_m, CFL). Bottom: comparison between DEM and EXP.

Figure 6.7 displays the comparison between the best DEM results and the ADCR results, with again the experimental results not reported to clarify the comparison between these computed evolutions. Apart from the pressure peak, the evolutions provided by both methods are very close (and compare rather well with experiment). The ADCR model gives a higher pressure peak, of order 240 bars at this sensor, that is even overpredicted with respect to experiment. Note again that, as already mentioned, the predicted global force is actually not significantly affected by this difference.

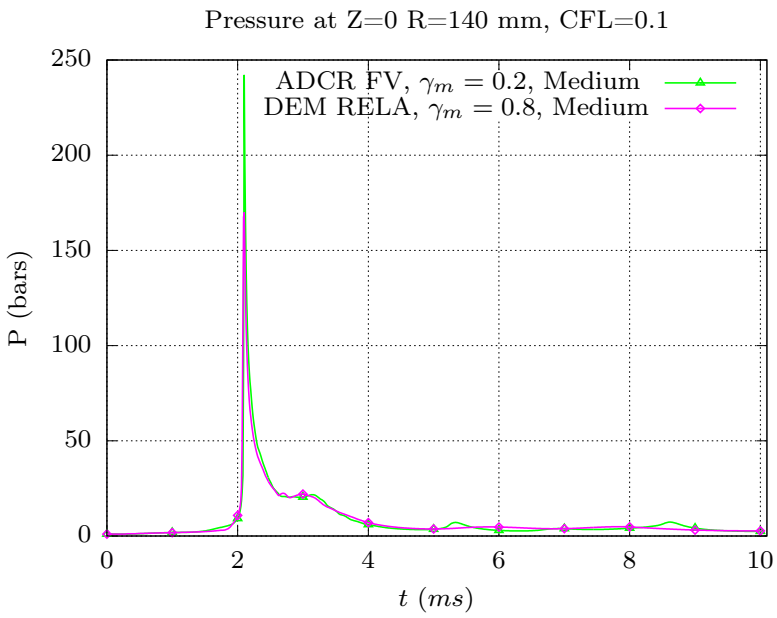

Figure 6.7: MARA problem. Evolution of the pressure under the slab at $Z = 0, R = 140$ mm. Comparison between DEM and ADCR.

Besides the pressure under the slab, the displacement of the vessel is another important information to assess the performance of the fluid-structure coupling strategies developed in EUROPLEXUS. The comparison between the experiments and different models are presented in Figures 6.8, 6.9 for radial displacements and in Figure 6.10, 6.11 for vertical displacements.

In Figure 6.8, we present the time evolution of the radial displacement at point O and A computed with the DEM method using various numerical choices (verification and validation study): coarse or medium grid with associated mesh deformation parameter and choice of CFL number. Points O and A are located in the bulge region (see Figure 6.2 left for a reminder of their location also detailed in Table 6.8 and see Figure 6.3 bottom right for the displacement field). The bulge begins to form in the experiment and in the DEM computations at time instants very close to each other: approximately 3 ms in the experiment and 2.8 ms in the DEM numerical results. The evolution of the radial displacement is more rapid in the computations. It should be emphasized at this point the experimental evolution displayed in Figure 6.8 does not specifically correspond to a measurement at point O or at point A. Rather, it is the maximum radial displacement reported in the experiment at each physical time [Galon, 2002]. In practice, this maximum radial displacement takes place between point O and point A. When looking at the DEM results for point O (top plot of Figure 6.8) and for point A (bottom plot of Figure 6.8), we can conclude the computed maximum radial displacement is close to point A, that is around 100 mm under the slab with respect to the non-deforming state.

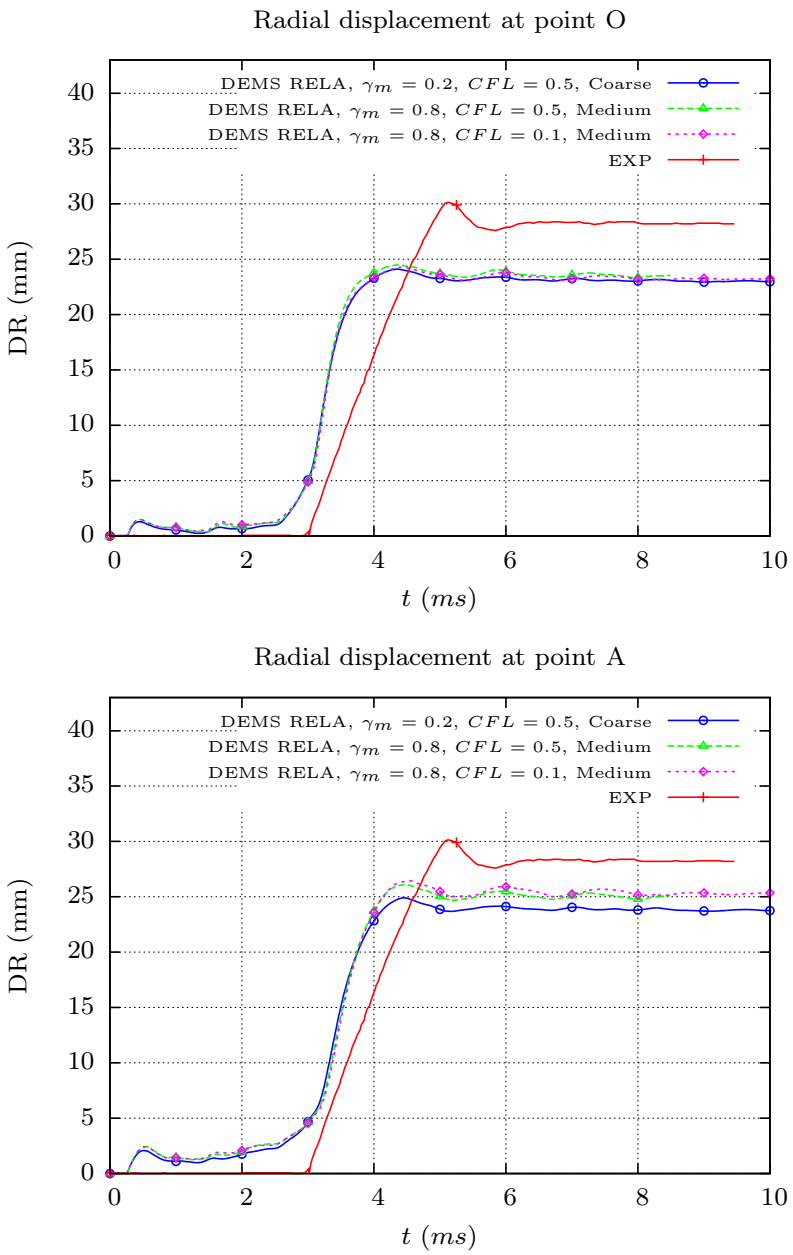

Figure 6.8: MARA problem. Time-evolution of the radial displacement at point O (top) and A (bottom). DEM verification and validation study.

In Figure 6.9, we compare the numerical results obtained at the two points PO and PA around the critical position (that is the position corresponding to the maximum radial displacement) using DEM and ADCR with the experimental evolution of the maximum radial displacement. At $t = 10$ms, the maximum radial displacement is about $\Delta R \approx 28mm$ in the experiment corresponding to 8% of the initial radius. This is very close to the numerical results $\Delta R/R_0 = 7.1\%$ with DEM method on medium mesh at point PA. The radial displacement predicted by ADCR and DEM at point A are very close to one another. This is also true for the prediction at point O, with ADCR predicting a slightly larger displacement (even a bit closer to the experiment, but with the same dynamics for the bulge formation as the one predicted using DEM). Here again, the key conclusion of this comparison is the ability of the DEM strategy to provide results which are fully consistent with the ADCR model, considered as a reference strategy for such HCDA calculations.

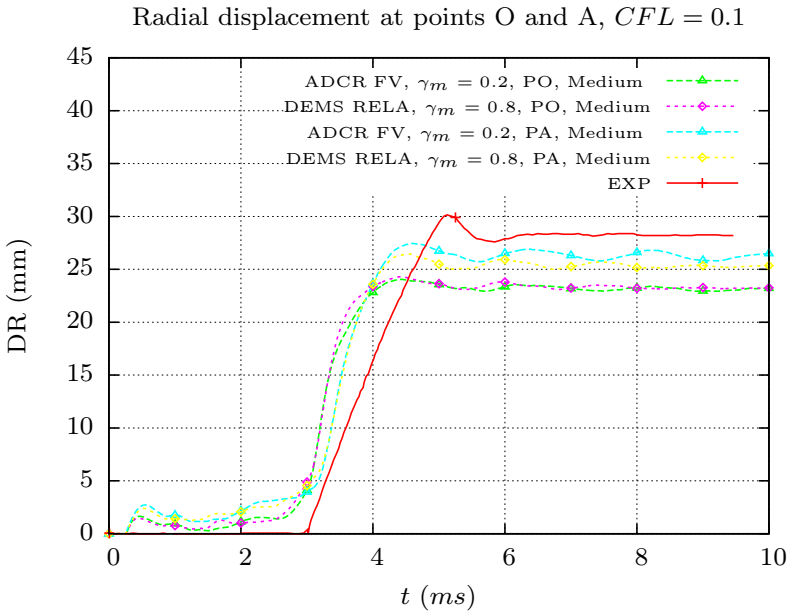

Figure 6.9: MARA problem. Time-evolution of the radial displacement at points O and A. Comparison betwen ADCR, DEM and experiment.

Figure 6.10 displays the time evolution of the vertical displacement at point PBOT which is the lowest position on the axis of symmetry. The bottom of the vessel reaches the maximum elongation at $t = 3.1$ ms in the experiment and at $t = 2.8$ ms in the computations (with DEM method on the medium mesh) which corresponds respectively to 10.5% and 10.2% of the initial height. Note that the sensitivity of this result to the grid refinement is less noticeable than for other quantities of interest.

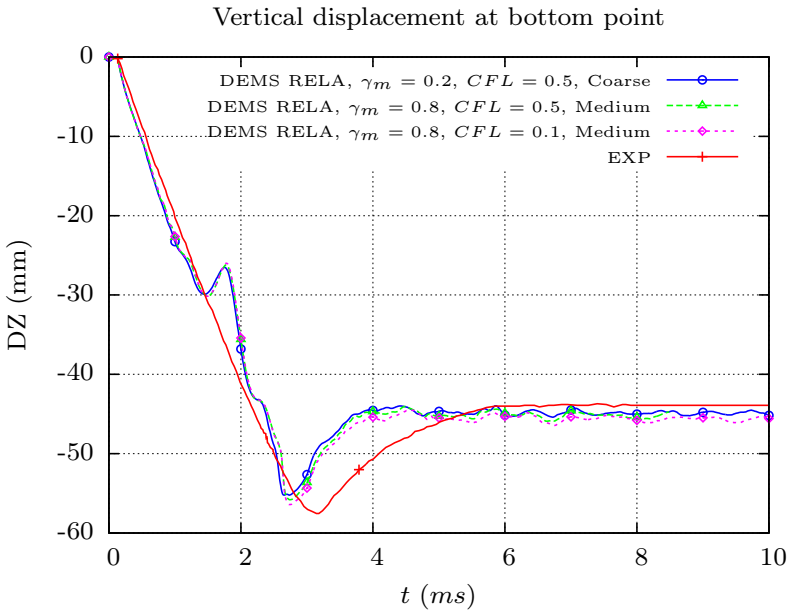

Figure 6.10: MARA problem. Time-evolution of the vertical displacement at the bottom point PBOT. DEM verification and validation study.

Figure 6.11 displays the comparison between the DEM and ADCR numerical results on one hand and the experimental measurement on the other hand. It can be observed the DEM strategy appears slightly better than the ADCR approach for predicting the final vertical displacement at this bottom point. Both numerical methods predict however an evolution of this vertical displacement with a similar faster dynamics with respect to the experiment. Here again, it can be concluded that DEM offers an interesting alternative to ADCR for computing HCDA problems.

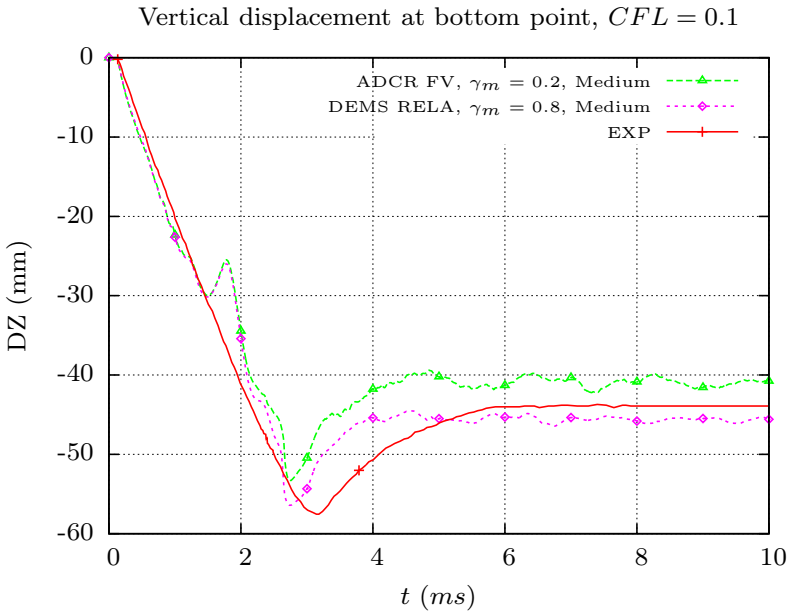

Figure 6.11: MARA problem. Time-evolution of the vertical displacement at the bottom point PBOT. Comparison between ADCR, DEM and experiment.

6.1.6 Computational cost

The previous comparison of numerical results with experiments has made clear that the DEM approach and the ADCR model can provide good / reliable results when computing the MARA problem. It is however important to also assess these numerical strategies from an efficiency viewpoint. First, it should be emphasized that DEM is more expensive than ADCR because of the numerous RP to be solved at the cell interfaces for various phase configurations. From the DEM and ADCR calculations performed in the same (medium) mesh with the same CFL number ($CFL = 0.1$) it is possible to estimate the extra-cost induced by DEM with respect to ADCR is around 40%.
Going back to the low-Mach context of the present work, it should be noticed that both ADCR and DEM are not efficient when computing low-Mach problems since their stability time step remains constrained by the sound speed of liquid. As already mentioned, the initial pressure level for the bubble considered in the actual MARA experiment is such that this MARA problem is not a low-Mach problem: with an initial pressure in the bubble of approximately 6 kbars, the fluid velocity can locally reach $400\,m/s$. Therefore, the overall computational cost will not be really impacted by the low-Mach efficiency limitation of these fully compressible ADCR and DEM approaches. The original MARA problem had nonetheless to be solved in order to gain confidence in the possibility to accurately solve this HCDA problem using DEM - and this has been indeed established thanks to the available MARA experimental measurements. Going back now to the core problem of this work, namely the efficient (and accurate) computation of bubble expansion problems, we propose to define an adapted low-Mach MARA problem which will allow a comparison between the fully compressible DEM approach and the newly proposed DEM-LM strategy.

6.2 Low-Mach MARA problem

6.2.1 Problem description

In this section, we consider a problem of HCDA or MARA type but we choose to decrease the initial pressure of the bubble in order to remain in a low-Mach number regime. The drawback of this choice of "weak" compression is that the slower flow dynamics would require to perform computations over an extended period of physical time to evidence significant variation of the flowfields (more particularly the impact on the vessel wall boundaries). To fix this issue, we also increase the initial radius of the bubble ($R_0 = 17$ cm, see Figure 6.12).

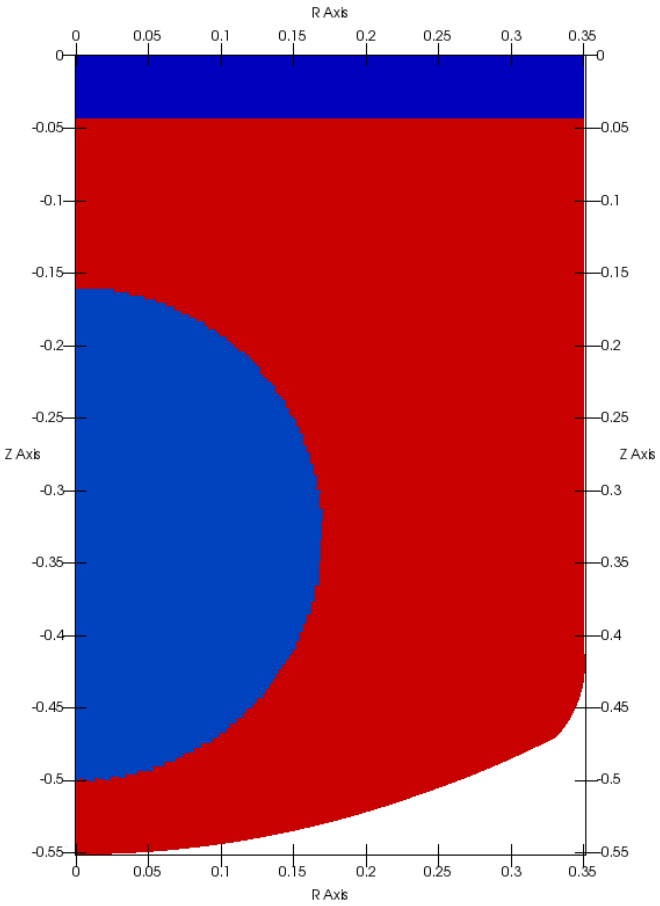

Figure 6.12: Configuration for the low-Mach MARA problem (2 bars)

The initial position of the bubble center and the overall dimension of the problem stay unchanged with respect to the previous MARA testcase. The computations are performed using DEM-LM and DEM methods, with solutions provided by each method compared on both accuracy and efficiency properties. The initial conditions and parameters of this test case are given in Tables 6.9, 6.10.

	Region 1 (bubble)	Region 2 (water)	Region 3 (air)
ρ (kg/m^3)	2.1092	998.3	1.206
P (Pa)	2×10^5	1×10^5	1×10^5
u (m/s)	0.0	0.0	0.0

Table 6.9: MARA bas-Mach. Initial conditions.

Artificial sound speed		
	$c_{AC,water}$ (m/s)	$c_{AC,gas}$ (m/s)
eff = 2.86	542	120

Table 6.10: MARA bas-Mach. Artificial sound speed.

Comments:

- The value of the initial density of the bubble region is obtained by supposing that it is made of perfect gas which is isentropically compressed:

From 1 to 2 bars:

$$\rho_{B,0} = \left(\frac{P_{B,0}}{P_{A,0}}\right)^{1/\gamma_B} \rho_{A,0} = \left(\frac{2\times 10^5 \text{Pa}}{1\times 10^5 \text{Pa}}\right)^{1/1.24} 1.206 \text{ kg/m}^3 \approx 2.1092 \text{ kg/m}^3$$

- The material properties are similar to those used in the MARA test case (see Table 6.2).
- The (physical) initial sound speeds in water and gases in the domain are approximately 1550 m/s and 342.9 m/s. With an efficiency factor set equal to eff = 2.86, the artificial sound speeds used in the liquid and gas for the DEM-LM simulations are those reported in Table 6.10. We will comment later in this section the choice and influence of this important parameter eff for the DEM-LM simulations.
- In each region, we suppose that there are two phases (gas and liquid) and there is initially a small volume fraction of residual phase which is at mechanical equilibrium with the other. These residual volume fractions are set equal to $\alpha_{res} = 10^{-6}$ for all DEM and DEM-LM calculations.

We also wish to emphasize that we do not consider the fluid-structure interaction in this low-Mach MARA test case. This choice is motivated by two reasons:

- The actual displacement of the vessel is negligible with such a low level of energy released for the low-Mach situation under consideration.
- The stability time steps for the structure solver and the fluid solver are not yet separated in the current version of EUROPLEXUS when computing a fluid-structure interaction problem. The stability time step used for the computations is constrained in practice by the structural time-step. Consequently, the analysis of the efficiency gain expected from the DEM-LM fluid solver could be perturbed or even biased by taking into account the structure solver.

The calculation are performed using the coarse and medium grids previously used for the MARA problem.

6.2.2 Numerical results

In this section, we compare the solutions given by the DEM-LM and DEM on both the accuracy and the efficiency criteria when computing the low-Mach MARA problem. Note the DEM method is applied with the instantaneous relaxation procedure of [Saurel and Abgrall, 1999, Tang, 2012] for both pressure and velocity while the DEM-LM relaxes only the velocity (these choices being "optimal" for each method). DEM and DEM-LM methods share the following numerical choices:

- Second order accuracy in space using the limited linear reconstruction on primitive variables.
- Second order accuracy in time using 2-stage RK method.
- Anti-diffusive UDCS approach for the volume fraction [Tang et al., 2014a, Tang et al., 2014b, Tang, 2012].
- $CFL = 0.5$.

With respect to the MARA calculations of the previous section, we notice that it is not necessary to reduce the CFL number as we do not have fluid structure interaction in this case. The choice of a Courant number $CFL = 0.5$ ensures a stable second-order accurate calculation for both DEM and DEM-LM.
In Figure 6.13, we compare the pressure at different positions under the slab (see section 6.1.4). The DEM and DEM-LM method gives similar solutions, corresponding to an (almost) isentropic compression/expansion behavior of the air layer due to the upward/downward motion of the liquid. A closer analysis shows the radial evolution of the pressure time-evolution is not exactly the same between DEM and DEM-LM (see in particular the second pressure peak). A further grid refinement, not performed in the present

work, would be needed to draw a complete conclusion on this comparison in long time. What can be concluded at this stage is that the DEM-LM strategy is consistent with the DEM fully compressible approach.

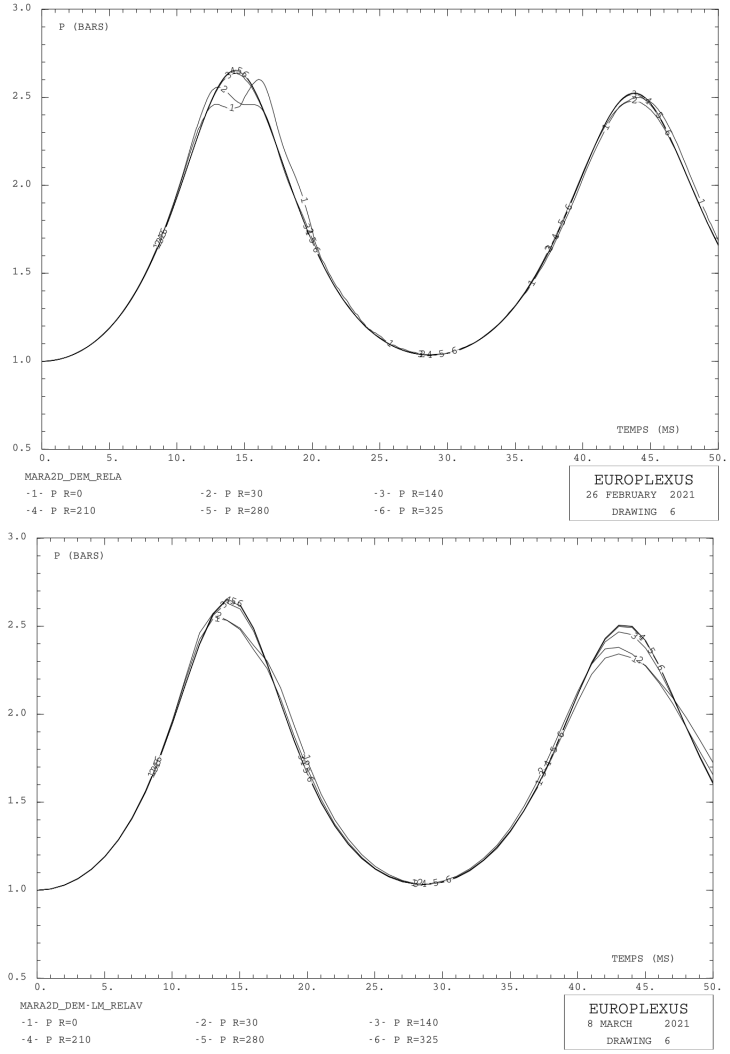

Figure 6.13: MARA bas-Mach. Time-evolution of the pressure under the slab. DEM (top) vs DEM-LM (bottom). Medium grid.

In Figure 6.14, we compare the average pressure in the bubble and the air layer computed with DEM and DEM-LM methods on the coarse and medium meshes. It is clearly observed that the average pressures computed using DEM and DEM-LM with the same mesh resolution are very close to each other. The effect of grid refinement (from coarse to medium) is the same for both methods with almost superimposed time-evolutions for the average pressure in region 1 on the medium grid and very close time-evolutions in region 3. The bubble pressure decreases from 2 bars to 1.31 bars when expanding and then increases to 1.95 bars when being in the contraction phase. Similarly, the air layer (region 3) is compressed from 1 bar to 2.6 bars by the water hammer. We can conclude from this comparison that the DEM-LM solutions are fully consistent with those given by DEM and we will detail in the next section the extent of computational gain offered by DEM-LM with respect to DEM.

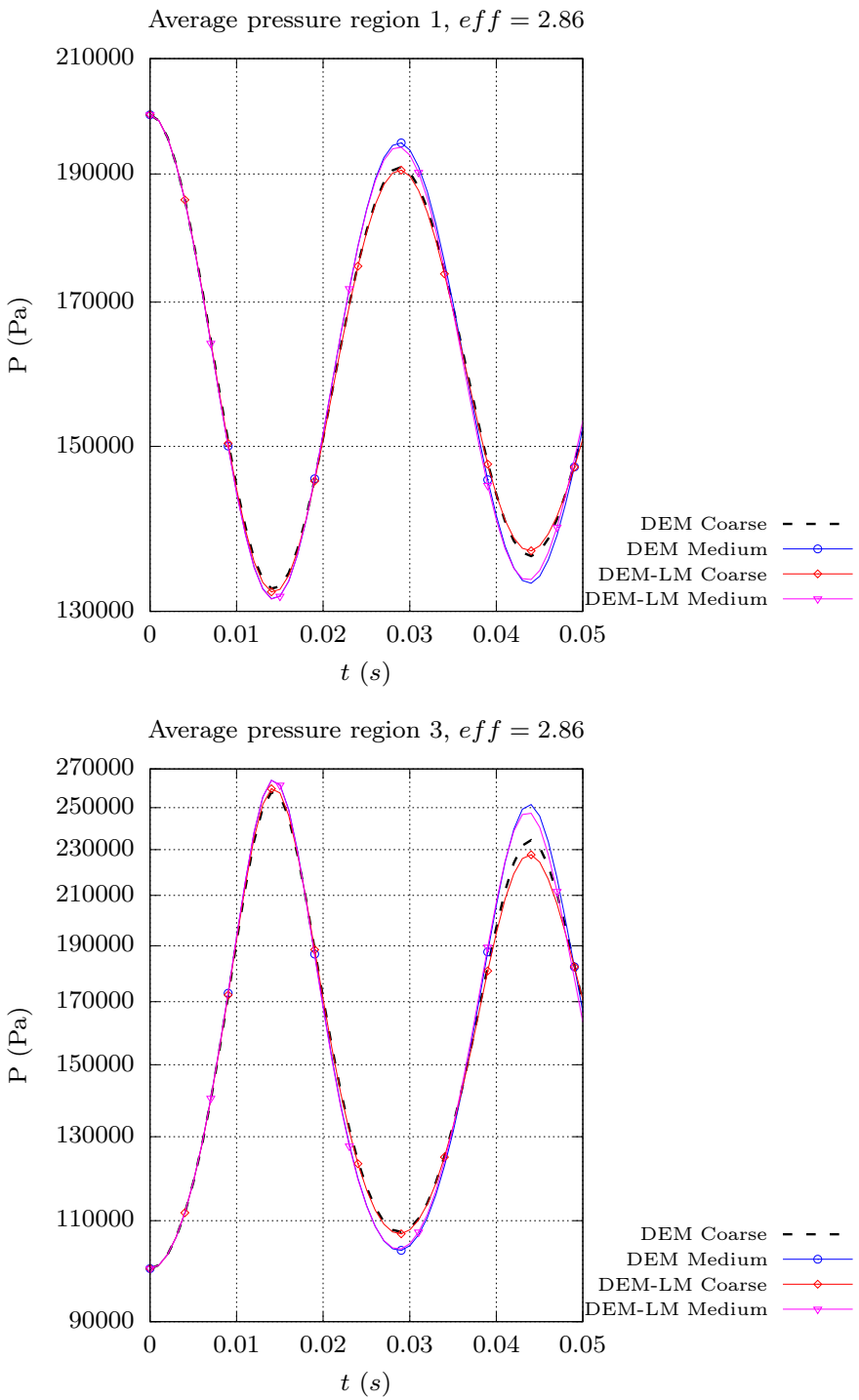

Figure 6.14: MARA bas-Mach. Comparison of the average pressures for the DEM and DEM-LM methods. From top to bottom: the average pressure in region 1 (bubble) and the region 3 respectively.

As a final accuracy indicator, Figure 6.15 displays the time-evolution of energy contributions for the DEM-LM calculation on the medium grid: the internal energy of gas regions, the kinetic energy of water. The total energy of the system is the sum of the previous energies neglecting the kinetic energy of gases and the internal energy of water. We observe that, in practice, the computed total energy is (almost) constant in time despite the fact that the DEM-LM model does not strictly ensure the conservation of this quantity from a theoretical viewpoint.

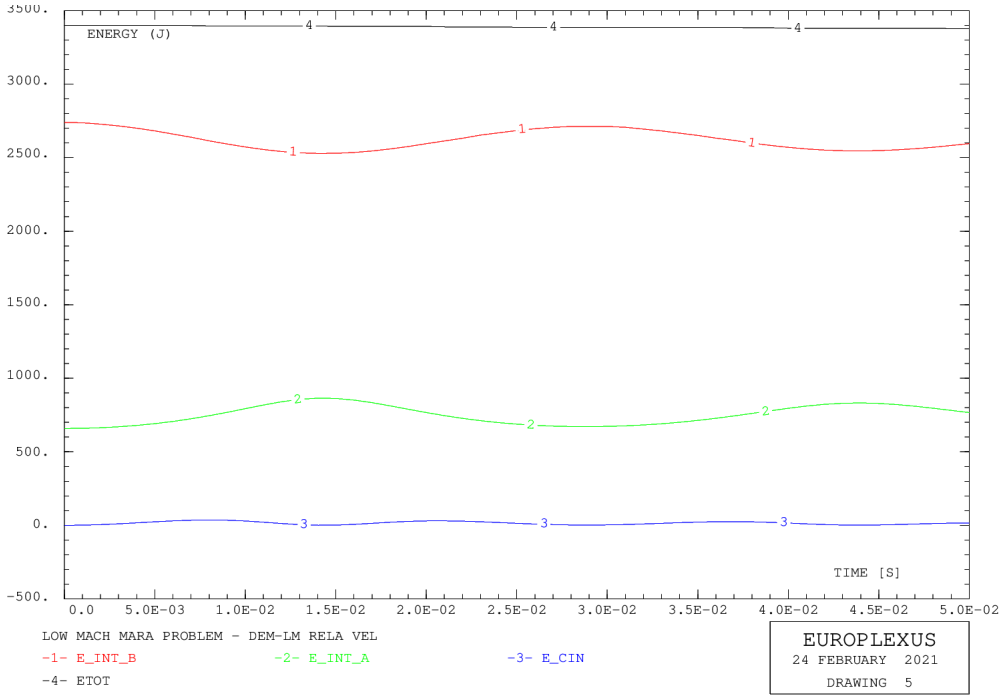

Figure 6.15: MARA bas-Mach. Medium grid DEM-LM solution. Time evolution of the internal energy of regions 1 and 3 (red and green curves), the kinetic energy of water (blue curve) and the total energy (black curve, sum of all contributions).

6.2.3 Computational cost

All the test cases in section 6.2 have been performed with sequential computations on a processor Intel(R) Xero(R) CPU E5-2630 v2 @ 2.60GHz. The CPU time consumption $TCPU(s)$ and the corresponding number of time steps n to reach the final physical time of the simulation are summarized in Table 6.11.

	DEM		DEM-LM		Speed-up
	TCPU (s)	n	TCPU (s)	n	DEM vs DEM-LM
Coarse	4208.96	41081	1471.22	14394	2.86
Medium	43656.53	104164	12594.7	28788	3.46

Table 6.11: MARA bas-Mach. Computational cost: DEM vs DEM-LM. $CFL = 0.5$

The DEM and DEM-LM solutions have been shown to be consistent in the previous section (both on the coarse and medium grids). This means the efficiency analysis of DEM/DEM-LM is performed for the same level of accuracy. For a computation on the coarse mesh with a final physical time $t_f = 50$ ms, the DEM method takes 41081 time steps while it is only 14394 for the DEM-LM method. The ratio of the maximum allowable time steps between DEM and DEM-LM $41081/14394 = 2.854$ corresponds as expected to the ratio between the physical and artificial sound speeds (or the efficiency coefficient eff). The overall computational time between DEM and DEM-LM is reduced by a similar ratio $4208.96/1471.22 = 2.861$ because the cost per point per iteration for both approaches is almost the same - the choice of a larger timestep for DEM-LM translates therefore entirely into a gain of computational time.
When refining the mesh from the coarse one to the medium one, the number of time steps is increased by a factor two in the DEM-LM model and the corresponding CPU time is increased by a factor close to 8,

which is logical since the factor 2 on the time-step combines with a factor 2^2 (cells are halved in each R and Z direction when going from coarse to medium) on the space loops. It can be noticed that for the DEM method the computational cost increases by a factor above 10 when going from the coarse to the medium grid. This extra cost was identified as being related to the relaxation process applied at each iteration on the pressure and velocity. Overall, it can be concluded results such as those reported in Figure 6.14 for the time-evolution of the averaged pressure can be obtained using DEM-LM for a computational time divided by a factor close to 3.5 with respect to the original DEM fully compressible approach.

Conclusion

In this final chapter, the DEM and DEM-LM methods introduced in the previous chapters and applied up to now to model problems (1D bubble expansions) have been applied to an industrial application: the multidimensional (2D axisymmetric) MARA experiment corresponding to an HCDA configuration of interest for nuclear safety analysis.

In a first step, the DEM approach has been applied to the MARA problem for initial conditions representative of the available physical experiments. It was thus possible to demonstrate the accuracy of the DEM approach, coupled with an existing fluid-structure interaction treatment in the EUROPLEXUS code, by comparing the computed results both with measurements and with another set of numerical results obtained using a well-established model for HCDA problems, namely the ADCR model implemented in EUROPLEXUS. It was thus clearly established that DEM provides results which are consistent both with ADCR and experiment. Once performed this validation of the DEM implementation for HCDA, it remained to deal with the core issue of the present work low-Mach bubble expansion. The original MARA experiment, useful for validation purpose, is not well-adapted to the assessment of the novel DEM-LM strategy developed in the thesis as it is not a low-Mach configuration.

The MARA problem was therefore adapted (through the choice of pressure level and size of the initial bubble) to become a so-called low-Mach MARA problem making the comparison between DEM and DEM-LM relevant. The significant gain of efficiency offered by DEM-LM with respect to the original DEM was demonstrated on this testcase and it was also proved this gain was ensured for an equivalent level of accuracy.

The remaining limitation for the DEM-LM approach, already pointed out in the previous chapter, is the lack of robustness of the solver applied to the solution of the first stage (hyperbolic system) of the DEM-LM strategy which needs to be improved in order to allow the application of DEM-LM to HCDA problems involving higher pressure levels in the initial bubble.

Conclusion

Conclusions and perspectives

Conclusions

An attractive numerical method capable of solving simultaneously the accuracy and the efficiency problems encountered with standard compressible flow solvers in the low-Mach number regime has been developed and implemented in the fast dynamic fluid-structure interaction code EUROPLEXUS, developed by CEA and Joint Research Center (JRC). With attention given to non-reactive and immiscible two-phase flows, the proposed method has relied on the DEM seven-equation model within a cell-centered finite volume framework.

The full development of the new method for the two-phase flow situation was preceded by a series of both analytical and numerical analysis for single-phase flows. It was firstly investigated in this work how the quality of the numerical solutions computed with the co-located finite volume upwind methods of Godunov-type degrades in the low-Mach number regime. This investigation was purely analytical and relied on the asymptotic analysis at both the continuous level (Euler equations for inviscid flows) and the discrete level, meaning the numerical schemes. It turns out that it is the wrongly scaled computed pressure fluctuation which is responsible for the accuracy problem faced by these conventional compressible solvers currently implemented in EUROPLEXUS.

A series of numerical experiments has been conducted using both well-prepared and not-well-prepared initial conditions. It was found by the numerical experiments that physical problems using not-well-prepared condition did not suffer from the accuracy issue. On the other hand, problems with the well-prepared initial conditions were falsely computed by the standard compressible solvers. The adaptation to the liquid case of some existing low-Mach numerical fixes [Dellacherie et al., 2016, Rieper, 2008] has shown their ability to correctly compute low-Mach flows. However, these methods solve only partially the low-Mach problems since the efficiency issue remains.

As stated, our purpose is to solve low-Mach flows accurately but also in an efficient way. With this motivation, we have developed a new numerical method which was first presented for the single-phase flow. It was tested on several piston problems and produced a promising efficiency with satisfactory accuracy.

The success of the new method for single-phase flows has motivated its extension to the two-phase situation. It is denoted as DEM-LM and can be regarded as the extension of the well-established DEM method in the low-Mach number regime. A one-dimensional bubble expansion and the MARA problems (bubble expansion in a vessel) have been computed in order to demonstrate the performance the new numerical scheme.

Summary of the method development

The DEM-LM solver is a two-step numerical scheme based on the artificial compressibility approach. The first step involves solving a hyperbolic non-reactive immiscible two-phase system for the artificial acoustic waves. The numerical efficiency is enhanced in this step by replacing the physical sound speed by an artificial sound speed. In the second step, the wrongly computed variables in the first step are corrected, supposing an isentropic transformation. Some key features of the DEM-LM method are:

- The method (implemented in EUROPLEXUS) is second order accurate in both space and time (thanks to a usual reconstruction technique on primitive variable and a standard 2-step Runge-Kutta time-integration) and is able to compute multi-dimensional problems.
- The anti-diffusive UDCS strategy [Tang, 2012, Tang et al., 2014a, Tang et al., 2014b] aiming at sharply capturing a fluid/fluid interface and also available in EUROPLEXUS can be combined with the current DEM-LM method.
- Problems with moving boundaries are taken into account by considering the ALE approach.
- The method is readily applied for fluid structure interaction problems.
- The DEM-LM method reduces to single-phase situation by considering two fluids of the same phase.

It was numerically shown that an efficiency factor of 16 could be obtained on the one-dimensional bubble expansion representative of an HCDA nuclear safety problem, while the time consumption is reduced by more than 3 times in the two-dimensional MARA-like configuration without fluid-structure interaction. This efficiency improvement was achieved with DEM-LM while preserving the accuracy of the computed solutions. However, the approach still suffers from a robustness issue since a (linear) acoustic solver was employed in solving the hyperbolic system associated with the first stage of the method. This prevents from computing problems with higher non-linearity (higher pressure levels in the initial bubble for instance).

Perpsectives

The limitation related to the robustness issue could be solved by employing other numerical fluxes capable of treating compressible flows with potentially large Mach numbers. Possible fluxes to apply would be the extension of Osher Riemann solver introduced in [Dumbser and Toro, 2011b, Dumbser and Toro, 2011a] or the HLLEM numerical flux [Dumbser and Balsara, 2016], suited to non-conservative hyperbolic and two-phase systems.

At the present time, the performance of the DEM-LM method has only been assessed for problems without fluid structure interaction. It is not a limitation of the method but rather the fact the current algorithm implemented in EUROPLEXUS prevents us from investigating properly the efficiency of our solver with fluid structure interaction taken into account. Indeed, the stability time steps of the fluid solver and the structural solver are currently not separated so that the stability time step applying to the fluid solver is actually constrained by the structure. Future tasks involve separating fluid-structure time steps to produce the expected efficiency of the current DEM-LM method when computing problems with deformable structure.

We finally conclude by emphasizing the long-term objective of numerical developments to come in EUROPLEXUS following the present thesis: building a numerical method capable of computing reactive low-Mach two-phase flows, to study in particular potential accidental situations occurring in a nuclear reactor containment and involving hydrogen-air combustion. The RDEM (Reactive Discrete Equation Method) [Le Métayer et al., 2005], an extension of the DEM for reactive flows, appears as an attractive starting point on which to extend the ideas of DEM-LM introduced and applied in our work.

Annexes

A

Conservative and primitive formulation

For the sake of simplicity, we demonstrate here the 1D transformation in the Cartesian coordinate system. The Euler system in conservative form is written as:

$$\begin{aligned}
\frac{\partial \rho}{\partial t} + \frac{\partial (\rho u)}{\partial x} &= 0 \\
\frac{\partial (\rho u)}{\partial t} + \frac{\partial (\rho u^2 + p)}{\partial x} &= 0 \\
\frac{\partial (\rho e^t)}{\partial t} + \frac{\partial ((\rho e^t + p) u)}{\partial x} &= 0
\end{aligned}$$

In primitive form, the mass conservation equation is written as:

$$\frac{\partial \rho}{\partial t} + u \frac{\partial \rho}{\partial x} + \rho \frac{\partial \rho}{\partial x} = 0 \tag{A.1}$$

The momentum conservation equation can also be written as:

$$u \left(\frac{\partial \rho}{\partial t} + \frac{\partial (\rho u)}{\partial x} \right) + \rho \left(\frac{\partial u}{\partial t} + u \frac{\partial u}{\partial x} \right) + \frac{\partial p}{\partial x} = 0$$

In which the first term disappears leading to the momentum equation in the primitive form as:

$$\frac{\partial u}{\partial t} + u \frac{\partial u}{\partial x} + \frac{1}{\rho} \frac{\partial p}{\partial x} = 0 \tag{A.2}$$

The total energy conservation equation can be written as:

$$e^t \left(\frac{\partial \rho}{\partial t} + \frac{\partial (\rho u)}{\partial x} \right) + \rho \left(\frac{\partial e^t}{\partial t} + u \frac{\partial e^t}{\partial x} \right) + p \frac{\partial u}{\partial x} + u \frac{\partial p}{\partial x} = 0$$

The first term disappears thanks to the mass conservation equation. By replacing the total energy by the sum of the internal and the kinetic energy $e^t = e + \frac{1}{2} u^2$, the above equation gives:

$$\rho \left(\frac{\partial e}{\partial t} + u \frac{\partial e}{\partial x} \right) + \rho u \left(\frac{\partial u}{\partial t} + u \frac{\partial u}{\partial x} \right) + p \frac{\partial u}{\partial x} + u \frac{\partial p}{\partial x} = 0$$

The term $\frac{\partial u}{\partial t} + u \frac{\partial u}{\partial x}$ can be replaced by $-\frac{1}{\rho} \frac{\partial p}{\partial x}$ thanks to the primitive form of the momentum equation which then gives the evolution equation for the internal energy:

$$\frac{\partial e}{\partial t} + u \frac{\partial e}{\partial x} + \frac{p}{\rho} \frac{\partial u}{\partial x} = 0$$

We now try to transform this equation into the evolution equation for the pressure. The internal energy is in fact the function of the pressure and the density. Indeed, the equation of state gives $e = e(p, \rho)$ and therefore we have:

$$de = \frac{\partial e}{\partial p}\Big)_{\rho} dp + \frac{\partial e}{\partial \rho}\Big)_{p} d\rho$$

Which then yields:

$$\frac{\partial e}{\partial t} = \frac{\partial e}{\partial p}\Big)_{\rho} \frac{\partial p}{\partial t} + \frac{\partial e}{\partial \rho}\Big)_{p} \frac{\partial \rho}{\partial t} \quad \text{and} \quad \frac{\partial e}{\partial x} = \frac{\partial e}{\partial p}\Big)_{\rho} \frac{\partial p}{\partial x} + \frac{\partial e}{\partial \rho}\Big)_{p} \frac{\partial \rho}{\partial x}$$

Replacing theses relations into the evolution equation for the internal energy yields:

$$\frac{\partial e}{\partial p}\Big)_{\rho} \left(\frac{\partial p}{\partial t} + u\frac{\partial p}{\partial x}\right) + \frac{\partial e}{\partial \rho}\Big)_{p} \left(\frac{\partial \rho}{\partial t} + u\frac{\partial \rho}{\partial x}\right) + \frac{p}{\rho}\frac{\partial u}{\partial x} = 0$$

The term $\frac{\partial \rho}{\partial t} + u\frac{\partial \rho}{\partial x}$ can be replaced by $-\rho\frac{\partial u}{\partial x}$ by the mass conservation equation and this equation can now be rewritten as the evolution equation for the pressure:

$$\frac{\partial p}{\partial t} + u\frac{\partial p}{\partial x} + \rho\frac{\left[\frac{p}{\rho^2} - \frac{\partial e}{\partial \rho}\Big)_{p}\right]}{\frac{\partial e}{\partial p}\Big)_{\rho}}\frac{\partial u}{\partial x} = 0$$

We define the sound speed as:

$$c^2 = \frac{\left[\frac{p}{\rho^2} - \frac{\partial e}{\partial \rho}\Big)_{p}\right]}{\frac{\partial e}{\partial p}\Big)_{\rho}} \tag{A.3}$$

And the pressure equation becomes:

$$\frac{\partial p}{\partial t} + u\frac{\partial p}{\partial x} + \rho c^2\frac{\partial u}{\partial x} = 0 \tag{A.4}$$

The equations (A.1), (A.2), (A.4) form the Euler system in the primitive form.
In the following, we demonstrate that the definition of sound speed in (A.3) is equivalent to the classical definition of sound speed in fluid dynamics:

$$c^2 = \frac{\partial p}{\partial \rho}\Big)_{s}$$

Where s is the entropy.
Indeed, from the first law of thermodynamics we have:

$$de = \delta Q + dW \Rightarrow de = Tds - pdV = Tds + \frac{p}{\rho^2}d\rho$$

Under the isentropic hypothesis, this relation becomes:

$$de = \frac{p}{\rho^2}d\rho$$

Since $de = \frac{\partial e}{\partial p}\Big)_{\rho} dp + \frac{\partial e}{\partial \rho}\Big)_{p} d\rho$, we obtain:

$$de = \frac{\partial e}{\partial p}\Big)_{\rho} dp + \frac{\partial e}{\partial \rho}\Big)_{p} d\rho = \frac{p}{\rho^2} d\rho$$

Which means:

$$\frac{dp}{d\rho} = \frac{\partial p}{\partial \rho}\Big)_{s} = \frac{\left[\frac{p}{\rho^2} - \frac{\partial e}{\partial \rho}\Big)_{p}\right]}{\frac{\partial e}{\partial p}\Big)_{\rho}} = c^2$$

B

The ADCR model of EUROPLEXUS

The ADCR model has been specifically developed to deal with HCDA. Details can be found in the Users Manual [Europlexus, 2020]. This section is a summary of [Beccantini, 2019, Appendix A].

This model involves three regions:

1. Gas bubble.
2. Liquid sodium.
3. Argon.

I.e. there are two phases (liquid and gas) and three species (sodium, gas bubble and argon).

On one hand, it is supposed that the two gaseous species cannot occupy the same control volume. On the other hand, when a gaseous species and the liquid occupy the same control volume, it is supposed that they present the same pressure p and the same velocity $\mathbf{v}$ (**one pressure and one velocity two phase model**).

The governing equations are the **Euler equations** (conservation of the masses and of the momentum for non-viscous phenomena):

$$\begin{aligned} \frac{\partial \rho Y_i}{\partial t} + \nabla \cdot (\rho Y_i \mathbf{v}) = 0, \quad i = 1, 2 \\ \frac{\partial \rho}{\partial t} + \nabla \cdot (\rho \mathbf{v}) = 0 \\ \frac{\partial \rho \mathbf{v}}{\partial t} + \nabla \cdot (\rho \mathbf{v} \otimes \mathbf{v}) + \nabla p = 0. \end{aligned}$$

where ρ is the total mass, Y_i is the mass fraction of each species (the ratio between the mass of the species and the total control volume), $\mathbf{v}$ and p the speed and the pressure.

The conservation equation for the energy is not considered. For each species it is

$$\mathrm{d}e = -p\mathrm{d}\left(\frac{1}{\rho}\right) + T\mathrm{d}s. \tag{B.1}$$

where e is the internal energy per unit mass, T the temperature, s the entropy, $c_v$the constant volume specific heat, γ the heat specific ratio.

B.0.1 Gaseous phase

As far as the **argon** and the **bubble** are concerned, we suppose that they behave as a perfect gas, with

$$\mathrm{d}e = c_v \mathrm{d}T = \frac{R}{\gamma - 1}\mathrm{d}T$$

$$p = \rho R T$$

which, combined together, gives

$$e - e_0 = \frac{p}{(\gamma - 1)\rho}$$

("0" standing for the reference state), or

$$\mathrm{d}e = \frac{1}{\gamma - 1}\left(\frac{1}{\rho}\mathrm{d}p + p\mathrm{d}\left(\frac{1}{\rho}\right)\right) = \frac{p}{(\gamma - 1)\rho}\left(\frac{1}{p}\mathrm{d}p - \frac{1}{\rho}\mathrm{d}\rho\right). \tag{B.2}$$

If we combine equations (B.1) and (B.2), we obtain

$$\mathrm{d}e = \frac{1}{\gamma - 1}\left(\frac{1}{\rho}\mathrm{d}p + p\mathrm{d}\left(\frac{1}{\rho}\right)\right) = -p\mathrm{d}\left(\frac{1}{\rho}\right) + T\mathrm{d}s,$$

i.e.

$$T\mathrm{d}s = \frac{1}{\gamma - 1}\left(\frac{1}{\rho}\mathrm{d}p + \gamma p\mathrm{d}\left(\frac{1}{\rho}\right)\right). \tag{B.3}$$

Concerning the **argon**, we suppose that it behaves isentropically[1]. From equation (B.3) we obtain

$$\frac{1}{p}\mathrm{d}p = \frac{\gamma}{\rho}\mathrm{d}\rho$$

or

$$\frac{p}{p_0} = \left(\frac{\rho}{\rho_0}\right)^{\gamma}.$$

which also gives

$$\frac{T}{T_0} = \left(\frac{\rho}{\rho_0}\right)^{\gamma - 1}.$$

i.e. during an isentropic compression the temperature increases; vice-versa, during an isentropic expansion it decreases.

As far as the **gas bubble** is concerned, we suppose that the transformation is not isentropic. From a physical point of view, it is surrounded by hot corium, which continuously injects heat inside the bubble. For the sake of simplicity, we suppose that the process is polytropic, namely

$$\frac{p}{p_0} = \left(\frac{\rho}{\rho_0}\right)^{n}.$$

or

$$\frac{T}{T_0} = \left(\frac{\rho}{\rho_0}\right)^{n - 1}.$$

Then, for physical reason, the temperature should be greater than temperature during an isentropic expansion. As one can see from the previous equation during an expansion the temperature behaves as follows.

[1] We remind that, if the flow does not involve strong shocks, the conservation of the entropy implies the conservation of the total energy and vice-versa [Courant and Friedrichs, 1948]

- $n = \gamma$: the temperature decreases as in the isentropic case;
- $\gamma < n < 1$: the temperature decreases less that in the isentropic case;
- $n = 1$: the temperature is constant;
- $n < 1$: the temperature increases as the density decreases.

In the same manner, during a compression we should have $n > \gamma$. However, since the bubble mainly expands, **for the sake of simplicity we always take** $n < \gamma$. From equation (B.3) one obtains

$$dq = \frac{p}{(\gamma-1)\rho}\left(\frac{1}{p}\mathrm{d}p - \frac{\gamma}{\rho}\mathrm{d}\rho\right) = \frac{p_0}{(\gamma-1)\rho_0}\left(\frac{\rho}{\rho_0}\right)^n (n-\gamma)\frac{1}{\rho}\mathrm{d}\rho = \frac{(n-\gamma)p_0}{(\gamma-1)\rho_0}\left(\frac{\rho}{\rho_0}\right)^{n-1}\mathrm{d}\left(\frac{\rho}{\rho_0}\right).$$

which confirms that, when $n < \gamma$, dq is positive when $\mathrm{d}\rho$ is negative (during a bubble expansion).

Remark. Before concluding we emphasize that, from equation (B.1)) that for an isentropic transformation

$$\mathrm{d}e = p_0\left(\frac{\rho}{\rho_0}\right)^\gamma \frac{\mathrm{d}\rho}{\rho^2} = \left(\frac{p_0}{\rho_0}\right)\left(\frac{\rho}{\rho_0}\right)^{\gamma-2}\frac{\mathrm{d}\rho}{\rho_0}$$

and for a polytropic transformation,

$$\mathrm{d}e - dq = \left(\frac{p_0}{\rho_0}\right)\left(\frac{\rho}{\rho_0}\right)^{n-2}\frac{\mathrm{d}\rho}{\rho_0}$$

Namely for $n > 1$ we would obtain the same results as we considered an isentropic transformation for a perfect gas with specific ratio equal to n:

$$\mathrm{d}e' = \left(\frac{p_0}{\rho_0}\right)\left(\frac{\rho}{\rho_0}\right)^{n-2}\frac{\mathrm{d}\rho}{\rho_0} \tag{B.4}$$

Note that even in the case $n = 1$ we have a negative variation of e' during a polytropic expansion: ($\Delta T = 0$ but $c'_v = R/(n-1) = \infty$).

B.0.2 Liquid phase

We suppose that the liquid phase goes through isentropic transformations only. Moreover, we linearize the EOS in the form

$$p = p(\rho, s)$$

and we obtain

$$p \approx p_0 + \left(\frac{\partial p}{\partial \rho}\right)_s (\rho - \rho_0) = p_0 + c_s^2(\rho - \rho_0).$$

Then the internal energy variation is given by

$$\mathrm{d}e = \frac{p}{\rho^2}\mathrm{d}\rho + \underbrace{T\mathrm{d}s}_{0}$$

i.e.

$$e - e_0 = \frac{p_0}{\rho_0}\left(1 - \frac{\rho_0}{\rho}\right) + c_s^2\left(\ln\left(\frac{\rho}{\rho_0}\right) - \left(1 - \frac{\rho_0}{\rho}\right)\right)$$

We define

$$x = 1 - \frac{\rho_0}{\rho}$$

i.e.

$$\frac{\rho}{\rho_0} = \frac{1}{(1-x)}$$

If $x \approx 0$,

$$\ln(1+x) = x - \frac{1}{2}x^2 + 0\left((x^3\right)$$

$$\ln\left(\frac{1}{1-x}\right) = -\ln(1-x) = x + \frac{1}{2}x^2 + 0\left((x^3\right)$$

i.e.

$$e - e_0 \approx \frac{p_0}{\rho_0}\left(1 - \frac{\rho_0}{\rho}\right) + \frac{1}{2}c_s^2\left(1 - \frac{\rho_0}{\rho}\right)^2$$

B.0.3 Liquid-gas mixing

If a control volume is occupied by both liquid (L) and gas (G), the volume fraction modifies such that the liquid and the gas present the same value for the pressure. We call α the gas volume fraction. According to EOS for liquid

$$p_L = p_{L,0} + c_{s,L,0}^2(\rho_L - \rho_{L,0}) = p_{L,0} + c_{s,L,0}^2\left(\frac{\rho Y_L}{1-\alpha} - \rho_{L,0}\right) \tag{B.5}$$

Note that, for the definition above, (ρY_L) is the total mass of liquid per unit volume in the total control volume (occupied by both liquid and gas); $(\rho Y_L)/(1-\alpha)$ is the physical density of the liquid (which only occupies the fraction of the control volume $(1-\alpha)$).
According to the EOS for the gas

$$p_G = p_{G,0}\left(\frac{\rho_G}{\rho_{G,0}}\right)^n = p_{G,0}\left(\frac{\rho Y_G}{\rho_{G,0}}\right)^n \frac{1}{\alpha^n} \tag{B.6}$$

We suppose that the pressure equilibrium is an infinitely fast phenomenon. If follows that at a generic time t in each control volume the RHS of equations (B.5) and (B.6) are function of α only, which presents the value such that

$$p_L(\alpha) = p_G(\alpha). \tag{B.7}$$

We emphasize that $p_L(\alpha)$ is a monotone function which varies from a finite value ($\alpha = 0$, positive or negative), to a positive infinite value ($\alpha = 1$). $p_G(\alpha)$ is monotone function varying from a positive finite value ($\alpha = 1$) to a positive infinite value ($\alpha = 0$). It follows that there exists one and only one positive solution for equation (B.6).

During this infinitely fast phenomenon we have energy exchanges between liquid and gas; moreover, for the gas bubble, we have heat exchange when n is different from γ.

As far as the mixture energy is concerned, it is equal to the sum of the energies of the gas and the liquid phases:

$$\rho e = \rho_L e_L + \rho_G e_G = \frac{\rho Y_L}{1-\alpha} e_L + \frac{\rho Y_G}{\alpha} e_G$$

or

$$e = \frac{Y_L}{1-\alpha} e_L + \frac{Y_G}{\alpha} e_G.$$

As far as the sound speed is concerned, we observe that in an isentropic transformation in which mass fractions are constant, from (B.5) and (B.6) we have

$$\mathrm{d}p_L = c_{s,L,0}^2 \left(\frac{Y_L}{1-\alpha} \mathrm{d}\rho + \frac{\rho Y_L}{(1-\alpha)^2} \mathrm{d}\alpha \right)$$

and

$$\mathrm{d}p_G = c_{s,G}^2 \left(\frac{Y_G}{\alpha} \mathrm{d}\rho - \frac{\rho Y_G}{(\alpha)^2} \mathrm{d}\alpha \right).$$

Since $\mathrm{d}p_L = \mathrm{d}p_G = \mathrm{d}p$, by eliminating $\mathrm{d}\alpha$ from the previous formulae we find that

$$\left(\frac{(1-\alpha)^2}{Y_L \rho c_{s,L,0}^2} + \frac{(\alpha)^2}{Y_G \rho c_{s,L,0}^2} \right) \mathrm{d}p = \frac{1}{\rho} \left(\alpha + (1-\alpha) \right) \mathrm{d}\rho$$

i.e. the expected Wallis formula

$$\frac{1}{\rho c_s^2} = \left(\frac{(1-\alpha)}{\rho_L c_{s,L,0}^2} + \frac{\alpha}{\rho_G c_{s,G}^2} \right).$$

C

The 2D axisymmetric cylindrical piston problem with WPIC on triangular (TRI) mesh

For reasons of completeness, we present below the numerical results of the 2D axisymmetric cylindrical piston problem with WPIC using the HLLC solver on TRI mesh. The test case is a complement for the results presented in sections 2.1 and 3.5.3. The dimension and the initial conditions have already been discussed in section 3.5.3.

Comparison for case 1:

In Figure C.1, the computed velocity fields are shown on the QUAD and TRI meshes. It is clearly observed that the TRI mesh gives the expected one-dimensional behavior and help fix the wrong solution given on QUAD mesh. The corresponding projections for the TRI mesh results on the different lines and at different times are also presented in Figure C.3. These two instants correspond to different phases of the piston velocity: $t = 3.5 \times 10^{-1}$ s with $V_p = 1$ m/s (in the zero acceleration phase) and $t = 5.0 \times 10^{-1}$ s with $V_p = 0$ (in the deceleration phase). From these comparisons, we state that the HLLC solver on TRI mesh is able to produce a correct solution for the velocity in the low-Mach number regime: all numerical solutions projected on different angles -22.5, -45, -67.5 and the reference velocity field are superimposed every instants. Note that at $t = 5.0 \times 10^{-1}$ s, the velocity field given by (3.25) is equal to zero everywhere in the flow.
Concerning the projected pressure solutions presented in Figure C.2 at the same two instants, oscillations about the reference one are seen. However, as discussed in section 3.5.3, the pressure fluctuations are negligible from a practical viewpoint since it is very small when compared to the thermodynamic pressure of order 1.0×10^5 Pa.

Comparison for case 2:

In case 2, we add as discussed in section 3.5.2.2 the dynamic pressure in the initial pressure field. As observed in Figures C.4, this does not help improve the accuracy in computing the dynamic pressure. The velocity is always correctly computed as shown in Figure C.5. We emphasize in all cases that mesh refinement does not help the convergence towards the reference solution.
Despite giving goods solutions, the efficiency problem remains which requires developing novel methods with the aim at reducing the CPU time consumption.

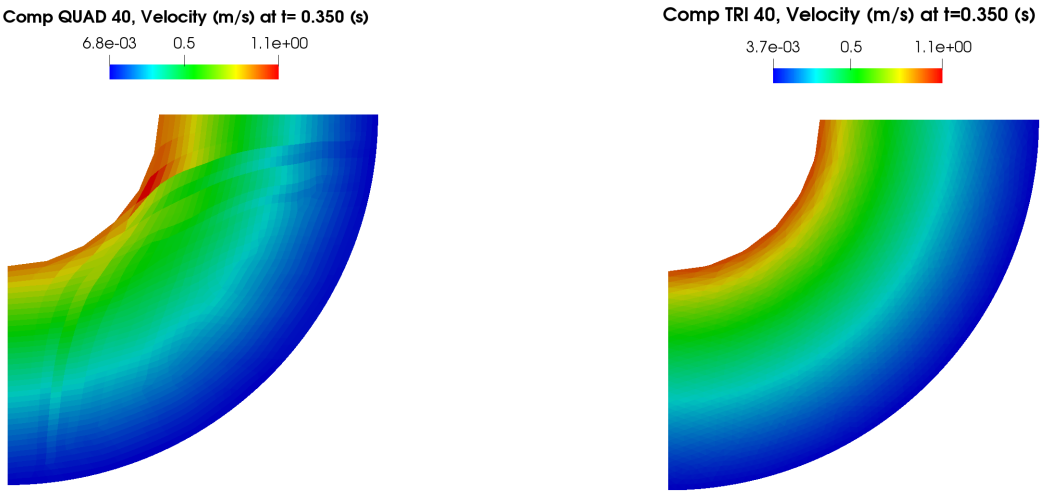

Figure C.1: 2D axisymmetric cylindrical piston problem with WPIC. Case 1: Velocity solutions at $t = 0.35$ s, $CFL = 0.5$. HLLC solver on coarse QUAD mesh (left), HLLC solver on coarse TRI mesh (right).

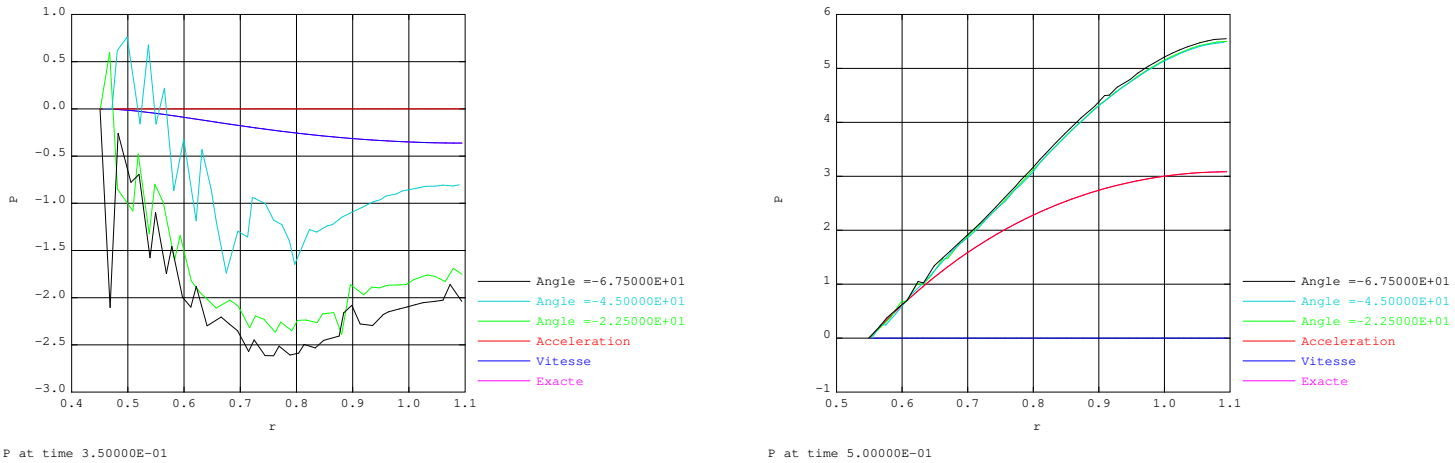

Figure C.2: 2D axisymmetric cylindrical piston problem with WPIC. Case 1: Projected pressures at $t = 3.5 \times 10^{-1}$ s (left) and $t = 5.0 \times 10^{-1}$ s (right). HLLC solver on coarse TRI mesh.

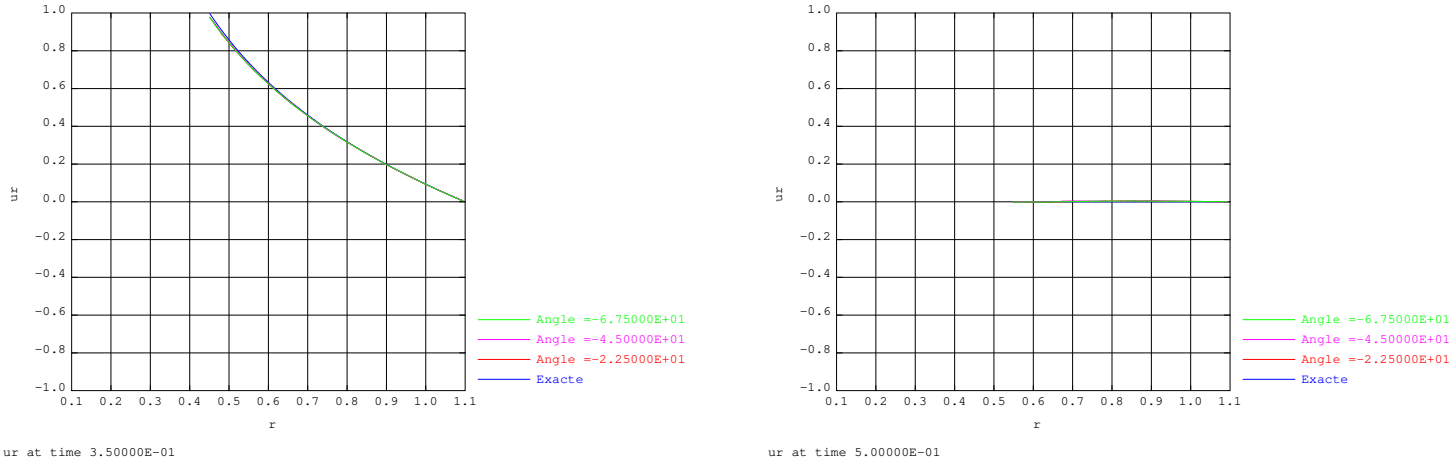

Figure C.3: 2D axisymmetric cylindrical piston problem with WPIC. Case 1: Projected velocities at $t = 3.5 \times 10^{-1}$ s (left) and $t = 5.0 \times 10^{-1}$ s (right). HLLC solver on coarse TRI mesh.

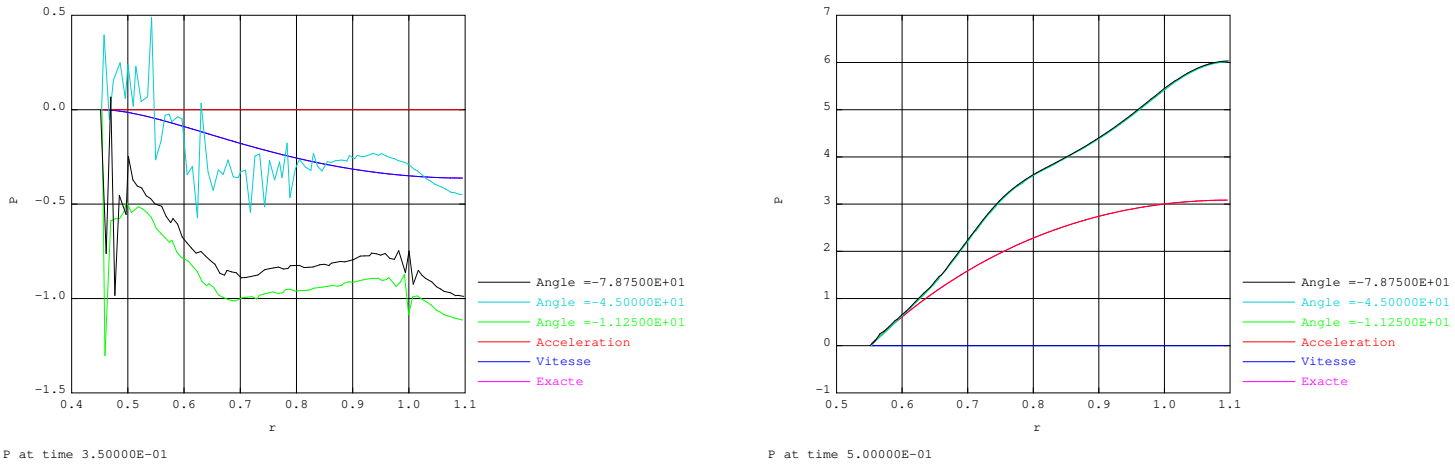

Figure C.4: 2D axisymmetric cylindrical piston problem with WPIC. Case 2: Projected pressures at $t = 3.5 \times 10^{-1}$ s (left) and $t = 5.0 \times 10^{-1}$ s (right). HLLC solver on coarse TRI mesh.

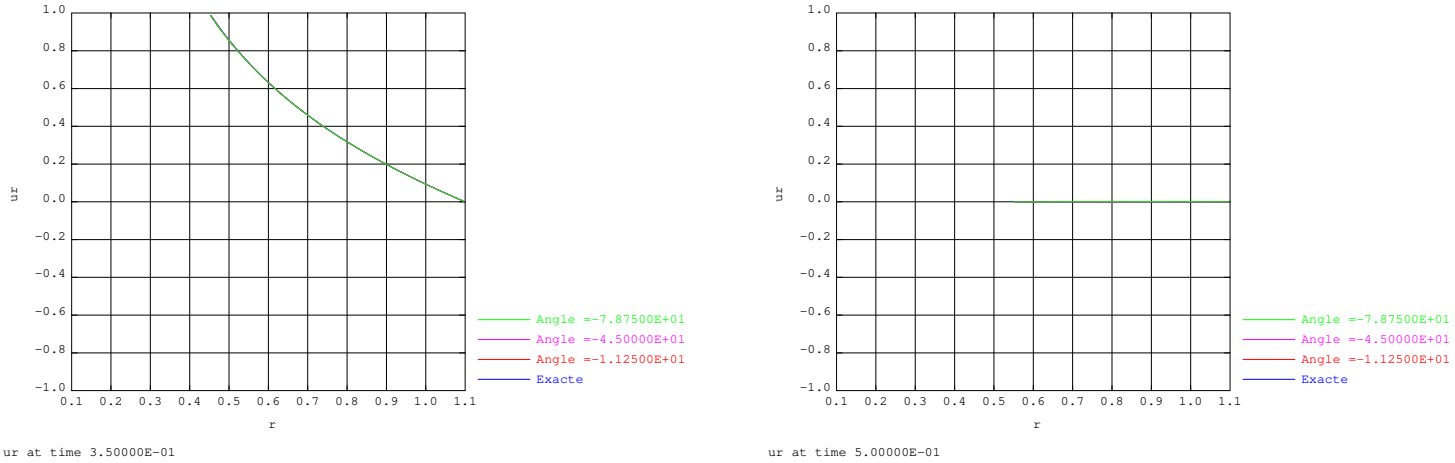

Figure C.5: 2D axisymmetric cylindrical piston problem with WPIC. Case 2: Projected velocities at $t = 3.5 \times 10^{-1}$ s (left) and $t = 5.0 \times 10^{-1}$ s (right). HLLC solver on coarse TRI mesh.

D

Some analytical verification for the developed numerical methods

D.1 Verification of the AC-LM method for single-phase flow

In this section, we consider a simple example in order to verify the numerical schemes proposed in the previous section. In particular, we investigate the density solution given by the 1D transport equation with the initial condition supposed to be piecewise constant qualitatively illustrated in Figure D.1 (top).

$$\frac{\partial \rho}{\partial t} + u\frac{\partial \rho}{\partial x} = 0$$
$$\rho(x, t^n) = \begin{cases} \rho_i^n, \ x \in C_i \\ \rho_{i+1}^n, \ x \in C_{i+1} \end{cases}$$

We neglect the contribution to the solution from the cell $i-1$. Moreover, we suppose that the density is transported to the left with a speed faster than the displacement speed of the intercell $|u_{m,i+1/2}| < |u^*|$. By supposing the solution structure in Figure D.1 (bottom), the exact density solution ρ_i^{n+1} is graphically illustrated in Figure D.2 and can be expressed as:

$$\begin{aligned} \rho_i^{n+1} &= \frac{S_{A'BDEHF'}}{\Delta x_i^{n+1}} = \frac{S_{A'BDC'} + S_{C'EHF'}}{\Delta x_i^{n+1}} \\ &= \frac{(\rho_{i+1}^n - \rho_i^n)\left[-u^* - (-u_{m,i+1/2})\right]\Delta t}{\Delta x_i^{n+1}} + \frac{\rho_i^n\left[\Delta x^n - (-u_{m,i+1/2})\Delta t\right]}{\Delta x_i^{n+1}} \end{aligned} \tag{D.1}$$

We now investigate the numerical scheme (3.17). With the solution structure in Figure D.1 (bottom):

- The velocity along the intercell $x/t = u_{m,i+1/2}$ is determined by:

$$u_{i+1/2} = u^*$$

- The numerical flux along the intercell $x/t = u_{m,i+1/2}$ is computed as:

$$F_{i+1/2}^{ALE} = \rho_{i+1}^n u^* - \rho_{i+1}^n u_{m,i+1/2} = (u^* - u_{m,i+1/2})\rho_{i+1}^n$$

The density solution can therefore be computed by the scheme (3.17) as:

$$\begin{aligned} \rho_i^{n+1} &= \rho_i^n \frac{\Delta x_i^n}{\Delta x_i^{n+1}} - \frac{(u^* - u_{m,i+1/2})\Delta t}{\Delta x_i^{n+1}}\rho_{i+1}^n + \frac{u^*\Delta t}{\Delta x_i^{n+1}}\rho_i^n \\ &= \frac{S_{CEHF}}{\Delta x_i^{n+1}} - \frac{-S_{A'BGF'}}{\Delta x_i^{n+1}} - \frac{S_{CDGF}}{\Delta x_i^{n+1}} = \frac{S_{A'BDEHF'}}{\Delta x^{n+1}} \end{aligned} \tag{D.2}$$

which is exactly equal to the formula (D.1).

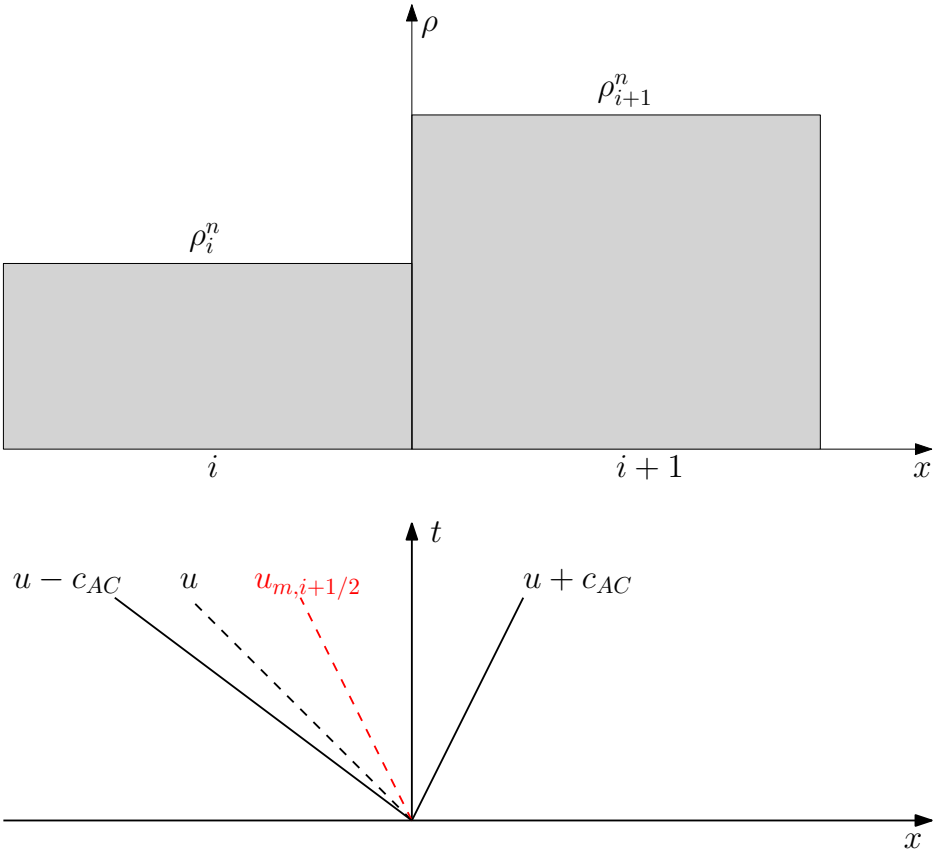

Figure D.1: Verification for the density solution: Initial density (top); Supposing solution structure for the Riemann problem (bottom).

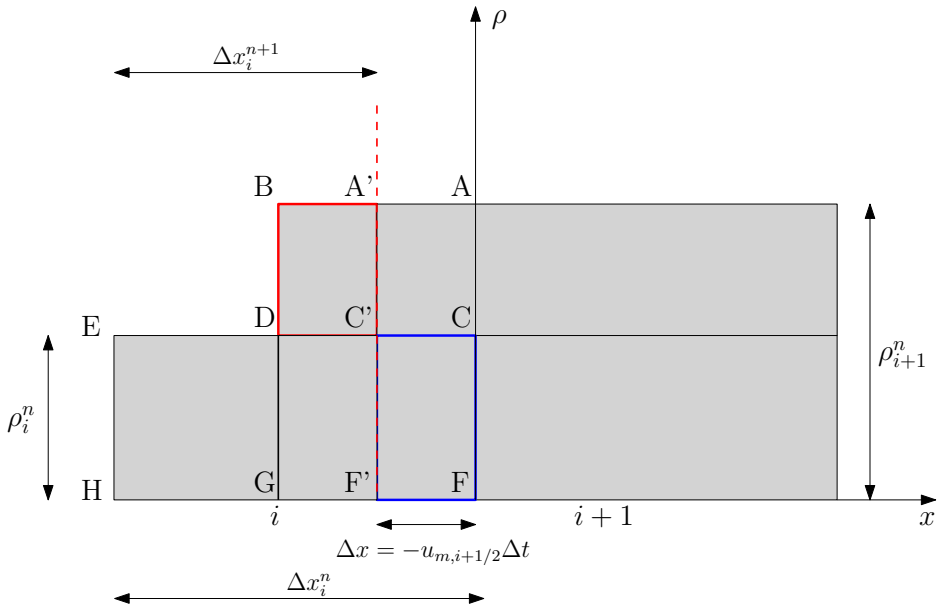

Figure D.2: Verification for the density solution: Density solution at $t = t^{n+1}$ before taking the cell average

D.2 Verification of the DEM-LM method for two-phase flow

We investigate in this section a simple example in order to verify the DEM-LM taking into account the moving cell boundaries by the ALE approach. In particular, we analyze the quantity $\alpha\rho$ for the phase Σ_1 shaded in Figure D.3 governed by the one-dimensional transport equation $(5.9)_2$:

$$\frac{\partial(\alpha\rho)}{\partial t} + u\frac{\partial(\alpha\rho)}{\partial x} = 0 \tag{D.3}$$

Moreover, we assume the IN Σ_1 case meaning the phase Σ_1 enters the cell i from its neighboring cell $i+1$ with a speed supposed to be faster than the speed of the intercell. The quantity $\alpha\rho$ takes initially the values $\alpha_i^n\rho_i^n$ and $\alpha_{i+1}^n\rho_{i+1}^n$ in the cells i and $i+1$ respectively with $\alpha_i^n\rho_i^n < \alpha_{i+1}^n\rho_{i+1}^n$.

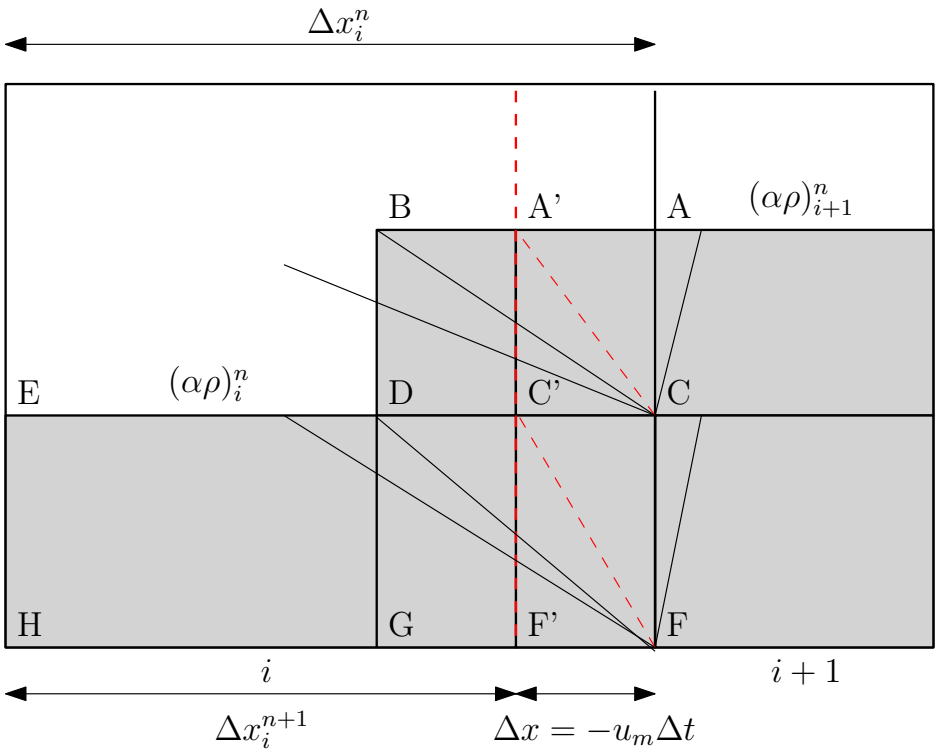

Figure D.3: IN Σ_1 ALE case

At the beginning, the quantity $\alpha\rho$ in cell i can be expressed graphically as:

$$(\Delta x\alpha\rho)_i^n = \Delta x_i^n(\alpha\rho)_i^n = S_{CEHF}$$

If we neglect the contribution from the intercell $i-1/2$, the quantity $\alpha\rho$ at later time will be transported with a velocity u^* supposed to be negative. By considering the moving intercell with the velocity $u_m < 0$, the quantity $\alpha\rho$ can be exactly calculated at $t^{n+1} = t^n + \Delta t$ as:

$$\begin{aligned}(\Delta x\alpha\rho)_i^{n+1} &= S_{A'BDEHF'} = S_{CEHF} + S_{ABDC} - S_{AA'F'F} \\ &= \Delta x_i^n(\alpha\rho)_i^n + \underbrace{(\alpha_{i+1}^n\rho_{i+1}^n - \alpha_i^n\rho_i^n)(-u^*)\Delta t}_{\text{added part to fixed mesh}} - \underbrace{\alpha_{i+1}^n\rho_{i+1}^n(-u_m)\Delta t}_{\text{removed part ALE}}\end{aligned} \tag{D.4}$$

The variation of the quantity $\Delta x\alpha\rho$ during Δt is:

$$\begin{aligned}(\Delta x\alpha\rho)_i^{n+1} - (\Delta x\alpha\rho)_i^n &= S_{ABDC} - S_{AA'F'F} \\ &= \underbrace{(\alpha_{i+1}^n\rho_{i+1}^n - \alpha_i^n\rho_i^n)(-u^*)\Delta t}_{\text{added part to fixed mesh}} - \underbrace{\alpha_{i+1}^n\rho_{i+1}^n(-u_m)\Delta t}_{\text{removed part ALE}}\end{aligned} \tag{D.5}$$

We now investigate the DEM-LM scheme in the ALE case (5.15) considering the transport equation (D.3) written in a more conservative form for the DEM-LM scheme as:

$$\frac{\partial(\alpha\rho)}{\partial t} + \frac{\partial(\alpha\rho u)}{\partial x} = \alpha\rho\frac{\partial u}{\partial x}$$

We notice that there is no contribution of the Lagrangian fluxes and the two main contributions are of the conservative fluxes and the source term associated to the divergence of velocity. Moreover, in the case of a simple transport equation, the velocity are the same on the intercells and on the contact waves, namely:

$$u^*_{i+1/2,2P} = u^0_{i+1/2,2P} = u^*_{i+1/2,1P} = u^0_{i+1/2,1P} = u^*$$

The conservative fluxes can be computed in terms of the contributions of the 1P and 2P RPs:

$$\begin{aligned}
(\alpha\mathbf{F}^{ALE})_{1,i+1/2,2P,IN\ \Sigma_1} &= (\alpha^n_{i+1} - \alpha^n_i)\rho^n_{i+1}(u^0_{i+1/2,2P} - u_m) \\
&= (\alpha^n_{i+1} - \alpha^n_i)\rho^n_{i+1}(u^* - u_m) \\
(\alpha\mathbf{F}^{ALE})_{1,i+1/2,1P,IN\ \Sigma_1} &= \alpha^n_i\rho^n_{i+1}(u^0_{i+1/2,1P} - u_m) = \alpha^n_i\rho^n_{i+1}(u^* - u_m)
\end{aligned}$$

And the total contribution of the conservative fluxes is the sum of two above formulas:

$$(\alpha\mathbf{F}^{ALE})_{1,i+1/2,IN\ \Sigma_1} = \alpha^n_{i+1}\rho^n_{i+1}(u^* - u_m)$$

Similarly, the source terms can be computed in terms of the contributions of the 1P and 2P RPs:

$$\begin{aligned}
\mathbf{B}_{1,i,2P} &= (\alpha^n_{i+1} - \alpha^n_i)\rho^n_{i+1}(u^*_{i+1/2,2P} - u^0_{i+1/2,2P}) = 0 \\
\mathbf{B}_{1,i,1P} &= \alpha^n_i\rho^n_i(u^0_{i+1/2,1P}) = \alpha^n_i\rho^n_i u^*
\end{aligned}$$

And the total contribution of the source terms is the sum of two above formulas:

$$\mathbf{B}_{1,i} = \alpha^n_i\rho^n_i u^*$$

Finally, the variation of the quantity $\Delta x\alpha\rho$ during Δt computed by (5.15) is:

$$(\Delta x\alpha\rho)^{n+1}_i - (\Delta x\alpha\rho)^n_i = (\alpha^n_{i+1}\rho^n_{i+1} - \alpha^n_i\rho^n_i)(-u^*)\Delta t - \alpha^n_{i+1}\rho^n_{i+1}(-u_m)\Delta t \tag{D.6}$$

Which is exactly equal to (D.5) calculated analytically.

E

Instantaneous relaxation procedure

For the sake of completeness, we briefly summarize basic principles of the relaxation procedure applied to our two-phase solvers (namely DEM and DEM-LM). We refer to [Tang, 2012], appendix C for detailed steps of the relaxation process.
The instantaneous relaxation procedure introduced in [Saurel and Abgrall, 1999] represents, in addition to the two-fluid system, an internal phase interaction inside each cell element, with the purpose of "relaxing" the system till both phases contain the same pressure and velocity. Another utility of the relaxation procedures consists in taking account of the two-phase physical mixtures [Saurel and Abgrall, 1999, Abgrall and Saurel, 2003, Guillard and Murrone, 2006].
The relaxation procedure already described in [Tang, 2012] is composed of two steps performed firstly for the velocity and next for the pressure. The process does not involve any Newton type iterative method and is applied:

- After each iteration of the DEM solver.
- After the resolution of part I (hyperbolic part) for the DEM-LM solver.

The instantaneous velocity relaxation procedure (see Figure E.1) assume that the fluids are incompressible and act as rigid bodies. Using the mass conservation principle, it follows that the densities of two phases before and after this process stay unchanged:

$$\rho_1^0 = \rho_1^{0'},\ \rho_2^0 = \rho_2^{0'}$$

The equilibrium velocity can be next determined by applying the momentum conservation equation (see [Tang, 2012], equations C.6, C.7). The new values for pressure of each phase can be updated using SG-EOS computed from the density and the new values of the internal energy calculated by considering the conservation of total energy.

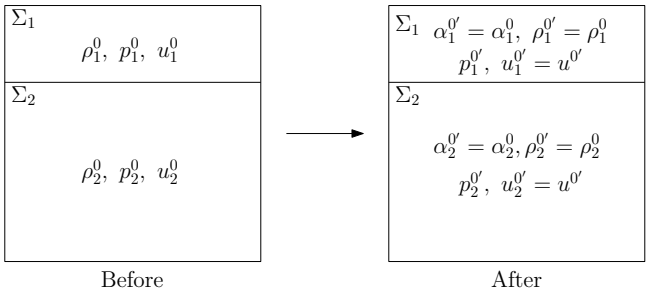

Figure E.1: Instantaneous relaxation procedure for the velocity.

The instantaneous pressure relaxation procedure considers a closed system supposing an adiabatic process of thermodynamics. The physical problem is similar to an isolated tank initially separated, by a moving boundary, into two chambers of compressible materials of different pressure, same density and velocity. The chamber with higher pressure will apply a force to move the boundary till the system finds its equilibrium state. It is obvious that the new equilibrium pressure together with the new values of density and volume (or volume fraction) of each phase must be determined by considering the basics conservation laws and thermodynamics principles (see [Tang, 2012], Appendix C.2) to obtain the final state.

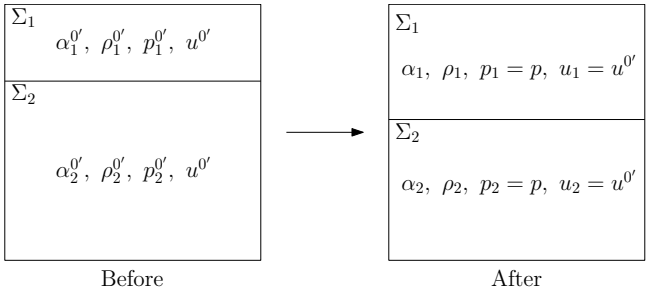

Figure E.2: Instantaneous relaxation procedure for the pressure.

Bibliography

[Abgrall and Saurel, 2003] Abgrall, R. and Saurel, R. (2003). Discrete equations for physical and numerical compressible multiphase mixtures. *Journal of Computational Physics*, 186(2):361–396.

[Acket et al., 1981] Acket, D., Benuzzi, A., Yerkess, A., and Louvet, J. (1981). MARA 01/02 - experimental validation of the SEURBNUK and SIRIUS containment codes. In *Proceedings of the Sixth International Conference on Structural Mechanics in Reactor Technology.*

[Batten et al., 1997] Batten, P., Clarke, N., Lambert, C., and Causon, D. M. (1997). On the Choice of Wavespeeds for the HLLC Riemann Solver. *SIAM Journal on Scientific Computing*, 18(6):1553–1570.

[Beccantini, 2017] Beccantini, A. (2017). 1D plane-, line- and point-symmetrical pressure waves generated by constant speed expanding piston in stiffened gases. Technical report, CEA/DEN/DANS/DM2S/SEMT/DYN/NT/17-004/A.

[Beccantini, 2019] Beccantini, A. (2019). Bubble expansion computations with two numerical models implemented in Europlexus . Homogeneous and 1D cases. Technical report, CEA/DEN/DANS/DM2S/SEMT/DYN/NT/2019-64237/A/DR.

[Beccantini et al., 2008] Beccantini, A., Studer, E., Gounand, S., Magnaud, J., and Kloczko, T. (2008). Numerical simulations of a transient injection flow at low Mach number regime. *International Journal for Numerical Methods in Engineering*, 76:662–696.

[Bruel et al., 2019] Bruel, P., Delmas, S., Jung, J., and Perrier, V. (2019). A low Mach correction able to deal with low Mach acoustics. *Journal of Computational Physics*, 378:723–759.

[Casadei and Halleux, 2009] Casadei, F. and Halleux, J.-P. (2009). Binary spatial partitioning of the central-difference time integration scheme for explicit fast transient dynamics. *International Journal for Numerical Methods in Engineering*, 78(12):1436–1473.

[Chorin, 1967] Chorin, A. J. (1967). A numerical method for solving incompressible viscous flow problems. *Journal of Computational Physics*, 2(1):12–26.

[Clausen, 2013] Clausen, J. R. (2013). Entropically damped form of artificial compressibility for explicit simulation of incompressible flow. *PHYSICAL REVIEW E*, 87(1).

[Courant and Friedrichs, 1948] Courant, R. and Friedrichs, K. O. (1948). *Supersonic flows and shock waves*. New York and London: Interscience Publishers, Inc.

[Couturier, 2011] Couturier, J. (2011). Prise en compte des accidents de type BORAX pour les réacteurs de recherche. Technical report, IRSN.

[Daude et al., 2014] Daude, F., Galon, P., Gao, Z., and Blaud, E. (2014). Numerical experiments using a HLLC-type scheme with ALE formulation for compressible two-phase flows five-equation models with phase transition. *Computers and Fluids*, 94:112–138.

[Dellacherie, 2010] Dellacherie, S. (2010). Analysis of Godunov type schemes applied to the compressible Euler system at low Mach number. *Journal of Computational Physics*, 229(4):978–1016.

[Dellacherie et al., 2016] Dellacherie, S., Jung, J., Omnes, P., and Raviart, P.-A. (2016). Construction of modified Godunov type schemes accurate at any Mach number for the compressible Euler system. In *Mathematical Models and Methods in Applied Sciences*. World Scientific Publishing.

[Drew and Passman, 1999] Drew, D. A. and Passman, S. L. (1999). *Theory of Multicomponent Fluids*, volume 135 of *Applied Mathematical Sciences*. Springer New York, New York, NY.

[Drikakis and Rider, 2005] Drikakis, D. and Rider, W. (2005). *High-Resolution Methods for Incompressible and Low-Speed Flows*. Computational Fluid and Solid Mechanics. Springer-Verlag, Berlin/Heidelberg.

[Dumbser and Balsara, 2016] Dumbser, M. and Balsara, D. S. (2016). A new efficient formulation of the HLLEM Riemann solver for general conservative and non-conservative hyperbolic systems. *Journal of Computational Physics*, 304:275–319.

[Dumbser and Toro, 2011a] Dumbser, M. and Toro, E. F. (2011a). A simple extension of the Osher Riemann solver to non-conservative hyperbolic systems. *Journal of Scientific Computing*, 48(1-3):70–88.

[Dumbser and Toro, 2011b] Dumbser, M. and Toro, E. F. (2011b). On universal Osher-type schemes for general nonlinear hyperbolic conservation laws. *Communications in Computational Physics*, 10(3):635–671.

[Europlexus, 2020] Europlexus (2020). Europlexus (visited in 2020). Europlexus, a computer program for the finite element simulation of fluid-structure systems under transient dynamic loading, http://www-epx.cea.fr.

[Fedkiw et al., 1999] Fedkiw, R. P., Marquina, A., and Merriman, B. (1999). An Isobaric Fix for the Overheating Problem in Multimaterial Compressible Flows. *Journal of Computational Physics*, 148(2):545–578.

[Fiche et al., 1985] Fiche, C., Louvet, J., Smith, B., and Zucchini, A. (1985). Theoretical Experimental Study of Flexible Roof Effects in an HCDA's Simulation. In *8th International Conference on Structural Mechanics in Reactor Technology*, pages 139–144.

[Galon, 2002] Galon, P. (2002). Rapport DM2S-Europlexus-Fiche de qualification: Essai MARA 02.pdf. Technical report.

[Giuliani, 1982] Giuliani, S. (1982). An algorithm for continuous rezoning of the hydrodynamic grid in Arbitrary Lagrangian-Eulerian computer codes. *Nuclear Engineering and Design*, 72(2):205–212.

[Godunov, 1959] Godunov, S. (1959). Finite difference method for numerical computation of discontinuous solutions of the equations of fluid dynamics. *Matematicheskii Sbornik*, 47(89)(3):271–306.

[Gresho and Chan, 1990] Gresho, P. M. and Chan, S. T. (1990). On the theory of semi-implicit projection methods for viscous incompressible flow and its implementation via a finite element method that also introduces a nearly consistent mass matrix. Part 2: Implementation. *International Journal for Numerical Methods in Fluids*, 11(5):621–659.

[Guillard, 2009] Guillard, H. (2009). On the behavior of upwind schemes in the low Mach number limit. IV: P0 approximation on triangular and tetrahedral cells. *Computers & Fluids*, 38(10):1969–1972.

[Guillard and Murrone, 2004] Guillard, H. and Murrone, A. (2004). On the behavior of upwind schemes in the low Mach number limit: II. Godunov type schemes. *Computers and Fluids*, 33(4):655–675.

[Guillard and Murrone, 2006] Guillard, H. and Murrone, A. (2006). A five equation reduced Model for compressible two phase flowproblems. Technical report, INRIA.

[Guillard and Viozat, 1999] Guillard, H. and Viozat, C. (1999). On the behaviour of upwind schemes in the low Mach number limit. *Computers & Fluids*, 28(1):63–86.

[Harten et al., 1983] Harten, A., Lax, P. D., and van Leer, B. (1983). On Upstream Differencing and Godunov-Type Schemes for Hyperbolic Conservation Laws. *SIAM Review*, 25(1):35–61.

[Ivings et al., 1998] Ivings, M. J., Causon, D. M., and Toro, E. F. (1998). On Riemann solvers for compressible liquids. *International Journal for Numerical Methods in Fluids*, 28(3):395–418.

[Joukowski, 1900] Joukowski, N. E. (1900). Memoirs of the Imperial Academy Society of St. Petersburg.

[Klein, 1995] Klein, R. (1995). Semi-implicit extension of a godunov-type scheme based on low mach number asymptotics I: One-dimensional flow. *Journal of Computational Physics*.

[Le Métayer et al., 2005] Le Métayer, O., Massoni, J., and Saurel, R. (2005). Modelling evaporation fronts with reactive Riemann solvers. *Journal of Computational Physics*, 205(2):567–610.

[Le Métayer and Saurel, 2016] Le Métayer, O. and Saurel, R. (2016). The Noble-Abel Stiffened-Gas equation of state. *Physics of Fluids*, 28(4):046102.

[Li and Gu, 2013] Li, X.-s. and Gu, C.-w. (2013). Mechanism of Roe-type schemes for all-speed flows and its application. *Computers & Fluids*, 86:56–70.

[Louvet et al., 1987] Louvet, J., Hamon, P., Smith, B., and Zucchini, A. (1987). MARA 10: An integral model experiment in support of LMFBR containment analyses. In *Proceedings of the Ninth International Conference on Structural Mechanics in Reactor Integrity*, Lausanne, Switzerland.

[Ma et al., 2015] Ma, R., Chang, X., Zhang, L., He, X., and Li, M. (2015). On the Geometric Conservation Law for Unsteady Flow Simulations on Moving Mesh. In *Procedia Engineering*, volume 126, pages 639–644. Elsevier Ltd.

[Madsen and Schäffer, 2006] Madsen, P. and Schäffer, H. (2006). A discussion of artificial compressibility. *Coastal Engineering*, 53(1):93–98.

[Miczek, 2012] Miczek, F. (2012). *Simulation of low Mach number astrophysical flows*. PhD thesis, Technische Universitat Munchen.

[Miczek et al., 2015] Miczek, F., Roepke, F. K., and Edelmann, P. V. F. (2015). New numerical solver for flows at various Mach numbers. *Astronomy & Astrophysics*, 576(A50).

[Nourgaliev et al., 2004] Nourgaliev, R., Dinh, T., and Theofanous, T. (2004). A pseudocompressibility method for the numerical simulation of incompressible multifluid flows. *International Journal of Multiphase Flow*, 30(7-8):901–937.

[Paolucci, 1982] Paolucci, S. (1982). On the filtering of sound from the Navier-Stokes Equations. *Sandia Nat. Lab. Rep.*, (SAND82-8257):54.

[Pelanti, 2017] Pelanti, M. (2017). Low Mach number preconditioning techniques for Roe-type and HLLC-type methods for a two-phase compressible flow model. *Applied Mathematics and Computation*, 310:112–133.

[Perrier, 2007] Perrier, V. (2007). *Numerical simulation of compressible multiphase flows with or without phase transition. Application to laser plasma interaction.* PhD thesis, University of Bordeaux.

[Rieper, 2008] Rieper, F. (2008). *On the Behaviour of Numerical Schemes in the Low Mach Number Regime.* PhD thesis, Brandenburgischen Technischen Universitat Cottbus.

[Rieper and Bader, 2009] Rieper, F. and Bader, G. (2009). The influence of cell geometry on the accuracy of upwind schemes in the low mach number regime. *Journal of Computational Physics*, 228(8):2918–2933.

[Robbe and Casadei, 2004] Robbe, M. F. and Casadei, F. (2004). Comparison of various models for the simulation of a Core Disruptive Accident in the MARA 10 mock-up. *Nuclear Engineering and Design*, 232(3):301–326.

[Robbe et al., 2003a] Robbe, M. F., Lepareux, M., and Cariou, Y. (2003a). Numerical interpretation of the mara 8 experiment simulating a hypothetical core disruptive accident. *Nuclear Engineering and Design*, 220(2):119–158.

[Robbe et al., 2003b] Robbe, M. F., Lepareux, M., Treille, E., and Cariou, Y. (2003b). Numerical simulation of a hypothetical core disruptive accident in a small-scale model of a nuclear reactor. *Nuclear Engineering and Design*, 223(2):159–196.

[Roller et al., 2005] Roller, S., Schwartzkopff, T., Fortenbach, R., Dumbser, M., and Munz, C. D. (2005). Calculation of low Mach number acoustics : a comparison of MPV , EIF and linearized Euler equations. *ESAIM: Mathematical Modelling and Numerical Analysis*, 39:561–576.

[Saurel and Abgrall, 1999] Saurel, R. and Abgrall, R. (1999). A Simple Method for Compressible Multifluid Flows. *SIAM Journal on Scientific Computing*, 21(3):1115.

[Schochet, 1994] Schochet, S. (1994). Fast Singular Limits of Hyperbolic PDEs. *Journal of Differential Equations*, 114(2):476–512.

[Szargut et al., 1988] Szargut, J., Morris, D. R., and Steward, F. R. (1988). *Exergy Analysis of Thermal, Chemical, and Metallurgical Processes.* Hemisphere Publishing Corporation.

[Tang, 2012] Tang, K. (2012). *Combining Discrete Equations Method and Upwind Downwind-Controlled Splitting for Non-Reacting and Reacting Two-Fluid Computations.* PhD thesis, Université de Grenoble.

[Tang et al., 2014a] Tang, K., Beccantini, A., and Corre, C. (2014a). Combining Discrete Equations Method and upwind downwind-controlled splitting for non-reacting and reacting two-fluid computations: One dimensional case. *Computers and Fluids*, 93:74–90.

[Tang et al., 2014b] Tang, K., Beccantini, A., and Corre, C. (2014b). Combining Discrete Equations Method and Upwind Downwind-Controlled Splitting for non-reacting and reacting two-fluid computations: Two dimensional case. *Computers & Fluids*, 103:132–155.

[Taylor, 1946] Taylor, G. I. (1946). The Air Wave Surrounding an Expanding Sphere. *Proceedings of the Royal Society A: Mathematical, Physical and Engineering Sciences*, 186(1006):273–292.

[Toro, 2009] Toro, E. F. (2009). *Riemann Solvers and Numerical Methods for Fluid Dynamics*, volume 9208. Springer Berlin Heidelberg, Berlin, Heidelberg.

[Toro et al., 1994] Toro, E. F., Spruce, M., and Speares, W. (1994). Restoration of the contact surface in the HLL-Riemann solver. *Shock Waves*, 4(1):25–34.

[Turkel, 1987] Turkel, E. (1987). Preconditioned methods for solving the incompressible and low speed compressible equations. *Journal of Computational Physics*, 72(2):277–298.

[Volpe, 1993] Volpe, G. (1993). Performance of compressible flow codes at low Mach numbers. *AIAA Journal*, 31(1):49–56.

dernière page de la thèse

AUTORISATION DE SOUTENANCE

Vu les dispositions de l'arrêté du 25 mai 2016,

Vu la demande du directeur de thèse

Monsieur C. CORRE

et les rapports de

M. S. VINCENT
Professeur - Université Gustave Eiffel - Laboratoire de Modélisation et Simulation Multi Echelle - Equipe Transferts de Chaleur et de Matière - 5, Boulevard Descartes – 77454 Marne-la-Vallée Cedex 2

et de

M. Y. HOARAU
Professeur - Université de Strasbourg - Laboratoire ICube UMR 7357 - 2, rue Boussingault - 67000 Strasbroug

Monsieur PHAN Cong Huan

est autorisé à soutenir une thèse pour l'obtention du grade de **DOCTEUR**

Ecole doctorale Mécanique, Energétique, Génie Civil et Acoustique

Fait à Ecully, le 31 août 2021

P/Le directeur de l'E.C.L.
Le directeur des Formations

ECOLE CENTRALE DE LYON
Service Scolarité
ECULLY

Grégory VIAL